Dissertation
submitted to the
Combined Faculties for the Natural Sciences and for Mathematics
of the Rupertus Carola University of Heidelberg, Germany
for the degree of
Doctor of Natural Sciences

presented by
Diplom-Physicist: Christoph S. Garbe
born in: Bochum

Oral examination: 20.12.2001

Measuring Heat Exchange Processes at the Air-Water Interface from Thermographic Image Sequence Analysis

Referees: Prof. Dr. Bernd Jähne
Prof. Dr. Ulrich Platt

Zusammenfassung

In der vorliegenden Arbeit wird eine neuartige Technik zur Erfassung des Wärmeaustausches an der freien Wasseroberfläche entwickelt. Erstmals werden Wärmeflüsse und Transfergeschwindigkeiten flächenhaft mit einer hohen zeitlichen Auflösung gemessen. Des weiteren werden die statistischen Eigenschaften des Transportprozesses beleuchtet und die sie charakterisierenden Parameter ermittelt. Aus dieser Analyse ergibt sich eine weitere Methode, den Wärmefluß zu bestimmen. Die Grundlage der vorgestellten Meßverfahren bilden thermographische Bildsequenzen in denen eine Bewegungsschätzung durchgeführt wird. Dabei wird die Form der Bewegung allgemein parametrisiert und physikalisch motivierte Helligkeitsänderungen in Form linearer partieller Differentialgleichungen in die Bewegungsschätzung integriert. Somit ist es möglich die Parameter physikalischer Prozesse, die sich durch solche Differentialgleichungen bestimmen lassen, in multidimensionalen Meßdaten zu identifizieren. Dazu werden Methoden entwickelt, die unter Berücksichtigung der Struktur des Rauschens, Schätzungen ohne systematischen Fehler ermöglichen. Durch Verfahren der robusten Statistik wird eine Unabhängigkeit gegenüber Ausreißer in den Meßdaten erzielt. Die Relevanz der entwickelten Methoden für andere wissentschaftliche Anwendungen wird anhand von Beispielen demonstriert. Die vorgestellten Techniken werden einer Genauigkeitsanalyse unterzogen. Nach einer Erprobung unter kontrollierten Laborbedingungen im Heidelberger Aeolotron kommen die Meßmethoden bei einer internationalen Feldkampagne erfolgreich zum Einsatz.

Abstract

In this thesis a novel technique for estimating heat transfer at the free air water interface is presented. For the first time spatially resolved heat flux and transfer velocity measurements are available with a high temporal resolution. The statistical properties of the transfer processes are deduced and the parameters characterizing them established. Based on this analysis a second way to estimate the heat flux is presented. These techniques are based on thermal image sequences on which a motion analysis is performed. The motion is modelled in a general parameterization and physically motivated intensity changes can be incorporated by means of linear partial differential equations. In the presented framework the parameters of physical processes described by such differential equations can be estimated in multidimensional data. To do so algorithms are developed that allow for unbiased estimates taking the structure of the noise into account. Methods from robust statistics are employed to correctly solve the estimation problem regardless if the data is corrupted by outliers. The relevance of the developed techniques to other scientific applications is shown. In an accuracy analysis confidence bounds of the proposed algorithms are established and limitations revealed. Following an examination under controlled laboratory conditions in the Heidelberg Aeolotron, the techniques are successfully applied at an international field campaign.

Contents

Chapter 1

Introduction

1.1 Motivation

In recent years the research to predict climatic changes has gained tremendous momentum. The global balancing of climatic active tracer gases such as carbon dioxide (CO_2) is of outmost importance for models allowing medium- and long-term predictions of the climatic evolution. The global temperature and atmospheric concentration of CO_2 are positively correlated as has been proven by measurements in Antarctic ice cores dating back 160.000 years [Barnola et al., 1987; Jouzel et al., 1987]. It is known that the concentration of atmospheric CO_2 has risen by roughly 25% since the industrial revolution 150 years ago. Even though sustained efforts are undertaken to slow down further emissions of CO_2 due to anthropogenic sources, the concentration of this gas is still rising notably. An associated rise in temperature, also known as the *"greenhouse effect"*, would entail drastic climatic changes.

The oceans cover roughly 70% of the earth's surface and present a major sink for binding atmospheric CO_2. These immense water masses present a reservoir of about 50 Tt (1Tt = 19^{18}g) carbon, while the combined uptake of both atmosphere and biosphere amounts only one tenth of that, namely 5 Tt [Siegenthaler and Sarmiento, 1993]. An important factor is the rate with which CO_2 can be transported into the oceans as this counters rising emissions. In order to make qualitative statements concerning the transfer velocity of tracer gasses across the air-water interface, a profound understanding of the underlying physical processes is indispensable. Only if the parameters influencing these transport processes are known, an accurate model can be developed. With such a model and global monitoring of its parameters, current uncertainties can be resolved and a more accurate prediction of the global climatic changes devised.

After years of intense field and laboratory measurements it is known that exchange rates depend on the wind speed. However the exact dependency is still subject to debate. Furthermore the question as to how other parameters effect these rates, such as the sea surface temperature (SST), the wave field and surfactant concentrations, remains still unanswered at large. All these questions can only be answered satisfactory by studying small scale atmosphere-ocean interactions. Only if the transport mechanisms on spatial scales of a few centimeters and time scales of seconds are understood, a precise parameterization can be developed. An understanding of these small scale interactions obviously needs accurate measurements of the transport processes and possible parameters involved.

Apart from being a reservoir for gasses such as CO_2 the oceans can moderate and limit climatic excursions in another way that is relevant for predictions of climatic change. Owing to the much higher mass of water as compared to that of air, the oceans present a far greater storage capacity of heat than the atmosphere. Therefore they act as a giant reservoir, particularly through the connection of the deep ocean with the surface layers. The same arguments stated for the transport of gasses also hold true for the transfer of heat from the ocean to the atmosphere and vice versa. Transport mechanisms are similar in principle and also not fully understood. Important for mid- and long-term predictions through changes in the heat content of the reservoir, anomalies in the transfer velocity of heat across the air-water interface can cause immediate climatic variations, such as the commonly known ENSO (El Niño Southern Oscillations) phenomenon. These effects makes an understanding of the exact processes of air-sea heat exchange equally important as the exchange of gasses. The importance is stretched even further when considering the similarities underlying the two types of transport. It has been predicted and verified experimentally that from the transfer velocity of heat that for any other tracer such as CO_2 can be inferred through an appropriate scaling [Jähne, 1980; Jähne et al., 1989]. This opens up completely new experimental techniques for studying transport phenomena across the air-sea interface.

Current state of the art techniques for measuring the transfer velocities of gasses are based on *mass balancing techniques* where tracer concentrations in the water are artificially modified and changes measured over time. The effect of changes in concentration caused by diffusion due to currents in the ocean can be accounted for by introducing a second tracer with a different diffusivity, a technique known as the *dual tracer method*. These kind of measurements present point measurements with integration times as long as days. Recently direct *eddy correlation techniques* have been introduced. Here the integration times are shortened somewhat to make measurements on time scales of less than an hour feasible. Still these measurements present point measurements with integration times too long to predict and link the transfer velocities to small scale interactions, often taking place on time scales of less than seconds. The same problems hold true for measurements of the transport of heat. Micro-meteorological techniques are similar to those for measuring gas transfer velocities. Integration times are of the order of tenths of minutes while still representing point measurements only. While these techniques may help in relating the mean transfer velocities to other mean quantities such as wind speed, roughness of the sea surface or whitecap coverage and thus help in finding semi-empirical parameterizations, they are not adequate for gaining a deeper understanding of the transport processes involved.

The situation was improved somewhat with the advent of the Controlled Flux Technique (CFT) where heat was used as a tracer for gasses and the temperature gradient measured for a fixed artificially introduced heat flux [Jähne, 1980; Jähne et al., 1989]. With this technique exchange rates could be measured non-invasively with a high temporal resolution for the first time [Libner, 1987]. This technique was later extended to be used with infrared cameras for measuring the temperature change of a water parcel heated up with an infrared laser [Reinelt, 1994]. The use of an infrared camera with its spatially resolved temperature measurement opened up new possibilities of studying air-water heat transfer. Spatial structures were observable for the first time, which allowed to draw conclusions for the transport processes involved [Haußecker, 1996] and an analysis of the predominant scales of turbulences [Schimpf, 2000]. The use of infrared cameras for measurements at the sea surface found

wider acceptance, as other parameters important to transport processes such as micro scale wave breaking could be detected with such devices as well [Jessup et al., 1997]. Still, the unsolved issue of estimating heat fluxes directly at the air-water interface to a high temporal and spatial resolution prevailed. Only by measuring the heat flux as well as the small scale processes influencing the transfer of heat on the same spatial and temporal scales, a deeper understanding of the transport phenomena involved can be attained.

In this thesis a novel technique is developed, closing the gap in the temporal resolution between measurements of important parameters of gas exchange and heat flux which previously existed. While integration times of a few minutes were necessary before, this new technique makes measurements in fractions of a second feasible for the first time. Furthermore the measurements are spatially highly resolved, with unprecedented length scales of just over a millimeter. This gives new insights into the processes governing the transport of heat at the air-water interface. Apart from this technique a method for verifying a model of gas and heat exchange was developed and its statistical properties verified, giving rise to a second alternative technique for measuring the net heat flux. Not only were these novel techniques substantiated under controlled laboratory conditions, but their applicability to field measurements proven in the GasExII experiment in the Equatorial Pacific. The relevance for understanding effects of air-water gas exchange were demonstrated in joined heat flux and gas transfer measurements in the Heidelberg Aeolotron, a purpose build facility for this type of measurement.

These methods for quantitatively measuring parameters of air-sea heat transfer have only been enabled by extensions and advances in spatio-temporal image sequence analyses proposed in this work. Techniques frequently used in computer vision have been extended to model brightness changes based on physical processes. Due to the type of brightness change model in the context of this work and the noise in the data introduced by the infrared camera, the accuracy of this technique was significantly increased by employing parameter estimators yielding reliable estimates for special covariance matrices of the noise. This type of estimation has been unprecedented in computer vision. The presented estimators are based on errors in variables framework, commonly referred to as the total least squares approach. Different estimators are presented that allow for the best estimate in a maximum likelihood sense under a variety of noise models perturbing the data.

1.2 Thesis Outline

This thesis is structured into three main parts. The first one is concerned with the physical transport phenomena encountered at the air-sea interface, encompassing Chapters two to five. Physical aspects of air-sea heat and gas exchange will be outlined and techniques for measuring important parameters thereof introduced. The algorithmic development and extensions of present digital image processing techniques is the topic of the second part, ranging from Chapters six to eight. Only through the advances presented in this part the breakthroughs in non-invasive measurements of parametric models describing transport phenomena at the air-water interface have been made possible. The third part, Chapters nine to twelve, is concerned with analyses of the framework proposed and the results of measurements conducted, both under laboratory conditions and in the field.

Chapter 2 recapitulates the models developed for describing physical transport processes with

application to the transport of energy and mass. Apart from diffusive and conductive processes, turbulent or advective, as well as radiative transport will be discussed. This Chapter concludes with a brief review of the models pertinent to the transport of matter and heat at the air-water interface.

In Chapter 3 important parameters characterizing the transport of mass and heat across the sea surface boundary are discussed. The connection between mass and heat fluxes is established, justifying the use of heat as a proxy tracer for gasses such as CO_2. Due to this fact parameters equivalent to those characterizing the transport of heat exist for the transport of mass. In this thesis the main focus is lying on the transport of heat, but results and parameterizations are equally applicable to that of other quantities by analogy.

Chapter 4 presents a short survey of current state of the art techniques for measuring mass and heat fluxes across the air-water boundary layers. Methods ranging from direct covariance techniques to semi-empirical bulk parameterizations are explained and limitations and drawbacks of the individual approaches summarized. From these approaches the parameters of heat and mass transfer can be deducted, hampered by shortcomings in the described techniques.

With the advent of commercially available low-noise infrared cameras significant improvements of estimating the parameters of air-water gas and heat transfer are achievable. Techniques developed in the context of this work circumvent the limitations of previous concepts for measuring heat fluxes. With the use of only one infrared camera in conjunction with novel digital image processing techniques, the parameters of air-water heat exchange can be estimated, as will be proposed in Chapter 5. Accuracy analyses are conducted for each of these techniques, specifying bounds on the properties of the imaging device used and the properties of the specific realization of the image processing framework.

The second part of the thesis commences with an excurse to the field of parameter estimation in Chapter 6. These estimation techniques present the foundations of latter image processing techniques for deriving the parameters of physical transport processes. Estimators are introduced that produce unbiased model parameters with data perturbed by noise. In contrary to the common assumption this noise will rarely be identical independently distributed (iid) Gaussian noise. Hence different estimators are presented that are capable of still producing optimal results in a maximum likelihood sense. Hypothesis testing is introduced as a framework for choosing the optimal model from a number of applicable possibilities of varying complexity in a statistical significant way.

However, the introduced estimators may be led arbitrary far away from the correct solution due to data points not correctly described by the model, commonly termed outliers. Robust extensions of the previous estimators are presented in Chapter 7, these are capable of detecting these outliers and fitting the models only to the applicable datums.

The concept of optical flow is introduced in Chapter 8 and a novel extension to the constraint equations developed. This extension allows for accurately modelling brightness change in image sequences due to underlying physical processes. This extended constraints can only be computed reliably with the estimators presented previously, to the authors knowledge never before used in the field of computer vision. Both the parameters of brightness change and optical flow can be estimated simultaneously in the framework presented. The chapter concludes with an overview of example applications of the novel technique to other fields, underlying the relevance of the framework.

In the last part of this thesis results of the algorithms proposed are presented. The accuracy of the image processing algorithms is scrutinized in Chapter 9 under varying noise levels.

The calibration of the imaging sensor is a key step to obtain highly accurate results. The calibration procedure will be discussed in Chapter 10.

In Chapter 11 the claim of highly accurate measurements or important parameters of air-water heat and gas exchange is sustained with laboratory measurements conducted in the newly build Heidelberg Aeolotron. The estimated parameters are compared to ground data derived from other measurements relying on the exceptional thermal properties of the facility. Also the results of a joint experiment are presented in which mass and heat fluxes were measured simultaneously.

The applicability of the novel technique was also attested in field experiments. First results of a campaign in the Equatorial Pacific are presented in Chapter 12 where also the use of the technique on two sea going platforms is outlined.

The thesis concludes with a summary and a possible outlook of further research in Chapter 13.

Part I

Exchange Processes

Chapter 2

Physical Transport Models

One aim of this thesis is the study of heat transfer at the air sea interface. Apart from being an important quantity in climatic phenomena, heat can also be used as a proxy for the transfer of other scalars such as mass. Therefore from the measurement of heat fluxes the fluxes of gasses across the interface, such as CO_2, can be predicted. An analysis of these transport processes is only possible through knowledge of the transfer phenomena involved. Although model formulation and rigorous mathematical analyses of heat and mass transfer were developed independently as branches of classical physics, fundamental aspects and equations are similar. This similarity will be outlined throughout this chapter. It is this similarity of the transport of both scalar that justifies using heat as a proxy tracer for mass transfer.

The transport of any quantity, be it momentum, heat or mass, takes place by either one of the two principal transport mechanisms. These are known as *diffusion* and *turbulence*, while heat can also be transported by a third mode of transport as will be explained later. Phenomenologically, the main difference between these two general mechanisms is that diffusion is a relatively slow process. In that respect diffusive transport will only play a noticeable role on very small scales or in systems where turbulent transport is suppressed, such as in solids or in close proximity to wall flows. The opposite is true for turbulent transport processes. This type of process is the more effective of the two and leads to a rapid spread of the substance over a wide range of scales and thus large distances.

Although similarities exist between the transport of heat and matter which will be stretched in the following sections, heat can be transported by a process unknown to the transport of matter. This transport process is known as *radiative transfer* which does not rely on any medium for transport, as opposed to diffusion and turbulence. It plays a predominant role for very hot objects as will be shown later on. Even though the sea surface will always be far from such high absolute temperatures, it is important to include this type of transport in a general model to avoid biases. Also, the heat transfer from other sources such as the sun to the sea surface might be dominated by this type of transport process.

In this chapter the concepts and fundamental equations necessary for subsequent analysis will be outlined. The field of transport phenomena is of course much too extensive and diverse for a thorough analysis in the context of this work. It includes topics such as fluid dynamics, boundary layer theory and concepts of turbulence and radiation. The interested reader is referred to the many

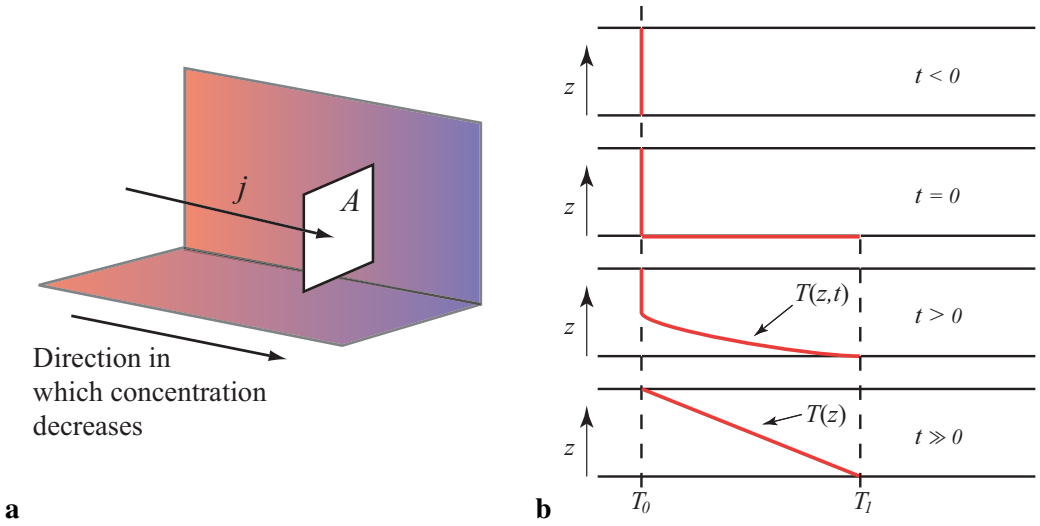

Figure 2.1: ***a*** *Illustration of the net flux j through the unit area A in the direction of decreasing temperature/concentration gradient. In* ***b*** *the development of the steady state profile is illustrated. Initially everything is at concentration/temperature T_0. At $t = 0$ the lower boundary is suddenly raised to concentration/temperature T_1. After an initial transition the linear profile is reached for large t ($t \gg 0$).*

excellent textbooks concerned with these topics such as Tennekes and Lumley [1972], Hinze [1975], Kundu [1990], Landau and Lifschitz [1991], Siegel and Howell [1992], Deen [1998], Schlichting and Gersten [1997] and Bird et al. [2001].

This chapter starts off with a brief introduction of transport by diffusion in Section 2.1. Turbulent transport is then unfolded in Section 2.2 with a recapitulation of the special case of isotropic turbulence in Section 2.2.1 and the inertial subrange in Section 2.2.2. The last remaining mechanism of transport, that is radiative transport of heat, is described in Section 2.3. The chapter concludes with an introduction to the special applications of transport models at the sea surface in Section 2.4.

2.1 Diffusive Transport

Diffusion is the process by which matter is transported from one part of a system to another due to random molecular motions driven by a concentration gradient. In the transport of heat by conduction, energy is also transported by random molecular motions where the transfer comes about due to a temperature gradient. As can be deduced by intuition there exists a strong analogy between the two processes. This was first recognized by Fick [1855], who derived diffusion on a quantitative basis by adopting the mathematical framework of heat conduction derived by Fourier [1822] earlier. The theory of diffusion in *isotropic substances* is therefore based on the hypothesis that the rate of transfer of a diffusing substance through a unit area of a section, also referred to as the *flux of the substance* [Bird et al., 2001], is proportional to the concentration gradient normal to the section, that is

$$\boldsymbol{j} = -k\boldsymbol{\nabla}T, \tag{2.1}$$

$$\boldsymbol{j}_m = -D\boldsymbol{\nabla}C, \tag{2.2}$$

where $\boldsymbol{j}$ is the *heat flux* and $\boldsymbol{j}_m$ the *mass flux*. This relationship of the fluxes to the gradient is illustrated in Figure 2.1. In *Fick's first law*, presented in Equation (2.2), the concentration gradient of the diffusing substance is denoted by $\boldsymbol{\nabla} C$ and the *diffusion coefficient* by D. In the equivalent Equation (2.1), also known as *Fourier's law* for the transport of heat, $\boldsymbol{\nabla} T$ is the temperature gradient and the coefficient of proportionality k is the *thermal conductivity*. The thermal conductivity will generally vary depending on the substance, local temperature and pressure. The thermal conductivity k is related to the *thermal diffusivity* κ by

$$\kappa = \frac{k}{\rho c_p}, \tag{2.3}$$

where ρ is the *specific density* as a measure for the mass per unit volume and c_p the *specific heat* at constant pressure. For sea water at a temperature of 15°C these constant are given as $\rho = 9.99126 \cdot 10^2$ kg m^{-3}, $c_p = 4.182 \cdot 10^3$ J kg^{-1} K^{-1}, $\kappa = 1.4 \cdot 10^{-7}$ m^{2}s^{-1} and the equivalent for air as $\rho = 1.293$ kg m^{-3}, $c_p = 1.014 \cdot 10^3$ J kg^{-1} K^{-1} and $\kappa = 2.15 \cdot 10^{-5}$ m^2 s^{-1}.

The steady state temperature profile for diffusive transports is linear. This can easily be seen from Equations (2.1) and (2.2). In steady state conditions the fluxes $\boldsymbol{j}$ and $\boldsymbol{j}_m$ are constant which subsequently also holds true for the gradient. The evolution of such a profile is illustrated in Figure 2.1.

From this linear profile the expression for the temperature gradient in Fourier's and the concentration gradient in Fick's first law from Equations (2.1) and (2.2) can be rewritten in the form

$$\boldsymbol{j} = -\kappa \rho c_p \frac{T_1 - T_2}{\delta_T}, \tag{2.4}$$

$$\boldsymbol{j}_m = -D \frac{C_1 - C_2}{\delta_C}, \tag{2.5}$$

where T_1 and T_2 are the temperatures at the depths z_1 and z_2 and $\delta_T = z_1 - z_2$. The notation is analogous for the mass flux j_m. These two equations give rise to the definition of the *transfer velocity* k_n of the substance n (also known as the *piston velocity*) which is defined as

$$k_{\text{heat}} = \frac{\kappa}{\delta_T} \quad \Rightarrow \quad \boldsymbol{j} = -k_{\text{heat}} \rho c_p (T_1 - T_2) \tag{2.6}$$

$$k_m = \frac{D}{\delta_C} \quad \Rightarrow \quad \boldsymbol{j}_m = -k_m (C_1 - C_2), \tag{2.7}$$

where k_{heat} is the transfer velocity of heat and k_m that of a mass m. The dimension of the transfer velocity is that of a velocity and commonly given in [cm/h] for fluxes at the sea surface. The transfer velocity or piston velocity can be thought of as the velocity with which a substance is pushed across the unit surface due to the presence of a flux.

Affixed to a heat flux j or a gas flux j_m is a transport of energy or mass, respectively. This is implied by the definition of the transfer velocity k_n. In that respect it is instructive to examine the corresponding equations of conservation of energy and mass. The conservation of energy is manifested in the *first law of thermodynamics*. It states that a change in internal energy equals the sum of work done and the heat added to a material volume [Kittel and Krömer, 1995], that is

$$T \, \mathrm{d}S = c_p \, \mathrm{d}T - \frac{1}{\rho} \mathrm{d}p - \sum_n \mu_n \, \mathrm{d}C_n, \tag{2.8}$$

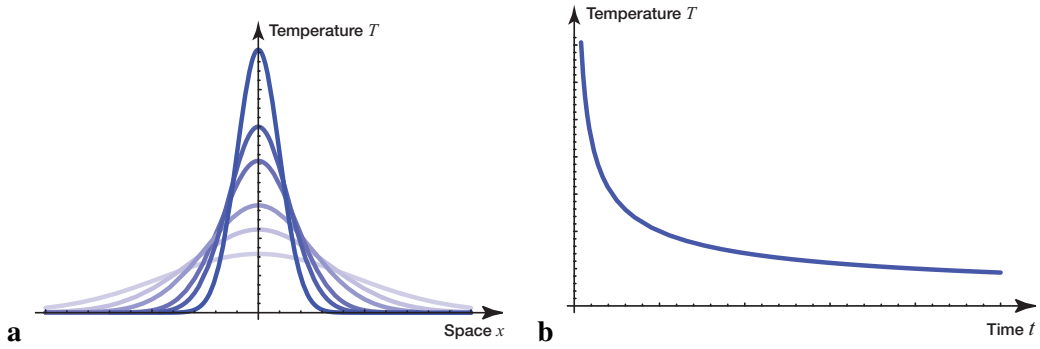

Figure 2.2: *Diffusive temperature decay in space at different times in* ***a*** *and the temperature at the origin during the passing of time.*

where S is the specific entropy, c_p the specific heat at constant pressure and μ_n is the specific chemical potential required to introduce a unit mass of a new substance n into the system.

Boussinesq [1903] suggested to neglect density changes in a fluid, except in the gravity term, and treat the properties of the fluid such as k and c_p as constants. A detailed analysis of this approximation and the conditions under which it holds is given by Spiegel and Veronis [1960]. Making use of this *Boussinesq approximation*, which is valid under several restrictions including that the flow speeds are slow compared to the speed of sound and that the temperature differences in the flow are small, and further assuming that the pressure remains constant, Equation (2.8) can be rewritten to equate the temperature change per unit mass and time by

$$c_p \frac{\mathrm{d}T}{\mathrm{d}t} = \frac{1}{\rho}\frac{\partial}{\partial x_i}\left(k\frac{\partial T}{\partial x_i}\right) + \epsilon + \sum_n \mu_n \frac{\mathrm{d}C_n}{\mathrm{d}t} - \frac{\partial j_{\mathrm{rad},n}}{\partial x_i}, \tag{2.9}$$

where k is the thermal conductivity, ϵ the frictional dissipation and $j_{\mathrm{rad},n}$ the net radiation flux. The terms on the right hand side of Equation (2.9) represent adiabatic heating produced by the convergence of a molecular flux of sensible heat, by frictional dissipation, by phase changes and by the convergence of a net radiation flux.

It can be shown that the heating due to viscous dissipation is negligible [Kundu, 1990]. For an incompressible fluid at rest, with no net absorption of radiation and without phase changes, the equation of heat conduction can be simplified to

$$\frac{\mathrm{d}T}{\mathrm{d}t} = \kappa \Delta T = -\frac{1}{c_p \rho}\boldsymbol{\nabla} \boldsymbol{j}. \tag{2.10}$$

where use was made of Fourier's law given in Equation (2.1). The *Laplace operator* is denoted by $\Delta = \partial^2/\partial x^2 + \partial^2/\partial y^2 + \partial^2/\partial z^2$. This equation can of course also be derived from the continuity equation $\mathrm{d}T/\mathrm{d}t = -\boldsymbol{\nabla} j$ by substituting the heat flux j from Fourier's law. A generic solution to this equation is found to be

$$T(x,t) = \frac{c}{\sqrt{t}} \cdot \exp\left(-\frac{x^2}{4\kappa t}\right), \tag{2.11}$$

which can be verified by differentiation. This solution is shown as a plot in Figure 2.2.

An analogous equation for the mass flux j_m can be derived from the conservation of matter applied to fluid flows, which can be written as [Landau and Lifschitz, 1991]

$$\frac{\mathrm{d}\rho}{\mathrm{d}t} + \boldsymbol{\nabla}\left(\rho \boldsymbol{u}\right) = 0, \tag{2.12}$$

with the specific density ρ, the velocity vector $\boldsymbol{u} = (u, v, w)^\top$ and the divergence denoted by $\boldsymbol{\nabla}$.

The equation of motion for a Newtonian fluid[1] is described by a non-linear differential equation of second order in the velocity $\boldsymbol{u}$, also known as the *Navier-Stokes equation* [Schlichting and Gersten, 1997]

$$\rho \frac{\mathrm{d}\boldsymbol{u}}{\mathrm{d}t} = \boldsymbol{f} - \boldsymbol{\nabla} p + \nabla \boldsymbol{\tau}, \tag{2.13}$$

$$\text{with} \quad \boldsymbol{\tau} = \nu \left(2\dot{\boldsymbol{\epsilon}} - \frac{2}{3} \mathbb{1} \boldsymbol{\nabla} \boldsymbol{u} \right), \tag{2.14}$$

where $\boldsymbol{f}$ are external forces, p is the pressure acting on the fluid and $\dot{\boldsymbol{\epsilon}}$ is the *strain rate tensor*, the elements of which are given by

$$\dot{\epsilon}_{ij} = \frac{1}{2} \left(\frac{\partial u_i}{\partial x_j} + \frac{\partial u_j}{\partial x_i} \right). \tag{2.15}$$

The Navier-Stokes equation was first introduced by Navier [1827] and Poisson [1831] and later derived for a Newtonian fluid by De St.Venant [1843] and Stokes [1849].

In a fluid made up of multiple constituents the specific density ρ_n of a substance n can be written as $\rho_n = C_n \rho$ with the specific concentration C_n and $\sum_n C_n = 1$. For C_n the conservation of matter can be written as

$$\frac{\mathrm{d}}{\mathrm{d}t} \left(\rho C_n \right) = -\boldsymbol{\nabla} \rho \left(C_n \boldsymbol{u} - D_n \boldsymbol{\nabla} C_n \right) + S_n, \tag{2.16}$$

with a source term S_n symbolizing the production of the nth constituent by phase changes and the molecular diffusivity D_n.

The flux $j_{m,n}$ of C_n is represented by the expression inside the brackets of Equation (2.16). It is made up of two components, one being bulk transport carried by the continuum velocity $\boldsymbol{u}$ and the other a flux produced by the random movement of molecules, driven by the concentration gradient $\boldsymbol{\nabla} C_n$. This is of course only true in the absence of other strong gradients such as temperature, density or salinity gradients, as these would inflict molecular fluxes as well.

With the aid of Equation (2.12) and an absence of phase changes, Equation (2.16) can be transformed to the conventional diffusion Equation of a moving fluid, that is

$$\frac{\mathrm{d}C_n}{\mathrm{d}t} = \frac{1}{\rho} \boldsymbol{\nabla} \left(\rho D_n \boldsymbol{\nabla} C_n \right) \approx D_n \Delta C_n, \tag{2.17}$$

with the Laplace operator Δ. This expression is the analogon to the heat conduction Equation (2.10) and is commonly called *Fick's second law*. For a single constituent fluid it equates to

$$\frac{\mathrm{d}C}{\mathrm{d}t} = D \Delta C = -\boldsymbol{\nabla} \boldsymbol{j}_m. \tag{2.18}$$

[1] A Newtonian fluid is an incompressible one in which Newton's linear law of friction holds. A fluid of this type can be regarded as a continuum, down to an infinitesimal volume element $\mathrm{d}V$.

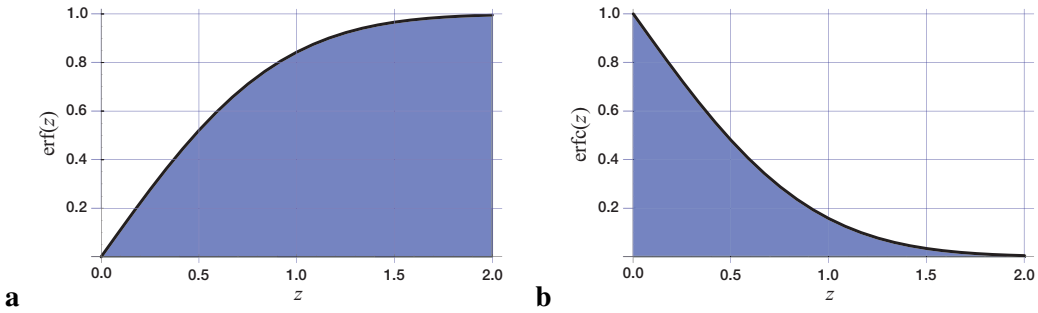

Figure 2.3: *Plots of the error function* $\mathrm{erf(z)}$ ***a*** *and the complementary error function* $\mathrm{erfc(z)}$ ***b*** .

The similarity in the equations governing diffusive heat and mass transfer emphasizes the similar transport mechanisms between the two processes. Generally, the equations derived for the transport of mass yield the analogous equation for heat transport simply by substituting the heat Q for the concentration C or $C \mapsto Q = \rho c_p T$.

The equation of heat conduction (2.10) can be used to relate the temperature change of a body of water to a heat flux across its boundary. Assuming no dependence of the heat flux j and the temperature change dT/dt with depth and no horizontal gradient present in the flux, integrating across the height of the body of water h leads to

$$\boldsymbol{j}_z = \int_0^h \frac{d}{dz}\boldsymbol{j}_z dz = -\int_0^h \rho c_p \frac{dT}{dt} dz = -\rho c_p h \frac{dT}{dt}, \tag{2.19}$$

with heat flux j to be directed upward from the surface $\left(\boldsymbol{j} = (0, 0, j_z)^\top\right)$. This equation can also be derived by relating the heat flux $\boldsymbol{j}$ to the change in heat $dQ = \rho A h c_p dT$ of the water body of volume $A \cdot h$ over the unit area A, that is

$$\boldsymbol{j} = -\frac{1}{A}\frac{dQ}{dt} = -\rho c_p h \frac{dT}{dt}. \tag{2.20}$$

This equation will be used for estimating the heat flux in laboratory experiments from a change in the bulk water temperature in Section 11.6.1.

Solutions to Equations (2.10) and (2.18) can be found by imposing certain boundary conditions. In the following two commonly employed sets of boundary conditions are used to solve the equations. Only the expressions for heat are presented here as the solutions for mass transfer are equivalent with the appropriate quantities exchanged.

For constant initial condition $T(z, t = 0) = T_{\mathrm{bulk}}$ and boundary temperature $T(z = 0, t) = T_{\mathrm{surf}}$ a solution to the equation of heat conduction (2.10) is given by [Crank, 1975]

$$T(z, t) = (T_{\mathrm{surf}} - T_{\mathrm{bulk}})\mathrm{erfc}\left(\frac{z}{2\sqrt{\kappa t}}\right) + T_{\mathrm{bulk}} \tag{2.21}$$

where erfc is the *complementary error function* shown in Figure 2.3 and defined by

$$\mathrm{erfc}(z) \equiv 1 - \mathrm{erf}(z) = 1 - \frac{2}{\sqrt{\pi}}\int_0^z e^{-\eta^2} d\eta. \tag{2.22}$$

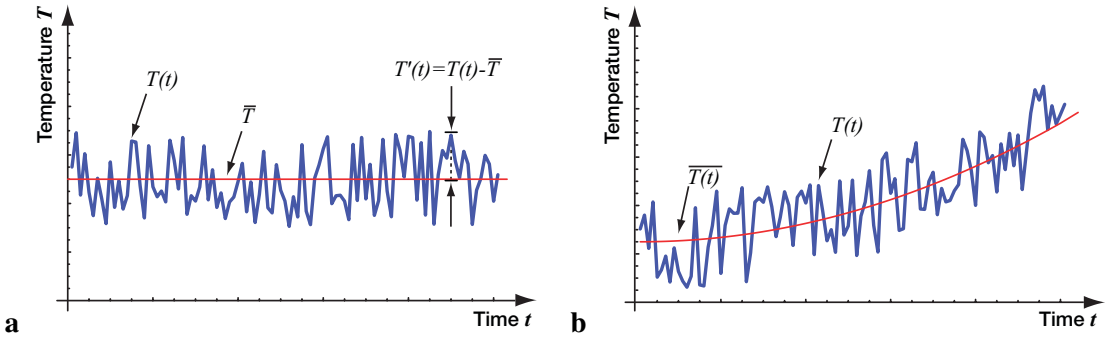

Figure 2.4: *Illustration showing the turbulent temperature $T(t)$ with respect to time t, as well as its fluctuating component $T'(t)$ and the time smoothed value $\overline{T}$. For the* steady turbulence *in* ***a*** *$\overline{T}$ does not depend on time, whereas it does increase with time in* ***b*** *.*

The corresponding heat flux density $j(z,t)$ at the interface ($z = 0$) can then be computed according to

$$j(0,t) = -k\left(\frac{\partial T}{\partial z}\right)_{z=0} = -k\frac{T_{\text{surf}} - T_{\text{bulk}}}{\sqrt{\pi\kappa t}}. \tag{2.23}$$

The boundary condition of constant heat flux j is a more appropriate description of the sea-surface in the case of heat transfer. The reason for this is the negligible dependence of latent and radiative heat fluxes on the temperature difference [Paulson and Simpson, 1981]. This boundary condition is given by the gradient at the interface, that is

$$\frac{\partial(T_{\text{surf}} - T_{\text{bulk}})}{\partial z} = -\frac{j}{k}. \tag{2.24}$$

By analogy the solution for the boundary condition of constant heat flux j across the boundary can be found, resulting in

$$j(0,t) = \frac{T_{\text{surf}} - T_{\text{bulk}}}{\alpha\sqrt{t}}, \quad \text{with} \quad \alpha = \frac{2}{\sqrt{\pi\kappa}c_p\rho}. \tag{2.25}$$

Solving this expression for the temperature at the surface results in

$$T_{\text{surf}}(t) = \alpha j\sqrt{t - t_0} + T_{\text{bulk}}, \quad t \geq t_0, \quad \text{with} \quad \alpha = \frac{2}{\sqrt{\pi\kappa}c_p\rho}. \tag{2.26}$$

This equation will be an important element in determining the net heat flux j at the surface with the novel technique presented in this thesis.

2.2 Turbulent Transport

Turbulent transport is highly complicated and thus eludes a detailed analysis. Akin to other fields of physics such as thermodynamics, the statistical aspects play a predominant role when studying turbulent flows. It is generally assumed that the fluid motion can be separated into a slowly varying mean flow and a rapidly varying turbulent component [Tennekes and Lumley, 1972], as sketched in

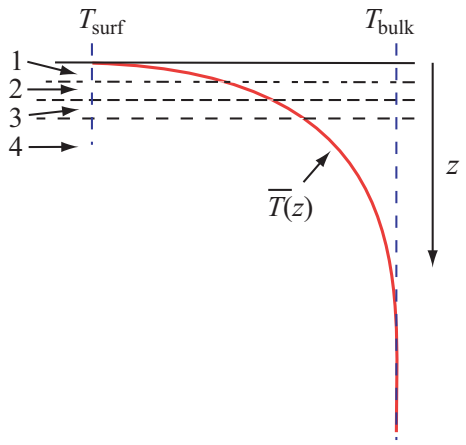

Figure 2.5: *In* ***b*** *the temperature profile for a constant heat flux j with depth z is schematically shown.The regions are the viscous sublayer (1), the buffer layer (2), the inertial sublayer (3) and the turbulent body (4).*

Figure 2.4. It is customary to indicate the average by an overbar and the fluctuating component by a prime, thus $T = \overline{T} + T'$. The averages of the fluctuations are zero by definition, that is $\overline{T'} = 0$. It is assumed that a representative mean of the ensemble average exists which is relatively stationary over time. This separation in a slowly varying mean and a fast fluctuating component is commonly referred to as *Reynolds decomposition* [Shaw, 1990].

The profile of the mean quantity near an interface is depicted in Figure 2.5 where the difference to the linear profile in the diffusive case presented earlier becomes apparent immediately. It is convenient to distinguish four regimes of the profile [Bird et al., 2001]:

1. The *viscous sublayer* near the interface, in which dissipation due to viscosity plays a major role an the profile is assumed to be given by the first terms of a Taylor Series expansion and can often be assumed linear to a first approximation.

2. The *buffer layer* in which the transition occurs between the viscous and the inertial sublayers.

3. The *inertial sublayer* at the beginning of the turbulent body, in which viscosity plays at most a minor role and energy cascades from bigger to smaller eddies. The profile follows a logarithmic expression in this layer.

4. The *turbulent body* of the fluid, in which the profile is nearly constant and viscosity is unimportant.

Albeit being somewhat arbitrary, this classification is commonly found in literature as it presents a convenient way to concentrate on different aspects of turbulent transport processes.

As was mentioned earlier, due to its higher efficiency, turbulent transport is the predominant form of transport away from boundaries where it might be suppressed. To this extent it is important to reformulate the equations of transport (2.10) and (2.16) for the turbulent case. The derivation of these equations of turbulent transport is analogous to the diffusive ones. Hence the diffusive entities can be

replaced by turbulent ones. Therefore, after Reynolds decomposition and averaging the equation of turbulent mass transport is derived from Equation (2.16) to be

$$\frac{\mathrm{d}}{\mathrm{d}t}\left(\rho C_n\right) = -\boldsymbol{\nabla}\overline{\rho_n}\left(\overline{C_n\boldsymbol{u}} + \overline{C_n'\boldsymbol{u}'} - D_n\boldsymbol{\nabla}C_n\right) + S_n. \tag{2.27}$$

The turbulent flux $j_{m,n}$ of the substance C_n is then simply given by

$$j_{m,n} = \overline{\rho_n}\left(\overline{C_n\boldsymbol{u}} + \overline{C_n'\boldsymbol{u}'} - D_n\boldsymbol{\nabla}C_n\right). \tag{2.28}$$

In the terminology of meteorology and oceanography fluxes produced by average velocities are called transport due to *advection* while *convection* is reserved for buoyancy-driven transport.

In the proximity of an interface such as the sea surface, horizontal variations play a subsidiary role as compared to vertical gradients that are much more pronounced. This allows to reduce the problem to an essentially one dimensional one along the z-axis directed upwards from the interface. Neglecting horizontal variations and substituting heat $Q = \rho c_p T$ for the substance C_n in Equation (2.27), the vertical transport of sensible heat is found to be

$$c_p\rho\frac{\mathrm{d}\overline{T}}{\mathrm{d}t} = -c_p\frac{\partial}{\partial z}\rho\left(\overline{Tw} + \overline{T'w'} - \kappa\frac{\partial\overline{T}}{\partial z}\right) \equiv -\frac{\partial j_{\mathrm{sens}}}{\partial z}, \tag{2.29}$$

with the sensible heat flux j_{sens}, thermal diffusivity κ and specific heat at constant pressure c_p. In analogy to equation (2.28) the sensible heat flux is then given by

$$j_{\mathrm{sens}} = c_p\overline{\rho}\left(\overline{Tw} + \overline{T'w'} - \kappa\frac{\partial\overline{T}}{\partial z}\right). \tag{2.30}$$

Here the distinction from the net heat flux j to the sensible heat flux j_{sens} was made to distinguish between the three mechanisms by which heat might be transported, namely by the transport of the heat Q which is called *sensible heat flux* j_{sens}, by phase change such as evaporation which is called *latent heat flux* j_{lat} and by radiation which shall be referred to as *radiative heat flux* j_{rad}.

An important quantity in the analysis of turbulence is the *correlation* or *cross-correlation* and the *autocorrelation* function. The correlation between two variables u and v is defined as $\overline{u\cdot v}$ and has previously appeared in the equations of mass and heat transport. The autocorrelation $R(t)$ of a single variable $u(t)$ at two times t and $t+\delta t$ is thus [Lindsey, 1995]

$$R(\delta) \equiv \overline{u(\boldsymbol{r},t)\cdot u(\boldsymbol{r},t+\delta)}. \tag{2.31}$$

Apart from correlating measurements of one variable at two different times, it is also possible to correlate simultaneous measurements at two locations $\boldsymbol{r}$ and $\boldsymbol{r}+\boldsymbol{\delta r}$ resulting in the autocorrelation

$$R(\delta r) \equiv \overline{u(\boldsymbol{r},t)\cdot u(\boldsymbol{r}+\boldsymbol{\delta r},t)}. \tag{2.32}$$

Also, autocorrelations at different times and locations are conceivable. In the following all these autocorrelations will be denoted by $R(\boldsymbol{\delta})$. It should be noted that time and space averages are interchangeable if a process is both *statistically stationary* and *homogeneous*.

A stationary time series is sketched in Figure 2.4 and can be represented in Fourier space. This representation has the advantage of describing the statistical properties of the data set, while not

providing any information about the chronological order or phase in time. The power spectral density $G(\omega)$ multiplied by $\mathrm{d}\omega$ represents a measure of the contribution made by fluctuations with frequencies between ω and $\omega + \mathrm{d}\omega$. The autocorrelation can here be written very similar to a convolution [Jähne, 1997]. The *power spectral density* $G(\omega)$ is thus given by the *Fourier transform* of the autocorrelation

$$G(\omega) = \frac{1}{\sqrt{2\pi}} \int_{-\infty}^{\infty} R(\boldsymbol{\delta}) e^{-i\omega\boldsymbol{\delta}} \, \mathrm{d}\boldsymbol{\delta}. \tag{2.33}$$

In analogy to the autocorrelation, a cross-correlation between two variables u and v, defined as $\overline{u \cdot v}$, can be represented in Fourier space. The cross-correlation does not necessarily have to be an even function. Therefore the Fourier transform will generally yield a complex number, the real part of which is called the *co-spectral density* function or *co-spectrum* and the imaginary part the *quadrature spectrum*.

2.2.1 Isotropic Turbulence

Isotropic turbulence is a turbulent state of complete randomness in which the statistical properties of the motion exhibit no preference in any direction. Hence there is no correlation between the different velocity components and the turbulent energy can be partitioned equally between the three dimensions of space. Therefore, the turbulent spectrum function $G(k)$ depends only on the length of the radius vector in the wavenumber domain, the integral over which represents the turbulent energy E, that is

$$E = \frac{1}{2} \sum_i \overline{u_i^2} = \frac{1}{2} q^2 = \int_0^{\infty} G(k) \mathrm{d}k, \tag{2.34}$$

where q is the root mean square turbulent velocity. The dissipation of energy ϵ associated with isotropic turbulence is defined as [Kraus and Businger, 1994]

$$\epsilon \equiv \frac{1}{2} \nu \left(\frac{\partial u_j}{\partial x_i} + \frac{\partial u_i}{\partial x_j} \right)^2, \tag{2.35}$$

which leads to the following equation for the isotropic case in which all the velocity components are represented by a set of harmonics with wave numbers k:

$$\epsilon = 2\nu \int_0^{\infty} k^2 G(k) \mathrm{d}k, \tag{2.36}$$

with the *kinematic viscosity* ν. The three dimensional wavenumber spectrum $G(k)$ could be obtained from simultaneous observations with an infinite number of spatially distributed sensors. Usually the turbulent motion is superimposed by an overall advection velocity $\boldsymbol{u}$. In this case the wave number spectrum $G_1(k_1)$, also known as the *downstream power spectrum*, can be obtained from observations at one single point making use of *Taylor's hypothesis* [Taylor, 1938]. This hypothesis assumes that a fluctuating field remains 'frozen' over periods that are long in comparison to the advection time scale $2\pi/l|\boldsymbol{u}|$, where $l = \omega/|\boldsymbol{u}|$ is the streamwise wavenumber. Therefore the downstream power spectrum $G_1(k_1)$ can be considered as a 'one dimensional cut' of the wavenumber spectrum $G(k)$. In locally isotropic motion the relation between the two spectra is given by [Hinze, 1975]

$$2G(k_1) = k_1^2 \frac{\partial^2 G_1}{\partial k_1^2} - k_1 \frac{\partial G_1}{\partial k_1}. \tag{2.37}$$

Plugging this term into the Equation (2.36) for the dissipation results in

$$\epsilon = 15\nu \int_0^\infty k_1^2 G_1(k_1) \mathrm{d}k_1. \tag{2.38}$$

In both Equations (2.36) and (2.38) the spectrum functions are weighted with the square of the wavenumber. This serves as an indication that the dissipation of energy will be mainly associated to the higher harmonics which are equivalent to the smaller eddies.

2.2.2 The Inertial Subrange

In the analysis of turbulence the ratio between inertia force and viscous force plays an important role. This ratio is called the *Reynolds number* Re which is written as [Hinze, 1975]

$$\mathrm{Re} = \frac{|\boldsymbol{u}|L}{\nu}, \tag{2.39}$$

where L is the extent of the motion pattern, U is the advection velocity and ν the kinematic viscosity.

For cases of very large Reynolds numbers ($10^6 - 10^9$), which is often encountered at both sides of the sea-surface interface [Kraus and Businger, 1994], there exists a large range of differently sized eddies. For large eddies the viscosity plays an insignificant role in their evolution, which can be deduced from their Reynolds number. In contrast, dissipation of turbulence plays a very important role for smaller eddies, for which the Reynolds number is of the order of 1. Subsequently there must exist a range of intermediate eddy sizes, for which neither the input nor the dissipation of energy plays a significant role. In the spectrum of turbulence this range is called *inertial subrange*, in which energy cascades down from larger to smaller eddies. This line of reasoning let Kolmogorov [1941] to his famous similarity argument.

The wavenumber k of the inertial subrange is given by

$$k_0 \ll k \ll k_d, \tag{2.40}$$

where k_d and k_0 are the characteristic wavenumbers of the energy containing eddies and the energy dissipating eddies, respectively. In this range the spectrum of turbulence kinetic energy $G(k)$ is entirely determined by the rate of dissipation ϵ and the wavenumber k. A dimensional argument leads to [Kolmogorov, 1941]

$$G(k) = \alpha \epsilon^{2/3} k^{-5/3}. \tag{2.41}$$

Following the same line of reasoning, the one dimensional downstream spectrum may be written as

$$G_1(k_1) = \alpha_1 \epsilon^{2/3} k_1^{-5/3}. \tag{2.42}$$

The constants α and α_1 are the *Kolmogorov constants*. The equivalent relations for other scalar quantities x such as temperature T or humidity q are given as

$$G_x(k_1) = \alpha_{x,1} \epsilon^{-1/3} N_x k_1^{-5/3}, \tag{2.43}$$

where N_x is the dissipation rate of the scalar x. Obviously the Kolmogorov constant α_x will depend on the transported substance and differ for velocity u, temperature T and humidity q fluctuations, denoted by α_u, α_T and α_q respectively.

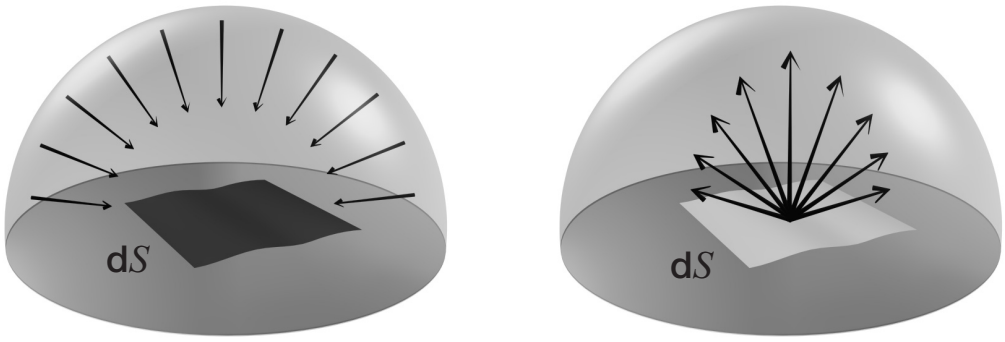

Figure 2.6: *Illustration of the irradiance E in* ***a*** *and the exitance M in* ***b*** *.*

The Kolmogorov constants can be determined from the direct-dissipation method which will be discussed in Section 4.4. Recent measurements by Fairall et al. [1990] resulted in $\alpha_{u,1} = 0.59$, although the range of uncertainty to other measurements is still large. Champagne et al. [1977] report values of $\alpha_{u,1} = 0.50 \pm 0.02$ and $\alpha_{T,1} = 0.82 \pm 0.04$, Williams and Paulson [1977] found $\alpha_{u,1} = 0.54 \pm 0.01$ and $\alpha_{T,1} = 1.00$, Paquin and Pond [1971] measured $\alpha_{u,1} = 0.55$ and $\alpha_{T,1} = 0.8$ and Dyer and Hicks [1982] reported $\alpha_{u,1} = 0.59 \pm 0.01$, $\alpha_{T,1} = 0.68 \pm 0.02$ and $\alpha_{q,1} = 0.76 \pm 0.03$. A review of experimental efforts to obtain values for the Kolmogorov constant can be found in Dyer and Hicks [1982].

2.3 Radiative Transfer

In the previous section the transport of heat by conduction and by convection has been discussed. Both modes of transport can only take place in the presence of a material medium. For conduction to take place, there must be a temperature difference between two neighboring bodies and for heat convection a freely moving fluid or gas to transport the energy is needed. The transport of energy by radiation is fundamentally different in that it allows energy to be transported with the speed of light by an electromagnetic mechanism through space devoid of matter.

The hemispheric radiation into a unit area per unit time is referred to as the *irradiance* E, while hemispheric radiation out of a unit area per unit time is called *exitance* M [Haußecker, 1999]. Both these quantities are illustrated in Figure 2.6. Whenever the radiation is in equilibrium with the solid surface both quantities are equal, as can be deducted from the law of energy conservation.

A *blackbody* is defined as an ideal body that allows all the incident radiation to pass into it and internally absorbs all the incident radiation. This is true for all wavelengths and all angles of incidence. Hence the blackbody is a perfect absorber for all incident radiation as it does not reflect nor transmit any energy [Siegel and Howell, 1992].

It has been shown by quantum mechanical calculations [Planck, 1901] and verified experimentally that for a blackbody the hemispherical emissive power e_λ in vacuum is given as a function of wavelength λ and the blackbody absolute temperature T by *Planck's spectral distribution of emissive*

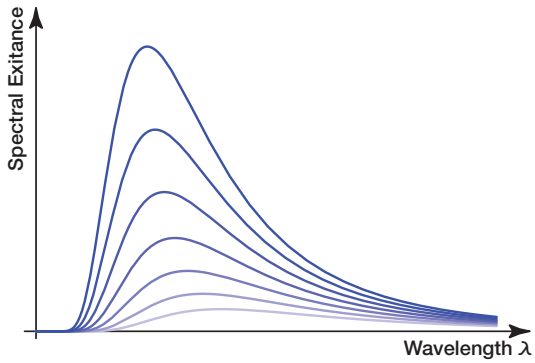

Figure 2.7: *The blackbody emissive power e_λ versus wavelength λ plotted for different values of the temperature T.*

power

$$e_\lambda(\lambda, T) = \frac{2\pi h c_0^2}{\lambda^5} \left(e^{\frac{hc_o}{k\lambda T}} - 1 \right)^{-1}, \tag{2.44}$$

where h is *Planck's constant* ($h = 6.6260755 \cdot 10^{-34}$ J·s), c_0 the speed of light in vacuum ($c_0 = 2.9979 \cdot 10^8$ m/s) and k is the *Boltzmann constant* ($k = 1.380658 \cdot 10^{-23}$ J/K). This spectral distribution is plotted for different temperatures in Figure 2.7.

The energy radiated per unit wavelength into vacuum has been given by Equation (2.44). Often it is of interest to know the *hemispherical total emissive power* e radiated over the whole spectrum of wavelengths. This is given by

$$\begin{aligned} e(T) &= \int_0^\infty e_\lambda(\lambda, T)\, \mathrm{d}\lambda = \int_0^\infty \frac{2\pi h c_0^2}{\lambda^5} \left(e^{\frac{hc_o}{k\lambda T}} - 1 \right)^{-1} \mathrm{d}\lambda \\ &= \frac{2\pi k^4 T^4}{h^3 c_0^2} \int_0^\infty \frac{\zeta^3}{e^\zeta - 1} \mathrm{d}\zeta = \sigma T^4, \quad \text{with} \quad \sigma = \frac{2\pi^5 k^4}{15 h^3 c_0^2}, \end{aligned} \tag{2.45}$$

where the substitution $\zeta = hc_0/(k\lambda T)$ was introduced and σ is the *Stefan-Boltzmann constant* ($\sigma = 5.67051 \cdot 10^{-8}$ Wm^{-2}K^{-4}). This is the *Stefan-Boltzmann law* [Stefan, 1879; Boltzmann, 1884], which has been verified experimentally. The hemispherical total emissive power e is equivalent to the total emitted energy flux j_{rad} from a black body. In real world situations idealized objects such as the blackbody do not exist. To account for the less ideal "blackness" of material bodies, the *emissivity* ϵ is introduced. It specifies how well a real body radiates energy as compared to a blackbody and is consequently unity for a blackbody. The radiant energy emitted by a black body is an upper limit of the radiant energy emitted by a real surface. The emissivity ϵ can therefore only attain values from an interval $0 \leq \epsilon \leq 1$ and has to be determined experimentally.

Kirchhoff's law states that at a given temperature the emissivity and absorptivity of any solid surface are the same when the radiation is in equilibrium with the solid surface [Kirchhoff, 1860]. It can be derived from conservation of energy. Hence the amount of incident energy flux not absorbed by the body has to be reflected of it, which leads to the reflected flux j_r of incident radiation j_i being equal to $j_t = (1-\epsilon) j_i$. The total emitted energy flux j_{rad} is composed of the emitted plus the reflected

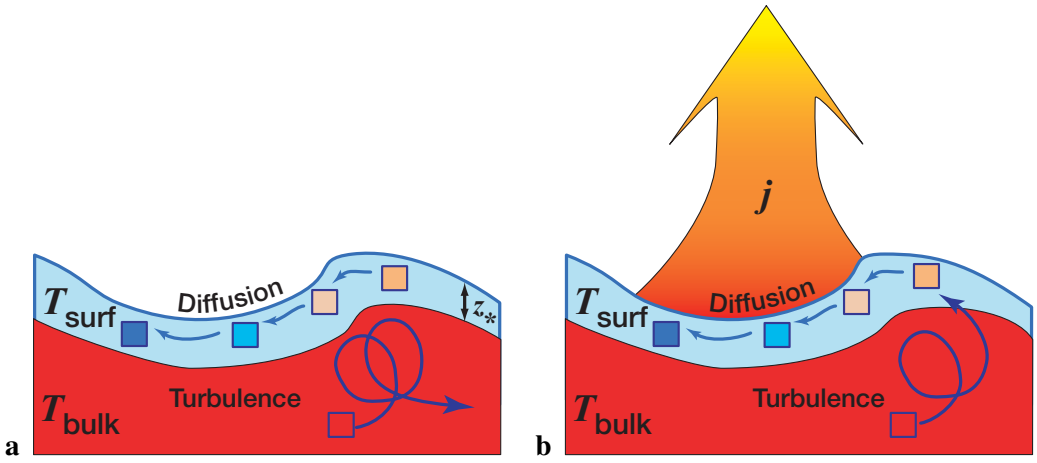

Figure 2.8: *Illustration of the thin film model can be seen in* ***a*** *, whereas the surface renewal model is pictured in* ***b*** *.*

energy flux j_i can thus be written as

$$j_{\mathrm{rad}} = \epsilon\sigma T^4 + (1-\epsilon)\, j_i. \tag{2.46}$$

This Equation is important for estimating the radiative heat flux at the sea surface as will be presented in Section 4.6.

2.4 Transport Models at the Sea-Surface

When studying transport phenomena at the sea surface it is important to have an understanding of the basic physical processes involved. Generally the turbulent structures underneath the interface are very complex and difficult to understand fully, both experimentally and theoretically. Simplified model assumptions are vital to gain insight into the predominant processes which in turn allows for indirectly measuring important quantities of air-sea mass and heat exchange. Due to the same fundamental structure of processes for heat and mass transfer, the models presented in the following are the same for both entities transported. In subsequent sections four models will be outlined that were successfully used in the last few decades for explaining certain properties of air-water heat and mass transfer. For a thorough analysis the reader is referred to Jähne [1980] and Münsterer [1996].

2.4.1 Thin Film Model

The *thin film model*, also known as *stagnant water film model*, is the most basic of the transport models. It assumes that the transport through the phase boundary can be divided into pure heat conduction through a stagnant film of boundary layer thickness z_* and pure turbulent transport below this depth. The transfer rate is thus controlled by the thin stagnant water film which separates the well mixed reservoirs with constant heat of air above and water below. From Equation (2.1) the temperature profile in the boundary layer will be linear in this kind of model, which contradicts measurements [Andreev and Khundzhua, 1975; Khundzhua and Andreyev, 1974; Ward and Redfern, 1999].

The appeal of this simplistic model is its ease of mathematical manageability. Although it has been proven not to describe measurements sufficiently close, it can be thought of as lower bound on the transport processes, as the influence of turbulence in the other models lead to an drastic increase of exchange rates. This kind of model was used by Saunders [1967] to derive an expression for the temperature gradient at the sea-surface interface (see Section 3.1).

2.4.2 Small Eddy Model

This model is based on the flow pattern seen at rigid wall boundaries where efficiency of turbulent diffusion decreases as the wall is approached. The turbulent eddies are not allowed to impinge upon the boundary. To this end the eddies will cascade down in size as they approach the boundary and finally diminish. This type of model gives rise to a turbulent diffusion constant K depending on the depth z. Usually this depth dependence is expressed by a term of the form $K(z) \propto z^2$, from which the concentration gradient can be assessed [Coantic, 1986]. Hasse [1971] employed this model in deriving his expression for the temperature gradient (see Section 3.1).

2.4.3 Surface Renewal Model

Considerable success has been obtained with a simple model which allows small parcels of water adjacent to the interface to be replaced randomly by water from the well mixed turbulent layers of the bulk of the water. This so called *surface renewal model* has been introduced in chemical engineering by Higbie [1935] who assumed periodic renewal of the water parcels. The model was then extended in chemical engineering to include statistically distributed random events by Danckwerts [1951], Hariott [1962] and Rao et al. [1971]. It was later applied to the air-sea interface by Brutsaert [1975a], Brutsaert [1975b], Liu and Businger [1975], Liu et al. [1979], Jähne [1980] and Soloviev and Schlüssel [1994].

Probability Density Function

Affixed to the surface renewal model is the probability density function $p(t)$ of times between consecutive surface renewal events. The importance and possible formulations for this pdf are presented in the following.

The motion of the molecular sublayer can be expected to remain locally laminar and parallel to the interface. As such the sea water at the sea surface cannot be easily replaced by the water from the bulk although it can come very close to it. It is instructive to consider an individual fluid parcel in the mixing layer. Because of the very high efficiency of turbulent transport it will be at the same temperature T_{bulk} of the bulk. Due to the stochastic renewal process it will be moved very close to the interface. On exposure to the surface, which has a different temperature T_{surf} as compared to the bulk, thermal conduction takes place and its temperature $T(z,t)$ is governed by heat conduction akin to molecular diffusion as was presented in Equation (2.10). Assuming that horizontal gradients are negligible in comparison to vertical gradients this equation may be written as

$$\frac{\partial T}{\partial t} = \kappa \frac{\partial^2 T}{\partial z^2}. \tag{2.47}$$

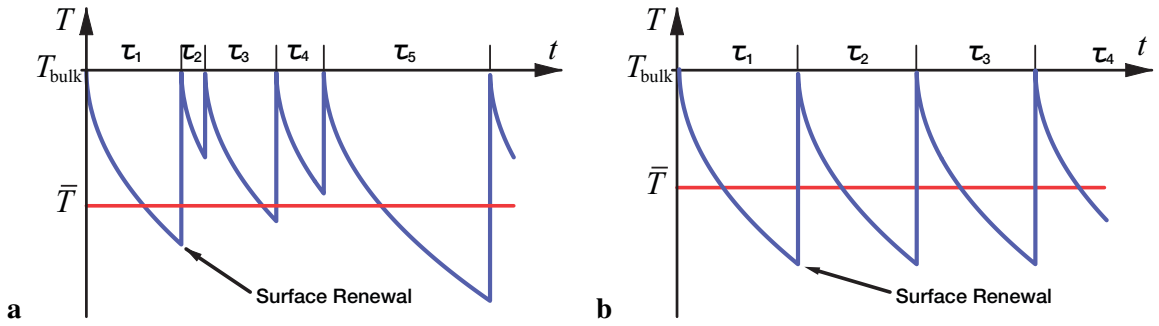

Figure 2.9: *Illustration of the sea-surface temperature T with respect to time t for two pdfs of surface renewal. The propagated logarithmic normal pdf of times in between surface renewal events τ in* ***a*** *and a strongly periodic surface renewal in* ***b*** *.*

Solutions to this equation with different boundary conditions were presented in Equations (2.21) and (2.26).

Following Kraus and Businger [1994] a probability density function (pdf) $p(t)$ is defined which represents the fractional area of the surface fluid elements that have been in contact with the interface for a time t. The average temperature and heat flux are then given by

$$T(z) = \int_0^\infty p(t)T(z,t)\mathrm{d}t \tag{2.48}$$

$$j(0) = \int_0^\infty p(t)j(0,t)\mathrm{d}t \tag{2.49}$$

The question arises as to what specific analytic expression for the probability density function $p(t)$ best describes the actual surface renewal process. Depending on the choice of $p(t)$ the integration of Equations (2.48) and (2.49) will yield different results. Basically three types of pdf have appeared in literature:

- The first possible distribution for $p(t)$ was introduced by Gulliver [1990]. It is assumed that the turbulence in the interior of the fluid governs the mechanism for replacing the surface elements. This represents a random process and it is argued that each fluid element has the same probability of being replaced, which can be expressed as

$$\frac{\mathrm{d}p(t)}{\mathrm{d}t} = -\frac{1}{t_*}p(t) \quad \Rightarrow \quad p(t) = \frac{1}{t_*}\exp\left(-\frac{t}{t_*}\right), \tag{2.50}$$

  where t_* is the characteristic residence time of fluid parcels at the surface.

- Kolmogorov [1962] and Soloviev and Schlüssel [1994] argue along the same line of reasoning but deduce a logarithmic normal distribution of the form

$$p(t) = \frac{1}{\sqrt{\pi}\sigma t/t'}e^{-\frac{(\ln t/t' - m)^2}{\sigma^2}}, \quad t > 0, \tag{2.51}$$

  where m is the mean value of $\ln t/t'$ and σ^2 the variance for the logarithm of the scaled random variable t. t' is a unit scaling factor. This type of model pdf was indicated by measurements of

Rao et al. [1971] and more recently of Garbe et al. [2001a]. The mean time between burst t_* is the expectation value of this distribution, given by

$$t_* = \int_0^\infty p(t)\, t/t'\, dt = t' \cdot e^{\frac{\sigma^2}{4}+m}. \tag{2.52}$$

- For rough estimations a purely periodic surface renewal model might be chosen, where the distribution of $p(t)$ is represented by Dirac's delta distribution

$$p(t) = \delta(t - t_*). \tag{2.53}$$

Although presumably not a very accurate description of the transport processes at the sea-surface, this distribution has big advantages in deriving analytical expressions for the parameters influencing air-water gas and heat exchange and thus facilitates a rough estimation of mean properties.

A comparison of the three probability distributions was performed by Haußecker [1996] on grounds of resulting temperature distribution on the sea surface and showed strong experimental evidence for the logarithmic normal distribution. The function of the sea surface temperature with respect to time for the logarithmic normal pdf and a strong periodic pdf are illustrated in Figure 2.9.

It is intrusive to perform the integration with the exponential pdf given in Equation (2.50). Substituting this equation together with Equations (2.21) and (2.23) in the Equations (2.48) and (2.49), the following expression for the temperature profile in the molecular sublayer results after integration:

$$\frac{T - T_{\text{bulk}}}{T_{\text{surf}} - T_{\text{bulk}}} = \exp\left(-\frac{z}{\sqrt{\kappa t_*}}\right). \tag{2.54}$$

From the gradient of this expression evaluated at the sea-surface (z=0) the sought net heat flux j is given from Equation (2.23) as

$$j = -k\frac{T_{\text{surf}} - T_{\text{bulk}}}{\sqrt{\kappa t_*}} = \frac{-\kappa}{z_T} c_p \rho (T_{\text{surf}} - T_{\text{bulk}}), \tag{2.55}$$

where $z_T = \sqrt{\kappa t_*}$ is the length-scale for the temperature profile. Experimental support of these equations was given by Khundzhua and Andreyev [1974] who measured the temperature profile to an accuracy of 0.05°C for temperature differences with a temperature probe consisting of a differential thermocouple with a transient time constant on the order of $1.5 \cdot 10^{-3}$ sec [Gusev et al., 1976].

2.4.4 Surface Strain Model

The *surface strain model* describes the steady state temperature profile at the free surface when the near surface turbulence provides a quasi-steady velocity strain on the thermal boundary layer. In this model water parcels at the sea-surface are replaced by those from the bulk. In that respect the model is similar to the surface renewal model. However, the hydrodynamics affecting the thermal boundary layer are parameterized by the strain rate β with $\beta^2 = \dot{\epsilon}/\nu$, rather than the surface renewal time. This is justified by the assumption of a slowly evolving strain flow acting on the thermal boundary

layer which differs from the classical surface renewal assumption that the temperature profile is the mean of a temporally growing thermal boundary layer. The surface strain is connected to the near-surface turbulent dissipation. This model was first introduced in chemical engineering by Fortescue and Pearson [1967] and later applied to air-sea mass fluxes by Csanady [1990] and to the thermal boundary layer by Leighton and Smith [2000].

2.4.5 Experimental Evidence of Models

With the different models presented in previous sections it is of course important to find experimental evidence favoring one above the others. Münnich et al. [1978] showed in laboratory experiments that the surface renewal model in section 2.4.3 yields a better approximation for heat and gas transfer than the thin film model. In contrast, Torgersen et al. [1982] presented evidence from gas exchange measurements in the field using gases with different diffusion coefficients favoring the thin film model. In ocean going gas exchange measurements the choice of models will generally not have a big impact as the differences in diffusivity among the gases of interest are sufficiently small [Broecker and Peng, 1982]. Münsterer [1996] showed that all the models basically predict the same transfer velocities for gas exchange. Hence from gas transfer measurements cannot be differentiated in between these models. However, the predicted profiles depend strongly on the model. To this end methods of measuring profiles such as the non-intrusive laser-induced fluorescence (LIF) technique Jähne [1991] or temperature probes [Gusev et al., 1976; Ward and Redfern, 1999] are needed to shed some light on the actual mechanisms of transport. Also, spatially resolved techniques such as the one presented in this work help to discern between the models.

2.5 Summary

In this chapter the basic transport mechanisms for heat and mass have been introduced. Basic equations describing the transport in diffusive, turbulent and radiative regimes have been presented and solutions to common boundary conditions outlined. Due to these modes of transport different models of air-sea heat and mass transfer are conceivable. Four common simplistic models describing this transfer were introduced. In the following sections common use will be made of these equations and models describing transport phenomena.

Chapter 3

Parameters of Sea-Surface Heat Transport

This thesis is mainly concerned with measuring the net heat flux at the sea surface. For one this is due to the significance of heat as the driving force in numerous climatic phenomena. Furthermore heat can be regarded as a proxy tracer for other scalars such as mass fluxes. In that respect the analysis of heat transfer at the sea surface gives some vital information concerning the air-water gas transfer. In this chapter parameters of the heat flux are presented. Also, the connection between heat and mass fluxes are established.

In Section 3.1 a phenomenon known as the cool skin of the ocean will be introduced. The net heat flux at the air-water interface will be subject of Section 3.2. This chapter concludes with the transfer velocity in Section 3.3 where the relevance of heat transfer as a proxy tracer for mass fluxes will become apparent.

3.1 The Cool Skin of the Ocean

The topmost layer of the ocean, also referred to as the *thermal boundary layer*, is influenced by many processes such as the net upward heat flux due to evaporation and sensible heat transfer, infrared and solar radiation, turbulences near the interface induced by wind stress which causes mixing, wave breaking and current shear [Katsaros, 1980a]. During night time, when no solar radiation is present and hence no heating of the upper two meters of the water column occurs [Fairall et al., 1996a], the effect on this roughly 1 mm thick boundary layer [Grassl, 1976] is a cooling by a few tenths of a degree as compared to the water bulk [Wick et al., 1996]. Here common conditions of a net heat flux j directed upward from the interface are assumed.

The first evidence of the cool skin of the ocean was given by Merz [1920] and later by Woodcock and Stommel [1947] who made more detailed measurements of the temperature profile in the air-water boundary layer of Jenkins Pond on Cape Cod, MA. The temperature depression across the sea-surface plays a major role in satellite based remote sensing. The satelite can only derive the temperature of the thermal boundary T_{surf} and comparisons to bulk temperature measurements obtained from

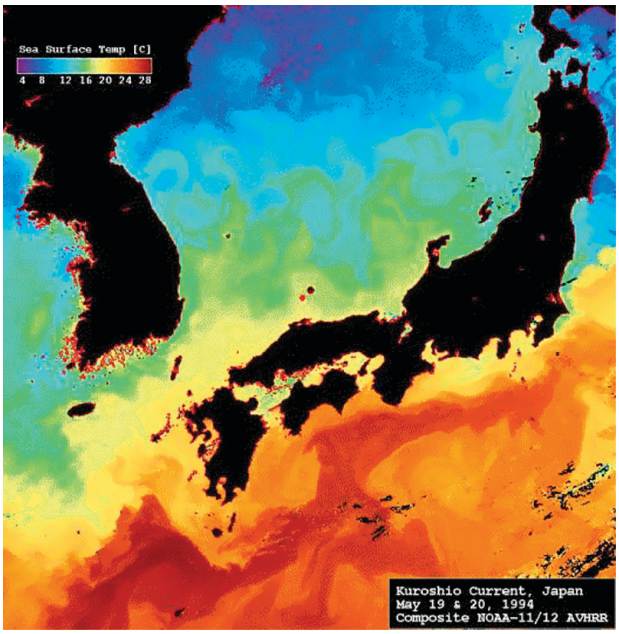

Figure 3.1: *The sea-surface temperature T_{surf} as measured with a satelite based Advanced Very High Resolution Radiometer (AVHRR). Shown are ocean circulation features off the coast of Japan with the warm Kuroshio current in the lower half of the image mixing with cold water mixing from north (warm temperatures are colored red and cold ones blue). These type of measurements need to be calibrated with buoy and ship based measurements, which commonly detect only the bulk temperature T_{bulk} [SeaSpace, 2001].*

buoys are of interest [Schlüssel et al., 1990; Emery and Yu, 1997]. An image of such a satelite based measurement of the sea surface temperature (SST) T_{surf} is presented in Figure 3.1. The parameters that govern the behavior of ΔT have been investigated in many studies [Ewing and McAlister, 1960; Saunders, 1967; McAlister and McLeish, 1969; Hasse, 1971; Paulson and Parker, 1972; Grassl, 1976; Katsaros, 1977; Liu et al., 1979; Katsaros, 1980a; Paulson and Simpson, 1981; Wu, 1985; Schlüssel et al., 1990; Coppin et al., 1991; Soloviev and Schlüssel, 1994; Wick et al., 1996; Ward and Redfern, 1999].

Principally different expressions for the temperature depression across the cool skin of the ocean can be derived, depending of the assumed underlying transport model. In Section 3.1.1 formulations resulting from the thin film and the small eddy model will be presented, whereas those derived under the assumption of the surface renewal model will be outlined in Section 3.1.2.

3.1.1 Temperature Depression from Thin Film and Small Eddy Models

An expression for the behavior of ΔT under conditions of forced convection was developed by Saunders [1967]. Using dimensional analysis and assuming the thin film model from section 2.4.1, he derived

$$\Delta T \equiv T_{\mathrm{bulk}} - T_{\mathrm{surf}} = \delta \frac{j}{k} = \lambda \frac{j\nu}{k u_*} \tag{3.1}$$

with the characteristic thickness of the cool skin δ, the net nighttime heat flux j, the thermal conductivity of sea water k, the kinematic viscosity of sea water ν and the sea surface friction velocity u_*.

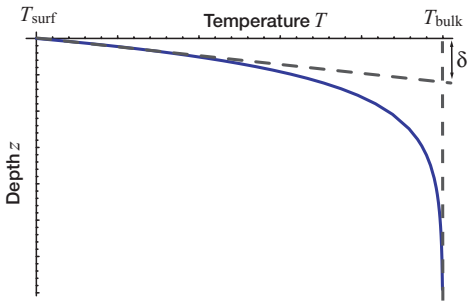

Figure 3.2: *Schematic drawing of the vertical temperature distribution for a negative heat flux j. δ is the characteristic thickness of the thermal sublayer and T_{surf} and T_{bulk} the surface and bulk temperatures respectively.*

The definition of the characteristic thickness of the thermal sublayer δ with respect to ΔT is illustrated in Figure 3.2. It is generally given by the gradient of the thermal temperature profile at the surface ($z = 0$). Saunders did not have sufficient data to determine the value of the coefficient λ but estimated it to be in the range of 5-10 [Saunders, 1967].

In subsequent years different values for λ were presented by Paulson and Parker [1972]($\lambda = 15$), Paulson and Simpson [1981]($\lambda = 6.5$) and Coppin et al. [1991]($\lambda = 6.5$), all of which concluded from their findings that λ is a constant value independent of wind speed. In contrast, Grassl [1976] and Schlüssel et al. [1990] presented tables of different λ suggesting λ to be a function of the wind speed. From the examination of previous data sets Wu [1985] concluded that λ is a linear function of the wind speed to about 7 m/s at which point it turns constant.

In contrast, Hasse [1971] developed a model based upon the equation for the effective water thermal diffusivity $j = -c_p \rho \kappa \partial T / \partial z$ and the small eddy model from Section 2.4.2. His expression for the night time temperature depression is given by

$$\Delta T = C \frac{j}{u_{10}} \tag{3.2}$$

with the wind speed u_{10} measured at 10m from the sea surface and the constant C varying slightly with depth and insignificantly with wind speed. For a bulk temperature measurement at a depth of 2.5 m, the value of C was found to be $1.48 \cdot 10^{-2}$ m^3 K/(W s). This equation is essentially the same as the previous one (3.1) derived by Saunders [1967] with an invariant λ.

As the wind speed tends to zero, both Equations (3.2) and (3.1) do not hold any more since the denominator approaches zero and the expressions become undefined. An explanation for this fact is based on the underlying physical processes where a transition from a shear-driven to a free convection regime takes place and the models have to be adapted accordingly. Based on a classical analysis of thermal instability Katsaros [1977] derived an expression that is analogous to a second model presented by Saunders [1967]:

$$\Delta T \propto \sqrt[4]{\frac{\kappa\nu}{\alpha g}} \left(\frac{j}{k}\right)^{3/4}, \tag{3.3}$$

where g is the acceleration of gravity, k the thermal conductivity, κ the thermal diffusivity and α the

coefficient of thermal expansion for water defined by

$$\alpha \equiv -\frac{1}{\rho}\left(\frac{\partial \rho}{\partial T}\right)_p, \tag{3.4}$$

where ρ is the density of water and the subscript "p" signifies that the partial derivative is to be taken at constant pressure.

The applicability of Equation (3.3) depends on whether the *Obukhov length* L, or alternately the Richardson number Ri, is sufficiently small. To first order the Obukhov length can be interpreted as the height at which shear and buoyant *turbulence kinetic energy* (TKE) production are approximately equal. It is given by [Obukhov, 1971]

$$L \equiv \frac{u_*^3}{K\overline{b'w'}}, \tag{3.5}$$

where K is called the *Karman constant* in honor of Kármán [1930] ($K \simeq 0.41$), $b = -g\rho'/\overline{\rho}$, or in the case of temperature $b' = -g\theta'/\overline{\theta}$, is the *buoyancy acceleration*, with the *potential temperature* θ,its fluctuating part θ' and the vertical velocity fluctuation w'. The potential temperature is defined as the temperature that would be acquired by air when brought adiabatically to standard pressure $p_0 = 1013$ hPa. The potential temperature θ can be derived from the actual temperature T according to Roedel [1992]

$$\theta = T\left(\frac{p_0}{p}\right)^{\frac{\chi-1}{\chi}}, \tag{3.6}$$

where p is the pressure and $\chi = c_p/c_v$ the fraction of specific heat at constant pressure and constant volume. In air the term $(\chi-1)/\chi$ is approximately given by $(\chi-1)/\chi \approx 0,286$.

The Richardson number Ri introduced by Richardson [1920] is the ratio of buoyant production to shear production and represents another measure for the applicability of Equation (3.3). It can thus be written as [Kraus and Businger, 1994]

$$\mathrm{Ri} \equiv \frac{g}{\overline{\theta}}\frac{\partial\overline{\theta}/\partial z}{(\partial\overline{u}/\partial z)^2} \tag{3.7}$$

with the mean velocity in x-direction $\overline{u}$.

Attempts were made to incorporate the two regimes of shear-driven and free convection into a single model of the form of Equation (3.1). Fairall et al. [1996a] accomplished it by using different expressions of the skin layer thickness δ in the two regimes and devicing a smooth transition between the two. In the shear-forced regime the same form of the skin layer thickness used by Saunders [1967] was used, whereas it was derived from Rayleigh number scaling in the free convection regime. The resulting expression for λ is thus given by [Fairall et al., 1996a]

$$\lambda = 6\left(1 + \left(\frac{16 j_{\mathrm{virt}}\ g\ \alpha\ \rho\ c_p\ \nu^3}{k^2\ u_*^4\ (\rho_a/\rho)^2}\right)^{3/4}\right)^{-1/3}, \tag{3.8}$$

where ρ_a is the density of air and the *virtual heat flux* j_{virt} follows from the relation of the density flux to the salinity fluxes [Paulson and Simpson, 1981]

$$j_{\mathrm{virt}} = j + \left(\frac{\overline{s_w}\beta_w c_p}{\alpha_w L_e}\right) j_{\mathrm{lat}}, \tag{3.9}$$

where $\overline{s_w}$ is the mean salinity, β_w the *salinity expansion coefficient*, L_e the *latent heat of vaporization* and j_{lat} the latent heat flux. The factor $\overline{s_w}\beta_w$ is relatively constant in the ocean (≈ 0.026), but the thermal expansion coefficient α decreases from about $3 \cdot 10^{-4}$ K^{-1} in the tropics to zero K^{-1} in the polar regions. Generally, the net heat flux j will differ from the virtual flux j_{virt} in light wind conditions by no more than 10% [Fairall et al., 1996a].

3.1.2 Temperature Depression from Surface Renewal Model

A different group of models to those presented in the previous section can be derived based on the surface renewal model from Section 2.4.3. Brutsaert [1975b] applied this model to gain insights into evaporation rates but stated that his results would equally be applicable to heat transfer. He assumed that the process of surface renewal is accomplished by the smallest possible eddies. Both length and timescales of these eddies are defined by the *Kolmogorov microscales*. Kolmogorov [1941] suggested that the size of turbulent structures depends on the parameters that are relevant to the smallest eddies. These parameters are the rate ϵ at which energy is dissipated by the eddies as introduced in Equation (2.35) and the kinematic viscosity ν. The *Kolmogorov microscale* η is then given by dimensional analysis ($[\nu]$ =m^2/s, $[\epsilon]$ =m^2/s^3, $[\eta]$ =m) as [Kundu, 1990]

$$\eta \equiv \sqrt[4]{\frac{\nu^3}{\epsilon}}. \tag{3.10}$$

Brutsaert [1975b] assumed that the transfer at the ocean surface occurs due to molecular diffusion and applied different expressions for diffusion and skin layer thickness for smooth and rough surfaces. The equivalent expressions for heat transfer are given by

$$\Delta T = C_{\mathrm{rough}} \frac{j}{\rho c_p u_*} \mathrm{Re}_r^{1/4} \mathrm{Pr}^{1/2} \quad \text{rough surface,} \tag{3.11}$$

$$\Delta T = C_{\mathrm{smooth}} \frac{j}{\rho c_p u_*} \mathrm{Pr}^{2/3} \quad \text{smooth surface.} \tag{3.12}$$

Here C_{rough} and C_{smooth} are proportionality constants and $\mathrm{Pr} = \nu/\kappa$ is a similarity parameter known as the *Prandtl number* that will be explained further in Equation (3.35). $\mathrm{Re}_r = z_0 u_*/\nu$ is the roughness Reynolds number introduced by Nikuradse [1933] and $z_0 = c u_*^2/g$ is the momentum roughness length with a proportionality constant c. Brutsaert [1975a] defined smooth surfaces as those with $\mathrm{Re}_r < 0.13$ and rough surfaces as those with $\mathrm{Re}_r > 2.0$. The proportionality constants C_{rough} and C_{smooth} were found to be 7.3 and 13.6, respectively [Brutsaert, 1975b].

It is noteworthy that the Equations (3.11) and (3.12) are equivalent to the corresponding equations of air-sea gas transfer, which will be introduced in Section 3.3. The reason for this equivalence is the similar transport mechanism involved in the transport of mass and heat at the sea surface, which is expressed in the independence of the transfer velocity k_x on the tracer x as will be explained in Section 3.3.

By relating the average surface contact time t_* to the depth of a stagnant layer with an equivalent heat flux sustained by molecular diffusion, Liu and Businger [1975] found

$$\Delta T = C \frac{j}{\rho c_p} \sqrt{\frac{t_*}{\kappa}}. \tag{3.13}$$

Following Brutsaert [1975b] the surface contact time is derived from the Kolmogorov microscale resulting in [Liu et al., 1979]

$$t_* \propto \sqrt{\nu z_0 / u_*^3}. \tag{3.14}$$

By plugging Equation (3.14) into Equation (3.13) it can be shown that this formulation of the surface temperature depression is identical to the one found by Brutsaert [1975a] in Equation (3.11). Liu et al. [1979] found the proportionality constant C of Equation (3.13) and Equation (3.11) to be $C = 9.3$ for typical conditions of the air-sea interface. They also noted that C would depend on interfacial roughness characteristics and that Re_r would approach a constant value for a smooth interface, making their findings consistent with Equation (3.12).

Soloviev and Schlüssel [1994] adopted different time scales for low, moderate and high wind regimes. Their time scales for the convective, moderate and high wind speed regime are

$$t_* \propto \sqrt{\frac{\nu \rho c_p}{\alpha g j}} = \sqrt{-\frac{\nu}{u_*^4 \mathrm{Rf}_0}} \quad \text{for} \quad |\mathrm{Rf}_0| > 1.5 \cdot 10^{-4} \tag{3.15}$$

$$t_* \propto \nu / u_*^2 \tag{3.16}$$

$$t_* \propto u_* / g \quad \text{for} \quad \mathrm{Ke} > 0.18 \tag{3.17}$$

with the *surface Richardson number* $\mathrm{Rf}_0 = -\alpha g j \nu / \rho c_p u_*^4$ representing the ratio of buoyancy to shear forcing. It was first introduced by Kudryavtsev and Soloviev [1981]. Soloviev and Schlüssel [1994] define the transition from free to forced convection in terms of the surface Richardson number. Free convection is assumed to apply for $|\mathrm{Rf}_0| > \mathrm{Rf}_{\mathrm{cr}} = 1.5 \cdot 10^{-4}$. Similarly the transition from moderate to the high wind speed regime is defined in terms of the *Keulegan number* $\mathrm{Ke} = u_*^3 / g\nu$ where the high wind regime is defined as $\mathrm{Ke} > \mathrm{Ke}_{\mathrm{cr}} = 0.18$, which corresponds to wind speeds of 10m/s. Soloviev and Schlüssel [1994] combined all of the three regimes into one simplified expression given by

$$\Delta T = T_* \Lambda \sqrt{\mathrm{Pr}} \frac{\sqrt{1 + \mathrm{Ke}/\mathrm{Ke}_{\mathrm{cr}}}}{\sqrt[4]{1 + \mathrm{Rf}_0/\mathrm{Rf}_{\mathrm{cr}}}} \quad \text{with} \quad T_* = \frac{j}{\rho c_p u_*}, \tag{3.18}$$

where the constant Λ was estimated to be $\Lambda = 13.3$.

The model put forward by Wick et al. [1996] is based upon Equation (3.13). It states that the renewal timescale should be applicable to all conditions of the interface, ranging from the shear driven to the free convection regime. The transition from the regimes should be smooth with the transition between them being governed by the surface Richardson number Rf_0, which is essentially the same argument that led Soloviev and Schlüssel [1994] to Equation (3.18). The following expression for t_* is fullfilling these characteristics:

$$t_* = t_{r\,\mathrm{shear}} + (t_{r\,\mathrm{conv}} - t_{r\,\mathrm{shear}})\, e^{-C/\mathrm{Rf}_0}. \tag{3.19}$$

This model is in good agreement with the formulation of Soloviev and Schlüssel [1994] in the applicable regimes [Wick et al., 1996]. Combining Equation (3.13) with (3.19) results in

$$\Delta T = \frac{j}{\rho c_p \sqrt{\kappa}} \sqrt{C_{\mathrm{shear}} \sqrt{\frac{\nu z_0}{u_*^3}} + \left(C_{\mathrm{conv}} \sqrt{\frac{\nu \rho c_p}{\alpha g j}} - C_{\mathrm{shear}} \sqrt{\frac{\nu z_0}{u_*^3}} \right) e^{-\mathrm{Rf}_{cr}/\mathrm{Rf}_0}}. \tag{3.20}$$

The proportionality constants are fit to the data sets, resulting in $C_{\text{shear}} \simeq 209 - 244$, $C_{\text{conv}} \simeq 3.13 - 2.29$ and $\text{Rf}_{cr} \simeq -2.25 \cdot 10^{-4} - -8.87 \cdot 10^{-5}$ [Wick et al., 1996].

Based on the statistical temperature distribution at the sea surface with assumptions made on the probability density function $p(t)$ a scheme for estimating ΔT from IR imagery was presented by Haußecker et al. [2001] which will be scrutinized in Section 5.2 due to its relevance for this work. For a derivation of the formulation the reader is referred to Appendix B. In this formulation it is assumed that the times between surface renewal events is logarithmic- normally distributed, evidence of which will be presented in Section 11.5.

3.1.3 Other Models

Apart from the formulations of the temperature depression based on the stagnant film, small eddy or surface renewal model, other expressions for ΔT can be found in the literature. A statistical model was introduced by Schlüssel et al. [1990]. In this model every component of the net heat flux is considered separately, resulting in

$$\Delta T = a_0 + a_1 u \left(T_{\text{surf}} - T_{\text{air}}\right) + a_2 \left(q_s - q_a\right) + a_3 j_{\text{rad}}, \tag{3.21}$$

where T_{air} is the air temperature, q_s the saturation specific humidity, q_a the specific humidity, u the wind speed and j_{rad} the net longwave radiative flux. The coefficients derived by Schlüssel et al. [1990] by regression against observations are $a_0 = -0.285\text{K}$, $a_1 = 0.0115\text{s/m}$, $a_2 = 37.255\text{K}$ and $a_3 = -0.00212\text{Km}^2\text{/W}$.

Another formulation is based on the surface strain model recently presented by Leighton and Smith [2000] introduced in Section 2.4.4. It is assumed that the straining field at the air-sea interface, which is steady and positive over a majority of the interface, has the form

$$\boldsymbol{u} = \begin{pmatrix} \beta x \\ -\beta z \end{pmatrix}, \tag{3.22}$$

where β is the local rate of strain given by $\beta = -\partial w/\partial z = \partial u/\partial x + \partial v/\partial y$. Another assumption made is that the convection-diffusion equation is steady, resulting in a steady solution for the temperature profile. The governing equation for this assumed steady velocity field is then given by

$$-\beta z \frac{\partial (T(z) - T_{\text{bulk}})}{\partial z} = \kappa \nabla^2 (T(z) - T_{\text{bulk}}), \tag{3.23}$$

where κ is the thermal diffusivity and $z = 0$ is measured at the surface with positive z defined upwards away from the sea-surface. The boundary conditions for the temperature at the free-surface at a constant heat flux j are given as

$$\frac{\partial (T(z) - T_{\text{bulk}})}{\partial z} = -\frac{j}{\kappa}, \quad \text{at} \quad z = 0, \tag{3.24}$$

$$T(z) - T_{\text{bulk}} = 0, \quad \text{at} \quad z \to -\infty. \tag{3.25}$$

The solution of this configuration is given by Csanady [1990] as

$$\Delta T(z) = -\sqrt{\frac{\pi \kappa}{2\beta}} \left(\frac{j}{k}\right) \text{erfc}\left(z \sqrt{\frac{\beta}{2\kappa}}\right). \tag{3.26}$$

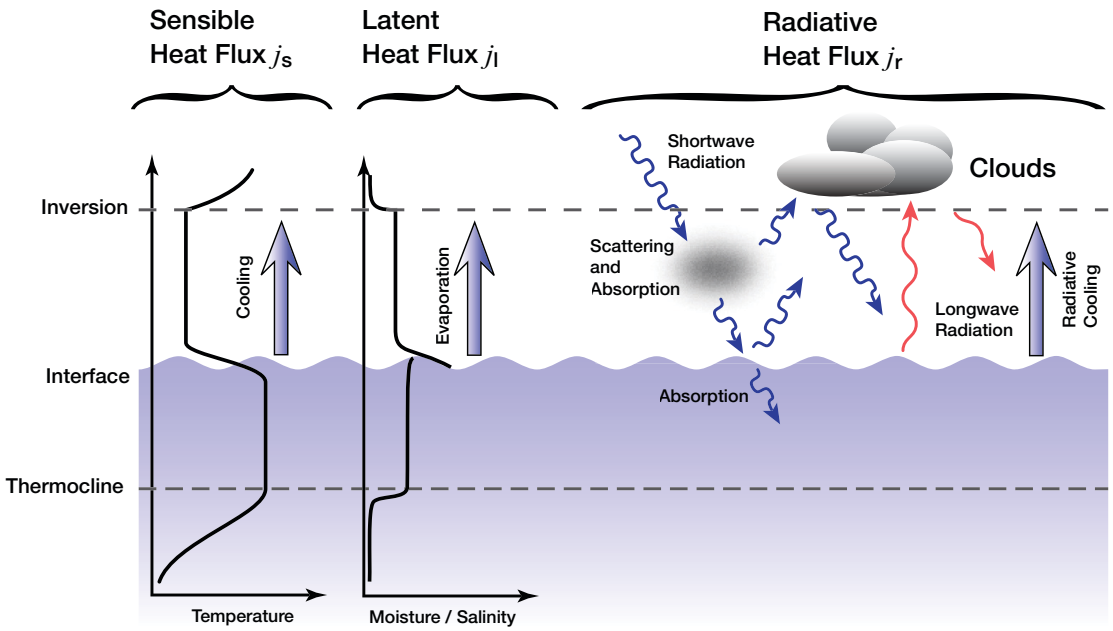

Figure 3.3: *An Illustration of the constituent fluxes of the net heat flux at the sea-surface. The sensible heat flux j_{sens} is driven by a temperature difference between water and air, the latent heat flux j_{lat} by evaporation of water and the radiative heat flux j_{rad} by radiative transfer.*

The temperature depression at the sea-surface is then simply given from Equation (3.26) at $z = 0$, thus [Leighton and Smith, 2000]

$$\Delta T = -\sqrt{\frac{\pi\kappa}{2\beta}}\left(\frac{j}{k}\right). \tag{3.27}$$

On current data sets it is still not possible to state which of the presented models describes the temperature depression ΔT most accurately. Often errors introduced by small scale wave breaking [Wu, 1995] make a comparison difficult. Most of the formulations of ΔT are parameterized by the net heat flux j. Another problem in the exact measurement of ΔT thus stems from the lack of exact coincidence between the heat flux and ΔT measurements [Wick et al., 1996], which might be solved by the techniques presented in this thesis.

3.2 Heat Flux

In the previous section the temperature difference ΔT across the thermal sublayer was introduced and formulations presented for parameterizing this quantity. This temperature difference comes about due to a heat flux j in the ocean. At the interface continuity requires that this net heat flux j is balanced by the total heat flux in the atmosphere, that is the *sensible heat flux* j_{sens}, the *latent heat flux* j_{lat} and the net *longwave radiation heat flux* j_{rad}:

$$j = j_{\mathrm{sens}} + j_{\mathrm{lat}} + j_{\mathrm{rad}}, \tag{3.28}$$

where a positive heat flux is defined in the direction of positive z-axis which is directed upwards from the interface. An illustration of these constituent fluxes can be seen in Figure 3.3.

The *sensible heat flux* j_{sens} is caused by a temperature gradient across the sea-surface. When heat is transported by conduction following Equation (2.10) or by turbulent transport according to Equation (2.30) the resulting flux is termed sensible. From a measurement of the temperature difference between air temperature T_{air} and sea-surface temperature T_{surf} the sensible heat flux j_{sens} can be approximated by [Jähne, 1980]

$$j_{\mathrm{sens}} = k_T^{\mathrm{air}} \rho_{\mathrm{air}} c_p^{\mathrm{air}} (T_{\mathrm{air}} - T_{\mathrm{surf}}), \tag{3.29}$$

where the density of air is denoted by ρ_{air}, the specific heat of air by c_p^{air} and the transfer velocities for heat in air by k_T^{air}. Under normal conditions found at the sea surface this temperature difference $T_{\mathrm{air}} - T_{\mathrm{surf}}$ is usually of the order of $T_{\mathrm{air}} - T_{\mathrm{surf}} \approx 1 - 2\mathrm{K}$, resulting in a flux of approximately $j_{\mathrm{sens}} \approx 30 W m^{-1}$.

Another process drawing heat from the sea-surface is the evaporation of water. For the phase change of water from the liquid to the gaseous phase, the *latent heat of evaporation* $L_e = 2.344 \cdot 10^{-6}$ J kg^{-1} is drawn from the air-water interface giving rise to the *latent heat flux* j_{lat}. Driving this heat flux is the relative humidity h of air close to the interface. From this quantity an approximation of the latent heat flux can be made, yielding [Jähne, 1980]

$$j_{\mathrm{lat}} = -k_q^{\mathrm{air}} L_e c_q (1 - h), \tag{3.30}$$

where L_e is the latent heat of evaporation, c_p^{air} the specific heat of air, c_q the saturation vapor density and k_q^{air} denotes the transfer velocities for water vapor in air. A value for the relative humidity h, frequently found over the ocean is about $h \approx 0.6 - 0.8$. The resulting latent heat flux j_{lat} can thus be roughly estimated to be $j_{\mathrm{lat}} \approx 140$ W m^{-2}.

The fluxes of latent and sensible heat both rely on matter for the transport of energy. As outlined in Section 2.3 this does not hold in the case for radiative transport of heat. Depending on the part of the wavelength spectrum, the radiative heat flux j_{rad} is decomposed into longwave and shortwave radiative fluxes. Details will be explained in Section 4.6. Driving the radiative heat flux at night is the difference of equivalent blackbody temperature of sea-surface and sky which can be up to 65 K [Saunders, 1967]. This results in a net radiative heat flux of approximately $j_{\mathrm{rad}} \approx 200$ W m^{-2}.

During night time these are the only terms in the energy equation and it can be inferred that the net heat flux j changes only slowly with depth [Saunders, 1967]. The situation is different during day time, as absorbtion of direct and diffuse solar radiation introduces an additional term in the energy balance of Equation (3.28). On a clear day the sun deposits on average about 500 W/m^2 into the ocean over the 12 daylight hours, half of which is absorbed in the upper 2 m [Fairall et al., 1996a]. Saunders [1967] estimates that about 5% of the net solar flux will be absorbed in the thermal boundary layer which in turn reduces the cooling effects considerably. Due to this absorption of solar radiation in the upper 2 m and the associated warming of this layer, a stably stratified surface layer develops, suppressing mixing and thus gas exchange [Fairall et al., 1996a]. Due to this stratification higher gas exchange rates are expected during night making accurate measurements during this time more important. During the remainder of this work only night time measurements of the net heat flux are considered, which is in part attributed to the higher importance of measurements during this time but also due to the experimental set-up. The strong solar radiation and reflexes introduced by it on the sea surface would swamp the IR camera used to measure the parameters of sea surface heat exchange, as will be explained in chapter 5.

3.3 Transfer Velocity

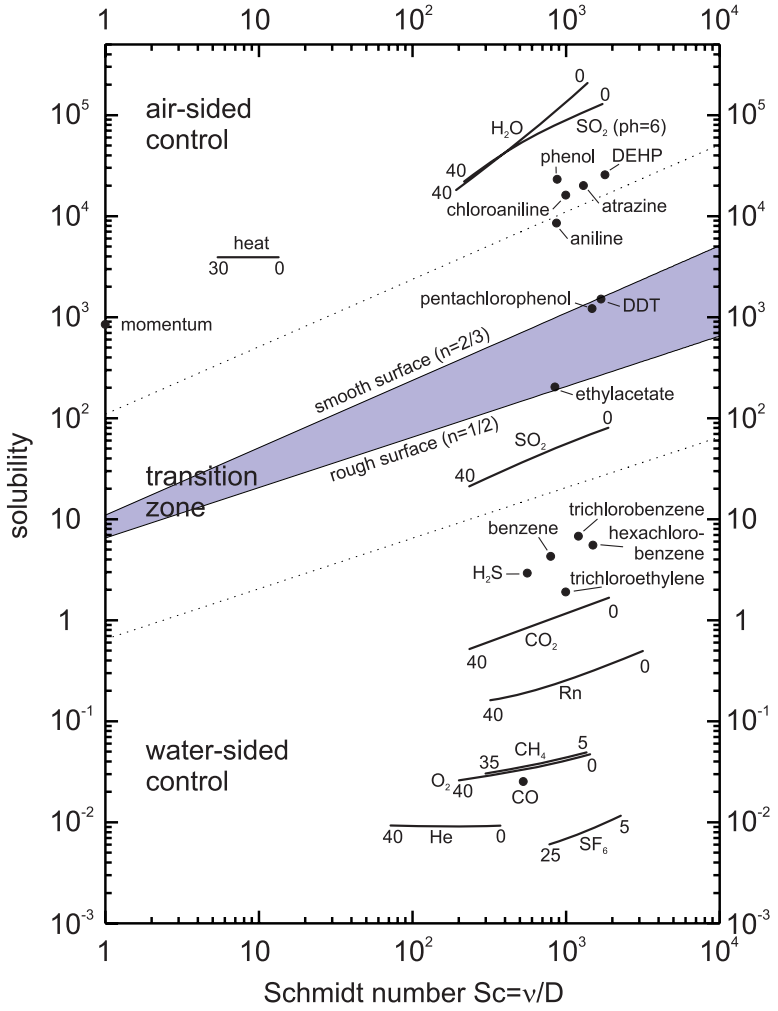

Figure 3.4: *A diagram of the Schmidt number* Sc *and solubility for various volatile tracers, heat and momentum for temperature ranges in [°C] as indicated. Filled circles are values taken at 20°C. The regions for air-sided, mixed and water-sided control of the transfer process between air and water, as well as equal transfer resistance in both phases (solid lines) are marked (from [Jähne and Haußecker, 1998]).*

The heat flux j_x can be expressed in terms of the heat transfer velocity k_x and the concentration difference of the transported substance x along its gradient, be it heat or mass as defined in Equations (2.6) and (2.7). At the sea-surface, due to continuity the fluxes at the gaseous boundary layer must balance those in the aqueous boundary layer. Hence the transfer velocities for heat k_{heat} and mass k_m can be written in terms of concentration differences across the aqueous layers, resulting in

$$k_{\mathrm{heat}} = \frac{j}{\rho c_p (T_{\mathrm{surf}} - T_{\mathrm{bulk}})} \tag{3.31}$$

$$k_m = \frac{j_m}{C_{\mathrm{surf}} - C_{\mathrm{bulk}}}. \tag{3.32}$$

One of the main benefits of parameterizing the air-water gas and heat transfer with the transfer

velocity k_x instead of the relevant fluxes j_x is the independence of the actual tracer. Jähne [1980] verified in accurate laboratory experiments that the friction velocity u_* depends on the transfer velocity k_x as [Jähne et al., 1987]

$$k_x = \beta_x^{-1} u_* Sc^{-n} \tag{3.33}$$

independent of the tracer x used. Here Sc is the *Schmidt number* and u_* the *friction velocity* which is a scaling velocity defined by $\tau \equiv \rho u_*^2$ with the surface stress τ. The surface stress τ is generally a function of the wind speed, but also of parameters effecting the surface roughness, such as surfactants. The parameter β is the dimensionless transfer resistance and n is the Schmidt number exponent. This exponent n can be derived to be $n = 2/3$ for smooth surfaces and $n = 1/2$ for a wavy interface equally from all the model of air-sea gas and heat exchange introduced in Section 2.4. However, the transition between these regimes is still subject of current research and needs to be verified experimentally.

The Schmidt number is a non-dimensional *similarity parameter*. Similarity parameters are often used in fluid dynamics as they allow to formulate equations in a non-dimensional form and thus facilitate the development of similarity relations for processes of different magnitudes. Also, by reducing the number of variables in equations, complex formulations can be handled much easier. Some similarity exist in between the equation for conservation of mass and the equations of motion if the *kinematic viscosity* ν is of the same order of magnitude as the molecular diffusivity D. A measure for this similarity is the above mentioned *Schmidt number* Sc defined as

$$Sc \equiv \frac{\nu}{D}. \tag{3.34}$$

The *kinematic viscosity* ν is related to the *dynamic viscosity* μ by $\nu \equiv \mu/\rho$, where ρ is the density. The dynamic viscosity is the constant of proportionality in *Newtons's law of friction*, relating *shear stress* τ to a velocity gradient, or $\tau = \mu \cdot du/dz$.

An equivalent similarity exists between the conservation of energy and the equations of motion, when the viscous time scale is of the same order of magnitude as the time scale of thermal diffusion. This similarity is expressed by the *Prandtl number* Pr, which is defined according to

$$Pr \equiv \frac{\nu}{\kappa}. \tag{3.35}$$

For water the Prandtl number is given as $Pr \approx 13$ at 0°C and ≈ 7 at 20°C, whilst in air $Pr \approx 0.7$. In the following the Prandtl number shall be used as the Schmidt number for heat to allow for a unified notation. A compilation of different Schmidt numbers of various volatile tracers, heat and momentum can be found in Figure 3.4.

The expected temperature or concentration difference ΔT and ΔC across the relevant sublayers can be derived from the Equations (3.31) and (3.32) for the transfer velocity of heat and mass as well as Equation (3.33) relating the transfer velocity to the friction velocity u_*. It follows

$$\Delta T = T_{\mathrm{surf}} - T_{\mathrm{bulk}} = \frac{j}{\rho c_p k_{\mathrm{heat}}} = \beta_{\mathrm{heat}} \frac{j}{\rho c_p u_*} Sc_{\mathrm{heat}}^n, \tag{3.36}$$

$$\Delta C = C_{\mathrm{surf}} - C_{\mathrm{bulk}} = \frac{j_m}{k_m} = \beta_m \frac{j_m}{u_*} Sc_m^n. \tag{3.37}$$

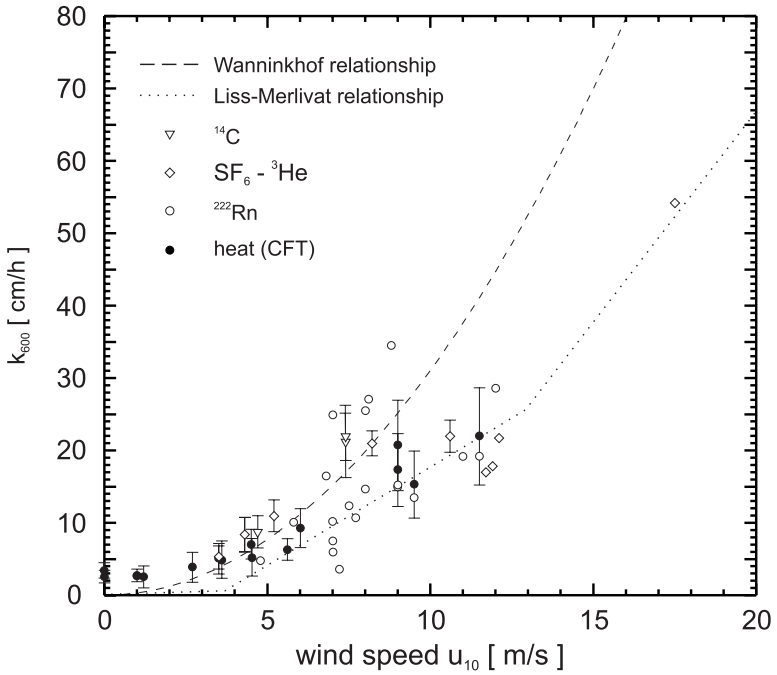

Figure 3.5: *Compilation of gas exchange measurements normalized to a Schmidt number of 600 plotted against wind speed with the* Wanninkhof relationship *[Wanninkhof, 1992] and the* Liss & Merlivat relationship *[Liss and Merlivat, 1986]. Plot from Jähne et al. [1998].*

Comparing Equation (3.36) with Equations (3.11) and (3.12) and remembering that that the Prandtl number Pr is the Schmidt number for heat Sc_{heat}, it becomes apparent that the proportionality constant C_{smooth} in Equation (3.12) is just equal to the transfer resistance β_{heat} and in the rough case the analogy $C_{\mathrm{rough}} = \beta_{\mathrm{heat}}/Re_r^{1/4}$ holds. Re_r is the roughness Reynolds number introduced previously.

As mentioned earlier, Equation (3.33) is independent of the actual tracer under consideration [Jähne, 1980]. Division of this equation for two different tracers a and b thus leads to

$$\frac{k_a}{k_b} = \left(\frac{Sc_b}{Sc_a}\right)^n. \tag{3.38}$$

This equation allows to relate the transfer velocity k_a of a tracer a to that of another tracer b by means of the respective Schmidt numbers. It is this relation that permits the use of heat as a proxy tracer for mass fluxes such as that of CO_2. Even though the Schmidt number for heat ($Sc_{\mathrm{heat}} \approx 7$) is smaller than that of CO_2 ($Sc_{CO_2} \approx 600$) by two orders of magnitude, Equation (3.38) still holds remarkably well, with a relative error of about 10% in the estimation of k_{CO_2} from k_{heat} [Jähne, 1980].

Apart from using heat as a tracer, experiments with other tracers such as sulfur hexafluoride (SF_6) [Wanninkhof et al., 1985, 1987] have been conducted successfully and helped to find experimental verification of Equation (3.38). Commonly used for gas transfer measurements is the so called *deliberate-* or *dual tracers technique* [Watson et al., 1991; Wanninkhof et al., 1993], where two tracers of different diffusivities (usually SF_6 and ^{3}He) are introduced in a patch of water. The dilution effect by tracer dispersion can be corrected for and absolute values for the transfer velocity for other gasses such as CO_2 computed, following Equation (3.38). Research in the accuracy of this technique

with respect to other measurement techniques such as the *eddy correlation technique* (see Section 4.2) is still ongoing [Jacobs et al., 2001a,b].

From Equation (3.33) a linear relationship of the transfer velocity k_x on the wind speed is implied through the parameterization with the friction velocity u_*. However, measurements indicate further dependence on the wave field and parameters influencing it such as surface films due to surfactants [Frew, 1997]. This dependence on the surface roughness gives rise to a transition in the Schmidt number exponent from smooth to rough surface regimes. It is through this additional dependence that significant scatters can be found in the measurements of transfer velocities as shown in Figure 3.5.

The exact Schmidt number exponent n in Equations (3.33) and (3.38) is still subject to current research. It is generally agreed that the exponent changes from $n = 2/3$ for low wind conditions and smooth water surface to $n = 1/2$ for a rough surface in higher wind conditions which has been established experimentally [Jähne, 1985; Jähne et al., 1987; Nightingale et al., 2000].

3.4 Summary

In this chapter important parameters of air-water gas and heat transfer were introduced. The foundation for the use of heat as a proxy tracer for mass transfer was presented. Different parameterizations of the temperature difference across the sea surface interface were introduced. The net heat flux and its constituent fluxes were established and its relevance as a proxy tracer confirmed. The importance of the transfer velocity as a measure of transport independent of the tracer was explained. Parameters influencing the transfer velocity such as wind speed and surface roughness were outlined.

Chapter 4

Meteorological Measurements of Fluxes

Measuring fluxes in the oceanic layer proves to be a very difficult undertaking. The main reason for this is the tiny boundary layer with depths of only 80µm which is obscured by wave motion in the regime of a few centimeters or even meters. Meteorological measurements cannot directly measure the net heat flux j but only its constituent fluxes, namely the sensible heat flux j_s, the latent heat flux j_l and the radiative flux j_r. Different techniques to measure these constituent fluxes as well as those for mass fluxes will be presented in the following sections.

A very practical technique of measuring the fluxes available is *bulk parameterization*, introduced in Section 4.1, which relates the fluxes to measurements of mean parameters at a reference height. In Section 4.2 the *eddy correlation* technique will be introduced which is the only direct method of measuring the fluxes. The demand on the instrumentation with respect to sampling rate and accuracy is very high, which is relaxed somewhat by the *eddy accumulation* and *conditional sampling* techniques, both of which will be outlined in Section 4.3. The *inertial dissipation* method is explained in Section 4.4 as a technique which is not as susceptive to platform motion at sea as the eddy correlation technique and offers the advantage of moderate requirements on the instrumentation. In Section 4.5 the *gradient technique* is introduced and the chapter concludes with an outline of how radiant fluxes are measured in Section 4.6.

4.1 Bulk Parameterization

The method of measuring the fluxes by bulk parameterization tries to relate the fluxes to measurements made at a reference height z_r. This can be accomplished by establishing a flux-gradient relationship [Geernaert, 1990]. The standard bulk expressions for the fluxes of latent and sensible heat are given by [Fairall et al., 1996b]

$$\tau = \rho C_d S(u_{\text{surf}} - u) \tag{4.1}$$

$$j_s = \rho c_p C_h S(T_{\text{surf}} - \theta) \tag{4.2}$$

$$j_l = \rho L_l C_l S(q_{\text{surf}} - q), \tag{4.3}$$

where C_d, C_h and C_l are the *bulk transfer coefficients* for stress, sensible and latent heat. θ is the potential temperature, q the water vapor mixing ratio and u the longitudinal wind velocity. In bulk

parameterization all the measurements are taken at some atmospheric reference height z_r and averaged long enough so that the mean of the turbulent fluctuating quantities equals zero. The average value of the wind speed relative to the sea- surface at z_r is S, T_{surf} the SST, u_{surf} the surface current and q_{surf} the interfacial value of the water vapor mixing ratio that is estimated from the saturation mixing ratio for pure water at the SST, or

$$q_{\mathrm{surf}} = 0.98 q_{\mathrm{sat}}(T_{\mathrm{surf}}). \tag{4.4}$$

The factor of 0.98 takes the reduction in vapor pressure caused by a typical salinity of 34 parts per thousand into account [Sverdrup et al., 1942].

The potential temperature θ in Equation (4.2) and the water mixing ratio q in Equation (4.3) can be measured from the air temperature T_z at z_r and the relative humidity RH according to

$$\theta = 0.0098 z_r + T \tag{4.5}$$

$$q = \mathrm{RH} q_s(T). \tag{4.6}$$

Due to the high convenience of the bulk parameterization method, many research efforts have been put into the determination of the bulk transfer coefficients in Equations (4.2) and (4.3) [Kondo, 1975; Liu et al., 1979; Geernaert et al., 1987; Smith, 1988; Bradley et al., 1991].

Under near-neutral conditions both C_h and C_l seem to have little independence of wind speed for a range of 5 to 20m/s with a value of about $1.2 \cdot 10^{-3}$ [Liu et al., 1979; Smith, 1988]. For increasing wind speeds C_s seems to decrease whereas C_l increases. Both effects are due to sea spray. While C_l increases due to an increase in evaporation from the spray, C_s decreases due to evaporative cooling as the droplets absorb much of the upward heat flux [Fairall et al., 1993]. Also the increasing effect latent and sensible heat carried across the sea- surface by air cycled through whitecap bubbles will be noticeable in stronger winds and needs to be corrected for [Andreas and Monahan, 2000]. For a thorough discussion of those and other effects that can be incorporated in bulk estimations the reader is referred to Fairall et al. [1996b].

4.1.1 Sources of Error

As pointed out by Ledvina et al. [1993] factors contributing to uncertainties in bulk aerodynamic flux estimates include:

1. Observation and instrumentation errors in the meteorological and oceanographic parameters used as input to the bulk formulae.

2. Insufficient or biased spatial sampling of bulk parameters [Weare and Strub, 1981].

3. Algorithmic differences such as the averaging method, the averaging period length and the bulk transfer coefficients used [Blanc, 1985].

4. The accuracy of the direct flux measurements used as a bias for the formulation of the bulk transfer schemes [Weare, 1989].

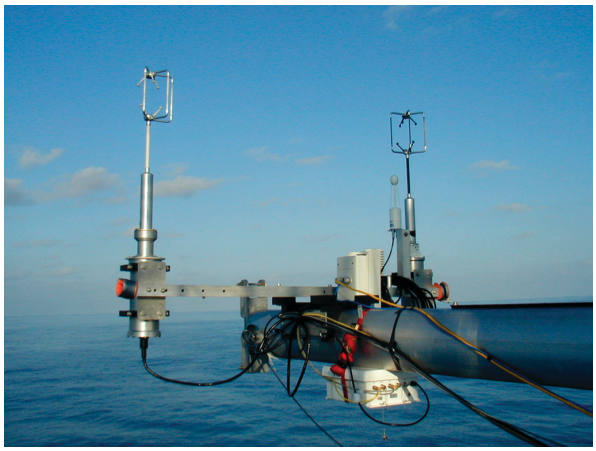

Figure 4.1: *Typical set-up for measuring fluxes with the eddy correlation technique. Sonic anemometer measure the wind velocity and temperature while other instruments measure the corresponding quantities of fluxes of interest such as the humidity.*

Because of these problems and the large variability under certain conditions, the estimates derived from the bulk formulations should always be treated with care, which is expressed in the need for formal error estimates to be included in all observational studies involving bulk-derived fluxes [Weare, 1989].

4.2 Eddy Correlation

The only direct meteorological technique for measuring the fluxes is the *direct covariance* or *eddy correlation* method. Further than a few centimeters away from the air-sea interface turbulent motion is the dominant mechanism of transport [Kraus and Businger, 1994]. In these regimes it is assumed that the fluxes are essentially constant with height from the surface to the level of measurement. Also, the covariance measure at a point must be representative of the ensemble average of the flux of the area of interest. This requires that conditions are horizontally uniform and stationary, which is usually the case for a height of observations less than 10m at a fetch larger than 1km [Kraus and Businger, 1994].

The turbulent flux j_C of a quantity C such as gas concentration, water vapor or temperature was given in Equation (2.28). It can be expressed by

$$j_c = \rho_n(\overline{w'C'} + wC), \tag{4.7}$$

where primed quantities indicate fluctuating components, following the notation used in Section 2.2 for the Reynolds decomposition. It is assumed that the time series is stationary, that is the average quantities does not vary appreciably in time, so that the second term in Equation (4.7) do not contribute to the flux, that is $wC = 0$. This assumption does not hold in the case of CO_2 fluxes, where this term may not be neglected and is dependent on latent and sensible heat fluxes [Webb et al., 1980].

The *momentum flux* τ can then be computed as the product of the density of moist air ρ and the eddy correlation of the fluxes of u' and w', the longitudinal and vertical wind velocity components.

The *sensible heat flux* j_s is given as the product of the *volumetric heat capacity* of air c_p and the covariance between vertical wind velocity and air temperature fluctuations T', while the latent heat flux is calculated as the product of the *latent heat of vaporization* L and the covariance between the vertical wind velocity w' and *specific humidity fluctuations* q'. These relations can be written as [Rogers, 1994]

$$\tau = \rho\overline{u'w'} \tag{4.8}$$

$$j_s = \rho c_p\overline{w'T'} \tag{4.9}$$

$$j_l = \rho L\overline{w'q'}, . \tag{4.10}$$

Generally, for computing the covariance, the measurement must embrace a frequency range from the turbulence dissipation scale (see Section 2.2.2) to a period long enough to include all flux-carrying wavelengths. In practice this entails recording continuous time-series at a resolution of 10-20 Hz [Friehe et al., 1991]. A typical sea-going experimental setup is pictured in Figure 4.1.

An in-depth discussion of this technique and its theoretical basis can be found in Businger [1986], Verma [1990] and Kanemasu et al. [1979].

4.2.1 Problems and Limitations

Although being a direct method for measuring fluxes, the eddy correlation method suffers from a few limitations and drawbacks. One major restriction is the need for a fast sensor to measure the tracer constituents considered. The frequency range required to obtain the fluxes is given by the variance spectrum of the vertical velocity w. As pointed out by Kaimal et al. [1972] this spectrum is dependent upon wind speed, measurement height and stability of the atmospheric profiles. Although eddy correlation measurements for latent and sensible heat are feasible [Caughey and Kaimal, 1977], the same for CO_2 has only recently emerged and is still subject to thorough research and testing [McGillis et al., 2001; Jacobs et al., 2001a,b].

Generally the eddy correlation technique has been used extensively over land but its straightforward application for measurements over the sea is limited to fixed towers or the R/V Flip, a custom-built "ship" that can be partially submerged and thus presents a very stable platform [Pond et al., 1971]. The reason is that the ships movement must be corrected for prior to estimating the correlation and hence the fluxes [Mitsuta and Fujitani, 1974; Edson et al., 1998]. This requires an expensive inertial navigation system (INS) and much higher computational effort [Fairall et al., 1990]. Also, due to the structure of the vessel and its effect on the flow, a great effort to reduce flow distortions is needed. Therefore the results obtained by eddy correlation at sea are still questionable.

The inaccuracy of the estimate for the fluxes is related to various fluxes and the *sampling problem*. By this is meant the problem of measuring the mean of a infinite variable by a finite number of samples. Due to the sampling problem the inaccuracy of the eddy correlation method is proportional to the square root of the ratio of the integral time scale to the duration of the sample. It is in the range of about 25% for the sensible heat flux for a one hour sample taken at the nominal height of 10m [Fairall et al., 1990]. These results agree with the findings of Hunt et al. [1988], who found a variability of 20% from the ensemble mean for one hour runs.

Depending on the observed tracer, the integration time of the eddy correlation method varies from a few minutes for heat fluxes to half an hour or longer for CO_2 fluxes [Kunz et al., 1995; Jacobs et al., 2001a]. These comparatively long integration times may be too long to resolve short term variations of the fluxes accurately.

Different sensors are needed to measure the fluctuations of vertical wind velocity and the other quantities such as specific humidity. Kaimal [1975] has formulated some criteria for the spatial placement and response time of the sensors. It turns out that the sensors need to respond to wavelengths as small as $z/3$ in order to measure the fluxes adequately. In order to avoid spectral attenuation from spatial averaging the sensors should be separated less than $z/3$ by a factor of 2π. Therefore, the minimum measurement height $z_{\min}$ is given for a separation of sensors d to

$$z_{\min} = 6\pi d. \tag{4.11}$$

For a sensor separation of 15cm the height of observations should be above 3m! This presents a major drawback, as it is desirable to conduct the measurement close to the sea-surface of interest.

Especially for CO_2 corrections to the measurements have to be applied, some of which are in the same order as the eddy correlation term $\overline{w'C'}$ itself. Often these corrections include measurements of other fluxes, introducing additional uncertainties in the estimate of the resulting flux [Jacobs et al., 2001b].

4.3 Eddy Accumulation and Conditional Sampling

As was stated in the preceding section, the need for fast sensors is one of the main drawbacks of the eddy correlation method, rendering it inappropriate for a number of applications. The need for fast sensors is relaxed by the *eddy accumulation method*, first introduced by Desjardins [1972]. With this technique, instead of determining the concentration of a tracer quickly, air is sampled conditionally first and the concentration is measured later. The vertical velocity is used to trigger the conditional sampling by either opening one valve or the other, depending on the sign of the vertical velocity. The amount of air being sampled is kept proportional to the vertical velocity w, which means that the positive and negative reservoirs will contain air given by

$$\overline{w'^{-}(C+C')} \quad \text{for} \quad w<0 \quad \text{and} \quad \overline{w'^{+}(C+C')} \quad \text{for} \quad w>0. \tag{4.12}$$

The flux can then be attained by adding these two quantities, resulting in

$$\overline{w'^{-}(C+C')} + \overline{w'^{+}(C+C')} = (\overline{w'^{-}} + \overline{w'^{+}})C + \overline{w'^{-}C'} + \overline{w'^{+}C'} = \overline{w'C'}, \tag{4.13}$$

were use was made of the fact that $\overline{w'^{-}}+\overline{w'^{+}} = \overline{w'} = 0$. The eddy correlation term in Equation (4.13)) can then be used to estimate the flux analogous to the eddy correlation method following Equation (4.7).

Essentially relying on the same basic principle is the *conditional sampling method* as proposed by Businger and Oncley [1990]. The simplification compared to the eddy accumulation method is that the air is no longer sampled proportionally to the vertical velocity w but instead at a constant flow rate.

In effect, the average concentration $\overline{C'^-}$ during downward velocities and the average concentration $\overline{C'^+}$ during upward velocities along with the variances of the vertical velocity w are measured. In the surface layer the flux is then obtained by assuming that

$$\overline{w'C'} = b\sigma_w \left(\overline{C'^-} - \overline{C'^-} \right), \tag{4.14}$$

where σ_w is the root of the mean square of the velocity fluctuations $\sigma_w \equiv \sqrt{\overline{w'^2}}$ and the coefficient b is to be determined experimentally. Direct measurements by Oncley et al. [1993] suggest that $b \simeq 0.6$ independent of stability, which has also been verified by simulations. The advantage of this method is that the coefficient b is independent of stability which allows for measurements of gas fluxes without simultaneous measurements of momentum and heat flux.

4.3.1 Drawbacks

The eddy accumulation method successfully solved some problems of the eddy correlation method. The experimental ease of employing this method is by no means much greater though. Most vertical velocity sensors possess a bias on w which is nonzero. Thus, wC can quickly become a term much larger than $\overline{w'C'}$ which makes this technique prone to errors. Also, it is very difficult to reliably open and close valves proportional to w', which is analyzed by Hicks and McMillen [1984].

Even though the conditional sampling method is less prone to errors than the eddy correlation method [Oncley et al., 1993], the introduction of an empirical coefficient does not make this method too appealing. This is somewhat compensated for by the offset due to the technical ease of realizing it.

4.4 Inertial Dissipation and Direct Dissipation

The *inertial dissipation* and *direct dissipation* methods are very similar and differ only in the method used to obtain the dissipation rates. They both rely on measuring the dissipation of the turbulent quantity of interest. In the direct dissipation technique one tries to measure this dissipation by means of a very fast sensor. Inertial dissipation measurements are somewhat less problematic by examining microturbulence at frequencies well below the dissipation range in the inertial subrange of isotropic turbulence as introduced in Section 2.2.2. The assumption that turbulence is isotropic in the high frequency end of the wavenumber domain seems to be valid in the ocean and the marine boundary layer at some distance d to the interface ($d_a \approx 10$m in the atmosphere and $d_s \approx 30$cm in the ocean) [Kraus and Businger, 1994].

Both dissipation techniques try to reduce the difficulties of the Eddy correlation technique from Section 4.2 by relaxing the range of turbulence that has to be measured. Also, the dissipation methods are based on autovariance statistics and as such approach the ensemble average more rapidly than for covariance statistics [Fairall et al., 1990]. This is a big advantage, as most of the errors in eddy correlation measurements under ideal conditions are due to atmospheric variability, which can be as high as $20 - 25\%$ for one hour averages [Hunt et al., 1988; Fairall et al., 1990].

The budget equations for total turbulent kinetic energy E', the variances of potential temperature θ' and specific humidity q' are given by [Lenshow et al., 1980]

$$S_E = \frac{\partial \overline{E'}}{\partial t} + \overline{u'w'}\frac{\partial u}{\partial z} + \overline{u'w'}\frac{\partial v}{\partial z} + \frac{\partial \overline{E'w'}}{\partial z} + \frac{1}{\rho}\frac{\partial \overline{p'w'}}{\partial z} - \frac{g}{T}\overline{\theta'_v w'} + \epsilon, \tag{4.15}$$

$$S_\theta = \frac{1}{2}\frac{\partial \overline{\theta'^2}}{\partial t} + \overline{\theta'w'}\frac{\partial \theta}{\partial z} + \frac{1}{2}\frac{\partial \overline{\theta'^2 w'}}{\partial z} + N_\theta, \tag{4.16}$$

$$S_q = \frac{1}{2}\frac{\partial \overline{q'^2}}{\partial t} + \overline{q'w'}\frac{\partial q}{\partial z} + \frac{1}{2}\frac{\partial \overline{q'^2 w'}}{\partial z} + N_q, \tag{4.17}$$

where primed letters denote turbulent fluctuations, S_E, S_θ and S_q represent the local sources and sinks of E, θ and q. The density of air is designated by ρ, the characteristic temperature by T and the pressure and acceleration of gravity by p and g respectively. From the virtual potential temperature θ_v the correlation is given by $\overline{\theta_v w} = \overline{\theta_w} + 0.61T\overline{qw}$ [Fairall and Larsen, 1986]. Assuming local isotropy (see Section 2.2.1), the dissipation rates for turbulent kinetic ϵ, temperature variance N_θ and humidity variance N_q can be computed from the time derivatives of the fluctuations, according to [Champagne et al., 1977]

$$\epsilon = 15\nu\overline{\left(\frac{\partial u'}{\partial x}\right)^2} = \frac{15\nu}{u^2}\overline{\left(\frac{\partial u'}{\partial t}\right)^2}B_u, \tag{4.18}$$

$$N_\theta = 3D_\theta\overline{\left(\frac{\partial \theta'}{\partial x}\right)^2} = \frac{3D_\theta}{u^2}\overline{\left(\frac{\partial \theta'}{\partial t}\right)^2}B_\theta, \tag{4.19}$$

$$N_q = 3D_q\overline{\left(\frac{\partial q'}{\partial x}\right)^2} = \frac{3D_q}{u^2}\overline{\left(\frac{\partial q'}{\partial t}\right)^2}B_\theta, \tag{4.20}$$

where ν, D_θ and D_q are molecular diffusivities and B_u and B_θ are factors that correct for inaccuracies in Taylor's hypothesis Champagne et al. [1977].

For stationary conditions, the temporal derivatives are equal to zero and near the surface the $\overline{u'w'}$-term can be neglected [Wyngaard and Coté, 1971]. The budget Equations (4.15)-(4.17) can then be made dimensionless by multiplying with the *Monin-Obukhov similarity* (MOS) scaling parameters [Geernaert, 1990], leading to

$$\epsilon\frac{Kz}{u_*^3} = \phi_u(\xi) - K\xi\frac{\partial}{\partial z}\left(\frac{\overline{E'w'}}{u_*^3}\right) - \phi_p(\xi) - \xi, \tag{4.21}$$

$$N_\theta\frac{Kz}{u_*\theta_*^2} = \phi_\theta(\xi) - \frac{K}{2}\xi\frac{\partial}{\partial z}\left(\frac{\overline{\theta'^2 w'}}{u_*\theta_*^2}\right), \tag{4.22}$$

$$N_q\frac{Kz}{u_* q_*^2} = \phi_q(\xi) - \frac{K}{2}\xi\frac{\partial}{\partial z}\left(\frac{\overline{q'^2 w'}}{u_* q_*^2}\right), \tag{4.23}$$

where $\xi = z/L$ is the normalized height with the *Monin-Obukhov length* $L = -u_*^3 T/(gK\overline{\theta_v w})$ and the *von Karman constant* K. The functions ϕ_u, ϕ_p, ϕ_θ, and ϕ_q are dimensionless profile functions [Businger et al., 1971]. Often it is assumed that the transport terms are negligible, thus Equation

(4.21)-(4.23) can be simplified to

$$\epsilon \frac{Kz}{u_*^3} = \phi_u(\xi) - \xi, \tag{4.24}$$

$$N_\theta \frac{Kz}{u_* \theta_*^2} = \phi_\theta(\xi), \tag{4.25}$$

$$N_q \frac{Kz}{u_* q_*^2} = \phi_q(\xi). \tag{4.26}$$

With knowledge of the dimensionless profile functions on the right hand side of Equations (4.24)-(4.25) only ϵ, N_θ and N_q have to be measured and the fluxes computed from the Monin-Obukhov surface scaling parameters according to

$$\tau = \rho\overline{u'w'} = -\rho u_*^2 \tag{4.27}$$

$$j_s = \rho c_p \overline{w'\theta'} = -\rho c_p u_* \theta_* \tag{4.28}$$

$$j_l = \rho L \overline{w'q'} = -\rho L u_* q_*. \tag{4.29}$$

This is the scheme of the direct dissipation method, which has the drawback of requiring measurement of the dissipations which calls for an instrumental response approaching 5kHz in the field. This is hardly possible for temperature and humidity sensors [Fairall et al., 1990].

Due to these instrumental difficulties most often the inertial dissipation technique is employed for flux measurements, whereas the direct dissipation method has its main merits in determining the Kolmogorov constant α_1 for the inertial subrange, as pointed out in Section 2.2.2.

In the inertial dissipation method the frequency response problem can be circumvented by examining microturbulences at frequencies well below the dissipation range in the inertial subrange of isothermal turbulence which was introduced in Section 2.2.2. The one dimensional variance spectrum $G_x(k)$ of the scalar quantity x ($x \in \{u, T, q\}$) was given in Equation (2.43) as

$$G_x(k_1) = 0.25 C_x^2 k_1^{-5/3} = \alpha_x \epsilon^{-1/3} N_x k_1^{-5/3}, \tag{4.30}$$

where k_1 is the downstream wavenumber, $N_u = \epsilon$, α_x are the Kolmogorov constants ($\alpha_u = 0.52$, $\alpha_T = \alpha_q = 0.8$ [Fairall and Larsen, 1986]) and C_x is the structure function parameter for the quantity x, defined as [Fairall et al., 1990]

$$C_x^2 = \frac{\left(x(\boldsymbol{r}) - x(\boldsymbol{r}+\boldsymbol{d})\right)^2}{|d|^{2/3}}. \tag{4.31}$$

Here $x(\boldsymbol{r})$ is the value of x measured at location $\boldsymbol{r}$ and $x(\boldsymbol{r}+\boldsymbol{d})$ denoted the measurement at a distance $\boldsymbol{d}$ from $\boldsymbol{r}$.

From Equation (4.30) the dissipation rates in Equations (4.24) - (4.26) can be measured with instruments offering a frequency response in tens of Hertz [Fairall et al., 1990]. When employing two instruments instead of one, the structure function from Equation (4.31) can be used, which is related to the dissipation variables through the *Corrsin relations*, given by [Fairall et al., 1990]

$$\epsilon = \left(0.52 C_u^2\right)^{3/2} \tag{4.32}$$

$$N_x = 0.32 C_x^2 \epsilon^{1/3} \tag{4.33}$$

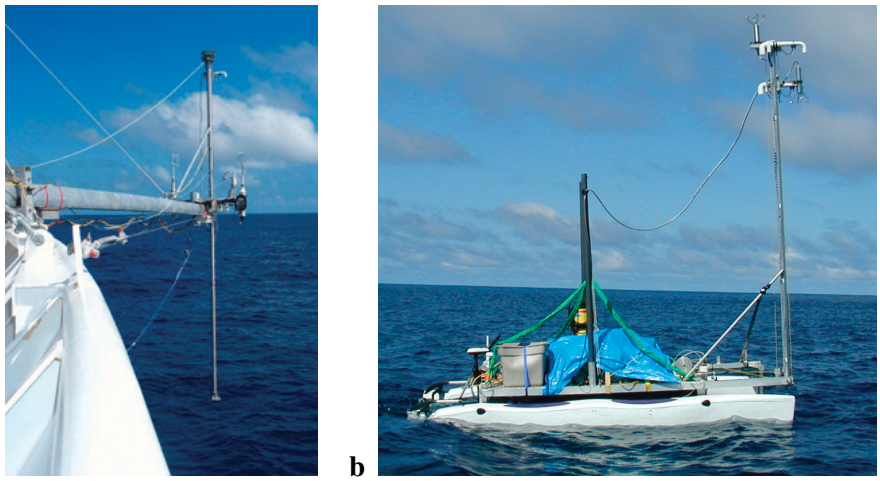

Figure 4.2: *Two experimental implementations of the gradient technique. In* ***a*** *the concentration of gasses is measured at two heights by a contraption suspended by a boom off a ship. In* ***b*** *gas concentrations are measured on board a catamaran by two probe inlets on a mast. The one inlet at the top is stationary, while the second one moves up and down the mast.*

The dissipation methods have the big advantage of being less sensitive to low frequency ship motions than the covariance method and probably less sensitive to platform distortions of the air flow than eddy correlation and profiling methods [Fairall and Larsen, 1986]. Fairall et al. [1990] describes a system that was successfully used in strong winds in the North Sea.

4.4.1 Problems

Mentioned before was the disadvantage of high instrumental frequency response for the direct dissipation technique. The inertial dissipation method relaxes the demand on high frequency response at the handicap of introducing empirical parameters. As formulated above, the inertial dissipation technique requires assumptions with regard to the values of the von Karman constant, K, the Kolmogorov constant K, and the form of the dimensionless functions $\phi_u(\xi)$, $\phi_\theta(\xi)$ and $\phi_q(\xi)$. These constants and functions are not independent and Fairall and Larsen [1986] have suggested a different formalism of the inertial dissipation method in terms of turbulence structure functions.

Another problem of the inertial dissipation method is the question of choosing the frequency limiting the inertial range [Mestayer, 1982].

4.5 Gradient Method

It is very difficult to measure the turbulent vertical transport directly. Therefore the *eddy transfer coefficients* K_c are introduced, relating the turbulent vertical transport parametrically to bulk quantities that are more easily attainable [Kraus and Businger, 1994]. The *gradient technique* is based on the assumption that the flux can be obtained by multiplying the vertical mean gradient by an eddy transfer coefficient, the basis of which is derived from semi-empirical profile relationships and the *Monin-*

Obukhov similarity. The eddy transfer coefficient can be formulated for sensible and latent heat which yields

$$\overline{\theta w} = -K_s \frac{\partial T}{\partial z} \tag{4.34}$$

$$\overline{q' w} = -K_l \frac{\partial \overline{q}}{\partial z},, \tag{4.35}$$

where K_s is the eddy transfer coefficient of sensible heat, or *eddy thermal diffusivity*, K_l the eddy transfer coefficient for water vapor, or *eddy diffusivity for water vapor*, and T the potential temperature mean component of the Reynolds decomposition. Similar expressions can be derived for mass fluxes such as that for CO_2 with the corresponding coefficients.

The expressions for the eddy correlations from Equations (4.34) and (4.35) can be used in the formulations of the fluxes from Equations (4.9) and (4.10) respectively, resulting in

$$j_s = -\rho c_p K_s \frac{\partial \Theta}{\partial z} \tag{4.36}$$

$$j_l = -\rho L K_l \frac{\partial \overline{q}}{\partial z}. \tag{4.37}$$

The gradient is determined by making measurements at two or more heights. Most profiles are close to logarithmic with height. Therefore the geometric mean height is used as the height where the tangent to the profile is equal to the gradient.

4.5.1 Problems and Sources of Error

The main problem for the gradient technique is the required accuracy of the measuring instrument. This is due to very small gradients found in the field under most conditions [Kraus and Businger, 1994]. This calls for very accurate measurements in order to obtain sufficiently accurate gradients. On most instruments the relative accuracy is far higher than the absolute accuracy. Instrumental error is thus kept small by using the same instrument for measurements at two different heights. The gradient method produces most accurate results under stable stratification and light wind. The accuracy requirements for the sensors for mass fluxes is discussed in detail in Businger and Delaney [1990].

The concept of the gradient method is based on semi-empirical formulations. This is of course not as appealing as a direct method, as some uncertainty exists in the empirical parameters. Also, the gradient technique is very prone to errors introduced by flow distortions from the platform and by motion induced at sea.

4.6 Radiative Fluxes

The components of radiant energy flux to and from the sea surface can be divided into shortwave (typically 0.3 to 3μm wavelength) and long wave (3 to 50 μm wavelength) fractions. The shortwave

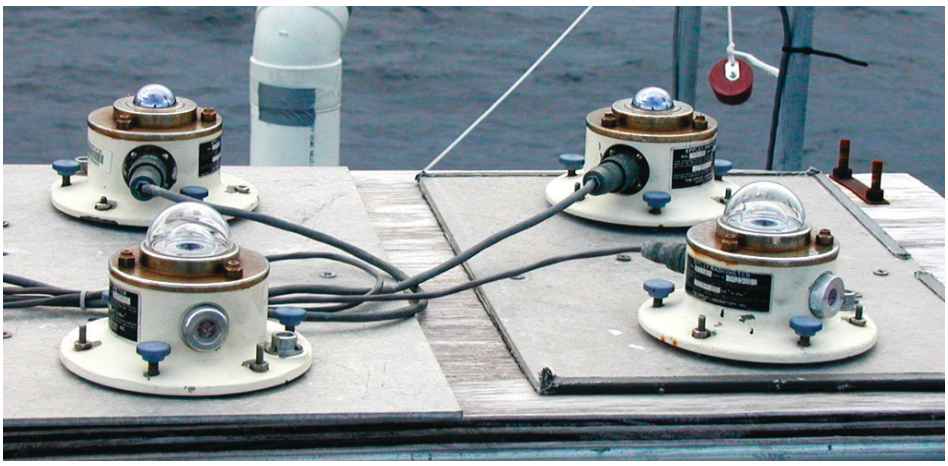

Figure 4.3: *The long wave and short wave irradiance is measured with pyranometers and pyrgeometers respectively. Pictured are two Eppley™PIR (pyrgeometer) in the back and two Eppley™PSP (pyranometer) in the front [Fairall and Hare, 2001].*

part of the spectrum stems from solar irradiation, whereas the long wave part is terrestrial radiation of heat. The net heat flux j_{rad} at the sea surface due to radiation is then given by [Katsaros, 1990]

$$j_{\mathrm{rad}} = E_{\mathrm{short}} + M_{\mathrm{short}} + E_{\mathrm{long}} + M_{\mathrm{long}}, \tag{4.38}$$

where the subscript indicates the shortwave or long wave fraction respectively and the irradiance E and exitance M were introduced in Section 2.3. Experimentally the four terms can be measured individually by hemispheric sensors. *Pyranometers* are used for short wave irradiance measurements, *pyrgeometers* for long wave irradiance and their total can be gained from *pyrradiometers* [Hinzpeter, 1980]. The basic design of modern pyranometers was introduced by Moll [1923] and is based on a blackened horizontal receiving surface bonded to a thermopile and protected by two concentric precision hemispheric glass domes. The pyrgeometer is of similar construction to the pyranometer, with differences only due to the different spectral range of the measured irradiance. Instead of the two glass domes in an pyrgeometer a single dome made from silicon or similar material transparent to the long wave band, coated on the inside with an interference filter to block shortwave radiation, protects the receiving surface. The long wave irradiance passing through the dome is only one component of the thermal balance of the thermopile. The remaining components come from various parts of the instrument and must be accounted for [Fairall et al., 1998].

The exitances M_{short} and M_{long} are difficult to measure to a high accuracy from obstacles such as ships at sea. However, they can be calculated quite accurately from well proven formulae when the sea surface temperature and the irradiance E_{short} are known, which is why they are seldom measured nowadays [Katsaros, 1990].

The shortwave exitance M_{short} can be calculated with good accuracy from direct measurements of the shortwave irradiance E_{short} and a value for the *albedo* A of the sea surface. The albedo is defined as the the ratio of all short wave radiation leaving the surface to the incident irradiance . It is not to be confused with the reflectance which is defined as the ratio of the reflected to the incident

radiance [Jerlov, 1976]. The albedo is thus given by [Thomas and Stamnes, 1999]

$$A = -\frac{M_{\text{short}}}{E_{\text{short}}}. \tag{4.39}$$

The albedo will generally depend on the roughness of the sea and thus wind speed. The first effect is the dependence on incident angle, which translates to 1 to 5% of E_{short} in wind speeds from 4 to 12 m/s [Katsaros, 1990]. In winds that are strong enough for wave breaking to occur, an increase of albedo occurs due to foam cover. This effect has been measured as the albedo increases from $A = 0.006$ for wind of about 15 m/s to $A = 0.012$ for winds of 20 m/s [Monahan and Woolf, 1989]. The shortwave exitance M_{short} is then simply given by

$$M_{\text{short}} = -A\frac{E_{\text{short}}}{E_{\text{short},0}}E_{\text{short}}, \tag{4.40}$$

where $E_{\text{short},0}$ is the irradiance at the top of the atmosphere, that can be estimated from knowledge of the solar constant, date, time and location [Paltridge and Platt, 1976].

Direct long wave exitance measurements are difficult and erroneous due to effects of ship movement or the ship blocking part of the solid angle. Therefore, the Stefan-Boltzmann law is usually used, resulting in [Hinzpeter, 1980]

$$M_{\text{long}} = \epsilon\sigma T_{\text{surf}}^4 + (1-\epsilon)E_{\text{long}}, \tag{4.41}$$

where ϵ is the emittance, σ the Stefan-Boltzmann constant and T_{surf} the sea-surface temperature in Kelvin. The average emittance value for sea water is about $\epsilon = 0.98$ in a wavelength range of 3-50μm, which depends slightly on temperature and salinity [Katsaros, 1980a].

4.6.1 Problems

The main difficulty in measuring the radiative heat flux with pyranometers and pyrgeometers lies in the calibration of the units. Given a careful calibration and operation the accuracy of a pyrgeometer can be between $\pm 2\text{W/m}^2$ [Philipona et al., 1995] and $\pm 5\text{W/m}^2$[Fairall et al., 1998].

Another source of error is caused by the platform motion. By definition the receiving surface must be horizontal, which cannot be guaranteed on the ocean. The magnitude of the errors introduced by platform motion or lean due to wind forcing depend on several factors such as cloudiness, latitude, season and time of day. Under unfavorable conditions (clear skies, high latitudes and 10° instrument tilt) the error can be as large as $10 - 20\%$ in the daily average [Katsaros and DeVault, 1986].

The pyrgeometer can be facing downward to measure longwave exitance, but on either a ship or a buoy it would need to be mounted at the end of a fairly long boom to exclude the platform itself from the field of view. There are obviously practical problems to this arrangement, and it is preferable and probably more accurate, to measure sea temperature and use the Stefan-Bolzmann law from Equation (4.41). This immediately raises a problem, because accurate IR radiometers are usually not available, and the sea temperature measured at some depth may be considerably different from T_{surf}, as was outlined in Section 3.1.

4.7 Summary

In this chapter meteorological techniques for measuring the fluxes of heat and mass were established. All of the techniques have different drawbacks ranging from high demands on the measuring instruments to relying on a number of model assumptions and empirical constants. All the meteorological techniques introduced have in common the reliance on the measurement of a number of different entities for the fluxes. This does of course introduce errors from the different instruments which are spatially separated. Inaccuracies due to cross calibration of the instruments are a major concern. All these techniques represent point measurements with integration times ranging from a couple of minutes to hours.

As far as the measurements of heat fluxes are concerned, none of the techniques are capable of measuring the net heat flux directly but only the constituent fluxes. This leads to an accumulation of errors for the net flux. The measurements are taken at some distance from the location of interest, the sea-surface. Hence they are not capable of locale measurements but have to extrapolate results.

Chapter 5

Estimating Heat Flux from IR Sequences

In the preceding chapter current state of the art experimental techniques for determining the heat flux j at the sea surface interface were presented. In common to all those techniques is their inability to accurate measure j with a high spatial and temporal resolution. Furthermore, they cannot measure the flux j locally at the sea surface, but have to extrapolate from data acquired away from it by up to 10m, depending on the actual technique employed.

All these limitations called for a novel technique utilizing infrared imagery. The use of cameras sensible in the mid to far infrared are not new in estimating the heat flux. Haußecker [1996] employed such cameras for the *Controlled Flux Technique* (CFT), pioneered with an infrared radiometer by Jähne et al. [1989], where a laser is used to heat up a patch of water. From the rate of change of the spot's temperature the net heat flux can then be deduced. This technique has successfully been used in the field [Haußecker and Jähne, 1995]. Jessup et al. [1997] utilized infrared imagery to measure the sea surface temperature and saw variations in the order of 0.1-0.2 K which the authors attributed to convergence-divergence zones in the local water motion. From these variations micro scale wave breaking was detected. An interesting approach was presented by McKeown and Leighton [1999] which is based on the differential absorption of water between 3.817 and 4.514 μm, based on a design by McAlister and McLeish [1970]. Here the temperature gradient in the aqueous thermal boundary layer is assumed to be linear. Knowing that the penetration depth in water depends on the wavelength this gradient can be measured from infrared imagery in two narrow wavelength windows. Since the gradient at the sea surface is directly proportional to the net heat flux this technique poses another means of determining this parameter. Measurements were conducted in a laboratory facility [McKeown and Leighton, 1999], but due to high demand on the imaging apparatus with respect to frame rate and noise level no in situ measurements were conducted yet. In this technique the interpretation of the results due to wave slope and reflexes poses a major difficulty in all but low wind conditions.

In this chapter novel techniques for measuring important parameters of air-water heat exchange as well as the heat fluxes themselves are presented. These techniques promise experimental simplifications as they all rely on only one commercial IR camera without the need for additional lasers, mirrors or filters.

In Section 5.1 the optical properties of water in the infrared window of interest are outlined, followed by a description of the statistical analysis employed for measuring the temperature depression

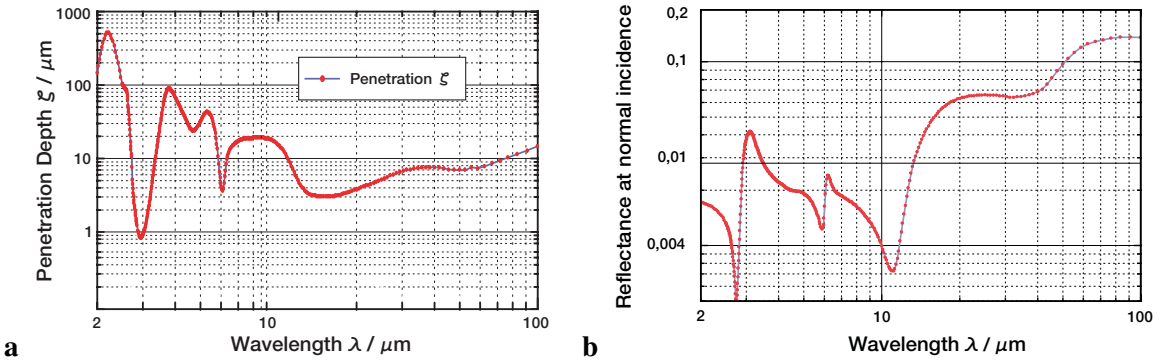

Figure 5.1: *A plot of the penetration depth ζ with respect to wavelength λ in* ***a*** *[Schimpf, 2000] and the reflectivity at normal incidence in* ***b*** *[Haußecker, 1996].*

ΔT across the cool skin of the ocean. A justification of the probability density function $p(\tau)$ of surface renewal events will be given in Section 5.3 with a technique for accurately measuring these parameters. Two novel techniques for measuring the net sea surface heat flux are presented in Section 5.4. This chapter concludes with an algorithm for computing the transfer velocity of heat k_{heat} with a high temporal and spatial resolution as presented in Section 5.5.

5.1 Optical Properties of Sea Water in the Far Infrared

When conducting measurements with an IR camera it is important to have a basic understanding of the optical properties of the object under observation. In the context of this work IR cameras sensitive in a spectral range of 3-5 μm were used to measure spatio-temporal patterns at the free air-water interface. An analysis of the optical properties of water was conducted by Downing and Williams [1975] and Wieliczka et al. [1989] with a thorough analysis on the implications for the CFT technique by Haußecker [1996]. Therefore, only a brief overview of the most important properties will be presented here.

For measuring the net heat flux j at the sea surface it is obviously important to know the depth range the detected radiation originates from. Since it is the 300μm - 1mm thick thermal boundary layer where the processes of interest take place, radiation stemming from regions beyond this depth are of no interest. In Figure 5.1 a plot of the penetration depth ξ for wavelenghts ranging from 2 to 100 μm is shown. The used IR camera is based on an InSb detector which is sensitive in a spectral window of 3-5 μm. In this spectral range the penetration depth varies by almost two orders of magnitude from about $\xi \approx 2 - 90$ μm. A measurement conducted with such a detector thus represents an integration over this depth. Since the integrated depth is embedded well within the boundary layer, which is almost one order of magnitudes thicker, accurate measurements of physical processes within the thermal boundary layer are possible.

Both reflectance and emittance are functions of the angle of emission, which is the incident angle between surface normal and the line of sight of the IR camera. This angle is of course affected by the nadir angle of the instrument and the wave slopes. Cox and Munk [1955] studied the down- and cross-wind slope distribution of waves and concluded that the rms slope is directly proportional to the

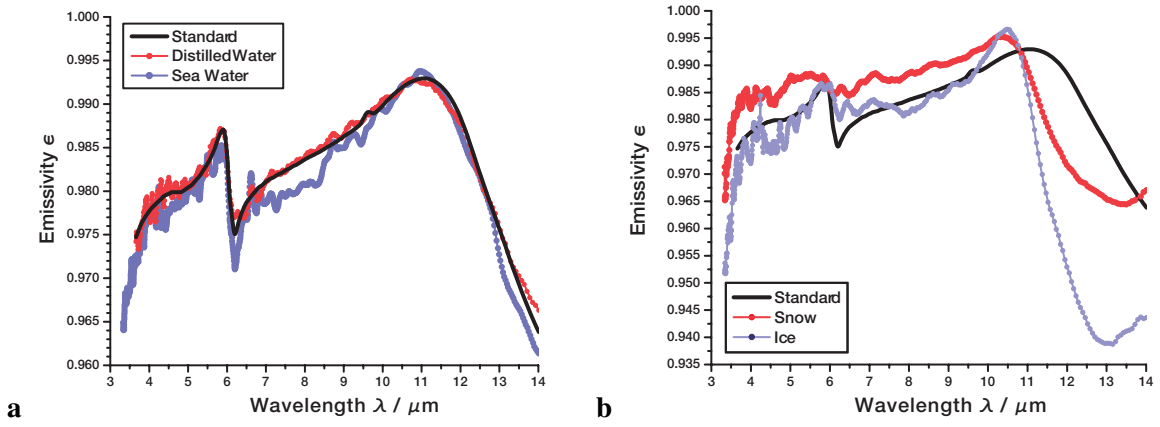

Figure 5.2: *The emissivity ϵ for the distilled water, standard, distilled water and sea water in* ***a*** *and for the distilled water standard, snow and ice in* ***b*** *(after Wan [1976])*

wind speed. For winds less than 15 m/s the rms wave slopes are generally less than 16°. Thus the roughness of the sea has no strong effect on the emittance, and the only important consideration is the nadir angle of the instrument [Katsaros, 1980b].

Generally, beyond 30° of normal the water reflectance is a strong function of incidence, similar to the behavior in the visible spectrum. However, for smaller angles the emissivity ϵ of water is almost constant with $\epsilon > 97$ for infrared wavelengths ranging from $3.5\mu\text{m} \leq \lambda \leq 13\mu\text{m}$ as can be seen from Figure 5.2. A discussion of the effects of salinity on the emissivity of sea water can be found in Querry et al. [1977]. To this end the water surface can effectively be treated as a black body, implying that its surface is perfectly diffuse or *Lambertian*. In this regime the measured intensity in the IR camera will not depend on surface slope, an important prerequisite for accurate measurements.

Reflexes at the sea surface can be greatly reduced by measuring polarized radiation at the Brewster angle, which is about 57° from zenith for water. At this angle the reflection is at a minimum for horizontally polarized radiation [Grassl, 1976]. However, polarizers will reduce the incident radiation by a factor of 2 and thus increase the noise level, assuming the same integration time of the sensor. The net reflectance of unpolarized radiation is the mean value of the reflectance of both polarizing planes. This will stay at a minimum value for angles from zenith to about 30°, which is why the angle of observation should be in this region. A plot of these reflectances is shown in Figure 5.3.

For measurements in the field, surfactant films on the sea surface are always present. These films may be due to organic deposition or produced by anthropogenic sources. The effect of a surfactant film may influence the sensed radiation in a number of ways [Katsaros, 1980b]:

1. Capillary waves are suppressed by surfactants. Since the turbulences induced by these waves reduce ΔT, a greater ΔT in areas of slick is anticipated.

2. Slicks provide an additional layer through which heat has to be transported by diffusion. This diminishes the net heat flux j through the surface.

3. Some organic materials decrease evaporation, which effectively lessens the net heat flux.

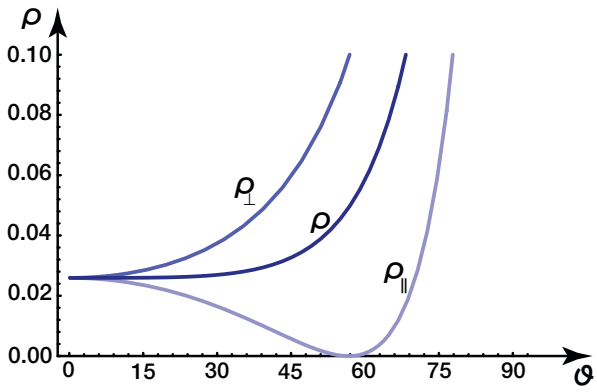

Figure 5.3: *The reflectance ρ as a function of the angle of incidence for horizontally and vertically polarized ($\rho_{||}$ and $\rho_{\perp}$) as well as for unpolarized radiation (ρ) (after Haußecker [1996]).*

4. The emittance of oil is less than water. Corrections for the sky reflections will be greater and the surface appear cooler.

Especially the increase of sky reflections induced by a surfactant film poses experimental difficulties for the techniques proposed in this thesis.

5.2 Determining the Cool Skin Temperature Depression

The temperature depression across the cool skin of the ocean is an important parameter in air-sea gas exchange, as was outlined in Section 3.1. Due to the minute thermal boundary layer thickness of less than 1 mm accurate measurements are difficult to obtain. With a statistical analysis this important parameter can be retrieved from infrared imagery [Haußecker et al., 2001].

The statistical analysis is based upon fitting an analytical function to the temperature distribution at the sea surface. The analytical function can be derived by assuming a surface renewal model, as introduced in Section 2.4.3, for an approximation of the predominant exchange process. Affixed to the surface renewal model is of course the probability density function (pdf) of times in between consecutive renewal events. In the context of this work strong experimental evidence is presented, that this pdf is logarithmic-normal in nature (see Section 5.3). It is thus justified to assume a pdf of this type for the derivation of an analytical expression for the temperature distribution at the sea surface.

Due to the statistical nature of this approach the probability of measuring a temperature T_{surf} at the surface is of key interest. The normalized likelihood $p(T_{\mathrm{surf}}|\tau)$ of measuring a temperature T_{surf} at a given time $\tau = t - t_0$ since the last surface renewal event is thus given by

$$p(T_{\mathrm{surf}}|\tau) = \frac{2}{\tau(\alpha j)^2}(T_{\mathrm{surf}} - T_{\mathrm{bulk}}), \tag{5.1}$$

where j is the heat flux, and the constant $\alpha = 2/(\sqrt{\pi\kappa}\rho c_p)$ depends only on material properties. For a thorough derivation of this equation and subsequent results the reader is referred to Appendix B.

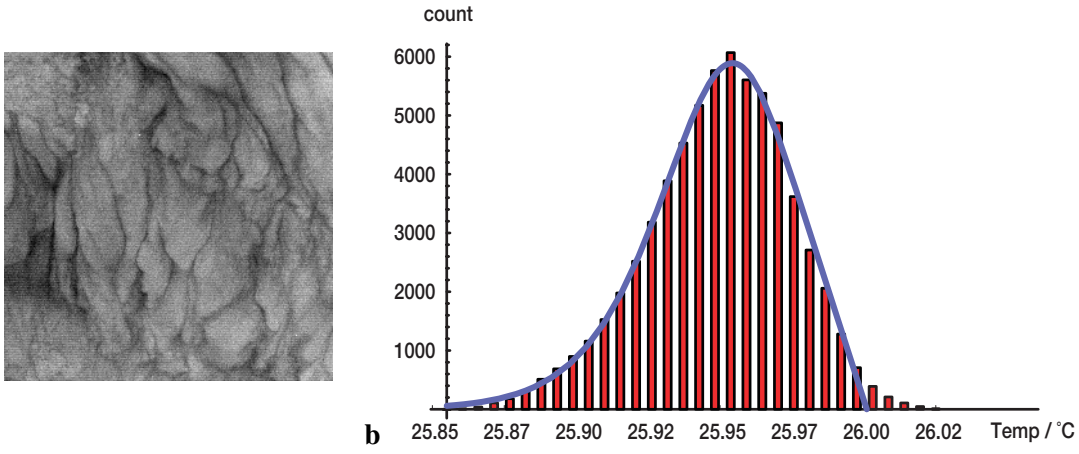

Figure 5.4: *The analytic function describes the temperature distribution of an IR image in* ***a*** *quite well, as can easily be verified in* ***b*** *.*

The probability density $p(T_{\mathrm{surf}})$ of finding a certain temperature T_{surf} at the sea surface is then found by integrating the expression from Equation (5.1) over all renewal times τ weighted with the probability density function $p(\tau)$ of a surface renewal event taking place at time τ, which leads to

$$p(T_{\mathrm{surf}}) = \int_{(\Delta T_{\mathrm{surf}}/\alpha j)^2}^{\infty} p(\tau)\; p(T_{\mathrm{surf}}|\tau)\; \mathrm{d}\tau \tag{5.2}$$

with the lower integration limit given by the minimum time needed to attain a temperature T_{surf}. Up to his point no hypothesis about the model of surface renewal have been made. However, in order to evaluate Equation (5.2) some assumptions concerning the probability density function $p(\tau)$ of the times between consecutive surface renewal events have to be made. As stated earlier, $p(t)$ is assumed to be a logarithmic normal distribution shown in Equation (2.51). This allows for the integration of Equation (5.2), resulting in

$$p(T_{\mathrm{surf}}) = \mathfrak{S}(\mathrm{sign}(j)\cdot\Delta T)\frac{|\Delta T|}{(\alpha j)^2}\exp\left[\frac{\sigma^2}{4}-m\right]\mathrm{erfc}\left[\frac{\sigma}{2}-\frac{m}{\sigma}+\frac{1}{\sigma}\ln\left(\frac{\Delta T}{\alpha j}\right)^2\right], \tag{5.3}$$

for $j \neq 0$ and $p(T_{\mathrm{surf}}) = \delta(\Delta T)$ for $j = 0$ [Haußecker et al., 2001; Schimpf et al., 1999]. Here $\Delta T = T_{\mathrm{surf}} - T_{\mathrm{bulk}}$ denotes the temperature depression, erfc is the complimentary error function defined in Equation (2.22), $\delta(x)$ denotes Dirac's delta distribution, $\mathrm{sign}(x)$ the sign function and $\mathfrak{S}(x)$ the binary step function

$$\mathrm{sign}(x) = \begin{cases} 1, & x \geq 0 \\ -1, & x < 0 \end{cases} \quad \text{and} \quad \mathfrak{S}(x) = \begin{cases} 1, & x \geq 0 \\ 0, & x < 0 \end{cases} . \tag{5.4}$$

A derivation of Equation (5.3) can be found in Appendix B.

From Taylors hypothesis the analytical function for the probability density function $p(T_{\mathrm{surf}})$ can be fitted to the frequency density function of the temperature distribution from an individual image, as can be seen in Figure 5.4. This allows for an estimation of the temperature of the bulk T_{bulk} with the frame rate of the IR camera. In practice the data from one frame might not always be statistically

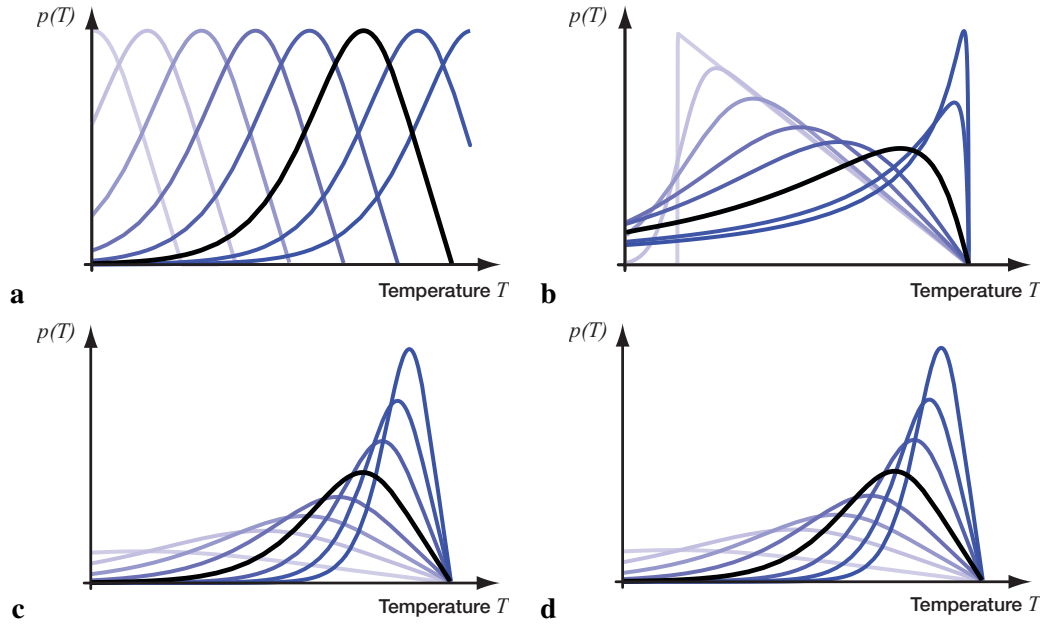

Figure 5.5: *Plot of the probability density function $p(T)$. Both T_{bulk} and σ can be estimated independently from the fit, as is evident from the plots of different T_{bulk} in* ***a*** *and the same for different values of σ in* ***b*** *. The values for j and m cannot be computed independently, as is apparent from the same plots for different m in* ***c*** *and different values of j in* ***d*** *.*

significant enough to legitimate this approach. In this case it might be necessary to include several images in the statistical analysis. The accuracy of determining the T_{bulk} in this way will be analyzed in Section 9.4.

From the expression for the pdf of the sea surface temperature $p(T_{\mathrm{surf}})$ in Equation (5.3) it becomes apparent that four parameters fully describe the distribution. The first is the temperature of the bulk water T_{bulk}, as was stretched before. The other parameter σ and m characterize the general form of the pdf of surface renewal and hence the temperature distribution at the sea surface. The last parameter is the heat flux j. It might be tempting to assume that it is possible to estimate all those parameters from a single fit of the analytical function to the temperature distribution. However, this is not the case as is illustrated in Figure 5.5. The dependence of the parameters to one another will be analyzed in the following section.

The mean temperature $\overline{T_{\mathrm{surf}}}$ at the sea surface is given as the expectancy value of the temperature distribution. The expectancy value is computed by the integral of the temperatures weighted by the probability density function of measuring that temperature at the sea surface, given by Equation (5.3). Hence

$$\overline{T_{\mathrm{surf}}} = \frac{\int_{-\infty}^{\infty} T_{\mathrm{surf}} \cdot p(T_{\mathrm{surf}})\, \mathrm{d}T_{\mathrm{surf}}}{\int_{-\infty}^{\infty} p(T_{\mathrm{surf}})\, \mathrm{d}T_{\mathrm{surf}}} = \int_{-\infty}^{\infty} T_{\mathrm{surf}} \cdot p(T_{\mathrm{surf}})\, \mathrm{d}T_{\mathrm{surf}}. \tag{5.5}$$

This integration can be solved numerically, resulting in a value for $\overline{T_{\mathrm{surf}}}$ that is much less prone to errors in the data than calculating $\overline{T_{\mathrm{surf}}}$ by just summing over the image intensities and dividing by the number of pixels. From the knowledge of both T_{surf} and T_{bulk} the temperature depression $\Delta T = T_{\mathrm{surf}} - T_{\mathrm{bulk}}$ can be computed. Since T_{bulk} is given by the statistical analysis over a spatio-

temporal neighborhood, it makes sense to use the mean surface temperature $\overline{T_{\mathrm{surf}}}$ as given by the integration from Equation (5.5).

5.2.1 Interdependence of Parameters

Even though the temperature of the bulk water T_{bulk} can be estimated from a statistical analysis of the temperature distribution of the sea surface, this frequency data does not hold enough information to independently estimate all parameters of the analytical function in Equation (5.3). An illustration of the interdependence of the parameter m and the heat flux j is presented in Figure 5.5.

The interdependence of the parameters m and j is expressed in the fact that the same analytical curve can be fitted for different values of m and j. This can easily be verified by looking at Equation (5.3). The terms in this equation can be divided into two groups, namely into terms that normalize the function and terms that are responsible for the general form of $p(T_{\mathrm{surf}})$. Responsible for the shape of the function $p(T_{\mathrm{surf}})$ are only terms depending on ΔT, which is only the $\Delta T \cdot \mathrm{erfc}(\cdots)$-term. All the other terms in front of the complimentary error function must be responsible for scaling only. Because the complimentary error function can only take values between zero and 1, the scaling terms have to be equal for the pdfs to be equal for two values of m and j, that is

$$\begin{aligned} \frac{1}{(\alpha j_1)^2} e^{\frac{\sigma^2}{4} - m_1} &= \frac{1}{(\alpha j_2)^2} e^{\frac{\sigma^2}{4} - m_2} \\ \Leftrightarrow \left(\frac{j_2}{j_1}\right)^2 &= e^{m_1 - m_2}. \end{aligned} \tag{5.6}$$

In order for the two histograms to be equal, not only their scaling does have to be the same, but also their outline. The same condition for the parameters m_1, m_2, j_1 and j_2 that make the scaling equal thus has to result in the same shape of the pdf. As it turns out, the same relation between m_1, m_2, j_1 and j_2 can be derived by taking the term of the complimentary error function for two values of m and j and equating them, this is justified, because $\Delta T \mathrm{erfc}(x_1)$ will equal $\Delta T \mathrm{erfc}(x_2)$ if and only if $x_1 = x_2$. Hence, the following relation is obtained:

$$\begin{aligned} \frac{\sigma}{2} - \frac{m_1}{\sigma} + \frac{1}{\sigma} \ln\left(\frac{\Delta T}{\alpha j_1}\right)^2 &= \frac{\sigma}{2} - \frac{m_2}{\sigma} + \frac{1}{\sigma} \ln\left(\frac{\Delta T}{\alpha j_2}\right)^2 \\ \Leftrightarrow m_1 - m_2 &= \ln\left(\frac{j_2}{j_1}\right)^2. \end{aligned} \tag{5.7}$$

It can in fact be shown, that the same histogram only results from different combinations of m and j, but not from combinations of j and σ, for instance. This can be done by solving for the scaling factor, which leads to

$$\begin{aligned} \frac{\Delta T}{(\alpha j_1)^2} e^{\frac{\sigma_1^2}{4} - m} &= \frac{\Delta T}{(\alpha j_2)^2} e^{\frac{\sigma_2^2}{4} - m} \\ \Leftrightarrow \ln\left(\frac{j_1}{j_2}\right)^2 &= \frac{\sigma_1^2 - \sigma_2^2}{4}. \end{aligned} \tag{5.8}$$

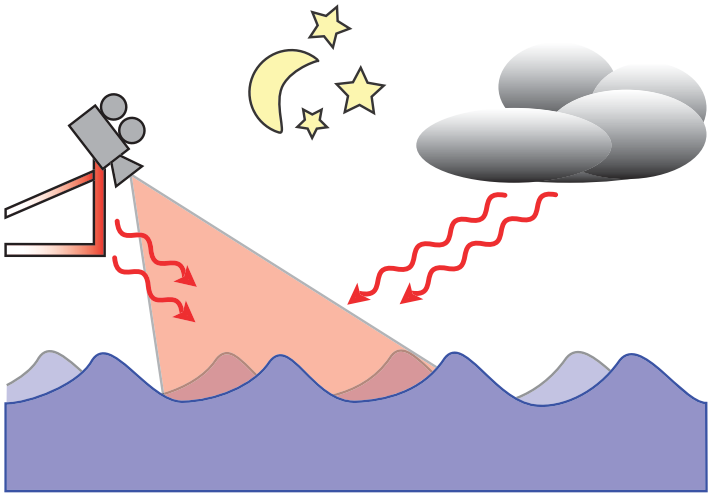

Figure 5.6: *A schematic illustration of the sources of reflexes in field measurements at night.*

The Equation for the form yields

$$\frac{\sigma_1}{2} - \frac{m}{\sigma_1} + \frac{1}{\sigma_1}\ln\left(\frac{\Delta T}{\alpha j_1}\right)^2 = \frac{\sigma_2}{2} - \frac{m}{\sigma_2} + \frac{1}{\sigma_2}\ln\left(\frac{\Delta T}{\alpha j_2}\right)^2$$

$$\Leftrightarrow \frac{\sigma_1^2 - \sigma_2^2}{4} = \left(\frac{\sigma_1 + \sigma_2}{2}\right)\left[\frac{1}{\sigma_2}\ln\left(\frac{\Delta T}{\alpha j_2}\right)^2 - \frac{1}{\sigma_1}\ln\left(\frac{\Delta T}{\alpha j_1}\right)^2 - \frac{m}{\sigma_2} + \frac{m}{\sigma_1}\right]. \tag{5.9}$$

Quite clearly the two Equations (5.8) and (5.9) can only be made to agree for $\sigma_1 = \sigma_2$ and consequently $j_1 = j_2$.

Even though the parameters σ, m and j can not be determined independently by the method described in this section, the bulk temperature T_{bulk} can be estimated accurately. As indicated by Figure 5.5, T_{bulk} represents the intersection of the function of Equation (5.3) with the abscissae, which is independent of the exact value of j, σ and m. Experimental verification of this method for determining the sea surface temperature depression can be found in Schimpf [2000].

5.2.2 Problems Introduced by Reflexes

The statistical analysis of the sea surface temperature is very susceptible to reflections on the sea surface [Garbe and Jähne, 2001]. Strong reflexes can be detected by the residual of the fitted analytical function. Whenever this residual, as a measure for the quality of the fit, is bigger than a threshold, the estimated values can be disregarded. Also, some bounds can be introduced on the parameters T_{bulk} and σ and observations falsified by reflexes detected. An example for such strong reflexes can be seen in Figure 5.8 **a** and **b** .

However, the matter is different for images influenced by less severe reflexes. This kind of reflexes cannot be segmented by thresholding their image intensities nor can they be detected from irregularities of the fit, as can be seen in Figure 5.7. Still they introduce a systematical bias on the image data as can be seen in Figure 5.8 **a** and **b** , and may lead to a higher estimate of T_{bulk}. However, this

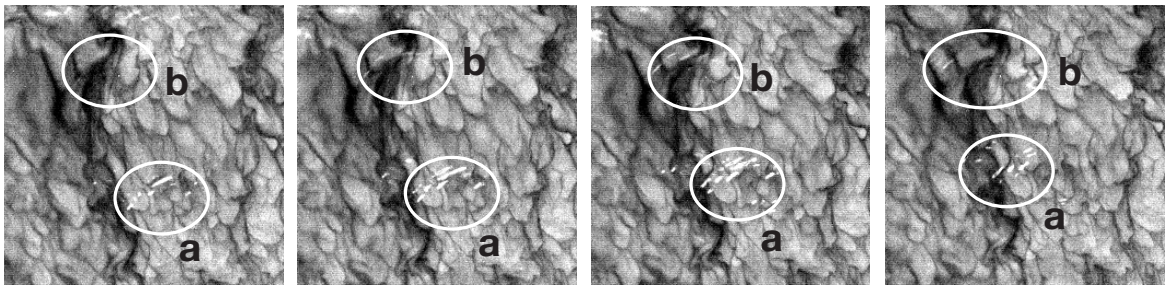

Figure 5.7: *A typical sequence as taken with an infrared camera at 100Hz. While the reflexes in region* ***a*** *are quite easy to detect, the reflexes in region* ***b*** *and in the left top corner of the images are hard to detect in the still frames. However, they potentially introduce significant errors in the estimation of important parameters such as the heat flux density j, the temperature depression ΔT and the probability density function $p(\tau)$.*

kind of reflex can be detected by performing a robust estimation of the sea surface velocity field prior to the statistical analysis. Due to the dependence of reflexes on the surface slope, they will appear to travel much faster than the underlying thermal structures. Also, their motion is not described by the optical flow equation, which will be introduced in Section 8.3. Reflexes in the image data will therefore appear as deviating data points and can thus be regarded as outliers as defined in Section 7.1. By employing a robust framework for computing the optical flow (cf Section 8.7), reflexes can be detected by the motion analysis and effectively segmented from the images.

5.3 Probability of Surface Renewal

As was stated in previous sections the probability density function (pdf) of the times in between consecutive surface renewal events $\tau = t - t_0$ is of great importance. It gives rise to speculations regarding the exact processes involved in the renewal events and justifies the statistical analysis of the sea surface temperature described in the previous section as well as some of the techniques in estimating the heat flux described later on.

In order to be able to make a quantitative statement on this pdf, Equation (2.26) for the temperature depression across the thermal boundary can be used. Reformulating the equation for τ leads to

$$\tau = \left(\frac{T_{\text{surf}}(\tau) - T_{\text{bulk}}}{\alpha j} \right)^2, \quad \text{with} \quad \alpha = \frac{2}{\sqrt{\pi \kappa} c_p \rho}. \tag{5.10}$$

In this equation T_{surf} can be derived from the IR images directly, while T_{bulk} is obtained from the analysis in the previous section. The analytical function for this statistical analysis was derived based on the assumption of a log-normal probability density function for the surface renewal process. It may seem questionable to use results gained from such an assumption for deducing it. However, T_{bulk} represents the intersection of the temperature frequency data with the abscissae and as such can be measured without imposing any model assumption other than that of surface renewal. It might also be measured directly in laboratory or field conditions by taking temperature measurements of the water.

As it turns out, all the the terms in Equation (5.10) can be measured directly from the IR imagery or by the method proposed in the previous section, except the heat flux j. The problem of having to

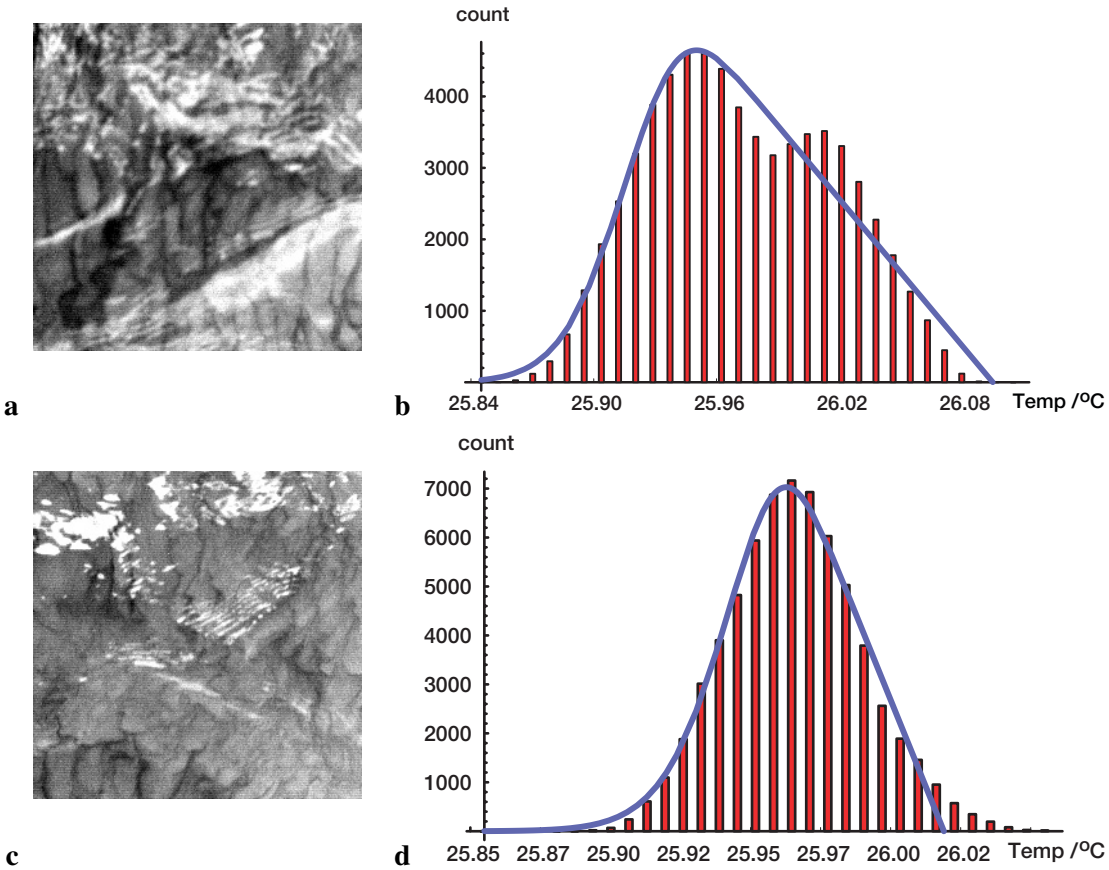

Figure 5.8: *It is not surprising that strong reflexes (**a**) induce errors in the estimation of the parameter σ and the temperature depression ΔT as shown in **b** . However, the distribution fits the data that is corrupted by smaller reflexes (**c**) almost perfectly and cannot be singled out by the residual of the fit (**d**). Still, the T_{bulk} from this fit is much higher than the true value.*

measure j can be circumvented by differentiating Equation (2.26) with respect to time and solving it for the heat flux j, results in

$$j = \frac{2\sqrt{\tau}}{\alpha} \frac{\mathrm{d}}{\mathrm{d}\tau} T_{\mathrm{surf}}(\tau). \tag{5.11}$$

Plugging Equation (5.11) into Equation (5.10) then leads to

$$\tau = \frac{1}{2} \frac{T_{\mathrm{surf}}(\tau) - T_{\mathrm{bulk}}}{\mathrm{d}T_{\mathrm{surf}}(\tau)/\mathrm{d}\tau} = \frac{1}{2} \frac{\Delta T(\tau)}{\dot{T}_{\mathrm{surf}}(\tau)}, \tag{5.12}$$

where in the dotted notation $\dot{x}$ indicates the total derivative with respect to time.

The question is of course what has been gained by the reformulation of the problem in Equation (5.12). Still ΔT can be derived from the IR images but now the total time derivative of the sea surface temperature (SST) has to be measured. This derivative can also be estimated from IR image sequences by the novel image processing algorithm proposed in Section 8.8.1. Therefore a value for τ can be derived at every pixel of the image sequence.

From Taylor's hypothesis [Taylor, 1938] the temporal statistics for τ can be extended on the spatial

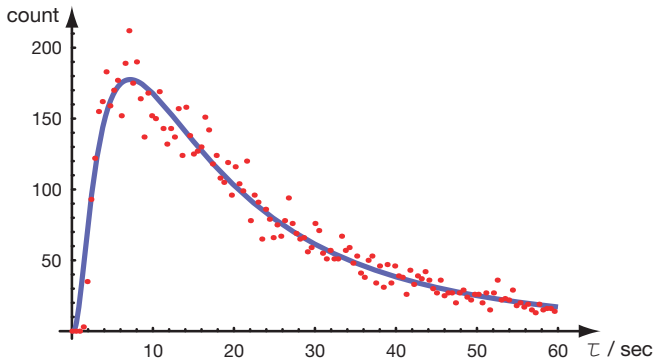

Figure 5.9: *The frequency data of the time of residence τ of a water parcel at the sea surface. The fitted log-normal distribution approximates the data taken at 2 m/s wind speed quite well.*

domain. A value is thus computed for every image point for which a valid $\dot{T}_{\text{surf}}$ was estimated. To increase the statistical significance this step is repeated for a number of images in a sequence and the number of occurrences plotted in a histogram akin to the statistical analysis for the temperature distribution at the sea- surface.

Given the theoretical logarithmic-normal pdf from Equation (2.51), the values for σ and m can be computed together with error estimates for the individual parameters. This is achieved by fitting the pdf to the histogram by means of least squares as can be seen in Figure 5.9. From the parameters σ and m the characteristic mean time between surface renewals t_* can be computed from Equation (2.52) according to

$$t_* = \int_0^\infty p(\tau)\, \tau/t'\, d\tau = t' \cdot e^{\frac{\sigma^2}{4}+m}. \tag{5.13}$$

This allows for a direct verification of the probability density function of surface renewal events.

5.3.1 Accuracy Bounds

When conducting scientific measurements error bounds of the measured entities are of equal importance as the quantities themselves. In that respect it is important to analyze possible errors in the estimation of the time of residence at the sea- surface τ by the proposed technique. Assuming the errors in the estimation to be distributed according to Gaussian statistics, the deviation in the estimate can be derived by error propagation. This leads to

$$\sigma_\tau = \sqrt{\left(\frac{\partial\tau(\Delta T, \dot{T}_{\text{surf}})}{\partial \Delta T} \cdot \sigma_{\Delta T}\right)^2 + \left(\frac{\partial\tau(\Delta T, \dot{T}_{\text{surf}})}{\partial \dot{T}_{\text{surf}}} \cdot \sigma_{\dot{T}_{\text{surf}}}\right)^2} \tag{5.14}$$

$$= \frac{1}{2\dot{T}_{\text{surf}}^2}\sqrt{\left(\dot{T}_{\text{surf}} \cdot \sigma_{\Delta T}\right)^2 + \left(\Delta T \cdot \sigma_{\dot{T}_{\text{surf}}}\right)^2}. \tag{5.15}$$

The relative error is then given by

$$\frac{\sigma_\tau}{\tau} = \sqrt{\left(\frac{\sigma_{\Delta T}}{\Delta T}\right)^2 + \left(\frac{\sigma_{\dot{T}_{\text{surf}}}}{\dot{T}_{\text{surf}}}\right)^2}. \tag{5.16}$$

In conditions typical for air-sea gas exchange the relative error of ΔT is well below 0.05% as will be shown in Section 9.4. The relative error for estimating $\dot{T}_{\mathrm{surf}}$ is found to be at around 10%, leading to a relative error in the estimation of τ at around this value, too.

5.4 Methods of Estimating the Heat Flux

Current state of the art meteorological techniques for measuring heat fluxes were presented in Chapter 4. Inherent problems of low spatial and temporal resolutions were identified. In this section novel techniques that remedy these drawbacks shall be explained. Conceptually three different methods of estimating the net heat flux j have been developed.

One possible way of deriving the heat flux relies on semi-empirical formulations of the temperature depression ΔT which have been introduced in Section 3.1. This temperature depression can be estimated from the statistical analysis introduced in Section 5.2. This way of measuring j will be outlined in Section 5.4.1.

Other techniques of measuring the net heat flux do not rely on any semi-empirical formulations and are thus much more appealing. They can estimate the flux directly from IR imagery and allow measurements of j on a high temporal and spacial resolution for the first time. In this work two algorithms relying on this concept are presented. Both depend on the consistent estimation of the change of surface temperature with respect to time, as described in Section 8.8.1. These two methods to calculate the heat flux are:

- The *square root method*: Here the heat flux can be calculated directly from the total time derivative $\mathrm{d}T/\mathrm{d}t$ and the temperature difference across the aqueous boundary layer ΔT. This allows high temporal and spatially resolved measurements of the heat flux j. The technique will be introduced in Section 5.4.2.
- The *pdf method*, which may be used to compute the mean heat flux over part of the sequence. For this technique to work, some assumptions have to be made on the statistical properties of surface renewal events. This method is termed the pdf method, as a statistical analysis on the time between surface renewal events is performed to evaluate the flux. Obviously some assumption on the pdf of surface renewal has to be made. A thorough analysis of this technique will be presented in Section 5.4.3.
- Another method of computing the net heat flux j is based on the surface strain model introduced in Section 2.4.4. Here not the total derivative of the sea surface temperature is of interest, but rather the divergence of the surface flow field.

In the following sections these different methods shall be further scrutinized.

5.4.1 Heat Flux from ΔT

A number of different formulations for the temperature depression of the cool skin of the ocean were presented in Section 3.1. These formulations were all based on the different models of air-sea gas

exchange introduced in Section 2.4. Among other parameters they all depend on the net heat flux j. Given knowledge of ΔT they can be solved for the net heat flux. This means, that based on certain model assumptions the heat flux j can be derived from an estimate of $\Delta T = T_{\mathrm{surf}} - T_{\mathrm{bulk}}$ as presented in Section 5.2.

However, this approach is not the most appealing one. All the mentioned formulations include a certain extend empirical parameters fitted to prior measurements. These measurements are sometimes found to disagree and all of them were made with flux measurements introduced in Section 4. Hence they are all limited in terms of long integration time and no spatial resolution. As pointed out by Wick et al. [1996] the lack of exact coincidence between the heat flux and ΔT measurements posed to be a mayor drawback of the measurements involved in verifying those models and deriving the empirical parameters.

From modern infrared cameras in conjunction with the novel image processing algorithms developed in the context of this work, it is possible to derive accurate measurements of δT and j in the same footprint. This allows for a profound analysis of the formulations and parameters introduced in Section 3.1. In order to estimate the heat flux independently of semi-empirical formulations other techniques were developed. They will be introduced in the following sections.

Nevertheless, it is still of interest to compare the semi-empirical formulations and analyze their estimates with those gained from the other techniques. From the parameterizations introduced only the ones relying on the surface renewal model are analyzed. Since strong experimental evidence for this type of model has been presented, analyzing parameterizations of the thin film or small eddy model does not seem promising. From the models, explained in Section 3.1.2, the one developed by Liu and Businger [1975] embraces the least number of empirical constants and thus seems to be most interesting in the context of this work. Solving the formulation of Liu and Businger [1975] for the net heat flux leads to

$$j = \Delta T \rho c_p C^{-1} \sqrt{\frac{\kappa}{t_*}}, \tag{5.17}$$

where the constant C was found to be $C = 9.3$ [Liu et al., 1979]. Apart from ΔT the characteristic time of surface renewal t_* needs to be measured to gain an estimate for the heat flux j from Equation (5.17). This can either be done with the parameters σ and m from the statistical analysis in Section 5.3 according to Equation (2.52) or from the Kolmogorov microscale following Equation (3.14).

5.4.2 Square Root Method

This method for calculating the heat flux seems the most promising one. It relies on no further assumptions concerning the probability density function of times between consecutive surface renewal events $p(\tau)$. The only physical model to enter the estimation is the equilibration of a fluid parcel adjacent to the surface by the equations of heat conduction.

From the surface renewal model introduced in Section 2.4.3 a fluid element was pictured over the course of time as it equilibrates with its surroundings at the sea- surface. From the assumption alone, that the heat transfer at the surface is governed by heat diffusion, Equation (2.26) was derived. This

equation can be solved for the heat flux j leading to

$$j = \frac{T_{\mathrm{surf}}(t) - T_{\mathrm{bulk}}}{\alpha\sqrt{\tau}}, \quad t \geq t_0, \quad \text{with} \quad \alpha = \frac{2}{\sqrt{\pi\kappa}c_p\rho}. \tag{5.18}$$

Of course, the exact measurement of $\tau = t - t_0$ with meteorological instruments poses a very difficult problem. However, in Section 5.3 it was shown that this quantity can be estimated from IR images according to

$$\tau = \frac{1}{2}\frac{\Delta T}{\mathrm{d}/\mathrm{d}t\, T_{\mathrm{surf}}}. \tag{5.19}$$

Substituting this expression in Equation (5.18) leads to

$$|j| = \frac{\sqrt{2}}{\alpha}\sqrt{\Delta T(t) \cdot \frac{\mathrm{d}}{\mathrm{d}t}T_{\mathrm{surf}}(t)} = \sqrt{\frac{\pi\kappa}{2}}c_p\rho\sqrt{\Delta T(t)\frac{\mathrm{d}}{\mathrm{d}t}T_{\mathrm{surf}}(t)}. \tag{5.20}$$

The exact same equation can of course be derived by differentiating Equation (2.26) with respect to time, leading to

$$\frac{\mathrm{d}}{\mathrm{d}t}T_{\mathrm{surf}}(\tau) = \frac{\alpha}{2}\frac{j}{\sqrt{\tau}}. \tag{5.21}$$

This expression can be solved for τ and plugged into Equation (5.18). The sign of the heat flux j in Equation (5.20) can be deducted from $\mathrm{d}T/\mathrm{d}t$ as can be seen in Equation (5.21).

Through the use of Equation (5.20) it becomes feasible to determine the heat flux j from measurements with a single infrared camera. ΔT can be assessed directly from the infrared imagery with the aid of a technique described in Section 5.2. The total time derivative of T_{surf} can be computed with the digital image processing technique as described in Section 8.8.1. All the other dimensions are material constants and well known for sea water.

This technique improves the current micro-meteorological techniques for measuring the heat flux as introduced in Section 4. The heat flux can be estimated at the frame rate of the camera. In modern IR cameras frame rates of 100Hz and faster are not uncommon. This allows for accurate heat flux measurements to be conducted with a temporal resolution of well less than a tenth of a second. Also an estimate of the heat flux is computed at every pixel at which dT_{surf}/dt could be gained. This allows for a spatial resolution of about 4 mm^2 when a camera with a moderate resolution of 256×256 pixel is used to image a footprint of 50×50 cm^2.

Accuracy of the Measurement

For specifying the error bounds of the square root method, errors can be assumed to be Gaussian distributed. Error propagation then leads to

$$\sigma_j = \sqrt{\left(\frac{\partial j(\Delta T, \dot{T}_{\mathrm{surf}})}{\partial \Delta T} \cdot \sigma_{\Delta T}\right)^2 + \left(\frac{\partial j(\Delta T, \dot{T}_{\mathrm{surf}})}{\partial \dot{T}_{\mathrm{surf}}} \cdot \sigma_{\dot{T}_{\mathrm{surf}}}\right)^2} \tag{5.22}$$

$$= \frac{1}{\sqrt{2}\alpha}\sqrt{\frac{\dot{T}_{\mathrm{surf}}}{\Delta T}\sigma^2_{\Delta T} + \frac{\Delta T}{\dot{T}_{\mathrm{surf}}}\sigma^2_{\dot{T}_{\mathrm{surf}}}} \tag{5.23}$$

with the relative error given by

$$\frac{\sigma_j}{j} = \frac{1}{2}\sqrt{\left(\frac{\sigma_{\Delta T}}{\Delta T}\right)^2 + \left(\frac{\sigma_{\dot{T}_{\mathrm{surf}}}}{\dot{T}_{\mathrm{surf}}}\right)^2}. \tag{5.24}$$

In general conditions of interest for air-sea gas exchange heat fluxes will be of around $j \approx 200$ W/m^2 at a temperature depression $\Delta T \approx 0.1$K. From Equation (5.20) the total time derivative of T_{surf} will therefore be roughly $\dot{T}_{\mathrm{surf}} \approx 0.1$K/s. The relative error as given by Equation (5.24) will thus be difficult to keep below a few per cent as the individual errors $\sigma_{\Delta T}$ and $\sigma_{\dot{T}_{\mathrm{surf}}}$ are amplified each by an order of magnitude.

From the rough estimates of the orders of magnitude for ΔT and $\dot{T}_{\mathrm{surf}}$ given above, the Equation (5.23) can be approximated by

$$\sigma_j = \frac{1}{\sqrt{2}\alpha}\sqrt{a\,\sigma_{\Delta T}^2 + \sigma_{\dot{T}_{\mathrm{surf}}}^2/a} \tag{5.25}$$

with the constant a for unit conversion, that is $a = 1/s$.

The intention of current heat flux measurements is to achieve an accuracy of $\sigma_j = 10$W/m^2 [Fairall et al., 1996b]. This leads to a desired summed accuracy of $a{\cdot}\sigma_{\Delta T}^2 + 1/a{\cdot}\sigma_{\dot{T}_{\mathrm{surf}}}^2 \approx 10^{-4}$K^2/s. Assuming the uncertainties $\sigma_{\Delta T}$ and $\sigma_{\dot{T}_{\mathrm{surf}}}$ to be equal in value, they can be approximated by $\sigma_{\Delta T} \approx 7$mK and $\sigma_{\dot{T}_{\mathrm{surf}}} \approx 7$mK/s. The noise in IR cameras is equivalent to a temperature deviation of about 25mK [Raytheon, 1995]. This implies that the noise level of the camera system is more than three times higher than the attainable accuracy needed for the targeted accuracy of 10W/m^2 for the estimate of the heat flux j.

The noise level of the images can be reduced somewhat by a concept well known in computer vision, namely the *Gaussian pyramid* [Jähne, 1999b]. When smoothing and subsampling every second pixel in every second row of an image iteratively, the resolution of the image as well as its size decreases by a factor of two in every level of this pyramid. The smoothing has to be performed to avoid aliasing effects in the subsampled images [Jähne, 1999a]. The constituent levels of the Gaussian pyramid thus represent a series of low-pass filtered images in which the cut-off wave numbers decrease by an octave from level to level. Therefore apart from a reduction in size the noise is also suppressed from one pyramid level to the next. Schimpf [2000] found the noise of the IR camera on the zeroth level of the Gaussian pyramid (original image) to be 26.07mK and on the first level to be just 6.27mK. By computing the parameters in the first level of the Gaussian pyramid, the effective noise level is in a range low enough for an accurate estimation of the heat flux to be possible. The computation on the subsampled image has the added advantage of reducing the computational cost, since only one fourth of the original data has to be processed. Also the structures on the sea surface move very fast at times, making the optical flow computations of Section 8.8.1 impractical and erroneous on the zeroth level. This also calls for the estimation of the heat flux j to be performed on the first level and thus on a subsampled image by a factor of 2. The loss of spacial resolution is not problematic as an effective resolution of better than 4mm on a 128×128 grid is still achievable in a standard set-up as presented in Section 11.2 and 12.2.1. This is still a resolution very much higher than ever before attainable for heat flux measurements.

5.4.3 The PDF Method

In the previous section a scheme for computing the net heat flux from infrared images was introduced. The main merit of the presented technique is that it does not rely on assumptions concerning details of the renewal process. In this section another procedure relying on a statistical analysis will be presented.

In contrast to the previous technique this method makes a few assumptions regarding the processes involved in the air-sea gas exchange. These assumptions are mainly the surface renewal model introduced in Section 2.4.3 with a log-normal probability density function (pdf) of the times in between consecutive surface renewal events. Also, thermal equilibration of a water element adjacent to the sea surface is assumed to take place by heat diffusion. A method to verify these assumptions was introduced in Section 5.3, with experimental evidence presented for laboratory conditions in Section 11.5 and for in situ measurements in Section 12.2.4.

The mean temperature difference across the aquatic boundary layer was given by Equation (2.26) as

$$\Delta T(t) = \frac{2j}{\sqrt{\pi\kappa}c_p\rho}\sqrt{t-t_0}, \quad t \geq t_0. \tag{5.26}$$

The average temperature difference across the cool skin of the ocean is given by Soloviev and Schlüssel [1994] as follows

$$\Delta\bar{T} = \int_0^\infty p(t)t^{-1}\left(\int_0^t \Delta T(t')dt'\right)dt. \tag{5.27}$$

The integration of this equation with the log-normal pdf from Equation (2.51) yields

$$\Delta\bar{T} = \frac{4j}{3\sqrt{\pi\kappa}c_p\rho}\sqrt{t_*}\exp(-\sigma^2/16). \tag{5.28}$$

This expression can be solved for the heat flux j, which together with Equation (2.52) leads to

$$j = \frac{3}{4}\sqrt{\pi\kappa}c_p\rho\Delta\bar{T}\exp\left[-\left(\frac{\sigma^2}{16}+\frac{m}{2}\right)\right]. \tag{5.29}$$

Both parameters σ and m can be calculated from a fit of the log normal distribution from Equation (2.51) against the histogram of $\mathrm{d}T/\mathrm{d}t$ as outlined in Section 5.3.

5.4.4 Heat Flux from Surface Divergence

The surface strain model introduced in Section 2.4.4 gives rise to another means of estimating the net heat flux. In this model the fluxes are not parameterized by the time of residence of a water parcel at the sea surface τ, but rather by the surface strain rate β with $\beta = -\partial w/\partial z = \partial u/\partial x + \partial v/\partial y$. In this model an expression for the temperature depression ΔT was derived which is presented in Equation (3.27), given by

$$\Delta T = -\sqrt{\frac{\pi\kappa}{2\beta}}\left(\frac{j}{k}\right), \tag{5.30}$$

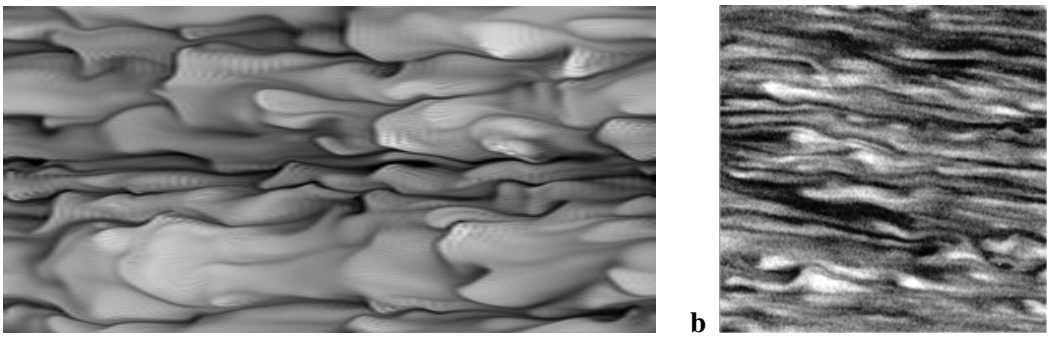

a **b**

Figure 5.10: *The simulated image based on the shear model in* ***a*** *[Leighton, 2000] and its close resemblance to an actual infrared image of the water surface, recorded in the Heidelberg Aeolotron. The footprints of the infrared and simulated images are different in size, but the similarity can easily be recognized.*

with the thermal diffusivity κ and the thermal conductivity k. Solving this equation for the net heat flux j results in

$$j = -\sqrt{\frac{2\beta}{\pi\kappa}}k\Delta T = -\sqrt{\frac{2}{\pi}\beta\kappa}\rho c_p \Delta T. \tag{5.31}$$

Again, ΔT can be derived from the statistical analysis presented in Section 5.2, and consequently all that is needed for an estimation of the net heat flux j is the surface strain rate β. Also this quantity can be derived from infrared image sequences by a parameterized flow model presented in Section 8.8.2. However, this method is not as straight forward as it might appear at first glance. Difficulties arise due to the projective nature of the imaging process where motion along the optical axis of the camera is represented as a divergence in the image sequences. Only with an accurate knowledge of the exact position of the sea surface and its movement along the optical axis of the camera can these divergences be corrected for and the actual divergence of the flow field of interest computed. A solution to this problem might be a stereoscopic set-up with two infrared cameras [Hilsenstein, 2003] or a stereoscopic imaging slope gauge [Fuß, 2003], both of which are presently developed.

Accuracy of the Method

It is of course important to develop a feeling for the accuracy of this technique and what the accuracy constraints are for the measured parameters. For this analysis a rough estimate for the order of magnitude of the surface strain rate β is needed. This can be gained by solving Equation (5.31) for this quantity, resulting in

$$\beta = \frac{\pi}{2\kappa}\left(\frac{j}{\rho c_p \Delta T}\right)^2. \tag{5.32}$$

In the field common flux conditions are $j \approx 200$ W/m^2 at a temperature depression of $\Delta T \approx 0.1$ K. Under such conditions a value for the surface strain rate of $\beta \approx 5$ s^{-1} can be expected. The surface strain rate is thus anticipated to be larger by an order of magnitude than the temperature depression ΔT.

From Gaussian error propagation the error in the estimate for the heat flux σ_j is then given as

$$\sigma_j = \sqrt{\frac{\kappa}{2\pi}}\rho c_p \sqrt{\frac{1}{\beta}\left(\Delta T^2 \sigma_\beta^2 + 4\beta^2 \sigma_{\Delta T}^2\right)} \tag{5.33}$$

and the relative error σ_j / j consequently to

$$\frac{\sigma_j}{j} = \frac{1}{2}\sqrt{\left(\frac{\sigma_\beta}{\beta}\right)^2 + 4\left(\frac{\sigma_{\Delta T}}{\Delta T}\right)^2}. \tag{5.34}$$

From this expression it becomes apparent that the relative error of ΔT plays a dominant role in this formulation of the heat flux j. Keeping in mind that the surface strain rate β is larger than the temperature depression ΔT by an order of magnitude under conditions found commonly at the ocean, one may hope that this quantity can be estimated quite accurately. This is of course offset by the need to estimate apparent divergences due to the motion of the sea surface along the optical axis. However, once this difficulty is solved this formulation should provide a highly accurate estimation of the net heat flux j. Given that the surface strain model describes the transport processes sufficiently precise, evidence by numerical simulations of which has been presented [Leighton et al., 1998; Handler et al., 2001]. A numerical simulation leads to data, closely related in appearance to real imagery. An example of such data is shown in Figure 5.10.

5.5 Heat Transfer Velocity

In Section 3.3 the importance of the transfer velocity k_x was a measure for the transport of heat, impulse or mass independent of the actual tracer x was outlined. It is this independence of the tracer that allows to deduce the transfer of one tracer such as CO_2 from that of another, such as heat in the context of this work, according to Equation (3.38). The transfer velocity for heat k_{heat} is related to the net heat flux j according to Equation (2.6) resulting in

$$k_{\mathrm{heat}} = \frac{j}{\rho c_p \Delta T}. \tag{5.35}$$

On the other hand, the heat flux at the sea surface is given by Equation (2.23) to

$$j = -k\left(\frac{\partial T}{\partial z}\right)_{z=0} = -k\frac{T_{\mathrm{surf}} - T_{\mathrm{bulk}}}{\sqrt{\pi\kappa t}}, \tag{5.36}$$

which can be transformed to a more a different form as explained in Section 5.4.2, yielding

$$j = \sqrt{\frac{\pi\kappa}{2}} c_p \rho \sqrt{\Delta T \dot{T}_{\mathrm{surf}}}. \tag{5.37}$$

This expression can then be plugged into the definition for the transfer velocity k_{heat} in Equation (5.35):

$$k_{\mathrm{heat}} = \sqrt{\frac{\pi\kappa}{2}} \cdot \sqrt{\frac{\dot{T}_{\mathrm{surf}}}{\Delta T}}. \tag{5.38}$$

Again, the resulting term only contains quantities that are given by the properties of sea water or can be estimated from the infrared image sequences, as has been stated in the previous sections. As was seen earlier in the estimation of the heat flux in Section 5.4.2, this formulation allows for an accurate estimation of the transfer velocity k_{heat} at the frame rate of the IR camera to a spatial resolution only depending on the image resolution of the camera and the extent of the footprint of interest.

Another formulation of the transfer velocity can be derived from the surface strain model and the heat flux computed by it. In Section 5.4.4 the net heat flux j was computed from the divergence of the surface flow field β, given by

$$j = -\sqrt{\frac{2}{\pi}\beta\kappa}\rho c_p \Delta T. \tag{5.39}$$

Again, using this expression in the definition of the transfer velocity in Equation (5.35) results in

$$k_{\mathrm{heat}} = \sqrt{\frac{2}{\pi}\beta\kappa}. \tag{5.40}$$

It is remarkable to note that the transfer velocity k_{heat} depends solemnly on the divergence β of the surface flow field. Errors due to calibration inaccuracies or the exact estimation of the temperature depression ΔT do not propagate into the estimate of the transfer velocity k_{heat}. If this divergence could be estimated sufficiently accurate, a promising technique for measuring the transfer velocity k_{heat} would result.

5.5.1 Error Analysis

As in previous sections, also for the heat transfer velocity k_{heat}, an error analysis can be conducted. Assuming Gaussian error distribution, error propagation results in

$$\sigma_{k_{\mathrm{heat}}} = \sqrt{\frac{\pi\kappa}{8}}\sqrt{\frac{1}{\Delta T \dot{T}_{\mathrm{surf}}}\,\sigma^2_{\dot{T}_{\mathrm{surf}}} + \frac{\dot{T}_{\mathrm{surf}}}{\Delta T^3}\,\sigma^2_{\Delta T}}, \tag{5.41}$$

leading to the relative error given by

$$\frac{\sigma_{k_{\mathrm{heat}}}}{k_{\mathrm{heat}}} = \frac{1}{2}\sqrt{\frac{\sigma^2_{\dot{T}_{\mathrm{surf}}}}{\dot{T}^2_{\mathrm{surf}}} + \frac{\sigma^2_{\Delta T}}{\Delta T^2}}. \tag{5.42}$$

It should be noted that this is the same expression for the relative error $\sigma_{k_{\mathrm{heat}}}/k_{\mathrm{heat}}$ as was derived for the relative error of the net heat flux σ_j/j according to Section 5.4.2. All remarks given for the accuracy of that method are equally applicable here.

A completely different result for the error results from the equation of the transfer velocity based on the surface strain model

$$\sigma_{k_{\mathrm{heat}}} = \sqrt{\frac{\kappa}{2\pi\beta}}\sigma_\beta. \tag{5.43}$$

Here the relative error can be formulated as

$$\frac{\sigma_{k_{\mathrm{heat}}}}{k_{\mathrm{heat}}} = \frac{1}{2}\frac{\sigma_\beta}{\beta}. \tag{5.44}$$

It is quite remarkable to note that the relative error of the derived heat transfer velocity is simply half the relative error in determining the divergence at the sea surface β. This should allow for an accurate estimation for the transfer velocity. Since both ΔT and $\dot{T}_{\mathrm{surf}}$ are relatively small quantities, the error of the transfer velocity computed from the surface strain model can be expected to be smaller than the equivalent from the surface renewal model, indicated in Equation (5.42).

5.6 Summary

In this chapter the algorithms for estimating important parameters of heat transfer at the sea surface have been introduced. The techniques proposed rely on image sequences acquired with an infrared camera. In the context of this work a camera sensitive in the wavelength spectrum from 3-5 µm was used. The suitability of such a camera for analyzing interfacial heat transfer processes was verified by surveying the optical properties of water in that wavelength spectrum. These properties lead to some guidance for an optimal experimental set-up.

Next the statistical analysis of temperature distributions was introduced. Through the fit of an analytical function to this distribution parameters such as the temperature of the bulk water T_{bulk} can be estimated. It was shown that not all parameters characterizing this analytical function can be estimated independently from the fit. In the present context this presents no limitation, as only the uniquely identifiable value for the bulk temperature T_{bulk} has to be estimated from this analysis. The problems introduced by reflexes at the sea surface was shown and solutions presented.

The techniques presented in this chapter are based on the assumption that water parcels at the sea surface are replaced by well mixed water of the bulk. A method for estimating the time of residence τ of such a water parcel at the surface was presented. It was shown that a logarithmic-normal distribution can be fitted to the frequency data of τ. A technique was presented for estimating the net heat flux from the parameters characterizing this log-normal distribution. Two other techniques for estimating the net heat flux at the sea surface were also presented. The first one does not rely on the specific distribution of τ and present the technique of choice for both spatially and temporal highly resolved estimates of the heat flux. The second one is a technique for estimating the heat flux from surface divergences. Next a method was presented for estimating the transfer velocity of heat. This is basically based on the estimate of the heat flux, as mentioned previously. All the techniques presented were analyzed in terms of their accuracy bounds by means of error propagation.

Part II

Digital Image Processing

Chapter 6

Parameter Estimation

Parameter estimation is an important aspect in a wide range of scientific fields in which model assumptions about the physical world have to be drawn on the basis of inferences from a set of observations. From the above it becomes apparent that in order for the parameter estimation to produce any useful results some prerequisites have to hold. First and most important is of course a model assumption that depicts the motivating aspect of the physical world sufficiently enough. Obviously the parameters of the model can only describe the observations as good as the model itself. Given that an adequate model is used to describe the data some restrictions have to be made on the observations themselves. Clearly, enough observations have to be taken in order to estimate all parameters of the model. Ideally these observations should be as independently as possible in the sense that one measurement should not influence the others but also that the measurements should cover as many different aspects of the model as possible. Collecting more information on top of this bare minimum makes for an increase in the statistical significance and allows for some conclusions to be drawn concerning the errors in the estimated parameters. From this data set and the model assumption the parameter estimation should supply the true model parameter as closely as possible. Usually no à priori knowledge is given of how good the model describes the actual data. In a good model the discrepancy between the predicted datum and the actually measured one should be due only to statistical fluctuations, a quantity that can be expressed in the residuum of the estimate. Apart from having a small residuum the parameters of the models should also be as independent from one another as possible. Otherwise they cannot be estimated correctly and may even contain essentially the same information. The correlation of the parameters is expressed in the off diagonal elements of the covariance matrix $\nexists$. In real world applications an error estimate of the parameters is of equal importance as the actual parameters themselves. Often the distribution of the input data is known and the question arises of how this error is propagated into the estimated parameters. It is the covariance matrix $\nexists$ that provides information to this issue.

In order to be useful for the parameter estimation in the context of this work all the topics mentioned above should be addressed by the estimator. In the following section the importance and dangers of scaling the observations is outlined, in Section 6.2 the ordinary least squares parameter estimator will be introduced. The bias of this estimator when all data are subject to error is addressed by the total least squares estimator outlined in Section 6.3. This estimator will not always estimate a unique solution, in which case a nongeneric solution can be found as explained in Section 6.3.1.

The total least squares estimator can be formulated differently than in Section 6.3 by means of normal equations. This formulation is widely used in digital image processing and thus its merits and drawbacks will be presented in Section 6.3.2. Another extension to the TLS estimator is the weighted total least squares estimator, which allows weighting individual observations differently. This estimator will be introduced in Section 6.3.3. Apart from the actual estimates a measure for the error in the parameters is important in scientific applications. The covariance matrix of the parameters can be deduced by making some assumptions on the noise of the data as will be shown in Section 6.3.4. The introduction of the total least squares estimator is completed with some notes on the implementation presented in Section 6.3.5. The key difference between the ordinary least squares and the total least squares estimators are interpreted geometrically in Section 6.4. The TLS estimator produces suboptimal results when some columns in the data matrix are known exactly, which is the case in a model with intersect of the type $y = b + \sum_i a_i x_i$. By mixing ordinary least squares and total least squares this problem can be overcome as will be shown in Section 6.5 with the implementation of this estimator in Section 6.5.1. In some applications the input data will not be identical independently distributed Gaussian noise. An efficient estimator under these circumstances is the generalized total least squares estimator presented in Section 6.6. As implied by the name this is the most general estimator presented in this work and can be considered an extension of the mixed OLS and TLS estimator from Section 6.5. The question of test for optimal model selection is then addressed in Section 6.7.

6.1 Scaling of Observations

The topic of scaling the input data prior to the parameter estimation is a difficult one. On one hand not performing a scaling of the data may lead to a bias in the estimation [Mühlich and Mester, 1999; Mester and Mühlich, 2001] while at the other extreme scaling might even lead to wrong estimates [Forsythe and Moler, 1967; Fermueller et al., 1999]. An illustration of this problem is presented in Figure 6.1.

Quantities of different magnitude pose two kinds of problems:

1. As will be outlined in Sections 6.2 and 6.3 OLS as well as TLS produce optimal results for observations of zero mean and equal variance in the sense that they are maximum likelihood estimators under these conditions. Even though not always noticeable in real world situation, a lack of scaling for this estimator might produce suboptimal results. By employing the GTLS estimator in Section 6.6 this problem is addressed without the explicit need for scaling.

2. Unscaled observations may lead to numerical instabilities as well as falsifying the results. Golub and van Loan [1996] showed that the Cholesky factorization used in the SVD computation has a dramatic effect on the errors if different order of magnitudes enter the computation.

Scaling, in the context of this work also known as tensor equilibrium [Golub and van Loan, 1996; Mühlich and Mester, 1999], can be formulated as follows. In a system of equations of the form $\boldsymbol{A}\boldsymbol{x} = \boldsymbol{b}$ the matrix $\boldsymbol{A}$ is replaced by the equilibrated matrix $\boldsymbol{A}' \rightarrow \boldsymbol{W}_L \boldsymbol{A} \boldsymbol{W}_R$, with suitably chosen non-singular weight matrices $\boldsymbol{W}_L$ and $\boldsymbol{W}_R$. Multiplication with non-singular matrices does not change the rank which is an important premise for TLS computations as will be shown in Section 6.3.

Setting $\boldsymbol{W}_L = \mathbb{1}$ the matrix $\boldsymbol{W}_R$ performs what is known as column scaling. Assume the data matrix $\boldsymbol{A}$ being corrupted by additive noise $\boldsymbol{N}$, that is $\boldsymbol{A} = \boldsymbol{A}_0 + \boldsymbol{N}$, where $\boldsymbol{A}_0$ is the unperturbed data matrix. The aim of column scaling is for the covariance matrix $\not\Sigma(\boldsymbol{N}')$ of the errors in the scaled matrix $\boldsymbol{A}'$ to be normally distributed with equal variance, that is $\not\Sigma(\boldsymbol{N}') = \sigma^2\mathbb{1}$. The choice of $\boldsymbol{W}_R$ is of course very important and can be based on à priori knowledge of the uncertainties in $\boldsymbol{A}$. Usually this knowledge is difficult to obtain. It can therefore be attained by setting

$$\not\Sigma(\boldsymbol{N}') = \langle \boldsymbol{N}'^{\top}\boldsymbol{N}' \rangle = \boldsymbol{W}_R^{\top}\langle \boldsymbol{N}^{\top}\boldsymbol{N} \rangle \boldsymbol{W}_R = \boldsymbol{W}_R^{\top}\not\Sigma(\boldsymbol{N})\boldsymbol{W}_R \stackrel{!}{=} \sigma^2\mathbb{1}. \tag{6.1}$$

Although arbitrary the constant σ in Equation (6.1) is usually set to unity. Therefore we chose $\boldsymbol{W}_R$ to be the inverse of the square root of the covariance matrix, that is $\boldsymbol{W}_R\boldsymbol{W}_R^{\top} = \langle \boldsymbol{N}^{\top}\boldsymbol{N} \rangle^{-1}$. The right hand scaling of the data matrix by $\boldsymbol{W}_R$ is sufficient to transform the data matrix $\boldsymbol{A}$ to a matrix $\boldsymbol{A}'$ whose errors $\boldsymbol{N}$ are uncorrelated with normal distribution and equal variance. This form of scaling is also known as the *Mahalanobis transformation* [Mardia et al., 1979]. The result of the TLS problem of $\boldsymbol{A}'$ corresponds to the maximum likelihood estimate, resulting in an unbiased estimate. It is important to note that a scaling with a right hand weighting matrix $\boldsymbol{W}_R$ effects the singular value. The threshold for determining the numerical rank of a matrix has therefore to be adapted accordingly.

Many different algorithms for standardizing the data are conceivable but most often the data are transformed to posses zero location and unit scale (that is their mean vanishes and their standard variation is equal to one). The simplest and most widespread scheme is called range scaling. In it the matrix or raw data x_{ij} is transformed in a matrix of y_{ij} given by

$$y_{ij} = \frac{x_{ij} - \min x_{ij}}{\max x_{ij} - \min x_{ij}}, \tag{6.2}$$

so that $0 \leq y_{ij} \leq 1$ for all i, j.

Statistically more sound is the so called z transform. Here first the mean $\bar{x}_j$ of the variable x_j is calculated according to

$$\bar{x}_j = \frac{1}{m}\sum_{i=1}^{m} x_{ij} \tag{6.3}$$

and the variation in the data is computed via the standard deviation s_j given by

$$s_j = \sqrt{\frac{1}{m-1}\sum_{i=1}^{m}(x_{ij} - \bar{x}_j)^2}. \tag{6.4}$$

As in other computations that rely on the L_2, s_j calculated in this way is very prone to outliers in the data, as will be scrutinized in Chapter 7. Only one outlier is enough to lead to vastly wrong estimates of s_j. One way of reducing the strong effects of outliers is simply to turn away from this norm and use the L_1 norm instead [Hampel et al., 1986]. This is done in calculating S_j:

$$S_j = \frac{1}{m}\sum_{i=1}^{m} |x_{ij} - \bar{x}_j| \,. \tag{6.5}$$

Assuming that S_j (or s_j if outliers are of no concern) is nonzero, the z transform is given by

$$z_{ij} = \frac{x_{ij} - \bar{x}_j}{S_j}. \tag{6.6}$$

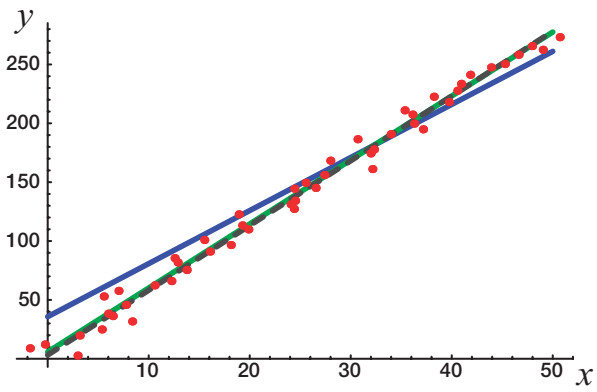

Figure 6.1: *An illustration of the importance of scaling parameters. The dotted line represents the correct parameters. The unscaled total least squares estimate (blue line) results in a wrong estimate, while the green line estimates the correct parameters.*

Even though the effects of outliers are reduced somewhat by using S_j instead of s_j they may still not be negligible. In the case of a larger number of outliers a robust estimation of the scaling is desirable. A robust scaling that can cope reliable with data corrupted by outliers by as much as 50% can be achieved by scaling with a robust adaptation of the z transform, simply by exchanging the summation against the median:

$$z_i j = \frac{x_{ij} - \text{median}_k x_{kj}}{1.4826 \ \text{median}_f |x_{fj} - \text{median}_k x_{kj}|}. \tag{6.7}$$

Where 1.4826 is a correction factor introduced for optimal results in the presence Gaussian distributed errors [Rousseeuw and Leroy, 1987].

For the estimation it may also be favorable to introduce weights (i.e. scales) on the rows of the data matrix $\boldsymbol{A}$. This is readily achieved by multiplication with the left hand weighting matrix $\boldsymbol{W}_L$. This is frequently used in image processing applications (see Section 8) by introducing masks on spatio-temporal neighborhoods or by robust estimators that are outlined in Section 7.2. The row scaling results in another estimator called weighted total least squares that will be treated in Section 6.3.3.

Since the gross size should not have any effect on the estimation of parameters, the raw data has to be scaled accordingly.

It should be noted that general scaling strategies are unreliable [Golub and van Loan, 1996]. Since scaling poses a modification to the data any technique used may in fact worsen the result of the computation than if no scaling whatsoever is used [Forsythe and Moler, 1967]. Therefore scaling should be preceded by a thorough analysis of the problem and scaling performed on the basis of the significance of each datum.

The importance of scaling or renormalizing has been recognized in a number of computer vision tasks, such as conic fitting [Kanatani, 1994], motion detection [Mühlich and Mester, 1999] or orientation analysis [Mester and Mühlich, 2001].

6.2 Ordinary Least Squares Parameter Estimation

Parameter estimation by means of ordinary least square (OLS) was introduced by *Euler* in the 18th century when he successfully predicted the movement of celestial bodies. It has been used extensively in many fields of sciences as well as in computer vision (Lawson and Hanson [1974], Menke [1989]). The p parameter $\boldsymbol{x}$ of the model are given as $\boldsymbol{x} = (x_1, x_2, \ldots, x_p)^\top$. The model will of course differ for the problem under consideration. It can generally be written as $b_i = a_{1i} \cdot x_1 + a_{2i} \cdot x_2 + \cdots + a_{pi} \cdot x_p$, where $i \in \{1, 2, \ldots, n\}$ represent n data points. In vector notation this set of equations can be formulated as $\boldsymbol{A}\boldsymbol{x} = \boldsymbol{b}$, relating the parameter vector $\boldsymbol{x} \in \mathbb{R}^p$ in the model and the observation vector $\boldsymbol{b} \in \mathbb{R}^n$. This type of model is commonly referred to as *Gauss-Markoff model*, in which one assumes that the expected values of the observations $\boldsymbol{b}$ are linear combinations of the given coefficients $\boldsymbol{A}$ and the unknown parameters $\boldsymbol{x}$ [Koch, 1988].

In a least squares framework the sought parameter vector $\boldsymbol{x}^{\text{est}}$ solves the model equation approximately, where the goodness of the approximation is defined by the residual $\text{res}(\boldsymbol{x})$ for the parameter vector $\boldsymbol{x}$ in the L_2 norm:

$$\text{res}(\boldsymbol{x}^{\text{est}}) = \boldsymbol{e}^\top \boldsymbol{e} = ||\boldsymbol{A}\boldsymbol{x}^{\text{est}} - \boldsymbol{b}||_2 = \left(\boldsymbol{A}\boldsymbol{x}^{\text{est}} - \boldsymbol{b}\right)^\top \left(\boldsymbol{A}\boldsymbol{x}^{\text{est}} - \boldsymbol{b}\right) \tag{6.8}$$

The method of OLS is based on the premiss that the residual res defined in Equation (6.8) is at a minimum for the estimated parameter vector $\boldsymbol{x}^{\text{est}}$. This leads to the definition of the ordinary least squares problem:

Definition 1 *Given an over determined set of n linear Equations $\boldsymbol{A}\boldsymbol{x} = \boldsymbol{b}$ with $\boldsymbol{A} \in \mathbb{R}^{n \times p}$, $\boldsymbol{b} \in \mathbb{R}^n$ and the sought parameter vector $\boldsymbol{x} \in \mathbb{R}^p$. The OLS problem seeks to*

$$\begin{aligned} &\textit{minimize} \quad ||\boldsymbol{b} - \boldsymbol{b}^{\text{est}}||_2, \quad \textit{with} \quad \boldsymbol{b}, \boldsymbol{b}^{\text{est}} \in \mathbb{R}^n \\ &\textit{subject to} \quad \boldsymbol{b}^{\text{est}} \in \text{range}(\boldsymbol{A}). \end{aligned} \tag{6.9}$$

Any minimizing $\boldsymbol{x}^{\text{est}}$ is called a linear ordinary least squares solution of the set $\boldsymbol{A}\boldsymbol{x} \approx \boldsymbol{b}$.

The *range* of a matrix $\boldsymbol{A}$ is defined as the subspace given by [Golub and van Loan, 1996]

$$\text{range}(\boldsymbol{A}) = \left\{\boldsymbol{y} \in \mathbb{R}^n, \boldsymbol{A} \in \mathbb{R}^{n \times p} : \boldsymbol{y} = \boldsymbol{A}\boldsymbol{x} \text{ for some } \boldsymbol{x} \in \mathbb{R}^p\right\}. \tag{6.10}$$

It is known from elementary calculus that the minimum of a function is found by setting its derivatives with respect to the parameters to zero and solving the resulting equations. Performing these calculations for Equation (6.8) results in $\boldsymbol{A}^\top \boldsymbol{A}\boldsymbol{x} - \boldsymbol{A}^\top \boldsymbol{b} = 0$. Assuming that $\left(\boldsymbol{A}^\top \boldsymbol{A}\right)^{-1}$ exists, the sought OLS solution of the problem $\boldsymbol{A}\boldsymbol{x} = \boldsymbol{b}$ is then given by

$$\boldsymbol{x}^{\text{est}} = \left(\boldsymbol{A}^\top \boldsymbol{A}\right)^{-1} \boldsymbol{A}^\top \boldsymbol{b}. \tag{6.11}$$

In the literature the matrix $(\boldsymbol{A}^\top \boldsymbol{A})^{-1} \boldsymbol{A}^\top$ is commonly referred to as the *Moore-Penrose* Inverse [Koch, 1988; Groetsch, 1993].

Gauss [1823] showed that the OLS estimate $\boldsymbol{x}^{\text{est}}$ has the smallest variance in the class of estimation methods, which display no systematic errors in the estimates (no bias) and whose estimates are linear functions of $\boldsymbol{b}$.

Apart from the estimated parameter vector $\boldsymbol{x}^{\mathrm{est}}$ another important entity of characterizing the model and its estimation is the covariance matrix $\not\Sigma$. The covariance matrix $\not\Sigma$ (also known as the variance-covariance or dispersion matrix) is defined as [Mardia et al., 1979]

$$\not\Sigma = \left\langle \left(\boldsymbol{x} - \langle \boldsymbol{x} \rangle\right) \left(\boldsymbol{x} - \langle \boldsymbol{x} \rangle\right)^{\top} \right\rangle, \tag{6.12}$$

where $\langle \cdot \rangle$ denotes the expectation value, that is

$$\langle x_i \rangle = \int_{\infty}^{\infty} x_i p(\boldsymbol{x}) \mathrm{d}\boldsymbol{x} \quad \text{with} \quad i = 1, \ldots, p, \tag{6.13}$$

where $p(\boldsymbol{x})$ denotes the probability density function of $\boldsymbol{x}$. From this definition follows, that for a linear system of Equations $\boldsymbol{b} = \boldsymbol{A}\boldsymbol{x} + \boldsymbol{v}$ the covariance matrix $\not\Sigma$ can be computed as [Koch, 1988]

$$\not\Sigma(\boldsymbol{b}) = \boldsymbol{A} \not\Sigma(\boldsymbol{x}) \, \boldsymbol{A}^{\top}. \tag{6.14}$$

Intuitively this equation is straight forward to understand as a linear system of equations can be thought of as a transformation between coordinate systems. The same transformation must then be applied to the covariance matrix as well, which is given by Equation (6.14).

The covariance matrix for the OLS estimator can then be derived by considering the expression for the estimated parameter $\boldsymbol{p}$ from Equation (6.11), that is

$$\begin{aligned} \not\Sigma(\boldsymbol{x}) &= \left(\left(\boldsymbol{A}^{\top}\boldsymbol{A}\right)^{-1} \boldsymbol{A}^{\top} \right) \not\Sigma(\boldsymbol{b}) \left(\left(\boldsymbol{A}^{\top}\boldsymbol{A}\right)^{-1} \boldsymbol{A}^{\top} \right)^{\top} \\ &= \left(\left(\boldsymbol{A}^{\top}\boldsymbol{A}\right)^{-1} \boldsymbol{A}^{\top} \right) \sigma_b^2 \mathbb{1} \left(\left(\boldsymbol{A}^{\top}\boldsymbol{A}\right)^{-1} \boldsymbol{A}^{\top} \right)^{\top} = \sigma_b^2 \left(\boldsymbol{A}^{\top}\boldsymbol{A}\right)^{-1}. \end{aligned} \tag{6.15}$$

The use of OLS in digital image processing applications has the major advantage that it can be interpreted as a linear shift-invariant filter (LSI) [Jähne, 1999c]. This allows for the implementation to rely on common digital image processing techniques and thus enables for a very fast estimation of the parameters.

6.3 Total Least Squares

Although the term 'Total Least Squares' appeared only recently [Golub and van Loan, 1980] this method of parameter estimation is not new and is known in statistical literature under the term *orthogonal regression* or *errors-in-variables regression*. The univariate line fitting problem ($\alpha + a \cdot x = b$) already appeared in the 19th century [Adcock, 1878]. Assuming that the errors of the observations are independently and identically distributed with zero mean and covariance matrix $\sigma \mathbb{1}$, it can be proven that the TLS solution estimates the true parameter values $\boldsymbol{p}$ consistently [Gallo, 1982; Gleser, 1981]. This means that the estimated parameter vector $\boldsymbol{p}^{\mathrm{est}}$ converges to the true vector $\boldsymbol{p}$ as the number of observations n tends to infinity. Furthermore it can be shown that this property of TLS estimates does not depend on any assumed distribution of the errors. This strongly contrasts the behavior of OLS estimates which are inconsistent in the presence of non Gaussian noise [Gelb, 1974]. Although

there exists a formal equivalence between OLS and TLS [Lemmerling et al., 1998], one should not confuse the two estimates as both will lead to different solutions. A geometric interpretation of the two estimators will be presented in Section 6.4.

The underlying assumption in OLS is that the errors only occur in the vector $\boldsymbol{b}$ and that the matrix $\boldsymbol{A}$ is exactly known (see Section 6.2). While for some application this prerequisite may hold, in a number of scientific applications and especially digital image processing the data matrix $\boldsymbol{A}$ is also effected by measurement or sampling errors. These errors are taken into account by perturbing not only $\boldsymbol{b}$ but $\boldsymbol{A}$ as well and formulating the TLS problem:

Definition 2 *Given an over determined set of n linear equations $\boldsymbol{Ax} = \boldsymbol{b}$ with $\boldsymbol{A} \in \mathbb{R}^{n\times p}$, $\boldsymbol{b} \in \mathbb{R}^n$ and the sought parameter vector $\boldsymbol{x} \in \mathbb{R}^p$. In the TLS problem it is then tried to*

$$\begin{aligned} &\textit{minimize} \quad || \, (\boldsymbol{A}, \boldsymbol{b}) - \left(\tilde{\boldsymbol{A}}, \tilde{\boldsymbol{b}}\right) ||_F, \quad \left(\tilde{\boldsymbol{A}}, \tilde{\boldsymbol{b}}\right) \in \mathbb{R}^{n\times(p+1)} \\ &\textit{subject to} \quad \tilde{\boldsymbol{b}} \in \mathrm{range}(\tilde{\boldsymbol{A}}). \end{aligned} \tag{6.16}$$

Any $\boldsymbol{x}$ satisfying $\tilde{\boldsymbol{A}}\boldsymbol{x} = \tilde{\boldsymbol{b}}$ is called a solution to the TLS problem for a minimizing $(\tilde{\boldsymbol{A}}, \tilde{\boldsymbol{b}})$.

In the above definition $|| \cdot ||_F$ denotes the Frobenius norm, that is $||\boldsymbol{A}||_F = \sqrt{\sum_i \sum_j |a_{ij}|^2}$. The range of a matrix $\boldsymbol{A}$ was defined in Section 6.2. The TLS problem can be reduced to a singular value analysis due to the *Eckart-Young-Mirsky matrix approximation theorem* which can be stated as follows [Van Huffel and Vandewalle, 1991]:

Theorem 1 *Given a matrix $\boldsymbol{A} \in \mathbb{R}^{n\times p}$ with its singular value decomposition $\boldsymbol{A} = \sum_{i=1}^{r} \lambda_i \boldsymbol{u}_i \boldsymbol{v}_i^\top$, $r = \mathrm{rank}(\boldsymbol{A})$ and a matrix $\boldsymbol{B} \in \mathbb{R}^{n\times p}$ with $k = \mathrm{rank}(\boldsymbol{B})$. If $k < r$, $\boldsymbol{A}_k = \sum_{i=1}^{k} \lambda_i \boldsymbol{u}_i \boldsymbol{v}_i^\top$ it can be shown that*

$$\min \quad ||\boldsymbol{A} - \boldsymbol{B}||_F = ||\boldsymbol{A} - \boldsymbol{A}_k||_F = \sqrt{\sum_{i=k+1}^{p} \lambda_i^2}, \quad p = \min\{n, p\}, \tag{6.17}$$

and

$$\min \quad ||\boldsymbol{A} - \boldsymbol{B}||_2 = ||\boldsymbol{A} - \boldsymbol{A}_k||_2 = \lambda_{k+1}. \tag{6.18}$$

The reader is referred to Eckhart and Young [1936]; Mirsky [1960] for the proof of this theorem.

The connection between the TLS problem and the Eckhart-Young-Mirsky theorem from Equation (6.17) comes about by writing the set of n linear equation in the form

$$(\boldsymbol{A}, \boldsymbol{b}) \begin{pmatrix} \boldsymbol{x} \\ -1 \end{pmatrix} = 0, \tag{6.19}$$

and thus embedding the space spanned by the matrix $\boldsymbol{A}$ in the one spanned by $(\boldsymbol{A}, \boldsymbol{b})$. The SVD of $(\boldsymbol{A}, \boldsymbol{b})$ is given by $(\boldsymbol{A}, \boldsymbol{b}) = \boldsymbol{U}\Lambda\boldsymbol{V}$ with $\Lambda = \mathrm{diag}(\lambda_1, \ldots, \lambda_{n+1})$. If $\lambda_{n+1} \neq 0$, then $\mathrm{rank}(\boldsymbol{A}, \boldsymbol{b}) = n + 1$. Consequently, the space $\mathcal{S}$ generated by the rows of $(\boldsymbol{A}, \boldsymbol{b})$ is $\mathcal{S} \in \mathbb{R}^{n+1}$. All solutions to the TLS problem lie in the null space $\mathcal{N}$ orthogonal to the space $\mathcal{S}$. The set of Equations (6.19) is incompatible and for a solution of the TLS problem to be found the rank of $(\boldsymbol{A}, \boldsymbol{b})$ has to be reduced

to $\mathrm{rank}(\boldsymbol{A}, \boldsymbol{b}) = n$ which results in a one dimensional space $\mathcal{N}$. Using the Eckhart-Young-Mirsky theorem the best rank n approximation $(\tilde{\boldsymbol{A}}, \tilde{\boldsymbol{b}})$ of $(\boldsymbol{A}, \boldsymbol{b})$ is given by $(\tilde{\boldsymbol{A}}, \tilde{\boldsymbol{b}}) = \boldsymbol{U}\tilde{\Lambda}\boldsymbol{V} = \sum_{i=1}^{n+1} \lambda_i \boldsymbol{u}_i \boldsymbol{v}_i^\top$ with $\tilde{\Lambda} = \mathrm{diag}(\lambda_1, \ldots, \lambda_n, \lambda_{n+1})$ and the singular values $\lambda_1 > \lambda_2 > \cdots > \lambda_n > \lambda_{n+1} \approx 0$. The TLS problem in Equation (6.16) can thus be written as

$$\begin{array}{lrcl} \min & || \, (\boldsymbol{A}, \boldsymbol{b}) - \left(\tilde{\boldsymbol{A}}, \tilde{\boldsymbol{b}}\right) ||_F & = & \lambda_{n+1}, \quad \text{with} \quad \mathrm{rank}\left(\tilde{\boldsymbol{A}}, \tilde{\boldsymbol{b}}\right) = n \\ \text{and} & (\boldsymbol{A}, \boldsymbol{b}) - \left(\tilde{\boldsymbol{A}}, \tilde{\boldsymbol{b}}\right) & = & \lambda_{n+1} \boldsymbol{u}_{n+1} \boldsymbol{v}_{n+1}^\top. \end{array} \tag{6.20}$$

The approximate equation $\left(\tilde{\boldsymbol{A}}, \tilde{\boldsymbol{b}}\right) \left(\boldsymbol{x}^\top, -1\right)^\top$ is now compatible with the solution given by the one-dimensional space $\mathcal{N}$ orthogonal to $\mathcal{S}$, spanned by $\boldsymbol{v}_{n+1}$. The TLS solution is then obtained by scaling $\boldsymbol{v}_{n+1}$ so that its last component is -1, that is

$$\begin{pmatrix} \boldsymbol{x} \\ -1 \end{pmatrix} = -\frac{1}{\boldsymbol{v}_{n+1,n+1}} \boldsymbol{v}_{n+1}, \quad \text{for} \quad \boldsymbol{v}_{n+1,n+1} \neq 0. \tag{6.21}$$

In case that $\boldsymbol{v}_{n+1,n+1} = 0$ the above procedure can of course not be conducted. However, this does not pose any limitation as $\boldsymbol{v}_{n+1,n+1} = 0$ means that $(\boldsymbol{A}, \boldsymbol{b})$ is of rank n already and the vector $\boldsymbol{v}_{n+1}$ is in the space $\mathcal{N}$. The solution is said to be *nongeneric* as the space $\mathcal{N}$ is m-dimensional with $m > 1$. This case will be treated in Section 6.3.1. It can be shown that there exists one unique solution to the TLS problem given by equation (6.21) if and only if $(\boldsymbol{A}, \boldsymbol{b})$ has full column rank [Van Huffel and Vandewalle, 1991].

The basic principle in the TLS problem is then that the noisy data matrix $\boldsymbol{D} = (\boldsymbol{A}, \boldsymbol{b})$ is modified with minimal effort into a matrix $\tilde{\boldsymbol{D}} = (\tilde{\boldsymbol{A}}, \tilde{\boldsymbol{b}})$ that is close to the original matrix in the Frobenius norm. The approximated matrix is rank-deficient so that its columns are linearly related. In this approach all the data are modified in contrast to the OLS approach where only one column of $\boldsymbol{D} = (\boldsymbol{A}, \boldsymbol{b})$ is modified.

6.3.1 Solution of the Nongeneric Total Least Squares Problem

In the previous section it was shown that there exists a unique solution to the TLS problem only if $\boldsymbol{v}_{p+1,p+1} \neq 0$. However, this may not always be the case and the problem is said to be nongeneric [Van Huffel and Vandewalle, 1988]. When trying to find a solution to the nongeneric TLS problem one has to distinguish between two cases:

1. The set of equations is highly conflicting and thus $\lambda_n \approx \lambda_{n+1} \gg 0$.
2. The matrix $\boldsymbol{A}$ is rank deficient and thus $\lambda_1 > \lambda_2 > \cdots > \lambda_k \approx \cdots \approx \lambda_{p+1} \approx 0$, with $k < p$.

The case 1 can easily be detected by introducing a threshold on the smallest singular value for which $\boldsymbol{v}_{p+1,p+1} \neq 0$. If this singular value is large it can be concluded that the data are not sufficiently closely approximated by the model assumption in which case either the model needs to be refined or, where this is not possible, the problem can be rejected as irrelevant from the linear modeling point of view.

Much more interesting in the context of this work is the case 2. It is analogous to the aperture problem in optical flow computations as will be clarified in Section 8.4. As the space $\mathcal{N}$ is of dimension higher than one all linear combinations of the vectors spanning this space are solutions to the TLS problem. In terms of stability and minimal sensitivity the only sensible solution to the TLS problem will be that solution with minimal norm. It can be shown that the solution that is minimal in the L_2 norm is also minimal in the Frobenius norm [Van Huffel and Vandewalle, 1991]. The minimum norm TLS solution can then be formulated as follows [Van Huffel, 1992]:

Definition 3 *Given $(\boldsymbol{A}, \boldsymbol{b})$ with the SVD $(\boldsymbol{A}, \boldsymbol{b}) = \sum_{i=1}^{p+1} \lambda_i \boldsymbol{u}_i \boldsymbol{v}_i^\top$ and assuming $\lambda_k > \lambda_{k+1} \approx \cdots \approx \lambda_{p+1}$ with $k \leq p$. If not all $\boldsymbol{v}_{p+1,i} = 0$, $i = k+1, \ldots, p+1$, then the minimum norm TLS solution $\tilde{\boldsymbol{x}}$ is given by*

$$\tilde{\boldsymbol{x}} = -\frac{\sum_{i=k+1}^{p+1} \boldsymbol{v}_{p+1,i} \cdot (\boldsymbol{v}_{1,i}, \ldots \boldsymbol{v}_{p,i})^\top}{\sum_{i=k+1}^{p+1} \boldsymbol{v}_{p+1,i}^2} = -\frac{\sum_{i=1}^{k} \boldsymbol{v}_{p+1,i} \cdot (\boldsymbol{v}_{1,i}, \ldots \boldsymbol{v}_{p,i})^\top}{1 - \sum_{i=1}^{k} \boldsymbol{v}_{p+1,i}^2}. \tag{6.22}$$

The validity of this minimum norm solution to optical flow estimations is shown in Spies [2001], while the reader is referred to Van Huffel and Vandewalle [1988] and Van Huffel and Vandewalle [1991] for a proof of the minimum norm solution given in Equation (6.22). The results obtained in this section for the minimum norm solution to the TLS problem also hold true for the OLS problem and can be applied without any modifications [Wei, 1992]. The same holds true for the other estimators encountered in the following sections of this chapter [Zoltowski, 1988].

6.3.2 TLS Estimates from Normal Equations

As stated before the key difference between TLS and OLS is that in TLS all the elements in the noisy data matrix $\boldsymbol{D} = (\boldsymbol{A}, \boldsymbol{b})$ are modified. This contrasts the OLS problem in which only one column of $\boldsymbol{D} = (\boldsymbol{A}, \boldsymbol{b})$ is modified.

This property of the TLS problem can of course not only be stated as previously in Equation (6.16). Other formulations can be used of which especially the formulation of normal equations is commonly used in computer vision and referred to as the structure tensor [Bigün and Granlund, 1987; Haußecker and Spies, 1999]. This formulation of the TLS problem is also known as the orthogonal L_2 approximation problem [Van Huffel and Vandewalle, 1991] which can be stated as follows:

Definition 4 *Given a data matrix $\boldsymbol{D} \in \mathbb{R}^{n \times (p+1)}$. We then seek to*

$$\begin{aligned} &\textit{minimize} && ||\boldsymbol{e}|| = ||\boldsymbol{D}\boldsymbol{p}||_2, \quad \boldsymbol{p} \in \mathbb{R}^p \\ &\textit{subject to} && \boldsymbol{p}^\top \boldsymbol{p} = 1, \end{aligned} \tag{6.23}$$

with the vector of residuals $\boldsymbol{e} = \boldsymbol{D}\boldsymbol{p}$. The constraint has to be posed on the parameter vector $\boldsymbol{p}$ to avoid the trivial solution $\boldsymbol{p} = 0$.

The orthogonal L_2 approximation problem in Equation (6.23), incorporating the constraint, can be solved by means of a Lagrange multiplier, minimizing

$$\boldsymbol{f} = \arg\min L(\boldsymbol{p}, \lambda), \quad L(\boldsymbol{p}, \lambda) = \boldsymbol{p}^\top \boldsymbol{J} \boldsymbol{p} + \lambda \left(1 - \boldsymbol{p}^\top \boldsymbol{p}\right), \quad \text{with} \quad \boldsymbol{J} = \boldsymbol{D}^\top \boldsymbol{D}, \tag{6.24}$$

where $\boldsymbol{J} \in \mathbb{R}^{p \times p}$. The functional $L(\boldsymbol{p}, \lambda)$ is minimized, when the partial derivatives with respect to all parameters are equal to zero, that is

$$\frac{\partial L(\boldsymbol{p}, \lambda)}{\partial p_i} = 2 \sum_{k=1}^{p} J_{ik} p_k - 2\lambda p_i = 0, \quad i \in \{1, 2, ..., p\}, \tag{6.25}$$

This system of Equations can be written in vector form, leading to

$$\boldsymbol{J}\boldsymbol{p} = \lambda \boldsymbol{p}. \tag{6.26}$$

Therefore, the solution to the minimization problem of Equation (6.23) is reduced to an eigenvalue problem of the symmetric matrix $\boldsymbol{J}$, as can be shown by use of Equation (6.26):

$$\min ||\boldsymbol{D}\boldsymbol{p}||_2 = \boldsymbol{p}^\top \boldsymbol{J}\boldsymbol{p} = \boldsymbol{p}^\top \lambda \boldsymbol{p} = \lambda. \tag{6.27}$$

Consequently, the eigenvector $\boldsymbol{e}_n$ to the smallest eigenvalue λ_n of $\boldsymbol{J}$ is the sought after solution to this minimization problem.

The appeal of this formulation of the TLS problem is its equivalences in classical mechanics as the *moment of inertia tensor* [Goldstein, 1980; Landau and Lifschitz, 1990] or in digital image processing as the structural tensor [Bigün et al., 1991] in orientation analysis, where the eigenvalue analysis represents a rotation of the tensor along its axis of smallest inertia or along its predominant texture. In this context the parameter estimation can be thought of as an orientation analysis, which offers an intuitive interpretation in optical flow computations as can be shown in Chapter 8.

Apart from this formulation in normal equations and the one from section 6.3 there exist other formulations of the TLS problem as well [Van Huffel and Vandewalle, 1991]. In terms of their solution they all can be reduced essentially to the same eigenvalue or singular value problem, respectively. This makes the choice of TLS formulation somewhat arbitrary. However, the main difference in between the two formulations presented in this work are either solving a singular value problem (section 6.3) or an eigenvalue analysis of a symmetric matrix (this Section). It cannot be stated in general which formulation is the more preferable, as both have their merits.

For the eigenvalue analysis Jacobi transformations of symmetric matrices [Press et al., 1992] can be employed. This method has the advantage of being very simple and foolproof. Performance wise it is not competitive with the symmetric QR algorithm, even though it converges quadratically. The poorer performance is noticeable for matrices of order greater than about 10 [Press et al., 1992], which is common in optical flow computations as presented in Chapter 8. Details of the chosen implementation of the TLS problem can be found in Section 6.3.5.

6.3.3 Weighted Total Least Squares

In the formulation of the TLS problem from the previous sections the rows in the data matrix were treated equal. This may not always be beneficial. In optical flow computations the observations are weighted differently depending on their relative location in a local neighborhood (see Chapter 8). When working with the robust estimators of Section 7.2 the observations must be weighted according to a weight function of their residuals. Guillaurne et al. [1998] weight the observations differently

to derive an estimator for linear time-invariant multivariable systems with maximum likelihood estimators. All these shortcomings in the previous formulation of the TLS problem call for an extension thereof, called weighted total least squares (WTLS). It can be formulated as follows:

Definition 5 *Given an over determined set of n linear Equations $\boldsymbol{A}\boldsymbol{x} = \boldsymbol{b}$ with $\boldsymbol{A} \in \mathbb{R}^{n\times p}$, $\boldsymbol{b} \in \mathbb{R}^n$ and a parameter vector $\boldsymbol{x} \in \mathbb{R}^p$ as well as a weight matrix $\boldsymbol{W} \in \mathbb{R}^{n\times n}$. In the WTLS problem it is then tried to*

$$\begin{aligned} \textit{minimize} \quad & || \left(\boldsymbol{W}[\boldsymbol{A}, \boldsymbol{b}]\right) - \left(\boldsymbol{W}[\tilde{\boldsymbol{A}}, \tilde{\boldsymbol{b}}]\right) ||_F, \\ \textit{with} \quad & \left(\tilde{\boldsymbol{A}}, \tilde{\boldsymbol{b}}\right) \in \mathbb{R}^{n\times(p+1)},\ \boldsymbol{W} = \mathrm{diag}(w_1, \ldots, w_n), \\ \textit{subject to} \quad & \tilde{\boldsymbol{b}} \in \mathrm{range}(\tilde{\boldsymbol{A}}). \end{aligned} \tag{6.28}$$

When comparing the WTLS problem with the TLS problem of Equation (6.16) it becomes apparent, that the TLS is just a special case of the WTLS with the weighting matrix $\boldsymbol{W} = \mathbb{1}$. The weighting matrix $\boldsymbol{W}$ can be regarded as the left hand weighting matrix $\boldsymbol{W}_L$ introduced in Section 6.1. We can therefore just write $\boldsymbol{A}' \leftarrow \boldsymbol{W}\boldsymbol{A}$ and $\boldsymbol{b}' \leftarrow \boldsymbol{W}\boldsymbol{b}$ and use the transformed matrix $(\boldsymbol{A}', \boldsymbol{b}')$ instead of $(\boldsymbol{A}, \boldsymbol{b})$ in the TLS problem of Section 6.3. All the results, limitations and algorithms derived for the TLS problem can thus be readily transferred to the WTLS problem.

6.3.4 Computing the Covariance Matrix

Following Nestares et al. [2000] the covariance matrix for the TLS parameter estimator can be derived by considering one linear equation $\boldsymbol{a}^\top \boldsymbol{x} = b$ contaminated by additive noise, that is

$$\boldsymbol{a} = \boldsymbol{a}_0 + \boldsymbol{n}_a \quad \text{and} \quad b = b_0 + n_b = \boldsymbol{a}_0^\top \boldsymbol{x} + n_b. \tag{6.29}$$

Due to the linearity of this equation it becomes apparent that the probability density function of $\boldsymbol{a}$ and b is just equal to the probability density function of the noise $p\left((\boldsymbol{n}_a^\top, n_b)^\top\right)$. Given $\boldsymbol{a}_0$ the variable b depends on $\boldsymbol{x}$ as can be seen from Equation (6.29), thus

$$p\left(\boldsymbol{a}, b|\boldsymbol{x}, \boldsymbol{a}_0\right) = p\left((\boldsymbol{n}_a^\top, n_b)^\top\right). \tag{6.30}$$

In the above formulation the dependance on the unperturbed observations $\boldsymbol{a}_0$ poses a major drawback, also known as the *nuisance parameters* [van der Vaart, 1998]. The reason for this is the growth of the dimension of the probability density function with the number of observations. This drawback can be circumvented by integrating over the true observations, making use of *Bayes'theorem* [Meyer, 1970]. To this end we derive

$$\begin{aligned} p(\boldsymbol{a}, b|\boldsymbol{x}) &= \int_{\boldsymbol{a}_0} p(\boldsymbol{a}, b, \boldsymbol{a}_0|x)\mathrm{d}\boldsymbol{a}_0 \\ &= \int_{\boldsymbol{a}_0} p(\boldsymbol{a}, b|x, \boldsymbol{a}_0)p(\boldsymbol{a}_0|\boldsymbol{a})\mathrm{d}\boldsymbol{a}_0 = \int_{\boldsymbol{a}_0} p((\boldsymbol{n}_a^\top, n_b)^\top)p(\boldsymbol{a}_0|\boldsymbol{x})\mathrm{d}\boldsymbol{a}_0. \end{aligned} \tag{6.31}$$

It might be tempting to assume that $\boldsymbol{a}$ is independent of $\boldsymbol{x}$ and thus $p(\boldsymbol{a}_0|\boldsymbol{x}) = p(\boldsymbol{a}_0)$. Due to the limit on the variance of $b_0|\boldsymbol{x}$ and the linear relationship between $\boldsymbol{a}_0$ and b_0, there must also be a limit

on the variance of $\boldsymbol{a}_0$ and thus $\boldsymbol{a}_0|\boldsymbol{x}$. It is practical to assume that the sum of the variances of $\boldsymbol{a}_0$ and b_0 remain constant for a given $\boldsymbol{x}$. Further it is assumed that this sum of variances be a Gaussian distribution, which yields an analytical solution for Equation (6.31). For a given $\boldsymbol{x}$ the linear equation poses the constraint $\boldsymbol{a}_0^\top \cdot \boldsymbol{x} - b_0 = 0$, which means that the probability density function $p(\boldsymbol{a}_0, b_0|\boldsymbol{x})$ has to be zero for all values of $\boldsymbol{a}_0$ and b_0 not subject to this constraint. Therefore $p(\boldsymbol{a}_0, b_0|\boldsymbol{x})$ will be proportional to the Dirac delta distribution $\delta(\boldsymbol{a}_0^\top \boldsymbol{x} - b_0)$ and can thus be written as

$$p(\boldsymbol{a}_0, b_0|\boldsymbol{x}) = \frac{k}{(2\pi\sigma_0^2)^{N/2}} \delta(\boldsymbol{a}_0^\top \boldsymbol{x} - b_0) \exp\left(-\frac{\boldsymbol{a}^\top \boldsymbol{a} + b_0^2}{2\sigma_0^2}\right), \tag{6.32}$$

with N being the dimension of the parameter vector $\boldsymbol{x}$. By integrating this equation over b_0 the unknown in Equation (6.31) can be derived, that is

$$\begin{aligned} p(\boldsymbol{a}_0|\boldsymbol{x}) &= \int_{b_0} p(\boldsymbol{a}_0, b_0|\boldsymbol{x}) \mathrm{d}b_0 \\ &= \frac{||\boldsymbol{x}||}{(2\pi\sigma_0^2)^{N/2}} \exp\left(\frac{-\boldsymbol{a}_0^\top \Sigma_x^{-1} \boldsymbol{a}_0}{2\sigma_0^2}\right), \quad \text{with} \quad \Sigma_x = \mathbb{1}_N - \frac{\boldsymbol{x}\boldsymbol{x}^\top}{||\boldsymbol{x}||}. \end{aligned} \tag{6.33}$$

Assuming $p((\boldsymbol{n}_a^\top, n_b)^\top)$ to be isotropic Gaussian noise with a covariance matrix $\Sigma\!\!\!/ = \sigma_n^2 \mathbb{1}_N$ and $\boldsymbol{d} \equiv \left(\boldsymbol{a}^\top, b\right)^\top$, $\boldsymbol{p} = \left(\boldsymbol{x}^\top, -1\right)^\top$, Equation (6.31) yields

$$p(\boldsymbol{a}, b|\boldsymbol{x}) = \frac{\gamma^{N/2}}{(2\pi)^{(N+1)/2}\sigma_0^N \sigma_n} \exp\left(-\frac{1}{2\sigma_n^2}\left[(1-\gamma)\boldsymbol{d}^\top \boldsymbol{d} + \gamma \frac{\boldsymbol{d}^\top \boldsymbol{p}\boldsymbol{p}^\top \boldsymbol{d}}{||\boldsymbol{p}||^2}\right]\right). \tag{6.34}$$

In the derivation of Equation (6.34) only one equation was looked at, which poses an underdetermined system of equations. As outlined in previous sections more than one observation is needed to solve the problem in an overdetermined system of equations, resulting in L equations of the form $\boldsymbol{A}_0\boldsymbol{x} = \boldsymbol{b}_0$. The rows of $\boldsymbol{A}_0$ are formed by the true values for each Equation $\boldsymbol{a}_0$ and $\boldsymbol{b}_0$ is a column vector containing the true values of b_0. With this notation previous results can readily be transferred to the case of multiple equations.

If the L Equations are independent, which is always assumed, the complete probability density function can be expressed as the product of the probability density functions of the individual equations, thus

$$p(\boldsymbol{A}, \boldsymbol{b}|\boldsymbol{x}) = \prod_{i=1}^{L} p(\boldsymbol{a}_i, b_i|\boldsymbol{x}). \tag{6.35}$$

In the case of identical independently distributed (iid) Gaussian noise with identical standard deviation in each Equation the complete probability density function of Equation (6.35) reduces to

$$p(\boldsymbol{A}, \boldsymbol{b}|\boldsymbol{x}) = \left(\frac{\gamma^{N/2}}{(2\pi)^{(N+1)/2}\sigma_0^N \sigma_n}\right)^L \exp\left(-\frac{1}{2\sigma_n^2}\left[(1-\gamma)\mathrm{tr}(\boldsymbol{D}\boldsymbol{D}^\top) + \gamma \frac{\boldsymbol{p}^\top \boldsymbol{D}^\top \boldsymbol{D}\boldsymbol{p}}{||\boldsymbol{p}||^2}\right]\right) \tag{6.36}$$

In this section we are set out to provide confidence bounds on the accuracy of parameters obtained. A standard procedure is to give the Cramer-Rao lower bound on the variance of the estimates, which is given by the inverse of the negative log of Equation (6.36) evaluated at the true values of the parameters [van der Vaart, 1998]. Because the true parameters are not known but only approximations

estimated, the Cramer-Rao lower bound can equally only be approximated. Among several possible approximations [Van Huffel and Vandewalle, 1991; Ohta, 1996; Branham, 1999] the one propagated by Nestares et al. [2000] was chosen as it only depends on the observations and promises higher accuracy [Nestares et al., 2000]. In this approximation the Cramer -Rao lower bound is given by the inverse of the Hessian, that is

$$\boldsymbol{H} = \frac{\gamma}{\sigma_n^2 ||\boldsymbol{p}||} \left(\boldsymbol{M} - \frac{1}{||\boldsymbol{p}||^2} \left(\boldsymbol{p}^\top \boldsymbol{J} \boldsymbol{p} \right) \mathbb{1}_N + \frac{4}{||\boldsymbol{p}||^4} \left[\left(\boldsymbol{p}^\top \boldsymbol{J} \boldsymbol{p} \right) \boldsymbol{x} - ||\boldsymbol{p}||^2 \left(\boldsymbol{M}\boldsymbol{x} - \boldsymbol{A}^\top \boldsymbol{b} \right) \right] \boldsymbol{x}^\top \right) \quad (6.37)$$

where $||\cdot||$ denotes the L_2-norm of a vector and $\boldsymbol{M} \equiv \boldsymbol{A}^\top \boldsymbol{A}$. The factor $\gamma \equiv \sigma_0^2/(\sigma_n^2 + \sigma_0^2)$ is related to the signal to noise ration (SNR), as $\gamma \approx 1$ for a high SNR (σ_0^2 is the signal strength and σ_n^2 the variance of the noise, thus for a high SNR: $\sigma_0^2 \gg \sigma_n^2$). Equation (6.37) is to be evaluated at the TLS solution for $\boldsymbol{p}$.

6.3.5 Implementation of the TLS Estimator

In this section the actual implementation used for the TLS estimator in the context of this work is outlined. Basically two distinct implementations are conceivable. The difference in between them depends by large on the formulation of the TLS problem in terms of a matrix approximation (see Section 6.3) or normal Equations (Section 6.3.2) and the subsequent singular value or eigenvalue analysis respectively. In the formulation of normal equation an eigenvalue analysis on a symmetric square matrix $\boldsymbol{J} = \boldsymbol{D}^\top \boldsymbol{D}$ has to be performed where the method of choice are Jacobi rotations [Press et al., 1992]. For the matrix approximation formulation a singular value analysis in terms of a singular value decomposition (SVD), see Section A.1, has to be performed. For a comprehensive overview of developments in the field of SVD the reader is referred to van der Vorst and Golub [1997].

The main disadvantage of the formulation of orthogonal equations and an subsequent eigenvalue analysis is concerned with the forming of the matrix $\boldsymbol{J}$ by an outer product. Due to this outer product information is lost when calculating $\boldsymbol{D}^\top \boldsymbol{D}$ due to roundoff errors, which may be quite significant when combining entities of different magnitude [Björck, 1990]. Also, small perturbations in the outer product have a much more dominant effect on the solution than perturbations of the same size in the matrix $\boldsymbol{D}$. A more thorough perturbation analysis shows that normal equation solution depends on the square of the condition number of $\boldsymbol{D}$. This condition number κ of a matrix $\boldsymbol{A}$ is defined as

$$\kappa(\boldsymbol{A}) = ||\boldsymbol{A}||_2 \cdot ||\boldsymbol{A}^I||_2 = \lambda_1/\lambda_r \,, \quad (6.38)$$

where the pseudoinverse is termed as $\boldsymbol{A}^I$, the biggest singular value is given by λ_1 and the smallest one by λ_r respectively. It follows that the condition number $\kappa(\boldsymbol{A}) = \infty$ for singular matrices $\boldsymbol{A}$. If $\kappa(A)$ is large, then $\boldsymbol{A}$ is said to be an ill-conditioned matrix.

Although the cyclic Jacobi method converges quadratically [Golub and van Loan, 1996], it is not competitive with the symmetric QR algorithm. The big advantage of the Jacobi rotations is that it can compute the eigenvalues with a smaller relative error if $\boldsymbol{J}$ is positive definite [Demmel and Veseliç, 1992]. In the context of this work the relative error of the eigenvalues is not that crucial however, as generally only the eigenvectors to the smallest eigenvalue make up the solution parameter vector (see Section 6.3).

It is due to these limitations of the formation and solution of the eigenvalue analysis that in the context of this work the solution of the TLS problem in its formulation of a matrix approximation formulation was chosen. Here the computation of a solution for the TLS problem is fairly straightforward.

Given a matrix $\boldsymbol{A} \in \mathbb{R}^{n \times p}$ and the vectors $\boldsymbol{b} \in \mathbb{R}^n$ as well as the parameter vector $\boldsymbol{x} \in \mathbb{R}^p$. To solve the TLS problem we seek a solution $\tilde{\boldsymbol{x}}$ for $\boldsymbol{A}\boldsymbol{x} \approx \boldsymbol{b}$. We then proceed a follows:

If $n > 5/3(p+1)$ the matrix $\boldsymbol{D} = (\boldsymbol{A}, \boldsymbol{b}) \in \mathbb{R}^{n \times (p+1)}$ is transformed to upper triangular form $\boldsymbol{R}$ by Householder transformations, thus $\boldsymbol{D} = \boldsymbol{Q}\boldsymbol{R}$ with $\boldsymbol{Q}^\top \boldsymbol{Q} = \mathbb{1}$. The reason for bidiagonalization of $\boldsymbol{D}$ was suggested by Chan [1982] and involves fewer computations for $n > 5/3(p+1)$. The SVD on $\boldsymbol{D}$ involves $4np^2 - 4/3p^3$ flops whereas the flop count for the SVD on the bidiagonalized matrix $\boldsymbol{R}$ is only $2np^2 + 2p^3$ [Golub and van Loan, 1996]. This step is valid as $\boldsymbol{R}$ and $\boldsymbol{D}$ have the same singular values and vectors, which is due to the fact that $\boldsymbol{Q}$ is an orthogonal matrix.

The singular value decomposition (SVD) of Equation (A.2) is then performed on $\boldsymbol{R}$ or $\boldsymbol{D}$ respectively. The right singular vectors $\boldsymbol{V} = (\boldsymbol{v}_1, \ldots, \boldsymbol{v}_{p+1})$ are saved. In a next step the numerical rank k of $\boldsymbol{D}$ is computed by imposing a threshold σ on the smallest singular value

$$\lambda_1^2 \geq \cdots \geq \lambda_k^2 > \sigma \geq \lambda_{k+1}^2 \geq \cdots \geq \lambda_{p+1}^2, \quad \text{with} \quad k \leq p. \tag{6.39}$$

If $k = p$ and $\boldsymbol{v}_{k+1,p+1} \neq 0$, then a generic solution given by the singular vector to the smallest singular value was found. The solution of the TLS problem is then obtained by scaling this singular vector according to Equation (6.21), that is $(\boldsymbol{x}^\top, -1)^\top = -\boldsymbol{v}_{n+1}/\boldsymbol{v}_{n+1,n+1}$.

For $k < p$ no single solution was found and only the nongeneric TLS solution from Section 6.3.1 can be given. Following Equation (6.22) this minimum norm solution $\tilde{\boldsymbol{x}}$ is given by

$$\tilde{\boldsymbol{x}} = -\frac{\sum_{i=k+1}^{p+1} \boldsymbol{v}_{p+1,i} \cdot (\boldsymbol{v}_{1,i}, \ldots \boldsymbol{v}_{p,i})^\top}{\sum_{i=k+1}^{p+1} \boldsymbol{v}_{p+1,i}^2}. \tag{6.40}$$

This algorithm requires about $2np^2 + 12p^3$ flops, most of which are associated with the SVD computation [Golub and van Loan, 1996].

6.4 Geometric Interpretation

The key difference between the OLS and TLS estimators is best illustrated geometrically. From the formulation of the TLS problem $(\boldsymbol{A}, \boldsymbol{b})(\boldsymbol{x}^\top, -1)^\top = \boldsymbol{D}\boldsymbol{p} = 0$ it is straight forward to verify that the solution to Equation (6.23) is given by

$$\frac{||\boldsymbol{D}\boldsymbol{p}||_2}{||\boldsymbol{p}||_2} = \sum_{i=1}^{n} \frac{\left(\boldsymbol{a}_i^\top \boldsymbol{x} - b_i\right)^2}{\boldsymbol{x}^\top \boldsymbol{x} + 1} = \lambda_{p+1}, \tag{6.41}$$

where $\boldsymbol{a}_i^\top = (a_{i,1}, \ldots, a_{i,p})$ is the ith row of $\boldsymbol{A}$. It can be derived quite easily from basic linear algebra that the quantity

$$\frac{\left(\boldsymbol{a}_i^\top \boldsymbol{x} - b_i\right)^2}{\boldsymbol{x}^\top \boldsymbol{x} + 1} \tag{6.42}$$

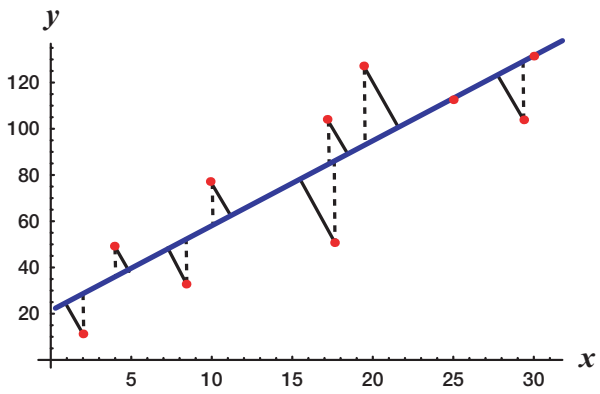

Figure 6.2: *The geometric interpretation of OLS versus TLS. The TLS tries to find the closest subspace $\mathcal{P}_x$ to the data points which is equivalent to minimizing the orthogonal distances (solid lines), whereas OLS tries to minimize the vertical distances (dotted lines).*

is the square of the distance from $(\boldsymbol{a}_i^\top, \boldsymbol{b})^\top \in \mathbb{R}^{p+1}$ to the nearest point in the hyperplane $\mathcal{P}_x$ defined by

$$\mathcal{P}_x = \left\{ \begin{pmatrix} \boldsymbol{a} \\ b \end{pmatrix} \middle| \boldsymbol{a} \in \mathbb{R}^p, b \in \mathbb{R}, b = \boldsymbol{x}^\top \boldsymbol{a} \right\}. \tag{6.43}$$

Thus from Equation (6.41) the TLS solution can be interpreted as minimizing the sum of squared orthogonal distances from n observations to the hyperplane $\mathcal{P}_x$. This is in contrast to the OLS estimatoer, which only tries to minimize the sum of squared vertical distances by minimizing $||\boldsymbol{b} - \boldsymbol{b}^{\text{est}}||_2$ (see Equation 6.9), which is illustrated in Figure 6.2.

6.5 Mixing Least Squares and Total Least Squares

In Section 6.3 it was stated that the estimated parameter vector $\boldsymbol{p}^{\text{est}}$ converges to the true vector $\boldsymbol{p}$ in the case of independently and identically distributed errors in the observations. That means that all observations should have the same standard deviation σ, which can be achieved by scaling the data accordingly (see Section 6.1). However, there are instances when one column in the data matrix is known *exactly*, that is it is not subject to any errors. This is the case in intercept models of the form

$$c + a_1 x_1 + \cdots + a_m x_m = b, \tag{6.44}$$

which is commonly used in the context of this work (see Section 8.8.1). Such a model gives rise to an overdetermined set of equations of the form

$$(1_N; \boldsymbol{A}) \begin{pmatrix} c \\ \boldsymbol{x} \end{pmatrix} = b, \tag{6.45}$$

where 1_N is first column of the data matrix that is exactly known ($1_N = (1, \ldots, 1)^\top$).

The accuracy of the estimated parameters can be maximized by requiring that the exactly known columns in the data matrix be unperturbed [Van Huffel and Vandewalle, 1991; Björck, 1990]. This can be achieved by reformulating the TLS problem in a more general form by mixing OLS and TLS:

Definition 6 *Given a set of n linear Equations with p unknown parameters $\boldsymbol{x}$*

$$(\boldsymbol{A}_1, \boldsymbol{A}_2)\,\boldsymbol{x} = \boldsymbol{b}, \quad \text{with} \quad \boldsymbol{A}_1 \in \mathbb{R}^{n\times p_1}, \boldsymbol{A}_2 \in \mathbb{R}^{n\times p_2}, \boldsymbol{x} \in \mathbb{R}^{p}, \boldsymbol{b} \in \mathbb{R}^{n}, \tag{6.46}$$

and $p_1 + p_2 = p$. The mixed OLS-TLS problem then seeks to minimize

$$\begin{aligned} &\min && [(\boldsymbol{A}_2, \boldsymbol{b})\,\boldsymbol{p}_2]^2 \\ &\textit{subject to} && (\boldsymbol{A}_1, \boldsymbol{A}_2)\,\boldsymbol{x} = \boldsymbol{A}_1\boldsymbol{x}_1 + \boldsymbol{A}_2\boldsymbol{x}_2 = \boldsymbol{b}, \end{aligned} \tag{6.47}$$

where $\boldsymbol{p} = \left(\boldsymbol{x}^\top, -1\right)^\top$, $\boldsymbol{p}_2 = \left(\boldsymbol{x}_2^\top, -1\right)^\top$ and $\boldsymbol{x} = \left(\boldsymbol{x}_1^\top, \boldsymbol{x}_2^\top\right)^\top$.

In the specific example of Equation (6.44) $p_1 = 1$ and $p_2 = m$. Equation (6.47) can thus be depicted as first finding a TLS solution on the reduced subspace of erroneous observations and than choosing from this set the one solution that solves the Equations of unperturbed data exactly.

In the event of all observations $\boldsymbol{A}$ being known exactly, the OLS-TLS solution reduces to the OLS solution, while at the other extreme of only erroneous data the problem reduces to the TLS problem. By varying p_1 from zero to p the formulation of equation (6.47) can thus handle OLS, TLS or any mixtures of the two.

6.5.1 Implementation of Mixed OLS-TLS Estimator

From what has been said in the previous section the implementation of the mixed OLS-TLS estimator is quite straightforward. First of all the columns of the data matrix A are permuted by the permutation matrix $\boldsymbol{P}$ in such a way, that the submatrix $\boldsymbol{A}_1$ contains the p_1 exactly known observations, that is

$$\boldsymbol{A} \cdot \boldsymbol{P} = (\boldsymbol{A}_1, \boldsymbol{A}_2)\,, \text{ where } \boldsymbol{A} \in \mathbb{R}^{n\times p}, \boldsymbol{A}_1 \in \mathbb{R}^{n\times p_1}, \boldsymbol{A}_2 \in \mathbb{R}^{n\times p_2}, \boldsymbol{P} \in \mathbb{R}^{p\times p}. \tag{6.48}$$

In a next step a QR factorization of the matrix $(\boldsymbol{A}_1, \boldsymbol{A}_2, \boldsymbol{b})$ is performed, thus

$$(\boldsymbol{A}_1, \boldsymbol{A}_2, \boldsymbol{b}) = \boldsymbol{Q} \begin{pmatrix} \boldsymbol{R}_{11} & \boldsymbol{R}_{12} \\ \boldsymbol{0} & \boldsymbol{R}_{22} \end{pmatrix}, \tag{6.49}$$

with $\boldsymbol{Q}$ being orthogonal and $\boldsymbol{R}_{11}$ upper triangular.

Then the TLS solution for the sub system of equations $\boldsymbol{R}_{22}\boldsymbol{p}_2 = 0$ is computed according to the algorithm presented in Section 6.3.5.

With the known estimate of $\boldsymbol{p}_2$ the system of equations $\boldsymbol{R}_{11}\boldsymbol{p}_1 + \boldsymbol{R}_{12}\boldsymbol{p}_2 = 0$ is solved for $\boldsymbol{p}_1$ by back-substitution. The parameter vector $\boldsymbol{p} = \left(\boldsymbol{p}_1^\top, \boldsymbol{p}_2^\top\right)^\top$ has than to be transformed back reversing the initial permutations of the columns by $\boldsymbol{p} \leftarrow \boldsymbol{P}^{-1}\boldsymbol{p}$.

6.6 Generalized Total Least Squares

In Section 6.3 the TLS estimator was introduced as a more global fitting technique of the OLS estimator from Section 6.2 in so far as errors in all observations were taken into account, not only that of $\boldsymbol{A}$ in the overdetermined system of equations $\boldsymbol{A}\boldsymbol{x} = \boldsymbol{b}$. Both, TLS and OLS still have in common,

that the errors on the measurements of $\boldsymbol{A}$ (and in the case of TLS $\boldsymbol{b}$ as well) have to be uncorrelated with zero mean and equal variance for the estimator to produce consistent results. In Section 6.5 the TLS estimator was extended to a mixed LS-TLS estimator in which the assumption of equal variance of errors in $\boldsymbol{A}$ was dropped in the respect that individual columns of $\boldsymbol{A}$ were allowed to be known exactly, that is are not subject to any variation. An illustrious example of this case is the intercept model. Although allowing individual columns of $\boldsymbol{A}$ to have zero variance, the remaining columns still have to satisfy the condition of errors with zero mean and equal variance. This, as well as the other estimators presented so far still have one debilitating drawback, namely that in real world situations errors might be *correlated* and *not* equal in variance. The off diagonal elements of their covariance matrix $\not\Sigma$ will therefore not be zero any more. To circumvent this drawback, the TLS formulation has to be generalized to maintain consistency of the results when solving problems without trying to scale and transform *à priori* errors, which might not even always be possible in real world situations [Van Huffel and Vandewalle, 1989]. Following Van Huffel [1991] the concept of this generalized TLS will be referred to as GTLS in the following. The GTLS estimation problem can be formulated as follows:

Definition 7 *Given a set of n linear equations in p unknowns $\boldsymbol{x}$, that is*

$$\boldsymbol{A} \cdot \boldsymbol{x} = \boldsymbol{b}, \quad \textit{with} \quad \boldsymbol{A} \in \mathbb{R}^{n \times p},\ \boldsymbol{b} \in \mathbb{R}^{n} \textit{ and } \boldsymbol{x} \in \mathbb{R}^{p}. \tag{6.50}$$

Both $\boldsymbol{A}$ and $\boldsymbol{x}$ can then be partitioned so that

$$\begin{aligned} \boldsymbol{A} &= (\boldsymbol{A}_1, \boldsymbol{A}_2), \quad \textit{with} \quad \boldsymbol{A}_1 \in \mathbb{R}^{n \times p_1},\ \boldsymbol{A}_2 \in \mathbb{R}^{n \times p_2},\ p = p_1 + p_2 \\ \boldsymbol{x} &= \left(\boldsymbol{x}_1^\top, \boldsymbol{x}_2^\top\right)^\top, \quad \textit{here} \quad \boldsymbol{x}_1 \in \mathbb{R}^{p_1},\ \boldsymbol{x}_2 \in \mathbb{R}^{p_2}\ . \end{aligned} \tag{6.51}$$

Analogous to the Mixed LS-TLS estimator in Section 6.5 the columns of $\boldsymbol{A}_1$ are taken to be known exactly. Furthermore the covariance matrix $\not\Sigma(\boldsymbol{\sigma}^\top \boldsymbol{\sigma})$ of the errors $\boldsymbol{\sigma} \in \mathbb{R}^{n \times (p_2+1)}$ in the perturbed data in matrix $(\boldsymbol{A}_2, \boldsymbol{b})$ is given by $\boldsymbol{C} = \gamma \not\Sigma(\boldsymbol{\sigma}^\top \boldsymbol{\sigma}) \in \mathbb{R}^{(p_2+1)\times(p_2+1)}$ with a factor of proportionality γ. Assuming the $\boldsymbol{C}$ to be nonsingular with the Cholesky decomposition $\boldsymbol{C} = \boldsymbol{R}_C^\top \boldsymbol{R}_C$, the GTLS solution of Equation (6.51) is then any solution of the set

$$\tilde{\boldsymbol{A}}\boldsymbol{x} = \boldsymbol{A}_1\boldsymbol{x}_1 + \tilde{\boldsymbol{A}}_2\boldsymbol{x}_2 = \tilde{\boldsymbol{b}}, \tag{6.52}$$

where $\tilde{\boldsymbol{A}} = \left(\tilde{\boldsymbol{A}}_1, \tilde{\boldsymbol{A}}_2\right)$ and $\tilde{\boldsymbol{b}}$ are computed according to

$$\begin{aligned} &\textit{minimize} \quad \left|\left|\left(\Delta\tilde{\boldsymbol{A}}_2, \Delta\tilde{\boldsymbol{b}}\right) \boldsymbol{R}_C^{-1}\right|\right|_F = \textit{minimize} \quad \left|\left|\left(\boldsymbol{A}_2 - \tilde{\boldsymbol{A}}_2, \boldsymbol{b} - \tilde{\boldsymbol{b}}\right) \boldsymbol{R}_C^{-1}\right|\right|_F \\ &\textit{subject to} \quad \tilde{\boldsymbol{b}} \in \operatorname{range}(\tilde{\boldsymbol{A}}). \end{aligned} \tag{6.53}$$

Here $||\cdot||_F$ denotes the Frobenius norm, that is $||\boldsymbol{B}||_F = \sqrt{\sum_i \sum_j |b_{ij}|^2}$. Whenever the solution to Equation (6.53) is not unique, GTLS extracts the minimum norm solution, denoted by $\tilde{\boldsymbol{x}}$ and described in Section 6.3.1.

It can easily be shown that this formulation of the GTLS reduces to the mixed OLS-TLS estimator in Section 6.5 by setting $\boldsymbol{C} \sim \mathbb{1}$. Subsequently the GTLS estimator can be varied to accommodate OLS from Section 6.2 to TLS in Section 6.3 by varying p_1 from $p_1 = p$ to $p_1 = 0$ (for $\boldsymbol{C} \sim \mathbb{1}$).

6.6.1 Implementation of GTLS

The TLS Algorithm, as described in Section 6.3, can be used to compute consistent estimates of the parameters $\boldsymbol{x}$ whenever $\sum\!\!\!\!\!\!\sim \sim \mathbb{1}$ as outlined in the previous section. In the event of a more general covariance matrix $\sum\!\!\!\!\!\!\sim$ the data can be scaled appropriately such that the transformed data satisfies the prerequisite of diagonal covariance matrix with equal variances. The TLS estimator can then be used on the transformed observations as suggested by Gleser [1981], Mühlich and Mester [1999] and Spies [2001]. As pointed out by Van Huffel and Vandewalle [1989] this modus operandi cannot be recommended in general though, as computing $(\boldsymbol{A}, \boldsymbol{b})\,\boldsymbol{R}_C^{-1}$ usually leads to unnecessarily large numerical errors in the observations for ill conditioned $\boldsymbol{R}_C$.

The GTLS algorithm introduced in this section makes use of the Generalized Singular Value Decomposition (GSVD) of Equation (A.3), which allows for estimation in the GTLS sense *without transforming* the data explicitly. In that respect only one transformation is needed, which is numerically very reliable and can handle nearly singular covariance matrices $\sum\!\!\!\!\!\!\sim$, rather than performing a host of transformations by scaling every transformation individually. A formulation of the GSVD can be found in Appendix A.2. The GTLS estimator can then be computed as follows:

Given a matrix $\boldsymbol{A} = (\boldsymbol{A}_1, \boldsymbol{A}_2)$ with $\boldsymbol{A} \in \mathbb{R}^{n\times p}$, $\boldsymbol{A}_1 \in \mathbb{R}^{n\times p_1}$, $\boldsymbol{A}_2 \in \mathbb{R}^{n\times p_2}$, $p = p_1 + p_2$ and a vector $\boldsymbol{b} \in \mathbb{R}^n$. The submatrix $\boldsymbol{A}_1$ has full column rank and all its columns are known *exactly*. A permutation might be necessary to partition the matrix $\boldsymbol{A}$ in this fashion, analogous to Section 6.5.1. Also, a matrix $\boldsymbol{C} \in \mathbb{R}^{(p_2+1)\times(p_2+1)}$, which is proportional to the covariance matrix $\sum\!\!\!\!\!\!\sim\left(\boldsymbol{\Delta}^\top\boldsymbol{\Delta}\right)$ of the errors $\boldsymbol{\Delta} \in \mathbb{R}^{n\times(p_2+1)}$ in the matrix $(\boldsymbol{A}_2, \boldsymbol{b})$ is given.

In a first step the QR factorization of $(\boldsymbol{A}_1, \boldsymbol{A_2}, \boldsymbol{b})$ is performed according to

$$\boldsymbol{Q}^\top \cdot (\boldsymbol{A}_1, \boldsymbol{A}_2, \boldsymbol{b}) = \boldsymbol{R} = \begin{pmatrix} \boldsymbol{R}_{11} & \boldsymbol{R}_{12} \\ \boldsymbol{0} & \boldsymbol{R}_{22} \end{pmatrix}, \quad \text{with} \tag{6.54}$$

$$\boldsymbol{R} \in \mathbb{R}^{n\times p},\ \boldsymbol{R}_{11} \in \mathbb{R}^{p_1\times p_1},\ \boldsymbol{R}_{12} \in \mathbb{R}^{p_1\times(p_2+1)},\ \boldsymbol{R}_{22} \in \mathbb{R}^{(n-p_1)\times(p_2+1)}.$$

Here $\boldsymbol{Q}$ is an orthogonal matrix and $\boldsymbol{R}_{11}$ upper triangular. In the case of $p_1 = p$ the GTLS reduces to the OLS of Section 6.2 and all we need to do to gain an estimate for $\boldsymbol{x}$ is to solve $\boldsymbol{R}_{11}\boldsymbol{x} = \boldsymbol{R}_{12}$ by back substitution. In the event of $p_1 = 0$ this step can of course be omitted by setting $\boldsymbol{R}_{22} = (\boldsymbol{A}, \boldsymbol{b})$.

Next the Cholesky decomposition of $\boldsymbol{C}$ is performed, assuming that $\boldsymbol{C} \nsim \mathbb{1}$, yielding

$$\boldsymbol{C} = \boldsymbol{R}_C^\top \boldsymbol{R}_C. \tag{6.55}$$

In a next step the GSVD (see Section A.2) of the matrix pair $\boldsymbol{R}_{22}$ and $\boldsymbol{R}_C$ is carried out according to

$$\boldsymbol{T}^\top \boldsymbol{R}_{22} \boldsymbol{Z} = \operatorname{diag}(\alpha_1, \ldots, \alpha_s), \quad \alpha_{s+1}\cdots\alpha_{p_2+1} = 0, \quad s = \min\{n - p_1, p_2 + 1\} \tag{6.56}$$

$$\boldsymbol{W}^\top \boldsymbol{R}_C \boldsymbol{Z} = \operatorname{diag}(\beta_1, \ldots, \beta_{p_2+1}), \tag{6.57}$$

with the generalized singular values $\lambda_{g,i} = \alpha_i/\beta_i$, $i = 1, \ldots, p_{2+1}$ sorted in decreasing order of magnitude. From the generalized singular values $\lambda_{g,i}$ and the corresponding singular vectors $\boldsymbol{e}_{g,i} = \boldsymbol{z}_i$ the solution to the GTLS problem can be computed analogous to the solution to the TLS problem from the singular values λ_i and singular vectors $\boldsymbol{e}_i$ in Section 6.3. The same hold true in the case of a nongeneric solution. In this event the minimum norm solution can be attained according to the technique used for TLS estimators derived in Section 6.3.1.

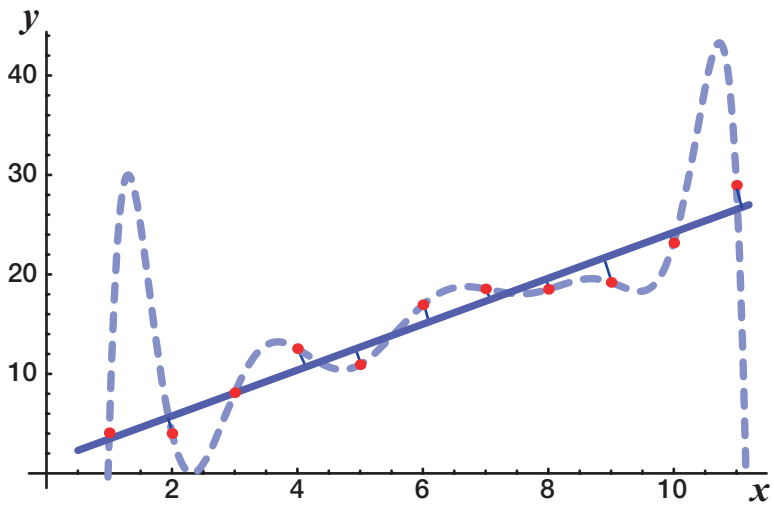

Figure 6.3: *Two models fitted to perturbed observations. Although the more complex model (dotted line) fits the data exactly, the less complex model (solid line) is the more sensible choice.*

6.7 Optimum Model Selection

When talking about parameter estimation there are usually different models for describing the problem at hand. The difference in models is often their complexity meaning the number of model parameters. Examples for this graduation in model complexity are a linear or quadratic fit in Section 10.2 or the use of an affine or linear model in optical flow computations in Section 8.3. An important question that arises is which model to choose. The answer to this question is not as straightforward as one might think. A model of higher complexity will fit a number observations better than a less complex model, in the sense that the sum of residuals or the total prediction error will always be smaller as is shown in Figure 6.3. Thus the relevant question has to be whether the fit for different models is significantly better in a statistical sense. Statistical significance means that the improvements in the fit have to be larger than the fluctuations in the observations. In order to quantitatively analyze the performance of one model against another the variance σ of the data d_i from the residual of the fit r_i is computed [Menke, 1989]

$$\sigma_d^2 = \frac{1}{n-p} \sum_{i=1}^{n} r_i^2, \tag{6.58}$$

where n is the number of observations and p the number of parameters in the model. The $n - p$ term takes care of the fact, that a more complex model can fit more observations exactly. The estimate of σ_d^2 from Equation (6.58) will usually be larger than the true variance of the data σ_d^2 since effects from a not perfect fit of the model are included as well. If two models (model α and model β) fit the data equally well, then their estimated variances of the data $\sigma_{d\alpha}^2$ and $\sigma_{d\beta}^2$ will be of equal size, the quotient $\sigma_{d\alpha}^2/\sigma_{d\beta}^2$ of which will be close to one. If one of the models is much better than the other, the ratio will differ significantly from one.

In the event that the data variances are nonuniform, the ratio cannot be formed of the estimated

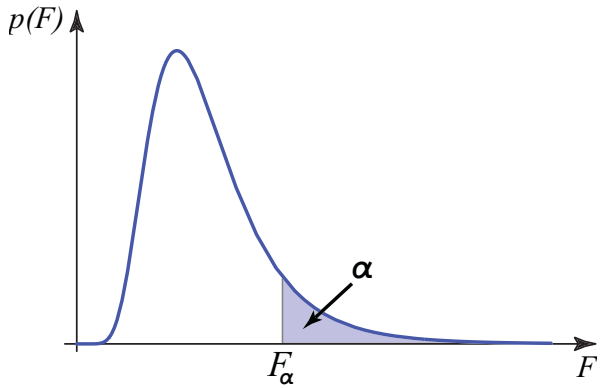

Figure 6.4: *A plot of the F-distribution $p(F)$. The ratios greater than F in 5% of the time are marked by the shaded area α.*

variances, but of the related quantity [Menke, 1989]

$$\chi^2_\nu = \frac{1}{\nu}\sum_{i=1}^{n}\frac{r_i^2}{\sigma_{d_i}}, \quad \text{with} \quad \nu = n - p, \tag{6.59}$$

where ν are the degrees of freedom and σ_{d_i} is the error of the data. The ratio of the χ^2_ν for the two models is then given by:

$$F = \frac{\chi^2_{\nu\alpha}}{\chi^2_{\nu\beta}}\,. \tag{6.60}$$

The distribution $p(F)$ of the F-ratio has been derived in statistical literature and is called the F- or *Fisher-distribution*. The functional form of this distribution is given by

$$p(F) = \frac{\Gamma\left(\frac{\nu_1+\nu_2}{2}\right)\left(\frac{\nu_1}{\nu_2}\right)^{\nu_1/2}F^{\nu_1/2-1}}{\Gamma\left(\frac{\nu_1}{2}\right)\Gamma\left(\frac{\nu_2}{2}\right)\left(1+\frac{\nu_1}{\nu_2}F\right)^{(\nu_1+\nu_2)/2}}, \tag{6.61}$$

a plot of which is shown in Figure 6.4. The *Gamma function* is denoted by Γ.

In the values for which the ratio is greater than or equal to F occur only 5% or 1% of the time are given in Appendix C.1 and C.2 respectively. If the computed F-ratio for the two models is greater than this critical value it is reasonable to assume, that there exist a statistical significant difference between the two models. Draper and Smith [1981] state that the F-ratio should be *four* times higher than the critical value in order for a model to be a satisfactory predictor of the data.

For a more stringent treatment of the F-Test and its derivation the reader is referred to Scheffé [1959]. More refined approaches for model selection are conceivable [Torr, 1999], but in the context of this work the presented scheme provided the necessary results.

The results from this analysis can be interpreted in two ways. The first is the obvious predication of whether the fit can be made more accurate by introducing a model of higher complexity. On the other hand, if a model assumption is physically motivated a model of lower complexity is the better choice based on the F-test. This leads to the complex field of experimental design [Atkinson and Donev, 1992; Bauer et al., 2000].

6.8 Summary

This chapter was an introduction to the task of parameter estimation in a generalized total least squares framework. The merits and malices towards scaling of observations were outlined. The ordinary least squares (OLS) estimator as an maximum likelihood estimator in the case of iid Gaussian noise on the observations was introduced. The bias of this estimator in the case of errors in all variables was circumvented with the introduction of the total least squares estimator (TLS). In a number of models, such as linear regression with intersect, some columns will be known without any errors. This leads to an error in TLS estimates which assumes all observations to be perturbed by the same iid Gaussian noise. A more accurate estimation is gained by the introduction of a mixes ordinary least squares - total least squares estimator, which computes the parameters of the perturbed data matrix in a total least squares sense and the exactly known columns by means of ordinary least squares estimation. The limitation of this estimator proofed to be its reliance on iid Gaussian noise on the observation, a prerequisite which does not always hold in applications. The most general estimator put forward in this chapter, the general total least squares estimator (GTLS) solves this issue and is applicable to problems where the perturbations of observations can not be model by iid Gaussian noise but a general covariance matrix. Furthermore, in this highly efficient framework some columns in the data matrix might even be known without any errors whatsoever. The important question of selecting the optimal model in a statistical significant sense was answered by means of F-tests which allows to differentiate between models with different numbers of parameters.

Chapter 7

Parameter Estimation in a Robust Framework

In the previous chapter parameter estimation in the L_2 norm was presented (OLS, TLS and variations thereof). Common to all these estimators is their failure if the observations are prone to outliers, that is 'wrong' observations that cannot be described by the model parameters to be estimated. In the L_2 norm these outliers have a strong effect on the computation and can lead the estimator astray. Since data in image processing task can often be corrupted by outliers (motion discontinuities, reflexes, corrupted pixels etc.) estimation schemes are needed to reliably classify data points into inliers and outliers. Within bounds this task is performed by robust estimators. When talking about robust estimators it is important to state what is meant by robustness. In the presented context we seek to employ a technique that is robust to outliers, which means that such data points should not be allowed to corrupt the result of the minimization problem. Hampel et al. [1986] defined the goals of robust estimators as:

- describe the structure best fitting the bulk of the data,
- identify deviating data points (outliers) or deviating structures for further treatment, if desired.

Both goals are fulfilled to varying degrees by the estimators presented in this chapter. In general, a robust estimator tries to correctly estimate the parameter vector $\boldsymbol{p} \in \mathbb{R}^p$ that best fits a model to a set of measurement data $\boldsymbol{D} \in \mathbb{R}^{n \times p}$ in cases where a certain fraction of the data deviates from the model assumption, this includes deviations both statistically or systematically in nature[1].

In the statistical literature many different types of robust estimators have been discussed, a recent performance analysis of a few of them can be found in Wisnowski et al. [2001]. Because of the high computational cost only a few robust estimators are applicable to computer vision. The most common ones are the class of estimators based on influence functions such as the M-Estimator [Huber, 1981; Hampel et al., 1986] and random sampling [Rousseeuw, 1984; Rousseeuw and Leroy, 1987], a review of which can be found in Meer et al. [1991], Torr [1995], Torr and Murray [1997] and more recently

[1] Systematical deviations might come about due to fractions of the data that cannot be described by the model assumption.

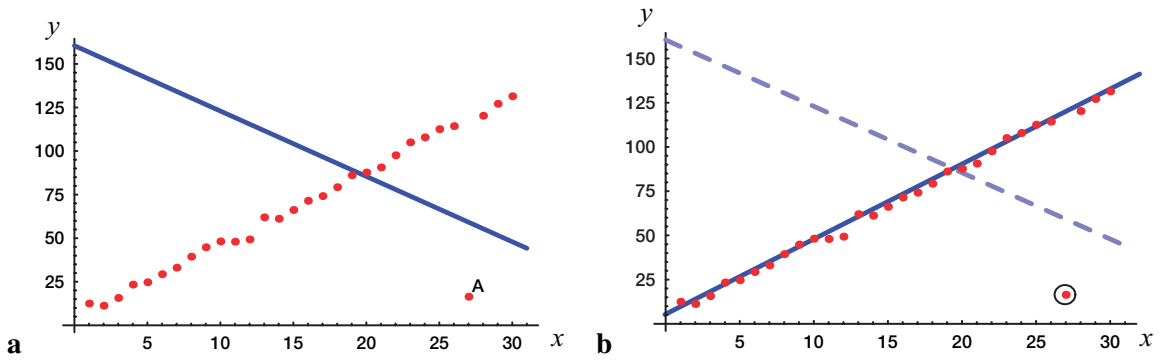

Figure 7.1: *One bad data point (***A***) is enough to send the TLS estimate astray, as can be seen in* ***a*** *. A robust estimator, depicted in* ***b*** *, should detect such outlying datums and find the correct estimates of the remaining data points.*

Stewart [1999]. A comparison of robust technique in terms of their biases can be found in Stewart [1997] who concludes that all current robust techniques present some form of bias at discontinuities.

In order to characterize the two classes of estimators some criterions are needed. These will be introduced in Section 7.1. In Section 7.2 the M-Estimator representing estimators based on influence functions will be outlined and with the Least Median of Squared Orthogonal Distances (LMSOD) estimator a random sampling estimator will be presented in Section 7.3.

7.1 Characterizing Robust Estimators

In order to choose a certain robust estimator for a given application it is important to find appropriate measures to characterize them. The three most common concepts employed to evaluate the regression method are:

- relative efficiency,
- breakdown point,
- time complexity.

The *relative efficiency* of an estimator is defined as the ratio between the lowest theoretically achievable variance for the estimated parameters and the actual variance provided by the given method. As a measure for the theoretically achievable variance usually the Cramer-Rao lower bound is given (see Section 6.3.4). The best possible relative efficiency of 1 is reached by OLS and TLS estimators in the presence of Gaussian noise on the observations. In contrast that of LMSOD is only $2/\pi = 0.637$ [Rousseeuw and Leroy, 1987].

The *breakdown point* of an estimator is the smallest fraction of contamination that can cause the estimator to take values arbitrary far away from the correct estimate. Theoretically the maximum achievable breakdown point is 50%. This is due to the fact that if more than half of the data are indeed outliers, they can sometimes be arranged in such a fashion that a fit through them will minimize the

objective function and thus makes them inliers. The breakdown point of OLS and TLS is $1/n \to 0$ as the number of samples n approaches large values while that of LMSOD is at the theoretical limit of 50% [Rousseeuw, 1984].

With *time complexity* the computational cost is meant. Generally as feasible considered are algorithms that require computations of a time complexity of at most $\mathcal{O}(n^2)$. The time complexity of OLS is $\mathcal{O}(np^2)$ where n is the number of observations and p the number of parameters to be estimated.

7.2 M-Estimators

As can be seen in Figure 7.1, one outlier is enough to send the TLS estimate astray. In fact, its breakdown point equals 1/n, which tends to zero as the sample size n increases.

Under the assumption that the errors in the data are distributed according to a Gaussian distribution, the TLS provides the maximum likelihood estimate. When outlieres are present in the data, the errors are quite clearly not Gaussian any more. As has been shown earlier, TLS may not converge to the correct estimate any longer. The same holds true for L_1 estimators that try to minimize the absolute value of the residual $|r_i|$ instead of r_i^2. Here outlieres may not have such a big effect as in the L_2 norm, but leverage points[2] can still render the estimate useless.

M-estimators follow maximum likelihood estimators with optimal weights for data under non-Gaussian condition [Hampel et al., 1986]. Hence the name M-estimator. The basic idea is to minimize the sum of a symmetric, positive-definite function $\rho(r_i)$ with a unique minimum at $r_i = 0$. Thus the squared residual r_i^2 in the formulation of the OLS or TLS problem (ie Equation (6.9)) is replaced by $\rho(r_i)$, yielding

$$\text{minimize} \quad \sum_{i=1}^{n} \rho(r_i). \tag{7.1}$$

The M-estimation problem can therefore be formulated as follows:

Definition 8 *Given a data matrix $\boldsymbol{D} \in \mathbb{R}^{n\times(p+1)}$. We then seek to*

$$\begin{aligned} &\textit{minimize} && \rho(\boldsymbol{r}) = \rho(\boldsymbol{Dp}), \quad \boldsymbol{p} \in \mathbb{R}^{p+1} \\ &\textit{subject to} && \boldsymbol{p}^\top \boldsymbol{p} = 1, \end{aligned} \tag{7.2}$$

with the vector of residuals $\boldsymbol{r} = \boldsymbol{Dp}$ and the estimation function ρ. The constraint has to be posed on the parameter vector $\boldsymbol{p}$ to avoid the trivial solution $\boldsymbol{p} = 0$.

This definition in form of normal equations was chosen for its intuitive comparison to the one of the TLS problem in Equation (6.23). When comparing the two formulations of Equation (6.23) and (7.2) it becomes apparent that TLS using the L_2 norm is just a special case of an M-Estimator.

[2] Leverage points are outliers in the observations that have the potential for strongly affecting the regression coefficients.

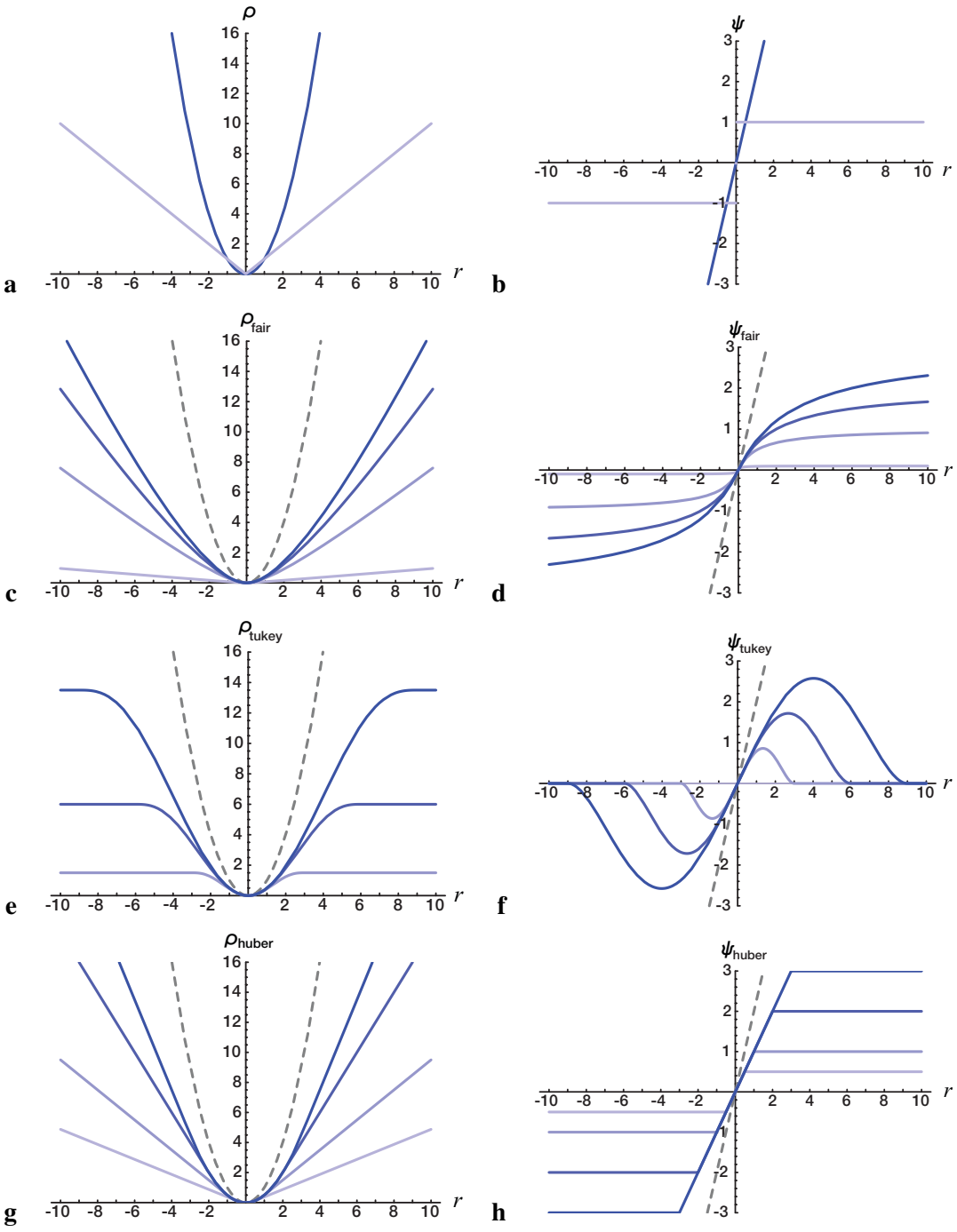

Figure 7.2: *A few representative plots of the estimators presented in Table 7.1 with different values of the tuning parameter σ. In **a** is the ρ-function of the L_1 and L_2 estimator with the corresponding ψ-function in **b** . The same functions for the Fair estimator in **c** and **d** respectively, for the Tukey estimator in **e** and **f** and **g** and **h** for the Huber estimator.*

This implies that all estimators in the L_n norm such as L_1 or least squares in L_2 can be treated as M-estimators and their estimator functions ρ can be compared directly to those optimized for robustness.

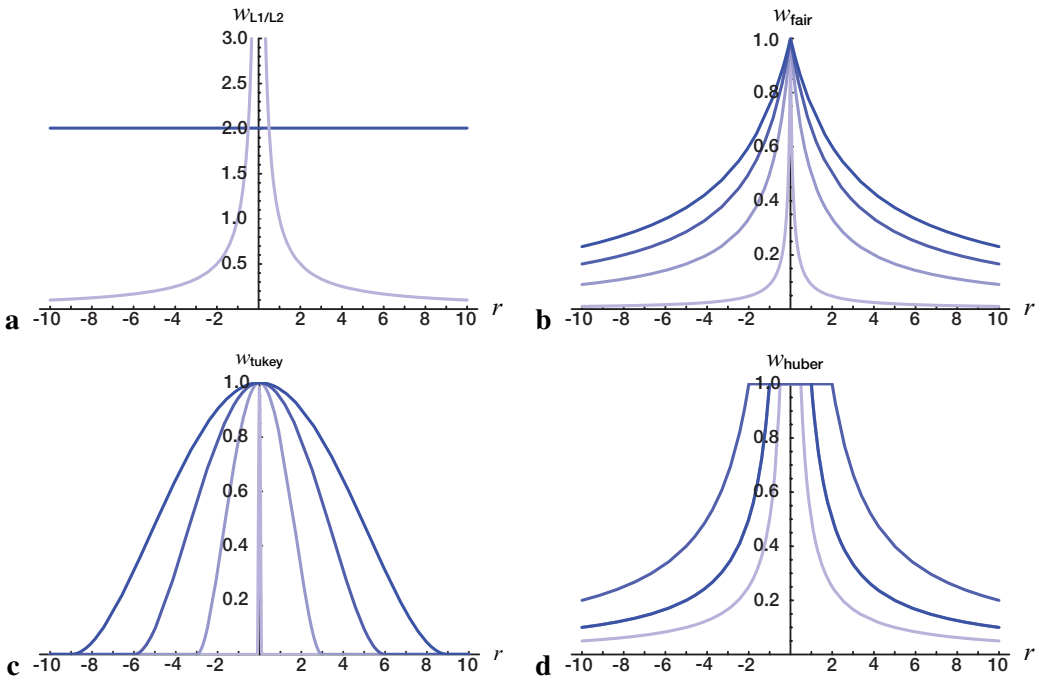

Figure 7.3: *The weight function $w(r_i)$ for the L_1 and L_2 estimator in **a** and for the Fair, Tukey and Huber estimator in **b** , **c** and **d** respectively.*

The big advantage of the M-estimator as compared to the estimators in the preceding chapter is that outlying observations can have their weights reduced depending on their residual, that is deviation from the model assumption. In an argument similar to the one in Section 6.3.2 the estimate can be derived by differentiating the minimization problem in Equation (7.2) with respect to the parameters and introducing Laplace multipliers to incorporate the boundary condition.

The minimization of Equation (7.2) leads to

$$\sum_i \psi(r_i)\frac{\partial r_i}{\partial p_j}, \quad \text{for} \quad j = 1, \ldots, p, \tag{7.3}$$

where the *influence function* $\psi(r_i)$ is defined as

$$\psi(r_i) = \frac{\partial \rho(r_i)}{\partial r_i}. \tag{7.4}$$

A plot of the most commonly used influence functions can be seen in Figure 7.2 with the corresponding ρ and influence functions given in Table 7.1.

The M-estimation problem can be solved in an iterative *weighted total least squares* approach (see Section 6.3.3), which can be shown by setting

$$\sum_i \rho(r_i) = \sum_i w_i (r_i)^2. \tag{7.5}$$

The minimization is conducted by taking the derivatives on both sides and setting the results to zero

$$\sum_i \psi(r_i) = 2 \sum_i w_i r_i \equiv 0. \tag{7.6}$$

Type	$\rho(r,\sigma)$	$\psi(r,\sigma)$	Reference
L_1	$\lvert r\rvert$	$\operatorname{sign}(r)$	
L_2	$\frac{1}{2}r^2$	r	
L_p	$\frac{1}{\sigma}\lvert r\rvert^\sigma$	$\operatorname{sign}(r)\lvert r\rvert^{\sigma-1}$	Ronner [1977]
Cauchy	$\frac{\sigma}{2}\ln\left(1+\left(\frac{r}{\sigma}\right)^2\right)$	$\frac{r}{(1+r^2)^2}$	Rey [1983]
Huber for $\lvert r\rvert\le\sigma$ / for $\lvert r\rvert>\sigma$	$\frac{1}{2}r^2$ / $\sigma\left(\lvert r\rvert-\frac{\sigma}{2}\right)$	r / $\sigma\operatorname{sign}(r)$	Huber [1964, 1972]
Tukey for $\lvert r\rvert\le\sigma$ / for $\lvert r\rvert>\sigma$	$\frac{\sigma^2}{6}\left[1-\left(1-\left(\frac{r}{\sigma}\right)^2\right)^3\right]$ / $\frac{\sigma^2}{6}$	$r(\sigma^2-r^2)^2$ / 0	Beaton and Tukey [1974]
Fair	$\sigma^2\left(\frac{\lvert r\rvert}{\sigma}-\ln\left(1+\frac{\lvert r\rvert}{\sigma}\right)\right)$	$\frac{\sigma\cdot\lvert r\rvert}{\sigma+\lvert r\rvert}$	Rey [1983]

Table 7.1: *Some of the most widely used influence functions for M-Estimators.*

The expression for the weights is then given be simplifying the above equation:

$$w_i = \frac{1}{r_i}\psi(r_i). \tag{7.7}$$

The weights for a few of the estimators from Table 7.1 is shown in Figure 7.3. From these plots it becomes apparent that the L_2 estimator cannot be robust, as all datums are weighted equally, regardless of their residual.

The estimation problem can thus be solved by setting initial weights to unity and employing one of the estimators presented in Chapter 6 best fit for the problem. In a next step the weights w_i are computed according to Equation (7.7) from which the corresponding weighted estimator from Chapter 6 is solved. These steps are repeated and the weights w_i further refined until some termination criterion is met, such as a fixed number of iterations or the summed square residual $|\boldsymbol{r}_2|$ drops below a threshold.

From this algorithm one potential danger of the M-estimators becomes evident. In the first step the initial values of the estimator have to be set. If these are chosen according to a non-robust estimator and are grossly inconsistent, in latter steps actual inlying datums might have their weights reduced, resulting in a wrong estimate for the sought parameters. This point is clarified by an illustration in Figure 7.4.

For adequate properties with respect to outliers there have to be certain requirements imposed on the influence function ψ and subsequently on the weights w_i:

- The first requirement is of course a bounded influence function ψ. Otherwise outliers have a significant effect on the estimate and lead to false model parameter as is the case in the L_2 estimator.
- The second is naturally the requirement of the robust estimator to be unique. This implies a unique minimum for the objective function of the parameter vector $\boldsymbol{p}$ to be minimized. This requires a convex ρ-function in its variable $\boldsymbol{r}$. Adopting the requirement of a unique minimum

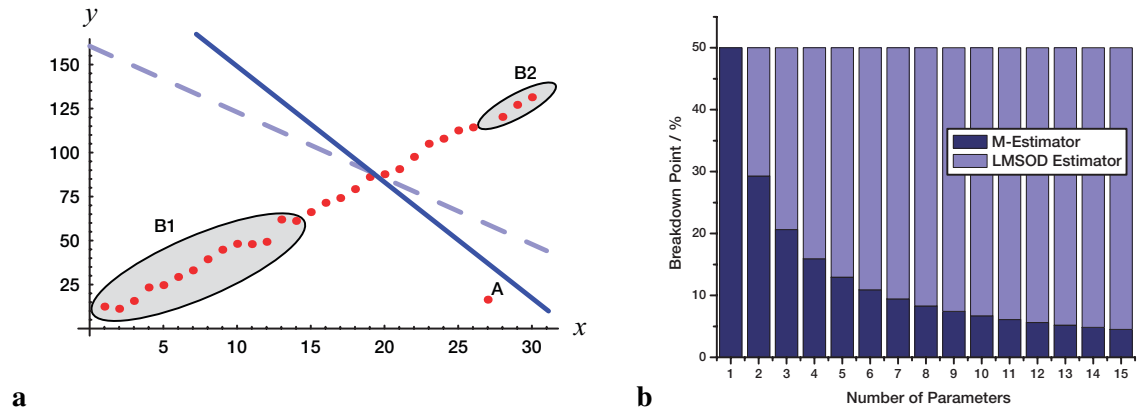

Figure 7.4: *An illustration in* ***a*** *of a configuration where the M-Estimator produces false results. Wrong initial parameters as found by a non robust estimator (dotted line) my lead the M-estimator astray and classify inliers as outliers (data in regions B1 and B2). The breakdown point of M-estimators as compared to that of the LMSOD estimator is depicted in* ***b*** *.*

for ρ is not sufficient because the convexity constraint is used, which is equivalent to imposing that $\partial^2\rho(r)/\partial r^2$ is non-negative definite.

- The third one is a practical requirement. Whenever $\partial^2\rho(r)/\partial r^2$ is singular, the objective should have a gradient, $\partial\rho(r)/\partial r \neq 0$. This avoids a search through the complete parameter space.

From these requirements on the ρ function some comments on the functions presented in Table 7.1 are in place:

- L_1 (absolute value) estimators are not stable because the ρ-function |x| is not strictly convex in x. Indeed, the second derivative at x=0 is unbounded and an indeterminant solution may result. This type of estimator reduces the influence of large errors, but they still have an influence because the influence function has no cut off point.

- L_2 (least-squares) estimators are not robust because their influence function is not bounded.

- The L_σ (least-powers) function represents a family of functions. The smaller σ, the smaller is the incidence of large errors in the estimate $\boldsymbol{p}$. It appears that σ must be fairly moderate to provide a relatively robust estimator or, in other words, to provide an estimator scarcely perturbed by outlying data. The selection of an optimum has been investigated, and for σ of around 1.2, a good estimate may be expected [Ronner, 1977]. However, many difficulties arise in the computation for the tuning parameter σ to be in the range of interest $1 < \sigma < 2$, as data with residuals of magnitude zero are troublesome.

- The *Fair function* possesses remarkable features. It will always yield a unique solution as it has continuous derivatives of the first three orders everywhere. The 95% asymptotic efficiency on the standard normal distribution is obtained with the tuning constant $\sigma = 1.3998$. The striking feature of this estimator is the relatively low sensitivity on the scaling parameter [Rey, 1983].

- *Huber's function* is a parabola in the vicinity of zero, increasing linearly at a given level $|x| > \sigma$. The 95% asymptotic efficiency on the standard normal distribution is obtained with the tuning constant $\sigma = 1.345$. This estimator produces satisfactory results on a wide range of data sets and has been recommended for almost all situations. Very rarely it has been found to be inferior to some other ρ-function [Rey, 1983]. However, from time to time difficulties are encountered, which may be due to the lack of stability in the gradient values of the ρ-function due to the discontinuous second derivative.

- *Cauchy's function*, also known as the *Lorentzian function*, does not guarantee a unique solution. With a descending first derivative, such a function has a tendency to yield erroneous solutions in a way which cannot be detected and singled out. The 95% asymptotic efficiency on the standard normal distribution is obtained with the tuning constant $\sigma = 2.3849$.

- *Tukey's biweight function* has the same shortcomings as the Cauchy function. As can be seen from the influence function, the weight of large errors is greatly reduced and outliers are suppressed. The 95% asymptotic efficiency on the standard normal distribution of the Tukey's biweight function is obtained with the tuning constant $\sigma = 4.6851$. It is this function which has been used extensively in computer vision [Black, 1992].

The break down point of M-Estimators is found to be $1 - (1/2)^{1/p}$ [Stewart, 1999]. With an increase in dimension of the parameter space the breakdown point decreases to very small values, which can be seen in Figure 7.4. For the estimation of optical flow in the context of this work the breakdown point will only be of about $16\% - 9\%$, depending on the parameterization of the optical flow field, see Section 8.2 and 8.3. This contrasts the break down point behavior of the Least-Median Squares of Orthogonal Distances (LMSOD) estimator introduced in the next section, which displays a breakdown point of 50% regardless of the dimension of the parameter space albeit with the penalty of a higher computational cost.

7.3 Least-Median Squares of Orthogonal Distances

As stated earlier the maximal theoretically achievable breakdown point is 50%. A robust estimator with this property is the concept of Least Median of Squares (LMedS), which first appeared in the statistical literature [Rousseeuw, 1984; Rousseeuw and Leroy, 1987]. It is based in concept on the Ordinary Least Squares (OLS) estimator from Section 6.2. This type of robust estimator has been used in optical flow computations successfully by Bab-Hadiashar and Suter [1997]. An extension to the principle of the TLS estimator was readily achieved by Bab-Hadiashar and Suter [1998b,c] who termed the resulting estimator Least-Median Squares of Orthogonal Distances (LMSOD), emphasizing the underlying errors in variables model. Results and properties found for the LMedS estimator are equally applicable for the LMSOD estimator.

For this estimator, the summation $\sum$ is replaced by a median, which is very robust. This estimator can be stated as follows:

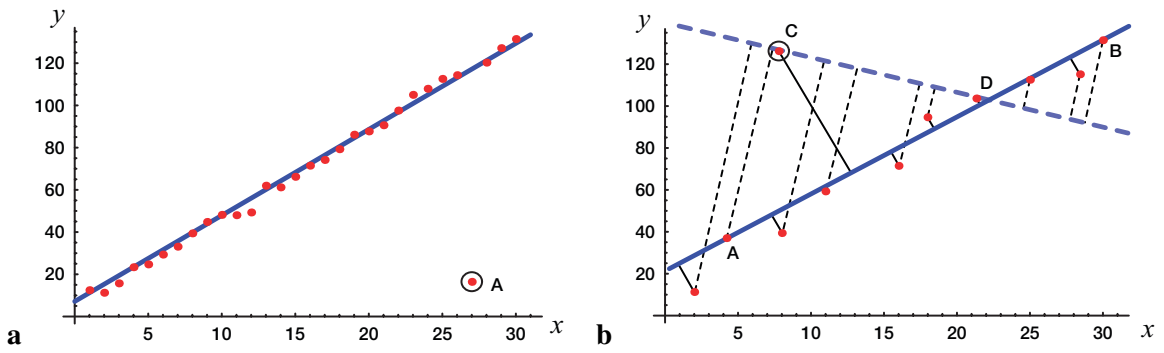

Figure 7.5: *As can be seen in* ***a*** *the robust Least-Median Squares of Orthogonal Distances estimator detects the outlier (Point A) and computes the correct parameters. An Illustration of the LMSOD estimator is shown in* ***b*** *. The solid line representing the correct estimate (connecting point A and B) has a much smaller median of squared residuals than the wrong estimate (the dotted line connecting point C and D). The wrong estimate is therefore rejected.*

Definition 9 *Given a data matrix* $\boldsymbol{D} \in \mathbb{R}^{n\times(p+1)}$*, we seek to*

$$\begin{aligned} &\textit{minimize} && \text{median}\left(\boldsymbol{r}^2\right) = \text{median}\left((\boldsymbol{Dp})^2\right), \quad \boldsymbol{p} \in \mathbb{R}^{p+1} \\ &\textit{subject to} && \boldsymbol{p}^\top \boldsymbol{p} = 1, \end{aligned} \tag{7.8}$$

with the vector of residuals $\boldsymbol{r} = \boldsymbol{Dp}$*.*

The algorithm can be described as follows. First, a subsample $D_s = (d_1, \cdots, d_p)$ of p observations is drawn, were p is equal to the number of parameters to be estimated. From such a subsample D_s, an exact solution for the parameters can be found, which is equal to solving a linear system of p equations. These exact solutions comprise the trial estimate vector $\boldsymbol{x}_s$. It is of course very likely, that these trial estimates will stray far from the sought estimate. Therefore, the residuum for this trial estimate is calculated from every observation, except those that comprise the subsample. These trial residuals make up the residuum vector $\boldsymbol{r}_s$ to a given subsample D_s. In a next step the median of the residual vector $\boldsymbol{r}_s$ is computed. The whole process is repeated for a number m of subsamples and the trial estimate $\boldsymbol{x}_{s,i}$ with the minimal med $\boldsymbol{r}_{s,i}$ retained.

Central to this estimator is the question how many subsamples J_i, $i \in (1, \ldots, m)$ one has to draw to converge to the right solution. The optimum, taking every possible subsample of size p, is not feasible in most applications, because the time complexity of such an algorithm would be very high. There are $\mathcal{O}(n^p)$ p-tuples for each of which the sorting takes $\mathcal{O}(n \log n)$ time. Further reductions in complexity are conceivable, such as approximation algorithms [Olson, 1997], which are not considered in the context of this work. The total amount of computation would thus be $\mathcal{O}(n^{p+1} \log n)$ which is far from being feasible.

The time complexity can be significantly reduced by employing a Monte Carlo type speed up scheme due to which the complexity is reduced to $\mathcal{O}(mn \log n)$. Further reductions in computational cost can be achieved by applying a linear-time median filter [Cormen et al., 1990], resulting in a cost of $\mathcal{O}(mn)$ only. The reduction in complexity is achieved by drawing a number of random selections for subsamples, such that the probability of at least one of the m subsample equating to the right

estimate is almost 1. Assuming that n/p is a large number, this probability Π is given by

$$\Pi = 1 - (1 - (1 - \epsilon)^p)^m \quad \Rightarrow \quad m = \frac{\ln(1 - \Pi)}{\ln(1 - (1 - \epsilon)^p)}, \tag{7.9}$$

where ϵ is the fraction of contaminated data. From Equation (7.9) it is clear, that we need to draw about m = 600 subsamples for an p=8 dimensional problem (which is common in affine flow with one physical parameter to be estimated), up to 50% outliers and the probability of at least one good subsample Π to be 99%. This is a relatively small number compared to sampling every possible combination of points, given by

$$m = \frac{n!}{(n-p)! \cdot p!}, \tag{7.10}$$

which would be of the same order of magnitude for only $n = 11$ data points.

The drawing of subsamples can of course be made more intelligent by selecting samples only from a small region or only those with high gradients [Ong and Spann, 1999]. In the special case of the data processed in the context of this work, the advantage of these sampling schemes was only very small and did not warrant its higher complexity and the danger of introducing additional biases.

Although being a very robust estimator as far as outliers are concerned, the LMSOD estimator has one debilitating drawback. When errors are normally distributed, LMSOD exhibits a lack of efficiency ($n^{-1/3}$ convergence). This is the big advantage of TLS and M-estimators, which are both maximum likelihood estimators under these conditions. Therefore two possibilities of increasing the efficiency exist:

1. The estimate of the LMSOD is chosen as an initial value for an M-estimator as a second step.
2. Outliers are removed from the data set by certain thresholds from the LMSOD estimation and a TLS estimator is used on the remaining observations.

In this work the second option was chosen, because the other one was not found to provide a significant improvement warranting its higher computational cost.

Detection and classification of outliers

For the detection and classification of outliers a good measure has to be found. As can be seen from Figure 7.5 the residual of outliers is much bigger than that of inliers. Because the estimator has to be applied to a wide range of possible data with different noise levels, it is not possible to threshold this residual. This is no big drawback, as the residual can be scaled with a scaling factor s that is dependent on the noise level of the data. This scaled residuum r^* can then be thresholded and outliers detected.

One possible way of calculating the scale factor is given in Rousseeuw and Leroy [1987]. First an initial scale estimate s^o is computed, according to

$$s^o = 1.4826 \cdot \left(1 + \frac{5}{n-p}\right) \sqrt{\operatorname{med} r_i^2}\,. \tag{7.11}$$

The median of the squared residuals has already been computed as it is the same value by which the final estimate was chosen. The computation of the preliminary scaling factor is thus very efficient.

The preliminary scale estimate s^o is then used to determine a weight w_i for the ith observation, that is

$$w_i = \begin{cases} 1 & \text{if } |r_i/s^o| \leq 2.5 \\ 0 & \text{otherwise} \end{cases} . \tag{7.12}$$

By means of these weights a final scale estimate S that is independent of outliers is calculated by

$$S = \sqrt{\frac{\sum_{i=1}^{n} w_i r_i^2}{\sum_{i=1}^{n} w_i - p}}. \tag{7.13}$$

With this final estimate the weights can then be recalculated according to Equation (7.12) with the final scale estimate substituted for the preliminary scale factor.

The LMSOD estimator presented in this section has one problem in common with a number of estimators with a high breakdown point. This is namely that they may "halucinate" a fit under certain conditions. This means that the estimator will always produce a fit to some part of the data, even if the statistical distribution does not suggest to do so. To address this problem Lee et al. [1998] proposed a robust estimator named the Adaptive Least K-th Order Squares (ALKS). In this technique, the estimator searches for a model which minimizes the K-th order statistics of the squared residuals where the so called optimum value for K is determined from the data. Similarly, Miller and Stewart [1996] proposed a robust estimator called the Minimum Unbiased Scale Estimator (MUSE) where the value of K is determined as the value which minimizes an unbiased scale estimate of the ordered residual. Bab-Hadiashar and Suter [1998a] tried to improve this scheme by suggesting the least K-th order statistical model fitting (LKS) estimator, which does not determine the value of K by a complex optimization routine. The drawback of these estimators is their higher time complexity, therefore they were not considered in the context of this work.

7.4 Least Trimmed Squares

As was pointed out previously the LMSOD estimator performs poorly with respect to asymptotic efficiency. This has been overcome in Section 7.3 by treating the LMSOD estimator as a means for gaining initial values for the M-estimator or detecting outliers followed by a weighted estimation from the previous chapter.

Another possible approach of addressing this lack of efficiency is through the *Least Trimmed Squares* (LTS) estimator [Rousseeuw, 1984; Rousseeuw and Leroy, 1987], which can be defined as follows:

Definition 10 *Given a data matrix $\boldsymbol{D} \in \mathbb{R}^{n\times(p+1)}$. The LTS estimator seeks to*

$$\begin{aligned} &\textit{minimize} && \sum_{i=1}^{h} \left(\boldsymbol{r}^2\right)_{i:n} = \sum_{i=1}^{h} \left((\boldsymbol{Dp})^2\right)_{i:n}, \quad \boldsymbol{p} \in \mathbb{R}^{p+1} \\ &\textit{subject to} && \boldsymbol{p}^\top \boldsymbol{p} = 1, \end{aligned} \tag{7.14}$$

with the vector of residuals $\boldsymbol{r} = \boldsymbol{Dp}$ and the ordered squared residuals $(\boldsymbol{r}^2)_{1:n} \leq \cdots \leq (\boldsymbol{r}^2)_{n:n}$.

In this approach the residuals are squared first and ordered in a second step. From the definition of the LTS estimator it becomes apparent, that this estimator is very similar to the well known OLS and TLS estimator. The only difference lies in effectively excluding outliers from the fit by not using the largest residuals in the summation. For best robustness the summation should be trimmed for $h = 1/2 * (n + p + 1)$. The breakdown point is then given by $((n - p)/2 + 1)/n$ [Rousseeuw and Leroy, 1987].

Agulló [2001] proposed a finite algorithm for computing the exact LTS regression estimate. For data sets p>5 and n> 50 the algorithm becomes computationally prohibitive and an approximate algorithm should be used. Recently, an approximate algorithm was proposed, which greatly speeds up the estimation [Rousseeuw and Van Driessen, 2000].

It has been shown that LMSOD performs slightly better in higher dimensional parameter spaces [Wisnowski et al., 2001]. Rousseeuw and Van Aelst [1999] found the LTS still suffering from higher computational cost as compared to the LMSOD estimator. For these reasons the LMSOD estimator was chosen in favor of the LTS estimator here.

7.5 Summary

In this chapter a robust extension to the parameter estimation framework introduced in Chapter 6 was presented. Following an introduction to concepts of characterizing robust estimators, a framework based on influence functions was outlined. This M-estimator allows accurate computations of parameters in the presence of some outliers with the benefit of a high asymptotic efficiency. Wrong initial values for the parameters of a higher number of outliers can however render the results of this estimator useless. The second class of estimators introduced circumvents this problem. Both, the LMSOD and LTS estimator have the maximum theoretical achievable breakdown point of 50%, however both suffer due to higher computational costs. The LMSOD estimator lacks asymptotic efficiency, which can be resolved by the methods outlined, such as identifying outliers and conducting a non robust estimation on the inliers or using the parameters of the LMSOD as initial values for an M-estimator. Due to its moderate time complexity the LMSOD is the robust estimator of choice in the context of this work, as a high breakdown point is of upmost importance.

Chapter 8

Optical Flow Computations

One of the most fundamental problems in computer vision is the measurement of *image velocity* or *optical flow* from image sequences. Optical flow is commonly described as the apparent motion of brightness patterns in an image sequence [Horn, 1986].

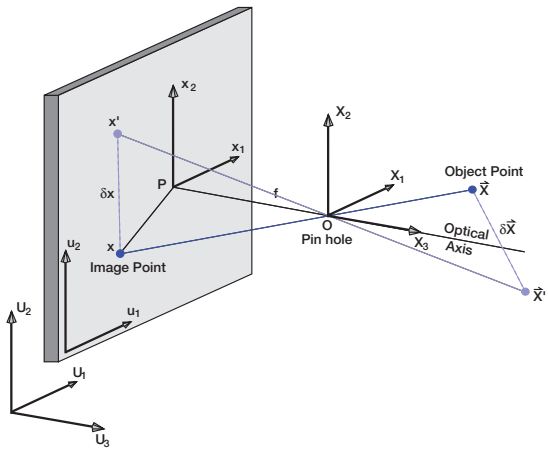

Figure 8.1: *An illustration of the connection between an optical flow translation ($\delta\boldsymbol{x}$) and the real world translation $\delta\boldsymbol{X}$ through projection in the pinhole camera model.*

It has been argued that the optical flow is in general different from the projected motion field of the scene objects [Verri and Poggio, 1987, 1989], since it is merely the projection of motions of objects relative to the imaging apparatus which is illustrated in Figure 8.1. Nevertheless, optical flow techniques have been used effectively for estimating 3D velocity fields [Vedula et al., 2000], reconstructing the 3D structure of objects [Adiv, 1985; Zhang and Faugeras, 1992; Maybank, 1993], analyzing rigid and nonrigid motion and segmenting images into regions based on their motion [Bouthemy and François, 1993; Chang, 1997; Mémin and Pérez, 1998]. Recently, optical flow computations have been successfully applied for scientific applications (eg. [Jähne, 1987, 1996; Haußecker et al., 1998]), that distinguishes themselves from common computer vision application through the requirement of a high level of accuracy [Jähne et al., 1998].

Many different methods to recover the optical flow exist [Beauchemin and Barron, 1995]. Comparisons of these with error analyses can be found in Barron et al. [1994], Mitiche and Bouthemy [1996] and Haußecker and Spies [1999]. These methods can be categorized into four groups:

1. The class of *gradient based* techniques rely on computing spatio-temporal derivatives of image intensity, which can either be first order [Fennema and Thompson, 1979; Horn and Schunk, 1981] or second order [Nagel, 1983; Tretiak and Pastor, 1984].

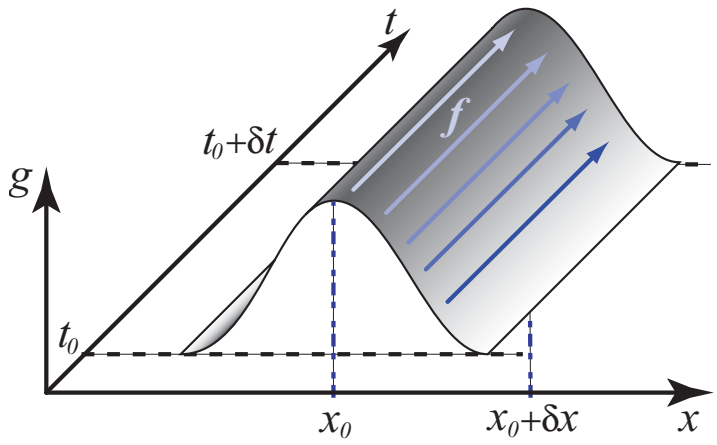

Figure 8.2: *Illustration of the brightness change constraint equation. A one dimensional grey value distribution is moved along the x-axis. During the translation from point x_0 to $x_0 + \delta x$ the grey value distribution stays the same over the period δt. This can be formulated as $dg/dt = 0$.*

2. *Region-based matching* may be employed when under certain circumstances (aliasing, small number of frames, etc.) it is inappropriate to compute derivatives of greyvalues. In this approach the velocity is defined as a shift giving the best fit between image regions at different times [Anandan, 1989; Glazer et al., 1983; Little et al., 1989].

3. Relying on the output energy of velocity-tuned filter are *energy-based methods* which are often referred to as *frequency-based methods* owing to their design in the Fourier domain [Adelson and Bergen, 1985; Heeger, 1988; Fleet, 1992].

4. Another class of methods is called *phase-based* because velocity is defined in terms of phase behavior of band-pass filter output and phase information is used for estimating the optical flow [Waxman et al., 1988; Fleet and Jepson, 1990].

In the context of this work a gradient based technique for optical flow estimation is used. Here optical flow computations are motivated by scientific applications. As such they were extended from current techniques derived in the computer sciences to parameterize the underlying physical processes. In the next few sections the application of the parameter estimation presented in the previous chapter to optical flow computations is outlined.

8.1 The Brightness Change Constraint Equation

A very common assumption in optical flow computations is the brightness change constraint equation (BCCE) [Horn and Schunk, 1981]. It is assumed that the image brightness of a scene point remains constant in a spatio-temporal neighborhood. That is the image intensity g at the location (x, y) at time t stays the same in a time interval ∂t during which a translation by $(\partial x, \partial y)$ took place. This brightness constancy model can be formulated as

$$g\left(x + \partial x, y + \partial y, t + \partial t\right) = g\left(x, y, t\right). \tag{8.1}$$

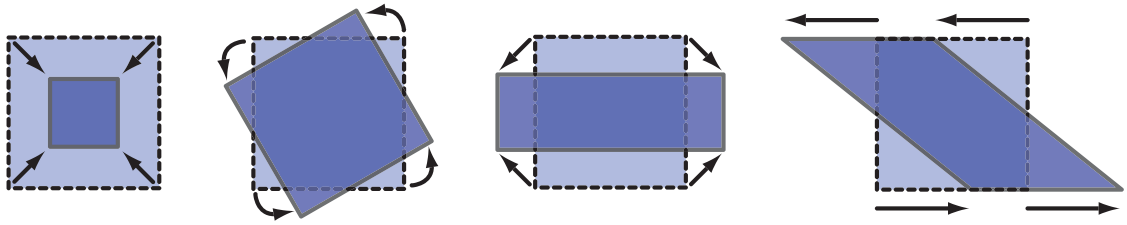

Figure 8.3: *Parameterization of affine flow model. The elementary geometric transformations of divergence, rotation, stretching and shear.*

Developing this equation up to first order in a Taylor series expansion leads to

$$g\left(x+\partial x, y+\partial y, t+\partial t\right) = g(x,y,t) + \frac{\partial g}{\partial x}\frac{\mathrm{d}x}{\mathrm{d}t}\partial t + \frac{\partial g}{\partial y}\frac{\mathrm{d}y}{\mathrm{d}t}\partial t + \frac{\partial g}{\partial t}\partial t + \mathcal{O}(\boldsymbol{f}^2). \tag{8.2}$$

The well known brightness change constraint Equation (BCCE) [Fennema and Thompson, 1979; Horn and Schunk, 1981] is then derived by simplifying Equation (8.2) and dividing by ∂t

$$\frac{dg}{dt} = \frac{\partial g}{\partial t} + \frac{\partial g}{\partial x}\frac{\mathrm{d}x}{\mathrm{d}t} + \frac{\partial g}{\partial y}\frac{\mathrm{d}y}{\mathrm{d}t} = g_t + (\boldsymbol{f}\boldsymbol{\nabla})g = 0. \tag{8.3}$$

With the optical flow $\boldsymbol{f} = (dx/dt, dy/dt)^\top = (u,v)^\top$, the spatial gradient $\boldsymbol{\nabla} g$ and the partial time derivative $g_t = \partial g/\partial t$. This formulation of the BCCE states that the image brightness $g(\boldsymbol{x},t)$ at the location $\boldsymbol{x} = (x_1, x_2)^\top$ should change only due to motion, that is, the total derivative of its brightness has to vanish, which is illustrated in Figure 8.2. Schunk [1986] and Verri and Poggio [1989] proved that this assumption holds provided that no illumination changes are present and the surface of the object are Lambertian in nature. In the following it is always assumed that the optical flow is to be computed for two dimensional data. In the case of volumetric or even higher dimensional data, the BCCE of Equation (8.3) and subsequent results can readily be extended by introducing additional terms similar to the two dimensional ones.

8.2 Parametric Models

The formulation of the BCCE in the previous section is generally only satisfied for orthographic projection and pure translational motion parallel to the scene [Beauchemin and Barron, 1995]. However, these hypotheses are not met by a number of applications which motivated the investigation of constraints applicable to a wider range of conditions. In this section the BCCE will be extended to cope with an arbitrary motion on the image plane. The prerequisite of no brightness change still holds though. This will be dropped in the subsequent section.

It is common in computer vision to model the velocity field $\boldsymbol{f}$ in a local neighborhood by an affine flow model [Black and Jepson, 1996; Farnebäck, 2000; Fleet, 1992]:

$$\boldsymbol{f} = \boldsymbol{t} + \boldsymbol{A}\boldsymbol{x} = \begin{pmatrix} t_1 \\ t_2 \end{pmatrix} + \begin{pmatrix} a_1 & a_2 \\ a_3 & a_4 \end{pmatrix} \begin{pmatrix} x \\ y \end{pmatrix}. \tag{8.4}$$

The parameters of the affine transformation matrix $\boldsymbol{A}$ can be used directly to estimate convergence and divergence of the flow field. This model is a superposition of uniform motion, rotation, dilation and shear. It is of great interest in applications such as the estimation of the flow field at the sea surface, where divergences are important parameters in sea surface gas exchange (see Section 2.4.4).

Another model used is the one propagated by Waxman and Wohn [1985]. It has been used successfully by Black and Jepson [1996] and assumes that regions of piecewise-smooth image intensities correspond to planar surfaces in a scene. The planarity of local surfaces can be extended to include 2nd order curved surfaces. This kind of model is described by 8 parameters and can be formulated as

$$\boldsymbol{f} = \boldsymbol{t} + \boldsymbol{A}\boldsymbol{x} + \boldsymbol{X}\boldsymbol{a} = \begin{pmatrix} t_1 \\ t_2 \end{pmatrix} + \begin{pmatrix} a_1 & a_2 \\ a_3 & a_4 \end{pmatrix} \begin{pmatrix} x \\ y \end{pmatrix} + \begin{pmatrix} x^2 & xy \\ xy & y^2 \end{pmatrix} \begin{pmatrix} a_5 \\ a_6 \end{pmatrix}. \tag{8.5}$$

In both Equations (8.4) and (8.5) the parameter $\boldsymbol{t} = (t_1, t_2)^\top$ represent the neighborhood center velocity whereas the a_i are 1st or 2nd order velocity derivatives.

Apart from these two motion representations a range of other models exist. Commonly used parameterizations include those that try to model 3d affine motion of planar patches under projective geometry [Tsai and Huang, 1981] or polynomial models that approximate the optical flow field by a variable number of parameters [Karczewicz et al., 1997]. A compilation of different parameterizations can be found in Stiller and Konrad [1999].

A more general parameterization of the flow field can be derived by replacing the flow vector $\boldsymbol{f}$ by a generalized transformation $\boldsymbol{S}(\boldsymbol{r}, \boldsymbol{a})$ [Haußecker et al., 1999]. In this notation $\boldsymbol{a} = (a_1, \ldots, a_p)^\top$ is the p-dimensional parameter vector and $\boldsymbol{S} = (S_1, \ldots, S_n)^\top$ an invertible transformation acting on an element $\boldsymbol{r} = (r_1, \ldots, r_n)^\top$ in the spatio-temporal space $\mathbb{R}^n$, that is

$$\boldsymbol{r} = \boldsymbol{S}(\boldsymbol{r'}, \boldsymbol{a}) \quad \text{and} \quad \boldsymbol{r'} = \boldsymbol{S}^{-1}(\boldsymbol{r}, \boldsymbol{a}). \tag{8.6}$$

The generalized transformation $\boldsymbol{S}$ is taken to be infinitely differentiable in $\boldsymbol{r}$ and analytical in $\boldsymbol{a}$. From the above properties of $\boldsymbol{S}$ and $\boldsymbol{r} = \boldsymbol{S}(\boldsymbol{r}, 0)$ it follows that $\boldsymbol{S}$ forms a one-parameter Lie group of transformations [Olver, 1986]. Therefore, the vector $\boldsymbol{r}$ can be expanded in a Taylor series about $\boldsymbol{a} = 0$ as

$$\boldsymbol{r} = \boldsymbol{r'} + \sum_{i=1}^{p} a_i \frac{\partial S(\boldsymbol{r'}, \boldsymbol{a})}{\partial a_i}. \tag{8.7}$$

Given a brightness function $g(\boldsymbol{r})$, its dependence on the transformation parameters a_i can be derived to be

$$\frac{\partial g(\boldsymbol{r})}{\partial a_i} = \sum_{j=0}^{n} \frac{\partial g}{\partial r_j} \frac{\partial r_j}{\partial a_i} = \sum_{j=0}^{n} \frac{\partial g}{\partial r_j} \frac{\partial S(\boldsymbol{r'}, \boldsymbol{a})}{\partial a_i} = \mathfrak{L}_i g(\boldsymbol{r}), \tag{8.8}$$

where Equation (8.7) was used. The infinitesimal generator of the Lie group $\mathfrak{L}_i$, $i \in \{1, \ldots, P\}$ is defined as

$$\mathfrak{L}_i = \sum_{j=0}^{n} \frac{\partial S_j}{\partial a_i} \frac{\partial}{\partial r_j}. \tag{8.9}$$

Using Equation (8.8) in expanding the brightness function $g(\boldsymbol{r})$ about $\boldsymbol{r'}$ with respect to the parameters a_i yields

$$g(\boldsymbol{r}) = g(\boldsymbol{r'}) + \sum_{i=1}^{p} a_i \frac{\partial g(\boldsymbol{r'})}{\partial a_i} = g(\boldsymbol{r'}) + \sum_{i=1}^{p} a_i \mathfrak{L}_i g(\boldsymbol{r'}) \,. \tag{8.10}$$

With the assumption of brightness conservation $g(\boldsymbol{r}) = g(\boldsymbol{r}')$ this equation reduces to the parametric brightness change constraint equation (PBCCE) given by

$$\sum_{i=1}^{p} a_i \mathfrak{L}_i g(\boldsymbol{r}') = (\mathfrak{L}g)^\top \boldsymbol{a} = 0, \quad \text{with} \quad (\mathfrak{L}g) \in \mathbb{R}^p, \boldsymbol{a} \in \mathbb{R}^p. \tag{8.11}$$

This equation is similar to the traditional BCCE where the spatiotemporal gradient is replaced by the p-dimensional vector of Lie derivatives $\mathfrak{L}g = (\mathfrak{L}_1 g, \ldots, \mathfrak{L}_p g)^\top$. It can easily be shown that the PBCCE reduces to the BCCE for the case of constant translation $\boldsymbol{S}(\boldsymbol{r}, \boldsymbol{a}) = \boldsymbol{r} + \boldsymbol{a}$ with the translation vector $\boldsymbol{a} = (\delta x, \delta y, \delta t)^\top$ and the resulting generators $\mathfrak{L}_1 = \partial/\partial x$, $\mathfrak{L}_1 = \partial/\partial y$ and $\mathfrak{L}_1 = \partial/\partial t$. Also the affine transformation of Equation (8.4) as a special case of this PBCCE can be verified straightforwardly by noting that $\boldsymbol{S}(\boldsymbol{r}, \boldsymbol{a}) = \boldsymbol{A}\boldsymbol{r} + \boldsymbol{t}$ with $\boldsymbol{a} = (a_1, \ldots, a_4, t_1, t_2, 1)^\top$. The infinitesimal generators can then be derived as $\mathfrak{L}_1 = x\partial/\partial x$, $\mathfrak{L}_2 = y\partial/\partial x$, $\mathfrak{L}_3 = x\partial/\partial y$, $\mathfrak{L}_4 = y\partial/\partial y$, $\mathfrak{L}_5 = \partial/\partial x$, $\mathfrak{L}_6 = \partial/\partial y$ and $\mathfrak{L}_7 = \partial/\partial t$. The presented parameterization by Lie groups has previously been successfully used for estimating the optical flow [Duc, 1994, 1997]. This formulation has some practical advantages as a number of transformations can be invariantly decomposed, such as the optical flow induced by perspective projection onto the image plan with added camera rotation [Kanatani, 1990].

The use of parametric models on a local neighborhood raises the question which model describes the local flow field best. An important factor is of course the size of the neighborhood, as in a very small domain a constant flow model might suffice while in expanding the neighborhood the parameterization of the optical flow will need to be more and more refined.

There are different solutions to the problem at hand. One was proposed by Ng and Solo [1998] and tries to find the optimal neighborhood size to a given parameterization. On the other hand, given a certain size of the neighborhood it is of interest to find the best parameterization. A viable approach is the variable-order fitting technique [Besl and Jain, 1988], where first the pure translational model $\boldsymbol{S}(\boldsymbol{r}, a) = \boldsymbol{r} + \boldsymbol{a}$ is fitted to the image grey values. In subsequent computations more and more complex models are used. For example, first the affine model of Equation (8.4) could be fitted, followed by the surface model of Equation (8.5). Finally the model with the smallest resulting residuals is adopted [Besl and Jain, 1988; Black and Jepson, 1996]. A statistically more sound approach would be to perform full multivariate confidence tests such as the F-test introduced in Section 6.7, rather than just taking the actual residual into account.

8.3 The Extended Brightness Model

The BCCE as well as its extension to the parameterized BCCE from the previous section do not take brightness variations into account. As such they are only applicable to situations of uniform illumination with motion parallel to the scene, as motion towards to or away from the imaging apparatus would change its image intensity according to the *inverse square law* [Haußecker, 1999]. First steps in solving this constraint were undertaken by Nagel [1989] who suggested that the BCCE should be explicitly based on geometric properties of the 3D scene,

$$g_t(\boldsymbol{x}, t) + \boldsymbol{f} \cdot \boldsymbol{\nabla} g(\boldsymbol{x}, t) = 4g(\boldsymbol{x}, t) \left(\frac{\boldsymbol{z}^\top \dot{\boldsymbol{r}}}{\boldsymbol{z}^\top \boldsymbol{r}} - \frac{\boldsymbol{r}^\top \dot{\boldsymbol{r}}}{||\boldsymbol{r}^\top \dot{\boldsymbol{r}}||} \right), \tag{8.12}$$

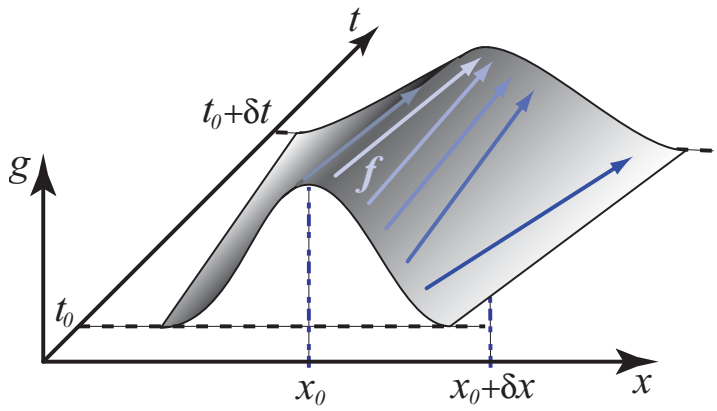

Figure 8.4: *Illustration of the brightness change constraint equation. A one dimensional grey value distribution is moved along the x-axis. During the translation from point x_0 to $x_0+\delta x$ the grey value distribution is changed according to a diffusion process. The BCCE estimates the optical flow f incorrectly.*

where $\boldsymbol{r}$ is a 3D point in world coordinates, $\dot{\boldsymbol{r}}$ is its 3D velocity and $\boldsymbol{z}$ is a unit vector along the line of sight. The drawback of this equation is that it assumes explicit knowledge of the scene geometry, which can be impractical or even impossible to obtain.

In medical magnetic resonance (MR) image sequences the brightness also changes making the BCCE inapplicable. Prince and McVeigh [1992] derived the *variable brightness optical flow* equation by modelling intensity changes over time as a function of MR parameters, motion and initial magnetically induced tag pattern.

Another approach was to allow for linear transformations of the image greyvalues over time and thus introduce a constant term c in the BCCE [Negahdaripour and Yu, 1993]:

$$g_t(\boldsymbol{x},t) + \boldsymbol{f} \cdot \boldsymbol{\nabla} g(\boldsymbol{x},t) = c. \tag{8.13}$$

This equation allows accurate optical flow computations under nonuniform illumination [Nomura et al., 1995a] or in scenes with a moving light source [Haußecker and Fleet, 2001]. It has also been successfully applied for optical flow computations in range data, that is on images where distances to the imaging system are coded as greyvalues [Spies, 2001; Barron and Spies, 2001].

An extension of this constraint equation was introduced by Zhang et al. [1999] who generalized it to include terms to take care of spatially non-uniform illumination, resulting in

$$g_t(\boldsymbol{x},t) + \boldsymbol{f} \cdot \boldsymbol{\nabla} g(\boldsymbol{x},t) = w(\boldsymbol{x},t) \cdot g(\boldsymbol{x},t), \tag{8.14}$$

where $w(\boldsymbol{x},t) = \alpha q(\boldsymbol{x}) + w(t)$ is a function incorporating effects due to spatially and temporally non-uniform illumination ($q(\boldsymbol{x})$ and $w(t)$ respectively). For added flexibility a weighting parameter α is introduced.

In order to cope with diffusion processes due to image blurring in addition to varying illumination Nomura et al. [1995b] and Nomura [2000] extended the BCCE to the *generalized basic constraint equation* given by

$$g_t(\boldsymbol{x},t) + \boldsymbol{f}\boldsymbol{\nabla} g(\boldsymbol{x},t) = \boldsymbol{\nabla} \cdot (D\boldsymbol{\nabla} g(\boldsymbol{x},t)) + c, \tag{8.15}$$

where D is a diffusion coefficient and c the rate of brightness generated at a pixel. This constraint equation proved to estimate the optical flow to a higher accuracy than the basic BCCE. An illustration of this equation is presented in Figure 8.4.

In the context of this work the processes imaged change the image brightness according to the underlying physical processes. Rather than just extending the BCCE in order to gain more accurate optical flow fields under changing illumination, the parameter of intensity change have a significant physical meaning. This is the case in heat flux measurements at the sea surface [Garbe et al., 2001a] or in quantifying water transport and heat transfer in plant leaves [Garbe et al., 2002].

In order to make the technique presented in the context of this work applicable to a wide range of scientific applications, a more general extension of the BCCE is chosen [Haußecker et al., 1999; Garbe et al., 2001b]. The brightness of a moving pattern is allowed to change according to an analytical function h, that is

$$g(\boldsymbol{x}) = h(g'(\boldsymbol{x}), \boldsymbol{b}), \quad \text{and} \quad g'(\boldsymbol{x}) = h^{-1}(g(\boldsymbol{x}), \boldsymbol{b}), \tag{8.16}$$

where $h(g(\boldsymbol{x}), \boldsymbol{b})$ is a scalar invertible transformation with the q-dimensional parameter vector $\boldsymbol{b} = (b_1, \ldots, b_q)^\top$ and the identity element $h(g(\boldsymbol{x}), 0) = g(\boldsymbol{x})$. In the case of h being analytical with respect to $\boldsymbol{b}$ the brightness variation can be expanded into a Taylor series around $\boldsymbol{b} = 0$, hence

$$g(\boldsymbol{r}) = g'(\boldsymbol{r}) + \sum_{k=1}^{q} b_k \frac{\partial h}{\partial b_k}. \tag{8.17}$$

A generalization of the BCCE, in the following referred to as GBCCE, can be derived by making use of this equation together with Equation (8.10)

$$\begin{aligned} g'(\boldsymbol{x}) - g'(\boldsymbol{x}') &= \sum_{i=1}^{p} a_i \mathfrak{L}_i g(\boldsymbol{x}') \\ \Leftrightarrow\ g(\boldsymbol{x}) - g'(\boldsymbol{x}') &= \sum_{i=1}^{p} a_i \mathfrak{L}_i g(\boldsymbol{r}') - \sum_{k=1}^{q} b_k \frac{\partial h}{\partial b_k} = 0. \end{aligned} \tag{8.18}$$

For the special case of constant brightness ($\boldsymbol{b} = 0$) this equation reduces to the PBCCE from Equation (8.11). In the derivation of Equation (8.18) $g(\boldsymbol{r}) = g'(\boldsymbol{r}')$ is used, which is due to the fact that the initial brightness g shifted from $\boldsymbol{r}$ to $\boldsymbol{r}'$ leads to the primed brightness g' at $\boldsymbol{r}'$.

Equation (8.18) can of course be written in vector notation, reducing to

$$\boldsymbol{d}^\top \boldsymbol{p} = 0, \quad \text{with} \quad \boldsymbol{d} \in \mathbb{R}^{p+q}, \boldsymbol{p} \in \mathbb{R}^{p+q}, \tag{8.19}$$

with the data term $\boldsymbol{d} = \left((\mathfrak{L}g)^\top, (\boldsymbol{\nabla}_b h)^\top\right)^\top$ and the parameter vector $\boldsymbol{p} = (\boldsymbol{a}^\top, -\boldsymbol{b}^\top)^\top$, where $\boldsymbol{\nabla}_b$ represents the gradient with respect to the parameters $\boldsymbol{b}$.

With the formulation of the generalized brightness change constraint Equation (8.19) it is now possible to estimate reliable optical flow in applications where the BCCE failed due to its limitations. Moreover, in scientific applications the image intensity change might be due to physical phenomena, the parameters of which can be estimated reliably from Equation (8.19). Examples of this new field of problems will be presented in Section 8.8.

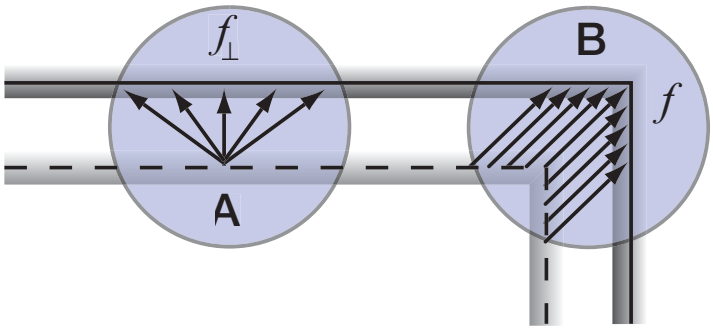

Figure 8.5: *The aperture problem illustrated by a moving edge. The edge is moved from the initial (dotted line) to the final location (solid line). In the neighborhood* **A** *an aperture problem is present and only the minimum norm solution* $\boldsymbol{f}_\perp$ *in the direction of the gradient can be estimated. In the neighborhood* **B** *enough structure (corner) is present to estimate the full flow* $\boldsymbol{f}$*.*

8.4 The Aperture Problem

Mathematically the BCCE poses an ill posed problem as there exists only one equation for the two unknowns u and v of the optical flow $\boldsymbol{f}$. However, from this one equation the motion component $\boldsymbol{f}_\perp$ in the direction of the local gradient can be estimated, an incident known as the *aperture problem* [Ullman, 1979]. It is given from Equation (8.3) as

$$\boldsymbol{f}_\perp = -\frac{g_t(x,y,t)\boldsymbol{\nabla} g(x,y,t)}{||\boldsymbol{\nabla} g(x,y,t)||_2^2}, \tag{8.20}$$

where g_t is the partial derivative of the image intensity with respect to time. This expression is equivalent to the minimum norm solution to the nongeneric TLS problem presented in Equation (6.22).

To solve the BCCE for the two parameters of the optical flow different methods have been successfully applied. Through a regularization framework the ill posed problem can be solved [Lai and Vemuri, 1998]. Assuming that the optical flow changes slowly from point to point global regularization schemes as introduced by Horn and Schunk [1981]. It can be formulated as

$$\int_D \left((\boldsymbol{\nabla} g \cdot \boldsymbol{f} + g_t)^2 + \lambda^2 \left(\boldsymbol{\nabla} \boldsymbol{f}\right)^\top \left(\boldsymbol{\nabla} \boldsymbol{f}\right) \right) \mathrm{d}\boldsymbol{x}, \tag{8.21}$$

where $\boldsymbol{x} = (x, y)$, $\boldsymbol{\nabla} \boldsymbol{f} = (\partial u/\partial x, \partial v/\partial y)^\top$ and λ is a parameter that controls the smoothness of the optical flow $\boldsymbol{f}$. The solution of $\boldsymbol{f}$ is given as a set of Gauss-Seidel equations which are solved iteratively through standard numerical routines. By employing multiscale stochastic algorithms the regularization scheme of Equation (8.21) can be solved non-iteratively with the added benefit of gaining confidence measures in terms of multiscale error covariance statistics [Luettgen et al., 1994].

Another approach for solving the aperture problem can be derived by differentiating the BCCE and thus gaining equations with second order intensity derivatives [Nagel, 1983, 1987; Tretiak and Pastor, 1984]. An equation of this form is given by [Uras et al., 1988]

$$\left(\boldsymbol{\nabla}\boldsymbol{\nabla} g(\boldsymbol{x}, t)\right) \boldsymbol{f}^\top = -\boldsymbol{\nabla} g_t(\boldsymbol{x}, \boldsymbol{t}). \tag{8.22}$$

This equation results in an analytical expression for both components of $\boldsymbol{f}$ at a single point. It should be noted however, that in order to compute the second derivative the region of support is larger than the region of support for first order derivatives. The computation of second order derivatives thus represents in effect a local neighborhood with the size of the region of support. Above that the Equation (8.22) is a much stronger constraint than the BCCE of Equation (8.3) in that first order deformations of intensity such as rotation or dilation are not permissable [Barron et al., 1994].

The aperture problem can be solved by another approach introduced by Lucas and Kanade [1981] and Lucas [1984]. Here the motion patterns are assumed to be constant in a local neighborhood. The optical flow problem can then be solved using a weighted ordinary least squares estimator (see Section 6.3.3)

$$\text{minimize } ||\boldsymbol{e}||_2^2 = \sum_{\boldsymbol{x}\in\mathcal{N}} w(\boldsymbol{x}) \left(\boldsymbol{\nabla} g(\boldsymbol{x},t)\cdot\boldsymbol{f} + g_t(\boldsymbol{x},t)\right)^2, \tag{8.23}$$

where $w(\boldsymbol{x})$ denotes a window function, $\mathcal{N}$ the local spatial neighborhood and $\boldsymbol{e}$ is the residual of the fit. In practical applications the window function w is realized by a Gaussian smoothing kernel, although different weighting functions are conceivable such as those outlined in Section 7.2. Generally the gradients of image intensity will be erroneous which introduces a bias in the estimation via OLS (see Section 6.2). Thus it is preferable to solve the system of linear Equations (8.23) in the weighted total leas squares framework of Section 6.3.3 [Chu and Delp, 1989]. This approach of solving the aperture problem in a local neighborhood is of course only viable if enough intensity structure is present in the neighborhood. If for example all gradients are parallel to one another, still only the component of the optical flow in the direction of this gradient can be computed following Equation (8.20). This problem is illustrated in Figure 8.5. It is important for optical flow computations to detect these regions where the aperture problem could not be solved and treat the solution accordingly. By using the estimators based on the total least squares principle introduced in Chapter 6, a measure for the aperture problem is available. Without enough intensity structure in the neighborhood the data matrix will be rank deficient and hence no unique solution can be found. In this case the nongeneric solution can be estimated as outlined in Section 6.3.1. The analogy between the aperture problem in optical flow computations and the nongeneric case in parameter estimation becomes apparent by comparing the two Equations (6.22) and (8.20), which are equivalent.

The results for computing the optical flow from Equation (8.23) can be stabilized and made more accurate by not only considering a spatial neighborhood $w(\boldsymbol{x})$ but also taking temporal information into account [Jähne, 1993, 1997]. This is the approach chosen in this work to solve the problem of optical flow estimation.

8.5 Estimating the Optical Flow

As outlined in the previous sections there exist a number of different methods to compute the optical flow. In the context of this work a gradient based technique was chosen which is based on the introduced generalized brightness change constraint Equation (8.19). The aperture problem is circumvented by assuming motion patterns to be constant on a local neighborhood. Depending on the size of this local spatio-temporal neighborhood $\mathcal{N}$ the model GBCCE is extended into an over determined

set of linear Equations. From Equation (8.19) this set is given by

$$\begin{pmatrix} (\mathfrak{L}g)_1^\top & (\boldsymbol{\nabla}_b h)_1^\top \\ (\mathfrak{L}g)_2^\top & (\boldsymbol{\nabla}_b h)_2^\top \\ \vdots & \vdots \\ (\mathfrak{L}g)_n^\top & (\boldsymbol{\nabla}_b h)_n^\top \end{pmatrix} \cdot \begin{pmatrix} \boldsymbol{a} \\ -\boldsymbol{b} \end{pmatrix} = \boldsymbol{D} \cdot \boldsymbol{p} = 0, \quad \text{with} \quad \boldsymbol{D} \in \mathbb{R}^{n \times (p+q)},\ \boldsymbol{p} \in \mathbb{R}^{p+q}\,, \tag{8.24}$$

where the subscript denotes the location in the spatio-temporal neighborhood in lexicographical ordering. The number of pixels in the neighborhood $\mathcal{N} \in \mathbb{R}^{i \times j \times k}$ is given by $n = i \cdot j \cdot k$. The elements of the parameter vector $\boldsymbol{p}$ obviously depend on the chosen model of the optical flow.

Depending on the application at hand different estimators can be chosen to compute the optical flow problem from Equation (8.24). Introduced in Section 6.3.2 was the estimation of a system of linear equation by formulating the total least squares problem by normal equations. This represents the commonly used method of computing the optical flow by a structural tensor approach [Bigün et al., 1991; Nagel and Gehrke, 1998; Haußecker and Spies, 1999]. The structural tensor $\boldsymbol{J}$ for the GBBCE from Equation (8.24) is defined as

$$\boldsymbol{J} = \boldsymbol{W}\boldsymbol{D}^\top\boldsymbol{D} = \begin{pmatrix} J_{1,1} & J_{1,2} & \cdots & J_{1,(p+q)} \\ J_{2,1} & J_{2,2} & \cdots & J_{2,(p+q)} \\ \vdots & \vdots & \ddots & \vdots \\ J_{(p+q),1} & J_{(p+q),2} & \cdots & J_{(p+q),(p+q)} \end{pmatrix} \quad \text{with} \quad \boldsymbol{J} \in \mathbb{R}^{(p+q)\times(p+q)}. \tag{8.25}$$

From this definition it becomes apparent that $\boldsymbol{J}$ is a symmetric positive definite tensor, thus $J_{i,j} = J_{j,i}$.

The big advantage of this formulation is that the elements of $\boldsymbol{J}$ can be computed quite efficiently with digital image processing techniques. They are given by

$$J_{i,j} = \int_{-\infty}^{\infty} w(\boldsymbol{x} - \boldsymbol{x}') D_{i,j} \cdot D_{j,i}\, \mathrm{d}\boldsymbol{x}', \tag{8.26}$$

with the weighting function $w(\boldsymbol{x} - \boldsymbol{x}')$ which defines the spatio-temporal neighborhood where the parameters are to be estimated. In computer vision it is common to use a Gaussian kernel for this function, although additional weights from equilibration (cf Section 6.1) or depending on the residual of the fit (see Section 7.2) might be introduced. Therefor the summation and multiplication with $w(\boldsymbol{x}-\boldsymbol{x}')$ can be computed by a smoothing operator which is essentially a convolution with a binomial mask. The multiplication with additional weights might be necessary. The components of $\mathfrak{L}g$ and $\boldsymbol{\nabla}_b h$ will generally be some functions of the image intensities or their spatio-temporal derivatives. These derivatives can be computed quite efficiently with differential operators, such as convolution with the Sobel or the optimized Sobel operator [Scharr, 2000].

Although ease of implementation with standard image processing convolutions are to the advantage of the solution to the optical flow problem with the structure tensor, it has some drawbacks. In the context of this work often the parameterization with a constant translation $\boldsymbol{S}(\boldsymbol{r}, a) = \boldsymbol{r} + \boldsymbol{a}$ with the translation vector $\boldsymbol{a} = (\delta x, \delta y, \delta t)^\top$ is used. The brightness change is taken to be linear (see Section 8.8.1) thus $h(g(\boldsymbol{x}), \boldsymbol{b}) = c \cdot \boldsymbol{b}$, which corresponds to the optical flow model propagated by Negahdaripour and Yu [1993]

$$g_t(\boldsymbol{x}, t) + \boldsymbol{f}\boldsymbol{\nabla} g(\boldsymbol{x}, t) - c = (-1, g_x, g_y, g_t) \cdot (c, u, v, 1)^\top = 0, \tag{8.27}$$

with the optical flow $\boldsymbol{f} = (u, v)^\top$. This equation can be interpreted as an intersect model analogous to the one in Section 6.5.

As the first column in the data matrix is known exactly (it has the value -1), the TLS estimator will compute suboptimal results. For this type of model the mixed OLS-TLS estimator or the GTLS estimator are the estimators of choice. However, they can not be applied to the structure tensor $\boldsymbol{J}$ from Equation (8.25) as in this formulation the perturbed and exactly known elements are mixed through the outer product. Therefore the formulation of normal equations $\boldsymbol{J} \propto \boldsymbol{D}^\top \boldsymbol{D}$ is not used in the context of this work but the estimators presented in Section 6 are used to computed the optical flow from the data matrix $\boldsymbol{D}$ in Equation (8.24) directly. Further advantages of this formulation have been discussed in Section 6.3.5. In this framework an extension to robust statistics as introduced in Section 7 can also be achieved more efficiently.

8.6 Characterizing Good Estimates

Apart from estimating the actual parameters of Equation (8.24) it is of equal importance to compute a confidence measure of the parameters. This confidence measure w_c should be close to one when good estimates are available and zero when problems in the estimation were detected such as the model assumption of the parameter estimation being violated by the actual data. To achieve this goal two threshold values τ_1 and τ_2 are introduced [Spies et al., 1999]. In the following the singular values of $\boldsymbol{D}$ are assumed to be sorted in ascending order:

$$\lambda_1 \leq \lambda_2 \leq \cdots \leq \lambda_{p+q}. \tag{8.28}$$

The structure tensor $\boldsymbol{J}$ can be thought of as the covariance matrix of the data matrix $\boldsymbol{D}$. Its trace is therefore simply the sum of the variances of its components. As outlined in Section 6.3.5 prior to the SVD of the matrix $\boldsymbol{D}$ a QR-decomposition is performed and the singular values of the diagonal matrix $\boldsymbol{R}$ computed. The trace of the matrix $\boldsymbol{R}$ has the analogous meaning as that of the structure tensor $\boldsymbol{J}$. However, it does not represent the sum of variances but instead is proportional to the sum of the squared variances which is equivalent to the sum of standard deviations of the data matrix.

When there is not enough variation in the data it does not make sense to try to compute any parameters. Thresholding the trace of $\boldsymbol{R}$ by τ_1 will therefore speed up the estimation significantly as the trace of a matrix is invariant under coordinate transforms so that it can be computed prior to the actual eigenvalue analysis. This will be the case in image sequences with considerable uniform areas, such as a background for instance. The choice of this threshold parameter is not very critical as its main objective is to speed up the estimation by excluding uniform areas.

The smallest singular value λ_0 directly provides the residual of the parameter estimation, as can be seen from Equation (6.20). If the model assumption fits the data exactly this singular value is equal to zero in the absence of noise or numerical errors. Therefore this singular value is used to reject unreliable estimates and defines a normalized confidence measure w_c. By introducing another threshold parameter τ_2 the estimate can be rejected if $\lambda_0 > \tau_2$. The confidence measure can then be

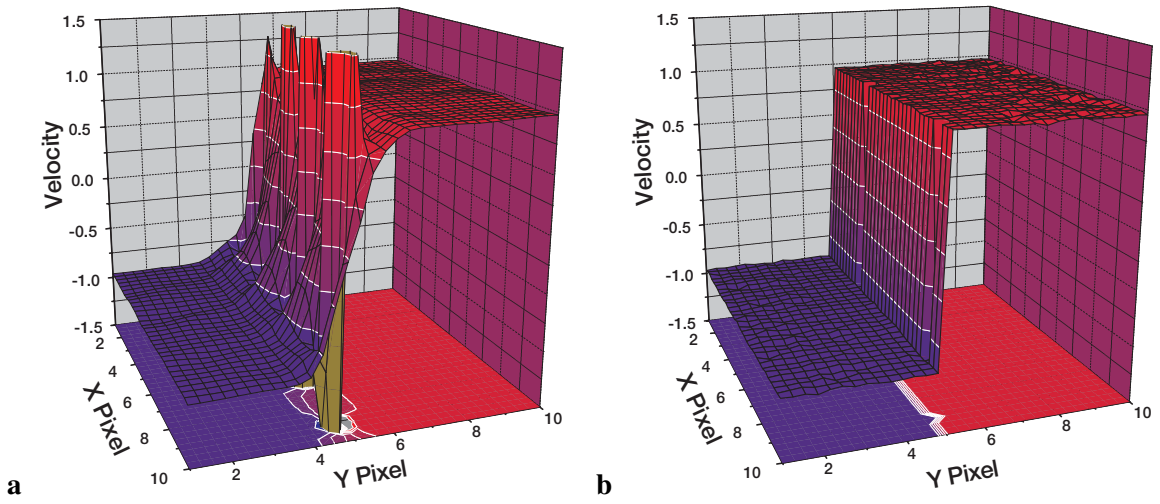

Figure 8.6: *The u component of the optical flow at a motion discontinuity with moderate noise. The computation based on TLS in* ***a*** *smoothes over the edge and produces wrong estimates while the robust estimation in* ***b*** *produces correct results.*

defined as a measure of how close λ_0 came to the threshold, that is

$$w_c = \begin{cases} 0 & \text{if} \quad \lambda_0 > \tau_2 \quad \text{or} \quad \text{trace}(\boldsymbol{R}) < \tau_1 \\ \left(\frac{\tau_2 - \tau_n}{\tau_2 + \tau_n}\right)^2 & \text{else.} \end{cases} \tag{8.29}$$

In the context of this work we characterize the quality of the TLS estimation simply by the residual. For a more thorough analysis one needs to extract covariance matrices for the estimated parameter as explained in Section 6.3.4.

8.7 Robust Optical Flow

It has been argued in Chapter 7 that the estimators presented in Chapter 6 only converge to the true parameter vector in the absence of outliers. In a host of scientific application data are corrupted by such outliers, a matter of facts to which the optical flow computation presented in this chapter poses no exception. The concept of robust estimators has been successfully applied to computer vision by Meer et al. [1991], Black and Anandan [1991], Black [1992], Black and Rangarajan [1996], Black et al. [2000], Stewart [1999] and Bab-Hadiashar and Suter [1997, 1998c]. In the context of this work the importance of employing robust estimation schemes becomes apparent. In Figure 8.6 the significant improvement of robust optical flow compared to standard optical flow is shown at a motion discontinuity. Such motion discontinuities might appear in image data in the presence of multiple moving bodies or might be due to pixel errors which are quite common in infrared imagery. Not only smoothes the non-robust estimation over the discontinuity, but also large errors in the estimation are present in close proximity to the edge. In field data presented in Chapter 12 reflexes at the sea surface are always present. By employing a high breakdown point scheme the effect of such reflexes are greatly suppressed and can be segmented by an outlier analysis. Optical flow computations in imagery corrupted by reflexes is shown in Figure 8.7.

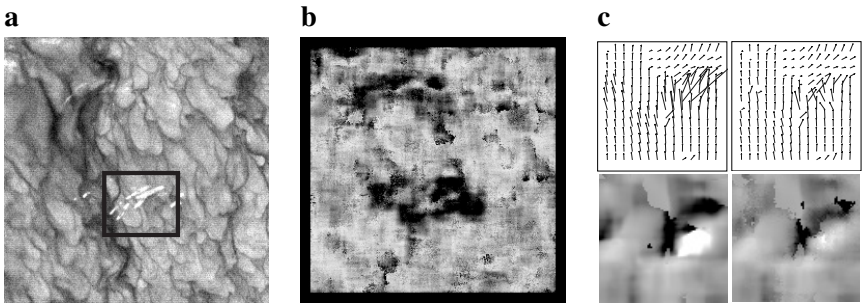

Figure 8.7: ***a)*** *An image from an IR-sequence,* ***b)****The number of weights as computed by LMSOD. Black areas indicate fewer weights which corresponds to reflexes.* ***c)*** *The flow field and the linear parameter for TLS and LMSOD inside the box in* ***a****. Black regions indicate where no parameters could be estimated.*

As was pointed out in Chapter 7 non of the robust estimators presented in this work are significantly better in all important aspects for characterizing robust estimators as introduced in Section 7.1. Generally a desirable high breakpoint has to be paid with a lower efficiency or higher computational cost. For that reason no general recommendation on any of the estimators can be made, but only their main characteristics outlined and the conditions under which they were applied in the context of this work.

Generally speaking, whenever only a small fraction of the data is corrupted by outliers and there is no problem with retrieving an initial, non-robust estimate, the M-estimator presented in Section 7.2 is the estimator of choice. This prerequisite turned out to be too limiting for the application considered in the context of this work. Moreover a high breakdown point at moderate computational cost was needed which was the reason for employing the LMSOD estimator introduced in Section 7.3. The efficiency of this estimator was increased by performing a weighted mixed OLS-TLS or, for known correlations in the data, a weighted GTLS estimation on the weights computed according to Section 7.3. The LTS sketched in Section 7.4 proved to be computational too complex with only minute improvements on the estimation, which limited its appeal.

8.7.1 Multiple Motion

The accurate detection of multiple motions in image sequences is difficult due to the distinct circumstances under which this type of motion might occur. Bergen et al. [1992] and Shizawa and Mase [1991] extended the BCCE to accommodate multiple motions, while for the detection of transparent motion a completely different framework is needed, such as one based on local phase information [Fleet and Jepson, 1990]. In this Section a simplistic approach is chosen to outline the value of robust optical flow estimations. It will of course only produce correct estimates for special cases, as it is not an approach as general as those presented by the cited authors.

Using a robust estimator exhibiting a high breakdown point of 50%, it is possible to detect certain cases of multiple motions iteratively. First, the dominant motion is detected, while data stemming from the other motions are viewed as outliers. Iteratively the observations processed for the motion are excluded from further analysis and the motion detection repeated, until a fixed number of motions have been accounted for or until no apparent motions are detectible in the remaining data. To illustrate this procedure two motions together with the parameters are plotted in Figure 8.8. This algorithm

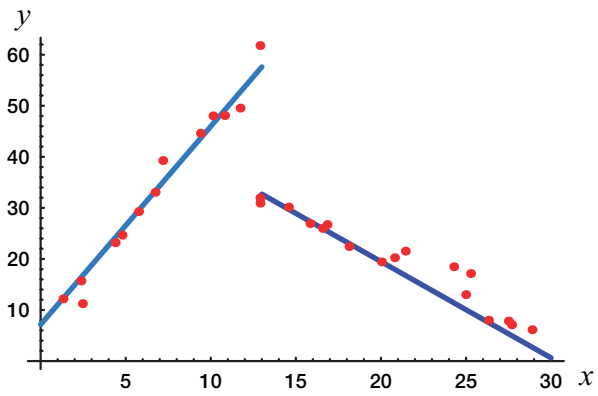

Figure 8.8: *When two motions are present it is possible to distinguish the two as one motion can be thought of as outliers. The second motion is then found by treating the first motion as outliers.*

produces quite good results at motion boundaries where the movements of several objects coincide in a local neighborhood.

8.8 Applications

In the preceding sections a framework was presented for simultaneously estimating the parameters of optical flow and brightness changes. These estimations are highly relevant for a number of applications, some of which will be presented in the following.

8.8.1 Estimating the Total Derivative of the SST

The main goal of this thesis is the estimation of the optical flow and parameters of underlying physical transport phenomena from infrared imagery. From this estimation insights in the processes governing air-sea heat and gas exchange can be deducted in a number of ways as presented in Chapter 5. In this context the total derivative of the sea surface temperature (SST) T with respect to time is of paramount importance. In Section 5.3 it can be used to measure the probability density of surface renewal and the characteristic time constant of surface renewal, the actual net heat flux density j in two ways outlined in Section 5.4.2 and 5.4.3 as well as estimating the heat transfer velocity k_{heat} in Section 5.5.

The total derivative of the sea surface temperature with respect to time dT/dt is given by

$$\frac{\mathrm{d}T}{\mathrm{d}t} = \frac{\partial T}{\partial t} + \boldsymbol{u}\boldsymbol{\nabla}T, \tag{8.30}$$

where T is the sea surface temperature and $\boldsymbol{u} = (u_1, u_2)^\top$ the surface flow.

In an infrared camera the temperature of a scene is mapped onto the image plane as an intensity distribution. An accurate description of this mapping of temperature to grey value, known as *radiometric calibration*, is very important for scientific applications and will be analyzed in Section 10.2. Due to this mapping temperatures can be regarded as image intensities and the Equation (8.30)

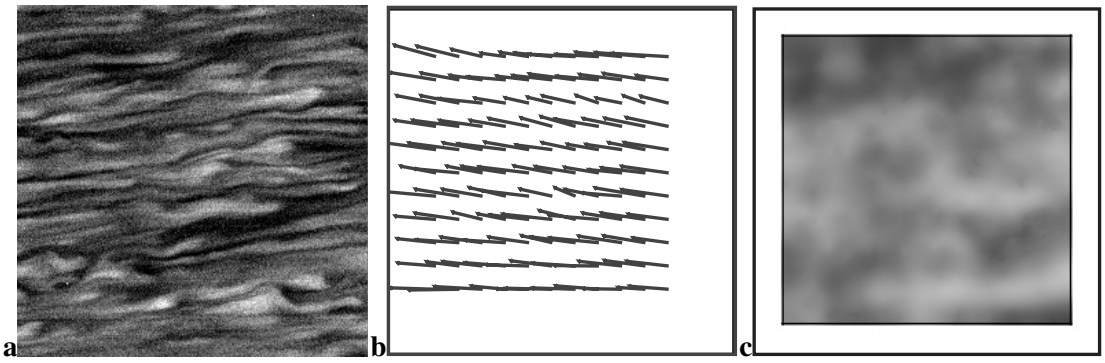

Figure 8.9: *An image from a sequence with the corresponding 2D optical flow and the total derivative of the temperature.*

compared to the BCCE in Equation (8.3), given by

$$\frac{\mathrm{d}g}{\mathrm{d}t} = \frac{\partial g}{\partial t} + \boldsymbol{u}\boldsymbol{\nabla} g = 0. \tag{8.31}$$

It is apparent that the BCCE does not hold in the context of this work, as the total derivative of the sea surface temperature would have to be equal to zero for the BCCE to be applicable. In order for the techniques presented in this chapter to reliably estimate the total derivative of the temperature the GBCCE (8.19) has to be applied to the special case of constant motion and a source term in the brightness change. This analogy between the optical flow equation and the continuity equation of an incompressible fluid was recognized. Accelerated motion due to waves or affine transformations create convergence and divergence which could be considered as well but are neglected in this section as the interest lies in the source term of the brightness change.

For constant translation the coordinate transform $\boldsymbol{S}$ in Equation (8.6) is given as

$$\boldsymbol{S}(\boldsymbol{r}, \boldsymbol{a}) = \boldsymbol{r} + \boldsymbol{a}, \tag{8.32}$$

where the parameter of the transformation $\boldsymbol{a} = (\delta x, \delta y, \delta t)^\top$ denotes the translation vector to be estimated. Following Equation (8.9) the infinitesimal generators are given as

$$\mathfrak{L}_1 = \frac{\partial}{\partial x}, \quad \mathfrak{L}_2 = \frac{\partial}{\partial y} \quad \text{and} \quad \mathfrak{L}_3 = \frac{\partial}{\partial t} \tag{8.33}$$

and the brightness change function h as

$$h(g(\boldsymbol{r}), \boldsymbol{b}) = c \cdot \boldsymbol{b}. \tag{8.34}$$

Consequently $\partial h(g(\boldsymbol{r}), \boldsymbol{b}) / \partial \boldsymbol{b} = c$ and the GBCCE (8.19) can be formulated yielding

$$\boldsymbol{d}^\top \boldsymbol{p} = (-1, g_x, g_y, g_t) \cdot (c, \delta x, \delta y, \delta t)^\top = 0, \tag{8.35}$$

where the subscripts denote partial derivatives.

The estimation is extended into a spatio-temporal neighborhood as introduced in Section 8.4 and the optical flow problem solved with the GTLS estimator according to Section 8.5.

On the IR image data structures are natured favorably so that the aperture problem is usually of no concern and full parameter field prevails. Therefore, following Section 6.6.1 the right general singular vector $\boldsymbol{e}_g = (e_1, e_2, e_3, e_4)^\top$ to the smallest general singular value λ_g of the data matrix $\boldsymbol{D}$ in

$$\begin{pmatrix} -1 & g_{x,1} & g_{y,1} & g_{t,1} \\ -1 & g_{x,2} & g_{y,2} & g_{t,2} \\ \vdots & \vdots & \vdots & \vdots \\ -1 & g_{x,n} & g_{y,n} & g_{t,n} \end{pmatrix} \cdot \begin{pmatrix} c \\ \delta x \\ \delta y \\ \delta t \end{pmatrix} = \boldsymbol{D} \cdot \boldsymbol{p} = 0, \quad \text{with} \quad \boldsymbol{D} \in \mathbb{R}^{n \times 4},\ \boldsymbol{p} \in \mathbb{R}^4 \tag{8.36}$$

represents the sought solution to the problem. The full parameter field for one image of a sequence is shown in Figure 8.9. The surface flow $\boldsymbol{f} = (\delta x/\delta t, \delta y/\delta t)^\top = (e_2/e_4, e_3/e_4)^\top$ and the total derivative of $\Delta T = c/\delta t = e_1/e_4$ can thus be estimated.

8.8.2 2D Flow with Affine Parameterization

In Section 8.2 the extension of the constant flow model to a number of possible parametric models was introduced. In terms of modelling actual physical processes the affine flow model is highly relevant. In a number of processes the affine matrix $\boldsymbol{A}$ from Equation (8.4) is an important quantity. For example, divergences can be gained directly, according to

$$\nabla \boldsymbol{f} = \frac{\partial f_1}{\partial x} + \frac{\partial f_2}{\partial y} = a_3 - a_2. \tag{8.37}$$

A negative divergence is commonly referred to as convergence. In oceanographic applications, divergence and convergence at the sea surface present an important parameter in air-water gas and heat exchange. For example, in the surface strain model introduced in Section 2.4.4, the transport processes are parameterized by the divergence or rate of strain given in Equation (8.37). At the sea surface a source term is still required as stated in Section 8.8.1. The set of equations solving this optical flow problem can be formulated as

$$\begin{pmatrix} -1 & g_{x,1} & g_{y,1} & x_1 g_{x,1} & y_1 g_{x,1} & x_1 g_{y,1} & y_1 g_{y,1} & g_{t,1} \\ -1 & g_{x,2} & g_{y,2} & x_2 g_{x,2} & y_2 g_{x,2} & x_2 g_{y,2} & y_2 g_{y,2} & g_{t,2} \\ \vdots & \vdots & \vdots & \vdots & \vdots & \vdots & \vdots & \\ -1 & g_{x,n} & g_{y,n} & x_n g_{x,n} & y_n g_{x,n} & x_n g_{y,n} & y_n g_{y,n} & g_{t,n} \end{pmatrix} \cdot \begin{pmatrix} c \\ \delta x \\ \delta y \\ a_1 \\ a_2 \\ a_3 \\ a_4 \\ \delta t \end{pmatrix} = \boldsymbol{D} \cdot \boldsymbol{p} = 0, \tag{8.38}$$

with $\boldsymbol{D} \in \mathbb{R}^{n \times 8}$ and $\boldsymbol{p} \in \mathbb{R}^8$. As explained in Section 8.2 the neighborhood center velocity is given by $\boldsymbol{t} = (t_1, t_2)^\top = (\delta x/\delta t, \delta y/\delta t)^\top$.

In botanical application, where the growth of plant leaves or roots is of interest, the divergence can be estimated directly and the regions of growth quantified. Due to constant illumination the source term c in Equation (8.38) is superfluous and can thus be removed together with the first column of the matrix $\boldsymbol{D}$. The resulting set of equations is thus of dimension $\boldsymbol{D} \in \mathbb{R}^{n \times 7}$ and $\boldsymbol{p} \in \mathbb{R}^7$.

It should be emphasized that because of the projective properties of the imaging system movement of objects in the line of sight of the camera also lead to an apparent divergence. The distance of the object to the camera has to be kept constant, or the change thereof has to be measured as well, if physically meaningful divergences are to be deducted from the estimation.

8.8.3 2D Flow with Exponential Decay

The equation for an exponential decay of the brightness is given by $H(g_0, t, a) = g_0 \exp(-at)$. The differential equation for this type of process is given by

$$f(g_0, t, a) = \frac{\mathrm{d}g}{\mathrm{d}t} = -ag_0 \exp(-at) = -ag. \tag{8.39}$$

The set of equations is thus given by

$$\begin{pmatrix} -g_1 & g_{x,1} & g_{y,1} & g_{t,1} \\ -g_2 & g_{x,2} & g_{y,2} & g_{t,2} \\ \vdots & \vdots & \vdots & \vdots \\ -g_n & g_{x,n} & g_{y,n} & g_{t,n} \end{pmatrix} \cdot \begin{pmatrix} a \\ \delta x \\ \delta y \\ \delta t \end{pmatrix} = \boldsymbol{D} \cdot \boldsymbol{p} = 0, \quad \text{with} \quad \boldsymbol{D} \in \mathbb{R}^{n \times 4},\ \boldsymbol{p} \in \mathbb{R}^4\,. \tag{8.40}$$

8.8.4 2D Flow with Isotropic Diffusion

Isotropic diffusion is a phenomenon commonly associated with heat. The corresponding set of equations is given by

$$\begin{pmatrix} -\Delta g_1 & g_{x,1} & g_{y,1} & g_{t,1} \\ -\Delta g_2 & g_{x,2} & g_{y,2} & g_{t,2} \\ \vdots & \vdots & \vdots & \vdots \\ -\Delta g_n & g_{x,n} & g_{y,n} & g_{t,n} \end{pmatrix} \cdot \begin{pmatrix} D \\ \delta x \\ \delta y \\ \delta t \end{pmatrix} = \boldsymbol{D} \cdot \boldsymbol{p} = 0, \quad \text{with} \quad \boldsymbol{D} \in \mathbb{R}^{n \times 4},\ \boldsymbol{p} \in \mathbb{R}^4 \tag{8.41}$$

where D is the constant of diffusion and $\Delta g_i = (\partial^2 g_i / \partial x^2 + \partial^2 g_i / \partial y^2)$ is the Laplace operator of the i-th pixel.

8.8.5 3D Flow with Anisotropic Diffusion

The case of a direction dependant three-dimensional diffusion can be modeled as follows:

$$g_x \cdot u + g_y \cdot v + g_z \cdot w + g_t - \boldsymbol{\nabla} \left(\boldsymbol{D} \cdot \boldsymbol{\nabla} \right) g = 0, \tag{8.42}$$

with the anisotropic diffusion tensor $\boldsymbol{D}$. This tensor is given by

$$\boldsymbol{D} = \begin{pmatrix} d_{00} & d_{01} & d_{02} \\ d_{10} & d_{11} & d_{12} \\ d_{20} & d_{21} & d_{22} \end{pmatrix} = \begin{pmatrix} d_{00} & d_{10} & d_{20} \\ d_{10} & d_{11} & d_{21} \\ d_{20} & d_{21} & d_{22} \end{pmatrix}, \tag{8.43}$$

where use was made of the fact that the diffusion tensor $\boldsymbol{D}$ is a symmetric tensor, that is $d_{ij} = d_{ji}$. Inserting this expression in Equation (8.42) leads to:

$$\begin{pmatrix} g_{x,1} & g_{y,1} & g_{z,1} & -g_{xx,1} & -g_{yy,1} & -g_{zz,1} & -2g_{xy,1} & -2g_{xz,1} & -2g_{zy,1} & g_{t,1} \\ g_{x,2} & g_{y,2} & g_{z,2} & -g_{xx,2} & -g_{yy,2} & -g_{zz,2} & -2g_{xy,2} & -2g_{xz,2} & -2g_{zy,2} & g_{t,2} \\ \vdots & \vdots & \vdots & \vdots & \vdots & \vdots & \vdots & \vdots & \vdots & \vdots \\ g_{x,n} & g_{y,n} & g_{z,n} & -g_{xx,n} & -g_{yy,n} & -g_{zz,n} & -2g_{xy,n} & -2g_{xz,n} & -2g_{zy,n} & g_{t,n} \end{pmatrix} \cdot (\delta x, \delta y, \delta z, d_{00}, d_{11}, d_{22}, d_{10}, d_{20}, d_{21}, \delta t)^\top = 0. \tag{8.44}$$

8.9 Summary

In this chapter a framework for the computation of motion from image sequences was presented. A general parametric model was introduced which allows for an accurate estimation of motions more complex than just pure rigid translation. It was shown how brightness changes can be model by linear partial differential equations. This allows to simultaneously estimate the parameters of motion and those describing physically motivated brightness changes. The aperture problem was explained and ways of circumventing it under certain conditions outlined. A method to characterize the estimates was introduced. This allows to differentiate between cases where a full set of parameters can be estimated and such where only a part of them can be found due to dependencies in the data. The concept of robust estimation was applied to optical flow computation allowing to obtain correct parameters in the presence of outliers. The chapter concludes with a number of applications of the proposed algorithms.

Part III

Experimental Results

Chapter 9

Accuracy of Algorithms

In this chapter the accuracy of the developed parameter estimation algorithms presented in Chapters 6 and 7, as well as for the subsequent computation of the optical flow field as introduced in Chapter 8, shall be analyzed. By systematically examining the techniques under varying parameters such as intensity changes and noise levels, insights into their performance can be gained. From this knowledge predictions regarding limitations and the applicability with respect to scene properties can be made. In a first step the techniques are applied to synthetic test data. Only in this type of data are exact values for the flow field and parameters of brightness change, the so called "ground truth", known exactly without added uncertainties due to image acquisition. In this way a precise error analysis of the estimates is achievable. Insights gained from the analysis of synthetic data can of course only serve as a lower bound for the expected performance of the algorithms on real world data. The performance on physical scenes with precise knowledge of true movement and intensity change has therefore been tested as well.

A brief introduction to the error measures used in subsequent analyses will be given in Section 9.1. In Section 9.2 the performance of the mixed Ordinary Least Squares/Total Least Squares (OLS-TLS) estimator, introduced in Section 6.5, is compared to the well established TLS estimator. The performance of the Least Median of Squared Orthogonal Distances (LMSOD) estimator is presented in Section 9.3.

9.1 Error Measures

In order to quantitatively compare the different estimators and methods for computing the optical flow proposed in this work, suitable error measures are needed. In subsequent analyses two measures for the error will be used. The first one is the relative error E_r between the estimated parameter $\boldsymbol{p}_{\mathrm{est}}$ and the correct one $\boldsymbol{p}_{\mathrm{corr}}$, given by

$$E_r = \left| \frac{|\boldsymbol{p}_{\mathrm{est}}| - |\boldsymbol{p}_{\mathrm{corr}}|}{|\boldsymbol{p}_{\mathrm{corr}}|} \right| \cdot 100 \ [\%]. \tag{9.1}$$

The relative Error E_r presents a measure for comparing the absolute difference between the magnitudes of the vectorial estimated parameter $\boldsymbol{p}_{\mathrm{est}}$ to the correct one $\boldsymbol{p}_{\mathrm{corr}}$. No directional information

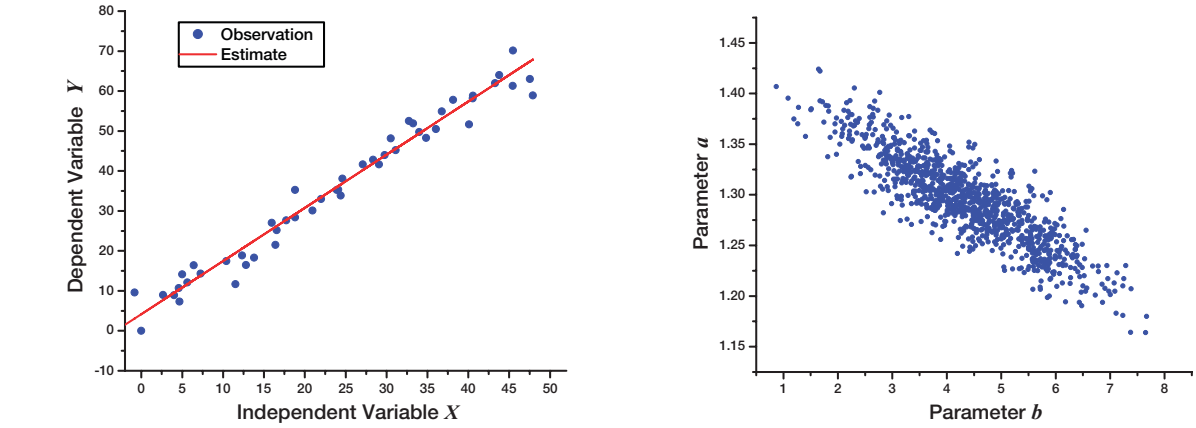

Figure 9.1: *Parameter estimation in the case of a two dimensional intersect model of the form $y = a \cdot x + b$. In this example the parameters were chosen as $a = 1.3$ and $b = 4.2$. In* ***a*** *the observations are falsified by noise and the parameters fitted with the OLS-TLS approach. In* ***b*** *the dependence of both parameters a and b are shown.*

is pertained to this measure. Hence a second measure is used, the angular error E_ϕ:

$$E_\phi = \arccos\left(\frac{\boldsymbol{p}_{\text{est}} \cdot \boldsymbol{p}_{\text{corr}}}{|\boldsymbol{p}_{\text{est}}| \cdot |\boldsymbol{p}_{\text{corr}}|}\right) \; [^\circ]. \tag{9.2}$$

This measure is commonly used in computer vision performance analyses [Fleet and Jepson, 1990; Fleet, 1992; Barron et al., 1994; Haußecker and Spies, 1999; Stewart, 1999; Spies, 2001]. E_ϕ quantifies the angle ϕ between the estimated and correct parameter vectors $\boldsymbol{p}_{\text{est}}$ and $\boldsymbol{p}_{\text{corr}}$. Apart from gauging directional accuracy in parameter space, this measure has the added benefit not to amplify at very small speeds, as may occur with the relative measure E_r [Barron et al., 1994].

9.2 Comparison of OLS-TLS and TLS

In the context of this work the brightness change constraint equation (BCCE) was extended to include dynamic brightness changes. A common change in brightness might be modelled by a source term as introduced in Section 8.8.1. The problem of computing the optical flow field from this constraint equation finds its analogy in two dimensions by fitting a straight line with intersect to a number of n observations. In Section 9.2.1 the performance of mixed OLS-TLS will be analyzed on this two dimensional problem as results can easily be presented and visualized. Insights gained from this model can readily be transferred to the actual problem of the optical flow computation, results of which will be presented in Section 9.2.2.

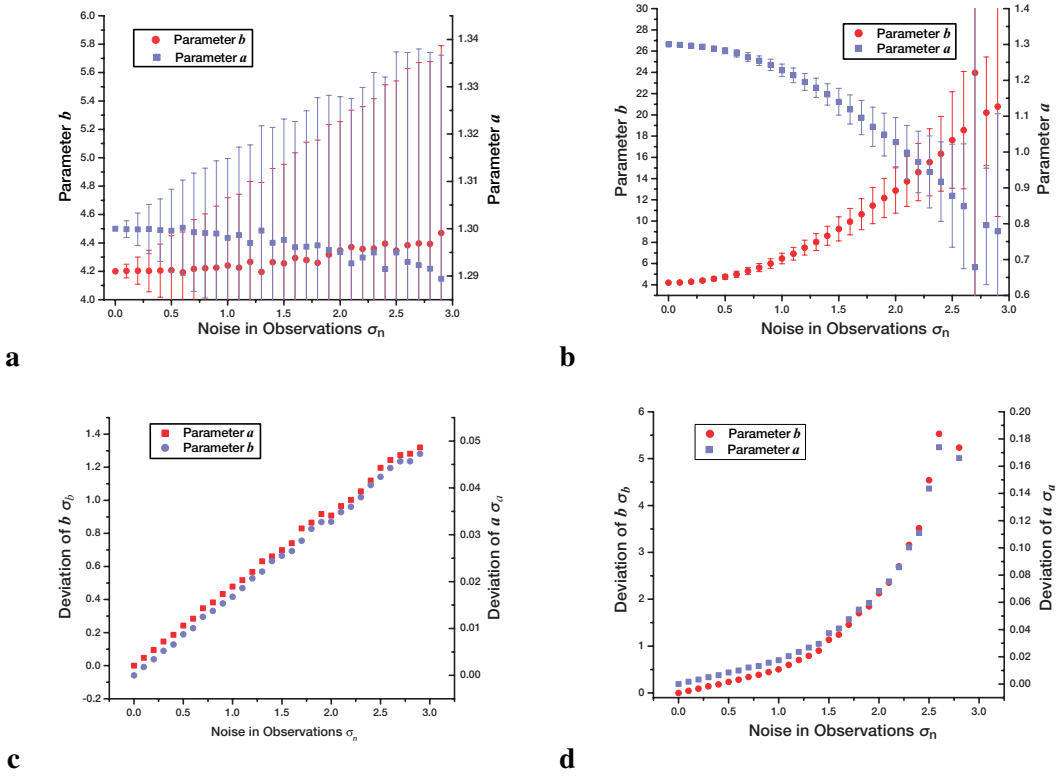

Figure 9.2: *Comparison of fitting the two parameters a and b to noisy data. In* ***a*** *the parameters were fitted with the mixed OLS-TLS estimator and in* ***b*** *with the unscaled TLS estimator. The corresponding variance of the parameters is plotted in* ***c*** *for the OLS-TLS and in* ***d*** *for the unscaled TLS estimator.*

9.2.1 Fitting a Line with Intersect

For a first evaluation of the basic properties of the mixed OLS-TLS estimator with respect to the TLS estimator, analyses are performed on a model with intercept, formulated according to

$$y = b + a \cdot x, \tag{9.3}$$

where both a and b are parameters to be estimated from the observations x and y. For n observations the parameters can be estimated from the set of equations

$$\begin{pmatrix} 1 & x_1 & -y_1 \\ 1 & x_2 & -y_2 \\ \vdots & \vdots & \vdots \\ 1 & x_n & -y_n \end{pmatrix} \cdot \begin{pmatrix} b \\ a \\ 1 \end{pmatrix} = \boldsymbol{D} \cdot \boldsymbol{p} = 0, \tag{9.4}$$

with the estimators introduces in Chapter 6.

In order to analyze the performance of these estimators, the correct parameter vector $\boldsymbol{p}_{\text{corr}} = (b_{\text{corr}},\ a_{\text{corr}})^\top$ is chosen and for $n = 50$ different values of x the corresponding values of y computed and the matrix $\boldsymbol{D}_{\text{corr}}$ obtained according to Equation (9.4). The columns $\boldsymbol{x} = (x_1, x_2, \ldots, x_n)^\top$ and

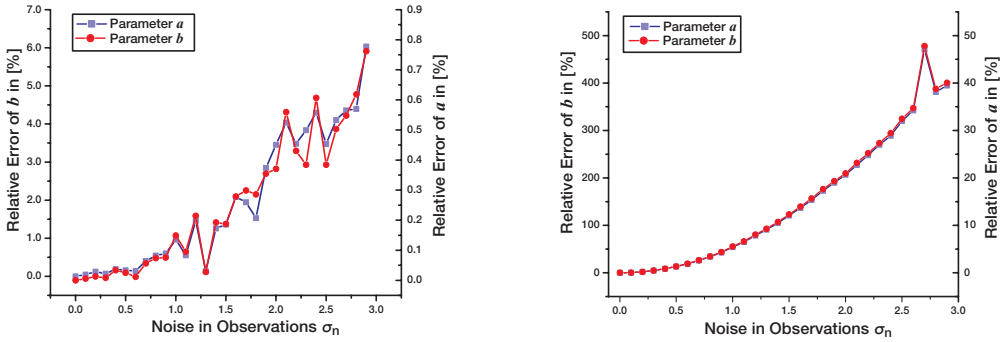

Figure 9.3: *The relative error measure E_r for the OLS-TLS and unscaled TLS estimators is shown in* ***e*** *and* ***f*** *respectively.*

$\boldsymbol{y} = (y_1, y_2, \ldots, y_n)^\top$ are than perturbed by independent normally distributed noise of zero mean and σ_n variance. It should be noted that the first column of $\boldsymbol{D}$ is not perturbed by noise as this is a constant term, not derived from observations. This perturbed matrix $\boldsymbol{D}_{\text{noise}}$ is then used to compute the parameter $\boldsymbol{p}_{\text{est}}$ which can be compared to the correct values by means of the error measures as introduced in Section 9.1. A plot of the perturbed observation with the fitted model from Equation (9.3) is presented in Figure 9.1. Also shown is the interdependence of the parameters a and b obtained by the mixed OLS-TLS estimator, which gives rise to non vanishing off-diagonal elements in the covariance matrix ∇.

The principal performance characteristics of the mixed OLS-TLS estimator in comparison to the TLS were analysed first on parameters of roughly equal magnitude, namely $a_{\text{corr}} = 4.2$ and $b_{\text{corr}} = 1.3$. The noise of the observations was varied from $\sigma_n = 0$ to $\sigma_n = 2.9$ in 30 steps. The matrix $\boldsymbol{D}_{\text{noise}}$ was regenerated and the fit repeated $m = 1000$ times to improve the statistical significance. In Figure 9.2 the results of this analysis are shown. The far superior performance of the mixed OLS-TLS estimator as compared to the unscaled TLS estimator become apparent immediately. The mean of the estimated parameters of the OLS-TLS fit reside very close to the correct ones with the standard deviation of the parameters increasing linearly with the noise level. In contrast a strong bias appears to exist in the unscaled TLS estimate as the mean of the fitted parameters tend to move away from the correct values with an increase in noise. Up to a noise level of about $\sigma_n = 1.25$ in this estimator the standard deviation of the estimated parameters seems to increase linearly, albeit at at higher level than seen earlier in the OLS-TLS estimate. At higher noise levels the standard deviation increases much more rapidly.

The relative error measure E_r of these two estimators can be seen in Figure 9.3. From this plot it becomes apparent that the relative error of the slope parameter a always stays significantly lower than that of the intersect parameter b. Even at the highest noise levels the error of the parameter a stays well below 1%, while that of b of reaches 60% at a noise level of $\sigma_n = 2.9$. This behavior can be explained graphically, as for a small change in slope a around a center of rotation away from the axes, a large change of intersect b will follow, as has been illustrated in Figure 9.4. Also through this illustration the interdependence of both parameters indicated by non-vanishing off-diagonal elements

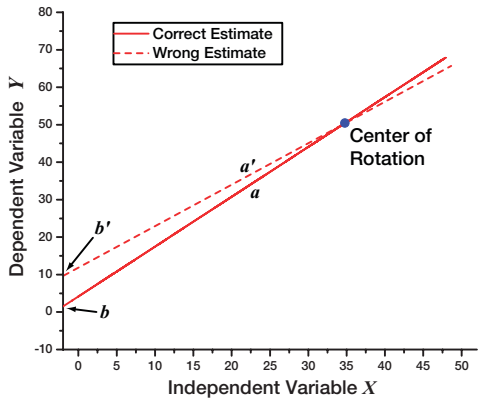

Figure 9.4: *An illustration of the way a small relative deviation of the slope a can lead to big relative errors in the intersect parameter b. Here the dotted line and primed parameters indicate the wrong solution.*

in their covariance matrix $\not\Sigma$ is clarified, evidence of which has been given in Figure 9.1. Again, the inferior performance of the unscaled TLS estimate is striking, as even for relatively low noise levels of $\sigma_n = 1$ the relative error of the slope parameter is already close to 10% and the intersect parameter is even higher at 80%! This means that the relative errors of the unscaled TLS estimate are almost 100 times as high as the equivalent errors in the OLS-TLS estimate. This makes the use of an unscaled TLS estimator illegitimate for estimations of this type of model with intersect.

These findings raise the question as to where the bias in the unscaled TLS estimator might originate from. As has been stated in Section 6.3 in the TLS estimate all elements in the data matrix $\boldsymbol{D}_{\text{noise}}$ are modified with minimal effort in finding the approximate matrix $\tilde{\boldsymbol{D}}_{\text{noise}}$ compatible with the solution vector $\boldsymbol{p}$. This does not exclude the exactly known first column $\mathbb{1}$ in Equation (9.4) which is modified by the same amount as the other erroneous columns. This must lead to a bias, as seen in the results of the analysis. It is this different treatment of the exactly known first column of the OLS-TLS estimator that presents the difference between the two estimates which subsequently removes the bias.

In Section 6.1 the scaling of observations has been introduced. It can be shown that the bias of the unscaled TLS estimate can be reduced somewhat by an adequate scaling of the data matrix $\boldsymbol{D}_{\text{noise}}$. In principle all elements of the data matrix are modified by the TLS estimate. The degree of this modification can be influenced by appropriate scaling factors. Through the column scaling scheme introduced in Section 6.1 the data elements can be thought of to be divided by their variances. For the first column, which is exactly known, the variance can be set to a much smaller value than that of the other columns. Here it was chosen to be four order of magnitudes smaller than the smallest variance found in the other columns. The significant improvement of the scaled TLS estimate can be seen in Figure 9.5. Although the bias is removed through this scaling and the curves of the OLS-TLS and scaled TLS estimator are very similar, close comparison indicates that the errors of the OLS-TLS are still a little smaller. The relative difference between the two estimators for the parameter b indicate, that the OLS-TLS estimator outperforms the TLS estimator by approximately 2% throughout the noise levels tested in this analysis.

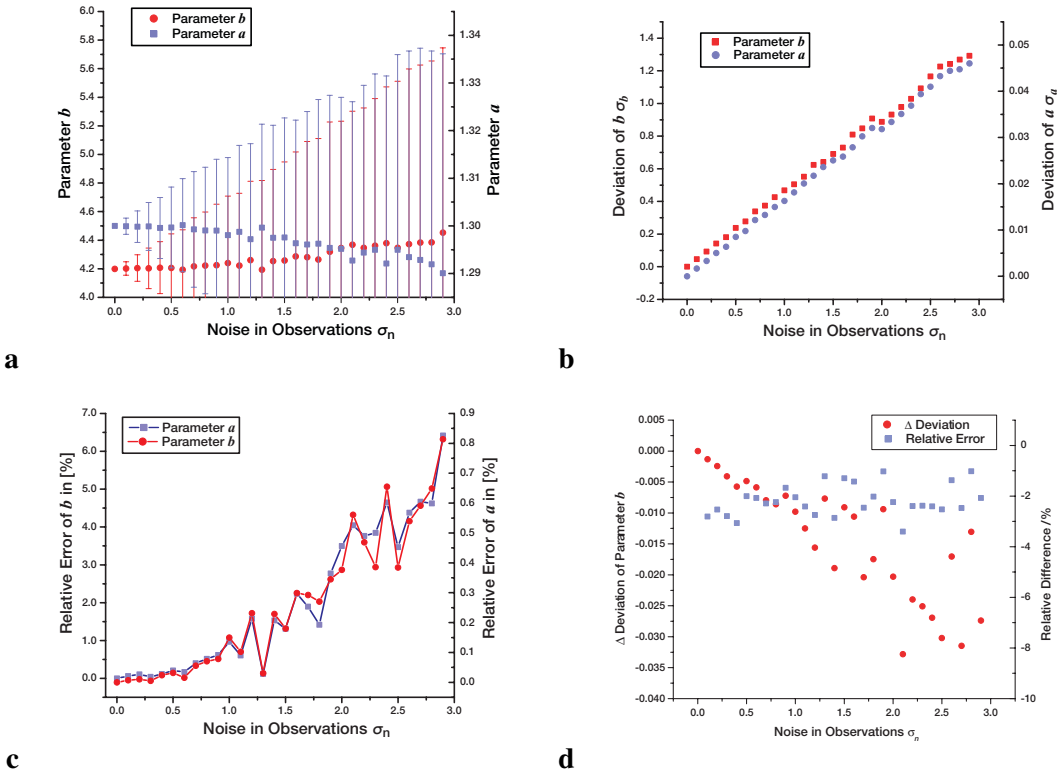

Figure 9.5: *Significant improvement in the TLS estimate can be achieved by scaling the data matrix* $\boldsymbol{D}_{\text{noise}}$*. Both the parameters are shown in* ***a*** *and their variance in* ***b*** *. The relative Error* E_r *of the scaled TLS estimate is shown in* ***c*** *. The relative difference between the two OLS-TLS and scaled TLS estimator is shown in* ***d*** *, indicating that the OLS-TLS estimator still has a better performance than the scaled TLS estimator by roughly* 2%*.*

It should be noted that no scaling of observations was performed on the OLS-TLS estimator in this comparison. To this end one may ask oneself what effect a scaling might have on the OLS-TLS estimator. To answer this question an equivalent scaling was performed on the OLS-TLS estimate. As the first column of the data matrix is not modified in this estimator and consequently treated as exactly known, no scaling was performed in these terms. A comparison of the scaled versus unscaled OLS-TLS estimate can be seen in Figure 9.6. As is evident from this analysis the scaling of observations has no notable effect on the OLS-TLS estimator, strongly contrasting the behavior of the TLS estimate. The results for the slope parameter a are equivalent. The reason for this apparent independence of scaling is of course, that the variances of noise for both data columns $\boldsymbol{x}$ and $\boldsymbol{y}$ in $\boldsymbol{D}_{\text{noise}}$ are of roughly equal dimension. A different behavior becomes apparent with strongly different noise levels. In this case also a bias is introduced in the OLS-TLS estimate, which can be removed by column scaling.This type of noise in the observations is expressed in a deviation from the unity matrix $\mathbb{1}$ for the right hand scaling matrix $\boldsymbol{W}_R$ as introduced in Section 6.1. An numerically efficient way of solving these cases without the need for explicit scaling is the GTLS estimator as explained in Section 6.6.

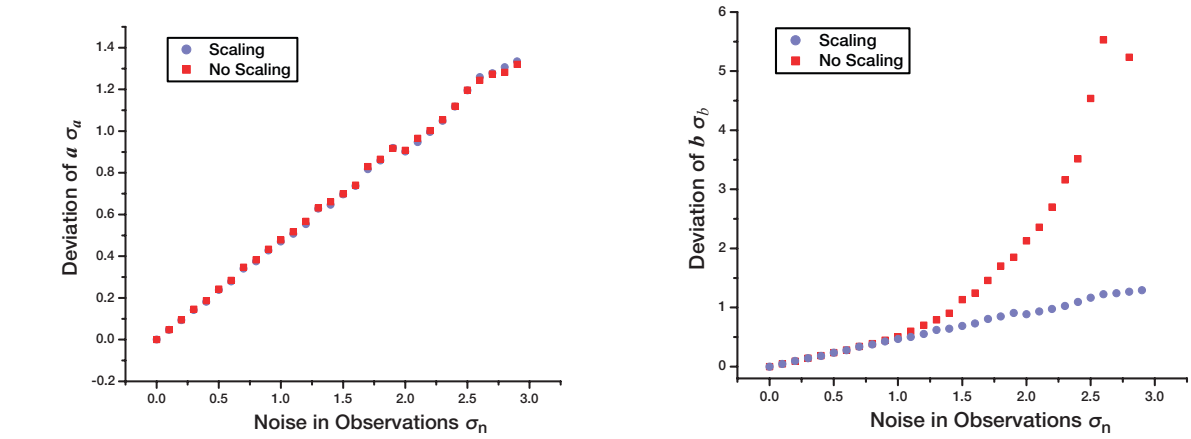

Figure 9.6: *The influence of column scaling on both the OLS-TLS estimator in* ***a*** *and of the TLS estimator in* ***b*** *. No significant dependence on the scaling is apparent in the OLS-TLS estimate, contrasting the behavior in the TLS case.*

9.2.2 Optical Flow Computations

In the previous section the performance of the TLS and mixed OLS-TLS estimators was analyzed on a two dimensional linear model with intersect. Insights gained can directly be transferred to this type of problem, such as the radiometric calibration of infrared cameras as explained in Section 10.2. Of more interest in the context of this work is the application of parameter estimation to the optical flow problem as outlined in Chapter 8. Here the Generalized Brightness Change Constraint Equation (GBCCE) with constant linear motion and the brightness change modeled with a source term will be commonly used, that is

$$\begin{pmatrix} -1 & g_{x,1} & g_{y,1} & g_{t,1} \\ -1 & g_{x,2} & g_{y,2} & g_{t,2} \\ \vdots & \vdots & \vdots & \vdots \\ -1 & g_{x,n} & g_{y,n} & g_{t,n} \end{pmatrix} \cdot \begin{pmatrix} c \\ \delta x \\ \delta y \\ \delta t \end{pmatrix} = \boldsymbol{D} \cdot \boldsymbol{p} = 0, \quad \text{with} \quad \boldsymbol{D} \in \mathbb{R}^{n \times 4},\ \boldsymbol{p} \in \mathbb{R}^4 \tag{9.5}$$

as introduced in Equation (8.36). Here n represents the size of the spatio-temporal neighborhood and $g_{i,j}$ the partial derivative of the grey value g with respect to the coordinate i at pixel location j. Comparing this set of equations with the one presented in Equation (9.4) illustrates the point that this formulation of the GBCCE represents a multivariate extension of the two dimensional Equation (9.3). Therefore it can be assumed that results gained in the previous section are equally applicable to the optical flow case.

Following [Barron et al., 1994] the algorithms were tested on a sinusoidal test sequence. The sequence is generated according to

$$g(\boldsymbol{x}, t) = A \cdot (\sin(\boldsymbol{k}_1 \cdot \boldsymbol{x} + \omega_1 t) + \sin(\boldsymbol{k}_2 \cdot \boldsymbol{x} + \omega_2 t)) + B(t), \tag{9.6}$$

where $g(\boldsymbol{x}, t)$ is the grey value at pixel location $\boldsymbol{x}$ at time t, A represents a parameter for the dynamic range of the sequence, $B(t)$ indicates the offset of the grey values g and both $\boldsymbol{k}_1$ and $\boldsymbol{k}_2$ represent the

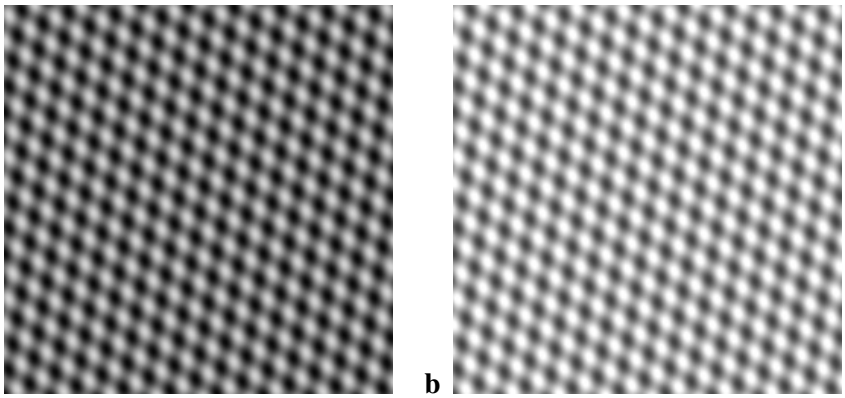

Figure 9.7: *In* ***a*** *the first frame of the used sinusoidal test sequence and in* ***b*** *a subsequent frame following an intensity change.*

wavenumbers of the sinusoidal in the direction of the coordinates x_1 and x_2 and ω_1 and ω_2 represent the movement of the pattern in direction of the respective coordinate directions. For the simulation of a linear brightness change the offset B is assumed to be a linear function of time t. The wavelenth used for the test sequence was chosen to be $\lambda_1 = \lambda_2 = 2\pi/k_1 = 2\pi/k_1 = 15.2$ pixel with an angle between k_1 and the x-axis of $80.5°$ and between k_2 and this axis of $-33.3°$. Two frames of such a test sequence are displayed in Figure 9.7.

For optical flow computation it is interesting to study the dependence of the computed optical flow $\boldsymbol{f} = (u, v)^\top$ depending on the noise added to the synthetic sequence. In the present context it is of equal importance to know how accurate the intensity change present in the sequence can be detected. To address these issues first a constant intensity change of $B(t) = B_0 + a \cdot t$ with $a = 1.5$ grey value / frame was uniformly added to the sequence. The magnitude of the flow was varied from no movement ($v_{\text{corr}} = 0$ pixel / frame) up to $v_{\text{corr}} = 10$ pixel / frame in 20 steps, with the direction of the velocity vector along one coordinate axis. Although this is not a common situation encountered in real world situations, most gradient filters poses optimum properties along this direction [Scharr, 2000]. Hence results presented here give a lower bound for movement along other directions. The reason for choosing this specific direction is that the performance of the optical flow computation was to be analyzed independent of the actual optimization of the gradient filter used. Along other directions the actual performance of gradient filters can vary significantly and is subject to filter optimization [Scharr, 2000].

The analysis was repeated for nine different noise levels of iid Gaussian noise added to the sequence. The variances of the noise chosen were $\sigma^2 \in \{0.0, 0.1, 0.5, 1.0, 1.5, 2.0, 3.0, 4.0, 5.0\}$, giving a good feeling for the dependence of the algorithm on camera noise which is usually well below $\sigma^2 = 1.0$. The result of this analysis is shown in Figure 9.8 for two dynamic ranges ($A \in \{50, 2000\}$ grey value) of the sinusoidal test pattern. The rise of the relative error E_r at high flow magnitudes is due to a correspondence problem, as here the flow magnitude is of almost equal size as the isotropic test pattern. This problem can also be identified in the angular error E_ϕ, which is roughly 180° at these large displacements.

The gradients can be computed more accurately at steeper gradients, which is why the results

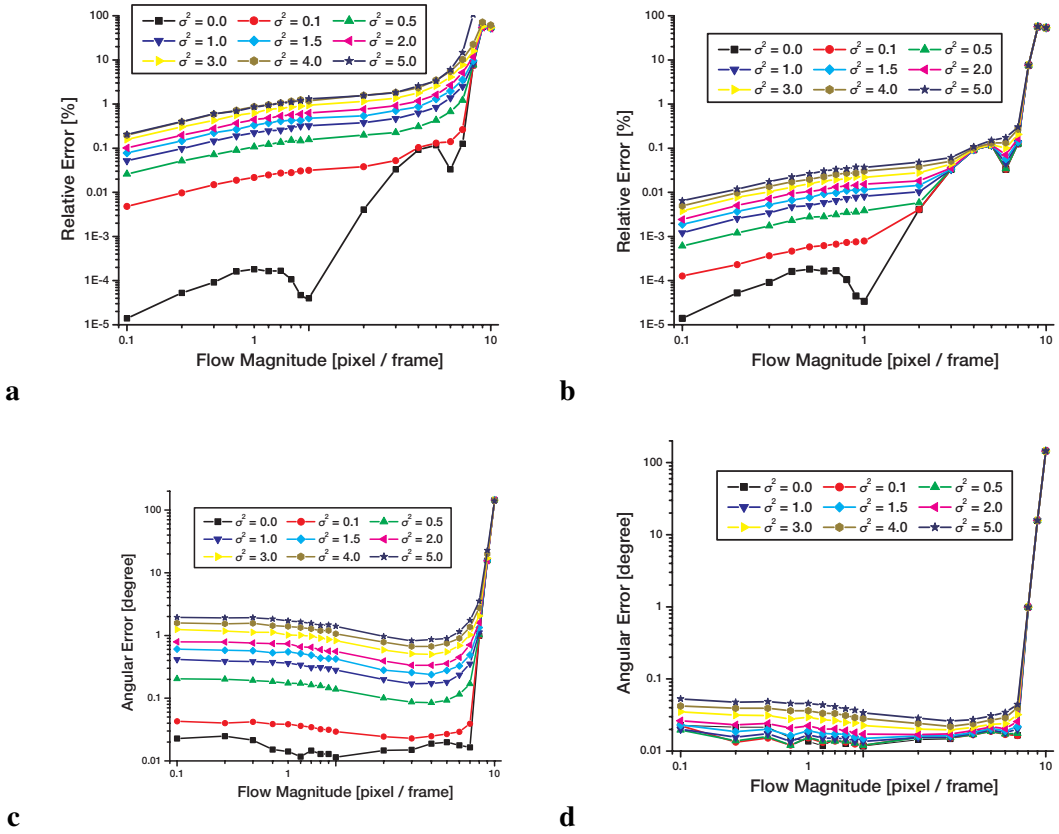

Figure 9.8: *Comparison of the relative error E_r of the flow magnitude for small an big dynamic range shown in* ***a*** *and* ***b*** *respectively and the corresponding angular errors E_ϕ in* ***c*** *and* ***d*** *.*

indicate far smaller angular and relative errors E_r and E_ϕ at the higher dynamical range of the test pattern. In subsequent analysis the smaller dynamic range of $A = 50$ grey value is chosen.

Following the analyses in the previous section it is of interest to note the difference between the mixed OLS-TLS estimator in the context of optical flow computations. To this end the accuracy of establishing an estimate for the parameter c of brightness change in Equation (9.5) was examined with the three alternate techniques, namely the mixed OLS-TLS, the scaled TLS and the plain TLS estimator. Also the accuracy of detecting the optical flow $f_{\text{est}} = (u_{\text{est}}, v_{\text{est}})^\top$ under different flow magnitudes and different intensity changes was inspected. Not all the resulting plots are presented in this thesis, but only some representative ones, as the results are similar and can readily be extrapolated from the presented cases. In Figure 9.9 the relative errors of the intensity changes are shown. As was found in the previous section, also in this case the OLS-TLS estimator presents the most accurate results, while the scaled TLS estimate is prone to slightly larger errors. The unscaled TLS technique proves to be quite inaccurate, most notably on higher noise levels. Generally all estimators exhibit the highest accuracy on large intensity changes, which were varied for $B(t) = B_0 + a \cdot t$ from $a = 0.0$ to $a = 10.0$ grey value / frame in 20 steps. The accuracy of recovering the flow magnitude proved to be independent of the intensity change in the OLS-TLS estimator and depends linearly on the noise level σ. The TLS estimate is biased towards higher intensity changes.

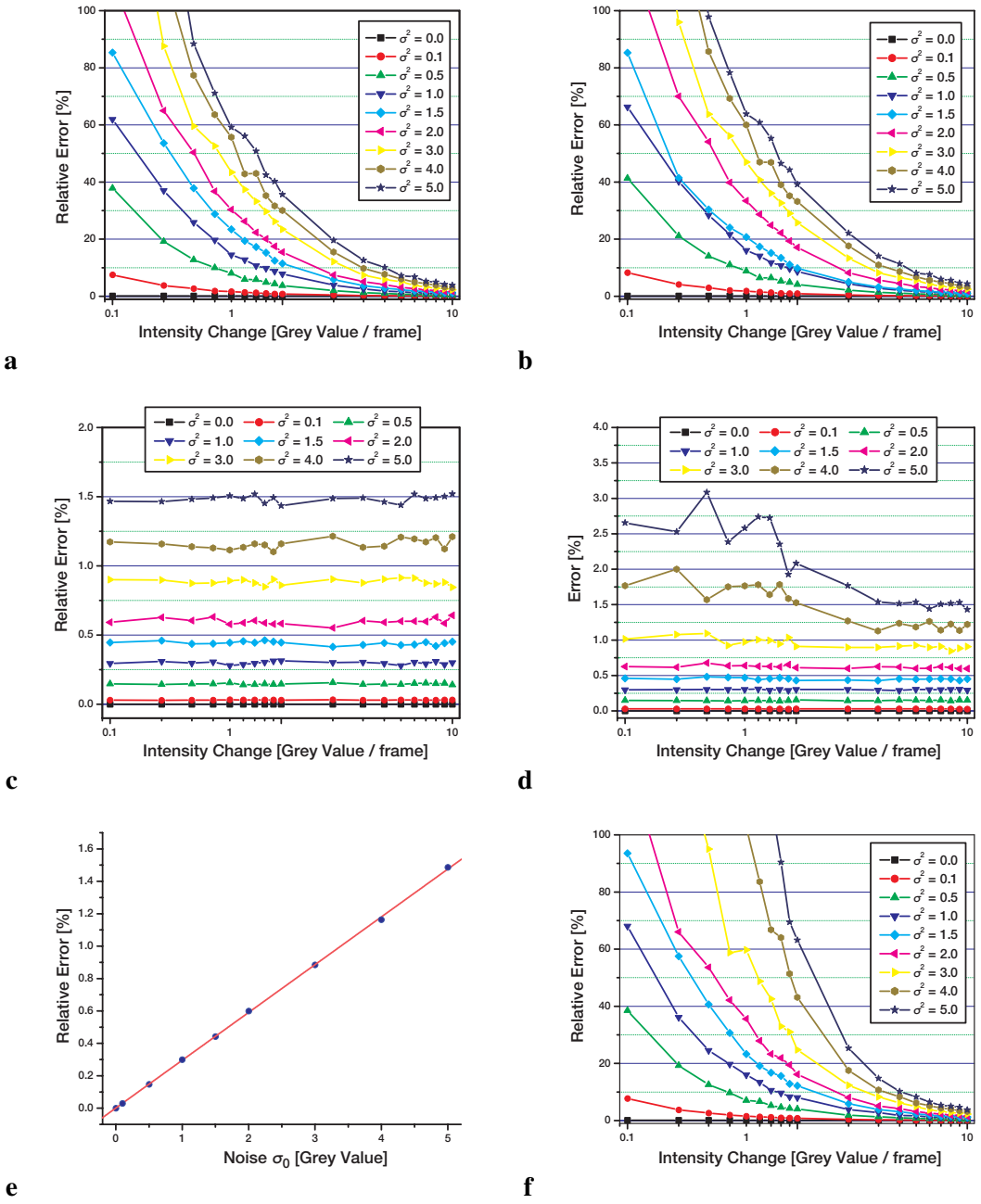

Figure 9.9: *Comparison of the relative errors in estimating an intensity change at fixed flow magnitude. In* ***a*** *the intensity change is computed from the mixed OLS-TLS estimator and in* ***b*** *with the scaled TLS estimator, proving that the OLS-TLS produces slightly more accurate results than the scaled TLS analogon. Shown in* ***c*** *and* ***d*** *are the relative errors in computing the optical flow magnitude* $|\boldsymbol{f}_{\mathrm{est}}|$ *for an increasing level of intensity change. While this accuracy is solemnly a linear function of noise level in the case of OLS-TLS as is shown in* ***e*** *, the accuracy increases with higher intensity change for TLS. The poor performance of the unscaled TLS is presented in* ***f*** *.*

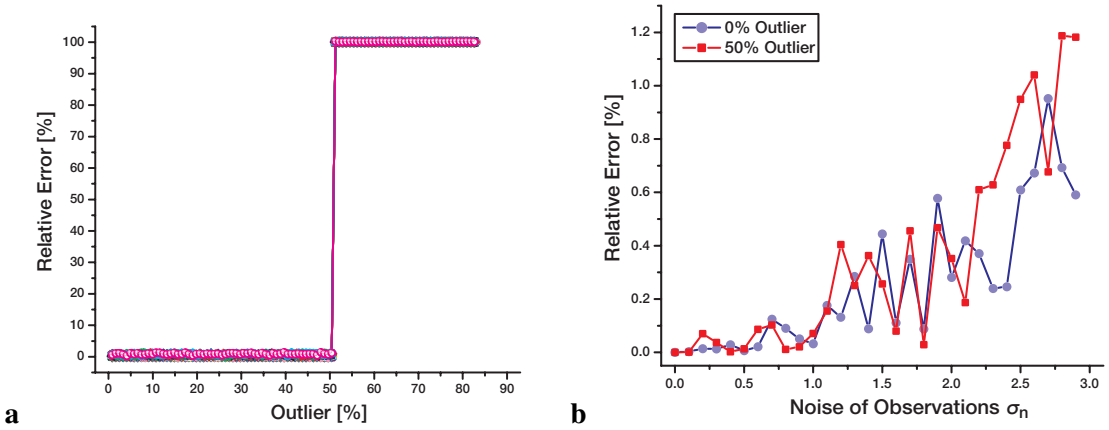

Figure 9.10: *The performance of the LMSOD estimator with respect to outliers. In* ***a*** *the relative error with respect to outliers is shown and in* ***b*** *the dependence of the relative error on the noise in the observations.*

Concluding it can be stated that the results found in line fitting with intersect from Section 9.2.1 were repeated for the multivariate extension of optical flow computations. The TLS estimator proofed to be too inaccurate for this type of problem. It was shown that it exhibits a strong bias and thus depends highly on the noise level and intensity change present in the imagery. By performing a column scaling of the data matrix $\boldsymbol{D}_{\text{noise}}$ as presented in Section 6.1, this bias could be removed somewhat. The virtual deviation of the exactly known first column of the data matrix has to be scaled with a variance of at least four orders of magnitude smaller than that found in the other columns. Numerically more attractive and also providing the most accurate results is the mixed OLS-TLS estimator presented in Section 6.5, which is the best unbiased estimator under iid Gaussian noise as examined in this section.

9.3 Results of the LMSOD Estimator

The Least Median of Squared Orthogonal Distances (LMSOD) estimator was introduced in Section 7.3. The interesting feature of this estimator is its high breakdown point of 50%, the highest theoretically achievable value. In this section the performance of the estimator is analysed with respect to a large number of outliers. In the same manner as in Section 9.2.1 the analysis is conducted on the two dimensional problem of fitting a line with intersect. The data space consisted of 121 data points. Iteratively the number of outliers was increased by setting the value of a random data point far away from the correct one. This procedure was continued until all the data points were in fact outliers. It could be verified that the estimator correctly estimates the parameters of the simple line model, until the number of outliers increases beyond the 50% marker. From this point onwards the line is fitted to the outliers, rendering the result useless. It is of course of interest as to what effect noise on the data points will have. For this reason the analysis was repeated for 30 equidistant levels of Gaussian noise, with a maximal standard deviation of $\sigma_n = 3.0$.

The results of this analysis are shown in Figure 9.10. It can be seen that there is no relevant dependence on the number of outliers, until the breakdown point of 50% is reached. As can be seen in

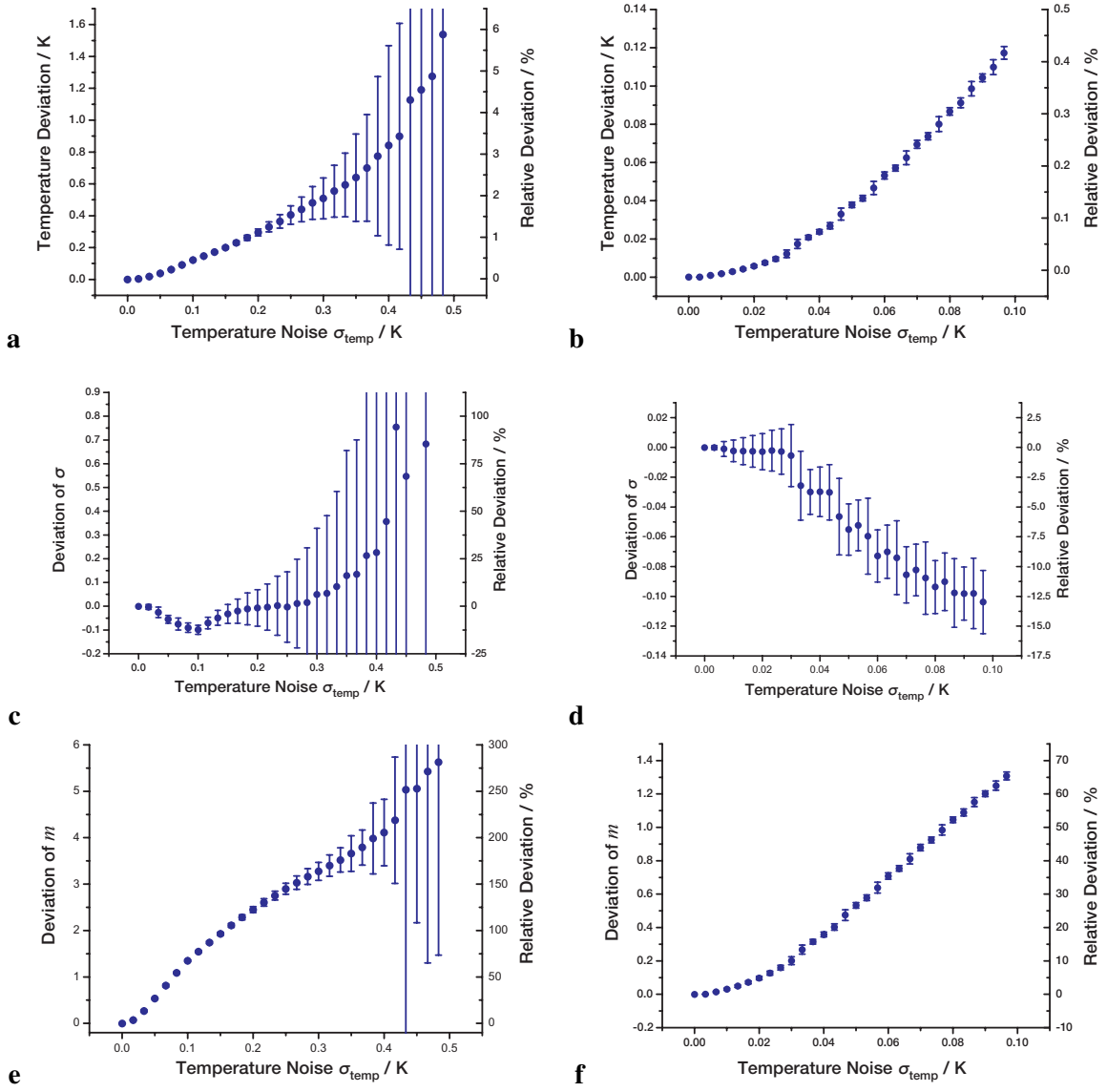

Figure 9.11: *The dependence of the extracted parameters from the statistical analysis on the noise. In* ***a*** *the dependence of the error of T_{bulk} on the noise ranging from 0.0 to 0.5 K is shown. In* ***b*** *the same for lower noise levels from 0.0 to 0.1 can be seen. In* ***c*** *,* ***d*** *,* ***e*** *and* ***f*** *the analogon for the error of the other parameters σ and m is given.*

Figure 9.10b the dependence on the noise level of the observations is the same, regardless whether no outlier is present or the highest possible number of just under 50%. The demonstrated independence of outliers makes for a very desirable feature in a robust estimator. This is the reason why this estimator was chosen in the context of this work.

9.4 Accuracy of Estimating the Temperature Depression

Apart from being an important parameter for air-sea gas exchange in its own right, the temperature depression across the cool skin of the ocean is an integral part of measuring the sea surface heat flux by the new technique presented in this thesis. For this reason a thorough analysis of this vital component is inevitable.

In order to examine the validity of results gained from the statistical analysis proposed in Section 5.2, the algorithm was applied to synthetical data. The effect of noise in the input data on the estimated parameters was investigated. For this reason a synthetical image was generated, presenting the same temperature distribution as an image of the sea surface. The relative errors in the fit parameters were computed under varying noise level of the input data. The results of this analysis is presented in Figure 9.11.

By comparing the results it becomes apparent that the bulk temperature T_{bulk} can be estimated with a relative accuracy of below on per cent for noise levels of 0.2 K. For the noise level of the infrared camera, typically 25 mK, the error in T_{bulk} was found to be well below 5 mK. This is in good agreement with previous findings on real data. In contrast to the errors of the other parameters there is only a small increase with a rising noise level. However, in subsequent analyses only the parameter T_{bulk} is used. Therefore the higher noise levels in the other parameters present no drawback.

9.5 Summary

In this chapter the performance of the proposed algorithms for optical flow computation have been analyzed. First the dependence of both the OLS-TLS and TLS estimator on the noise level of observations were tested in a linear two dimensional model with intersect. It was shown that in the case of iid Gaussian noise the OLS-TLS estimator provided an accurate fit of the model parameters with no dependence on column scaling as was the case for the TLS estimate. This estimator proved to be prone to a strong bias in the unscaled case. Hence for this type of problem the OLS-TLS estimator can be recommended. The same behaviour of the two estimators was verified on synthetic test sequences for optical flow computations. Here, the OLS-TLS estimator outperformed the TLS estimator in the presence of linear brightness changes. Also the noise dependence of the robust LMSOD estimator was analyzed with respect to outliers. The high breakdown point of this estimator was proven to be 50%. Also the relative error of the estimates was found to be independent of the number of outliers. For these reasons this estimator was chosen for the subsequent analyses.

Chapter 10

Calibration of an Infrared Camera

When recording image sequences with an infrared camera a three dimensional scene is mapped through a projective transformation onto the image plane. The temperatures of the physical world are transformed to image intensities as grey values. The actual process of image formation is fairly complicated and depends on all of the subsystems in the chain, ranging from the actual optics used, the focal plane array of the detector, read out electronics, amplification of the signals and digitizing them. Due to these highly complicated transformations with not all parameters known it is not possible to formulate a set of equations and solve the image formation process from a number of parameters given by the manufacturer of the acquisition system. However, some model assumption about the camera can be made with the parameters being measured by experiment. To this end a fairly accurate formulation of the mapping from three dimensional world objects to their representation on the image plane can be gained through a process commonly known as *calibration*. The calibration procedure can be separated into *geometric* and *radiometric* calibration. The geometric calibration is concerned with the projective transformation of three dimensional object coordinates into two dimensional image coordinates and will be explained in Section 10.1. On the other hand the radiometric calibration is concerned with the mapping of physical temperatures to grey values in the image. An analysis of this temperature calibration is presented in Section 10.2. For an accurate estimation of physical processes both calibrations must be accurately known. Otherwise uncertainties or biases are introduced in the estimation of parameters.

10.1 Geometric Calibration

The geometric calibration seeks to describe the mapping of an object in *world coordinates* $\boldsymbol{U} = (U_1, U_2, U_3)^\top \in \mathbb{R}^3$ through projective transformation into image coordinates $\boldsymbol{u} = (u_1, u_2)^\top$. Apart from this linear projection nonlinear effects due to distortions from imperfect lenses have to be modelled by the geometric camera model as well.

The camera model is uniquely defined by two sets of parameters, commonly referred to as *external* and *internal camera parameter*. The external camera parameters contain information of the relative position of the camera in relation to the world coordinate frame in terms of translation and rotation. The internal parameters describe the properties of the imaging system such as the focal length f,

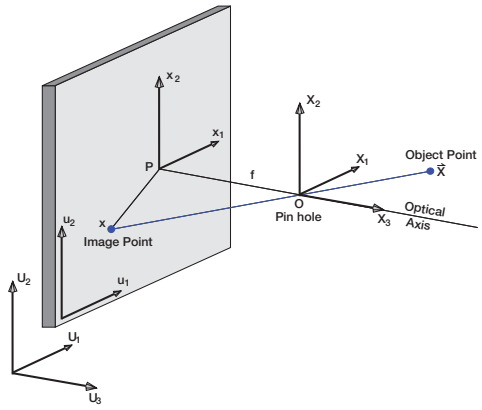

Figure 10.1: *An illustration of the pinhole camera model. The object point is described in world coordinates* $\boldsymbol{U}$ *and camera coordinates* $\boldsymbol{X}$ *and the image point in sensor coordinates* $\boldsymbol{u}$ *and image coordinates* $\boldsymbol{x}$*.*

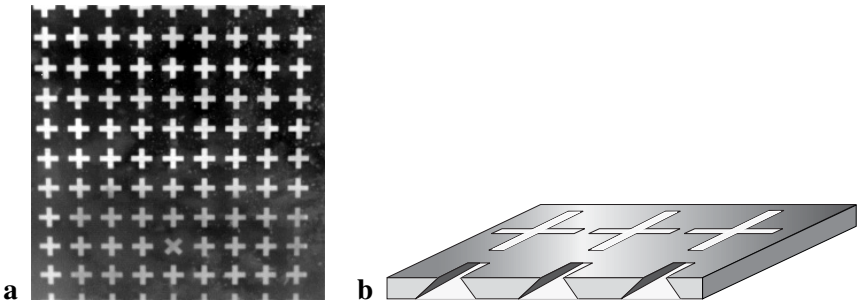

Figure 10.2: ***a*** *shows a picture of the used calibration target. The crosses are tapered as can be seen in* ***b*** *. This allows for an accurate image when the target is seen under an angle.*

principal point P, aspect ratio and geometric distortion factors. An illustration of these parameters and coordinate frames is presented in Figure 10.1. For an in depth discussion on different camera models and implications the reader is referred to Faugeras [1993] and Luhmann [2000].

In order to accurately determine the internal and external camera parameters, a correspondence between known world coordinates and image coordinates has to be constructed. This is done by means of a three dimensional calibration target. For experimental ease an aluminium plate was chosen with equidistant crosses as can be seen in Figure 10.2. The plate is moved to different locations to ensure a complete coverage of the region of interest with calibration points.

In field experiments it is impossible to move the plates accurately with a positioner. Out of a number of different calibration procedures [Garcia et al., 2000] the one propagated by Zhang [1998, 2000] was chosen as it allows for an estimation of the camera parameters from 3-4 non-parallel arrangements of the plate without knowledge of their relative positions. The high accuracy of this camera calibration procedure was examined by Sturm and Maybank [1999] who found an accuracy of 0.07% for parameters such as the focal length f under laboratory conditions.

In order to perform the calibration the crosses of the calibration plate have to be located accurately in the image plane. Lavest et al. [1998] conclude that an error of 0.5 pixel in the detection of the cross leads to significant deviations in the camera parameters. Therefore an analytical function has to be

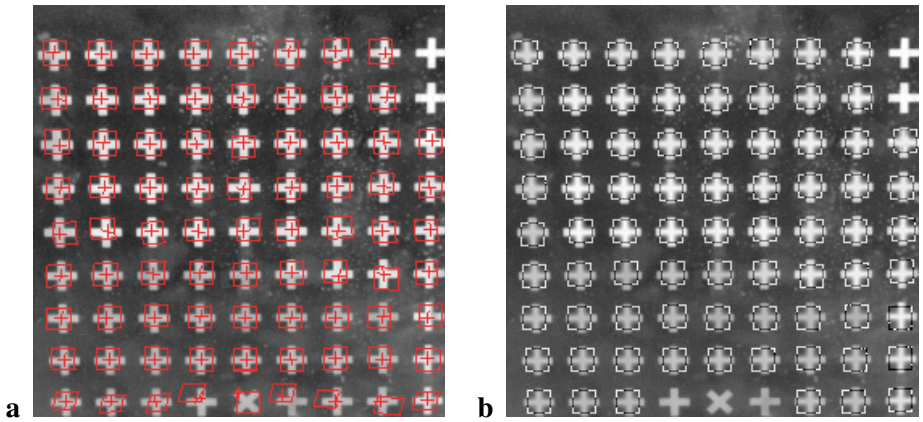

a **b**

Figure 10.3: *The location of the detected feature points can be seen in* ***a*** *and the sub-pixel accurate location of the grid points in* ***b*** *.*

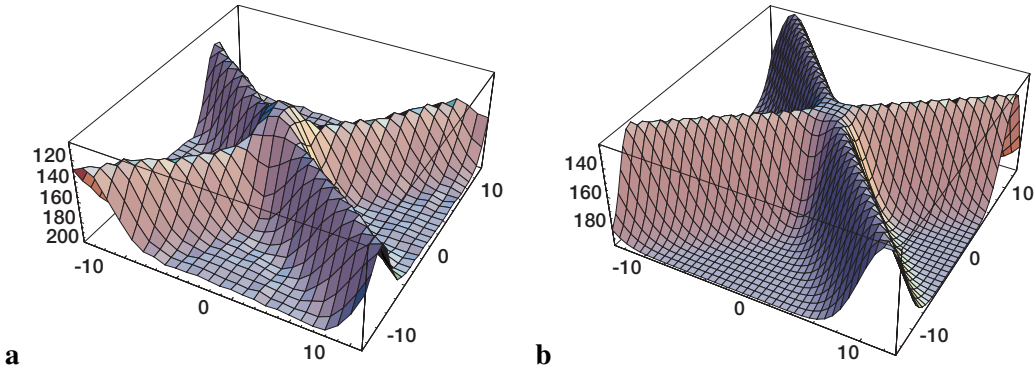

a **b**

Figure 10.4: *In* ***a*** *an example image intensity distribution of a calibration cross can be seen and in* ***b*** *the fitted analytical function.*

fitted to the image data with a non-linear *Levenberg- Marquardt* algorithm [Press et al., 1992].

This analytical function is shown in Figure 10.4 and can be formulated according to [Garbe, 1998]

$$F(x,y) = a - d \cdot \left(1 - e^{-w_1((y-l_2)\cos\theta_1 + (x-l_1)\sin\theta_1)^2}\right) \cdot \left(1 - e^{-w_2((y-l_2)\cos\theta_2 + (x-l_1)\sin\theta_2)^2}\right), \tag{10.1}$$

with the parameters

a	grey value of the background,
d	grey value elevation of the cross lines,
w_1, w_2	square of the reciprocal width of the lines,
l_1, l_2	relative position to local origin in x and y-direction,
θ_1, θ_2	angle in between the image rows and the cross lines.

Using this registration procedure the feature points are located with an accuracy of approximately $\approx 1/100$th of a pixel under real world conditions [Garbe, 1998]. Hence the calibration target has to be manufactured with an accuracy of 20 µm to allow for a sufficiently accurate estimation of the camera parameter under common experimental conditions.

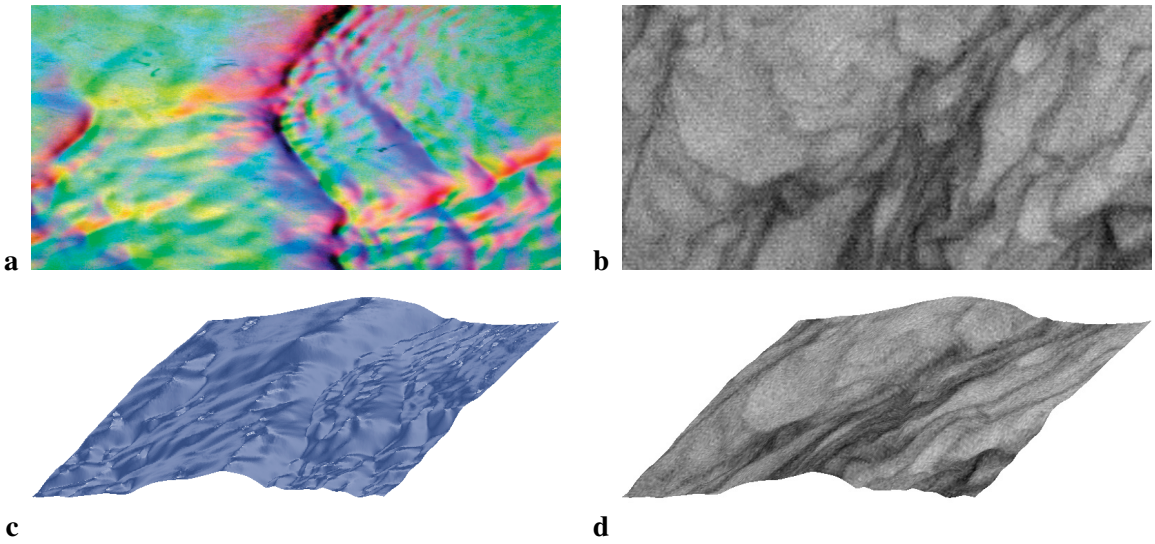

Figure 10.5: *The mapping of IR Data to height reconstructed slope data.* ***a*** *shows the slope data as gained from an ISG,* ***b*** *the registered IR data and* ***c*** *the height reconstruction of the water surface from the slope information. The IR data can then be mapped precisely to this height information and transport phenomena analyzed [Balschbach, 2001].*

From a single image and the camera parameters alone the three dimensional structure of objects under consideration can not be inferred fully, of course. However, in the absence of waves under conditions of low wind speed the sea surface can be represented to a first approximation by an infinite plane. From the camera parameters the image can then be projected onto this plane and thus effects due to distortions from the lens or viewing angle corrected for. This procedure, albeit a very crude one, is necessary if some conclusions are to be inferred from the optical flow field. This flow field will otherwise contain apparent motions due to deformations introduced by lens distortions or the viewing angle of the camera. Also, only through a correct calibration and reconstruction of the image information can the spatial extend of the footprint and the size of structures be estimated correctly.

The real benefit of geometric camera calibrations will however become apparent once the real three dimensional shape of the sea surface can be measured in the footprint of the IR image sequences. Only then can the observations be mapped correctly to undulations and thus new insights gained and current models refined. A simulation of such a mapping is illustrated in Figure 10.5. New experimental techniques are currently under development that will allow the accurate reconstruction of wave hight and slope based on a *stereo imaging slope gauge* [Fuß, 2003] or a stereoscopic set-up consisting of two infrared cameras [Hilsenstein, 2003], where the geometric calibration plays a central role in its own right.

10.2 Radiometric Calibration

While the geometric calibration is essential for deriving unobscured optical flow fields, the radiometric calibration is of equal importance for inferring actual temperature distributions in a scene from image intensities. This is a crucial step for subsequent analyses, as this mapping is the limiting factor of how

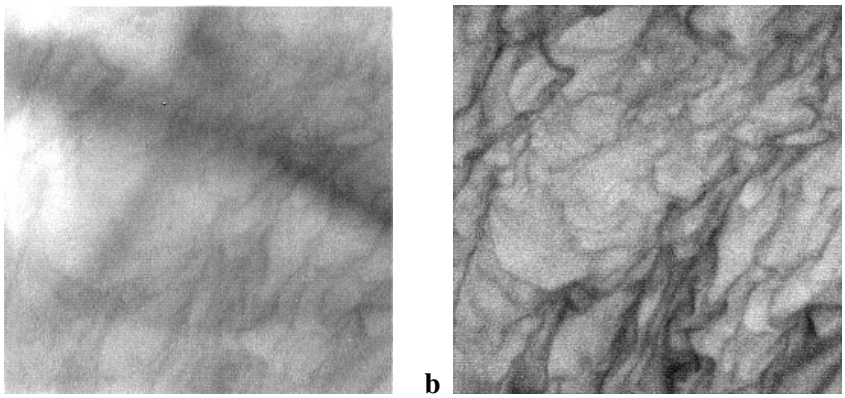

a **b**

Figure 10.6: *The importance of radiometric calibration for a reduction in infrared images can be seen from comparing an uncalibrated image in* ***a*** *with the calibrated analogon in* ***b*** *.*

Figure 10.7: *Shown is a Santa Barbara Infrared™Series 2100 blackbody akin to the one used for radiometric calibration in the context of this work.*

close the developed models can describe the actual physical processes. Additionally the InSb focal plane arrays of modern IR cameras are highly sensitive and as such every single image element will posses a slightly different grey value, even when imaging a completely homogeneous surface. This effect can be compensated by radiometric calibration only, rendering the images useless otherwise. This need for radiometric calibration in infrared imagery is very apparent as can be seen in Figure 10.6, while its importance for standard CCD cameras has been recognized only recently and attempts have been made for quantitative radiometric calibration of those imaging devices [Healey and Kondepudy, 1994; Gröning, 2002].

The signal S at a pixel of the camera, expressed as a grey value, is dependent on the temperature of the imaged object T. This dependency can be formulated according to [Haußecker, 1996]

$$S(T) = C_k \epsilon \int_0^\infty \frac{\mathrm{d}L(\lambda, T)}{\mathrm{d}\lambda} s(\lambda) w(\lambda) \, \mathrm{d}\lambda, \tag{10.2}$$

where $L(\lambda, T)$ is the radiance of the emitting surface, $s(\lambda)$ is the spectral sensitivity of the pixel, $w(\lambda)$ the weighting function due to the spectral transmittance of the optics and filter in front of the detector and C_k a constant of proportionality induced by the amplifiers and other effects of the camera. This

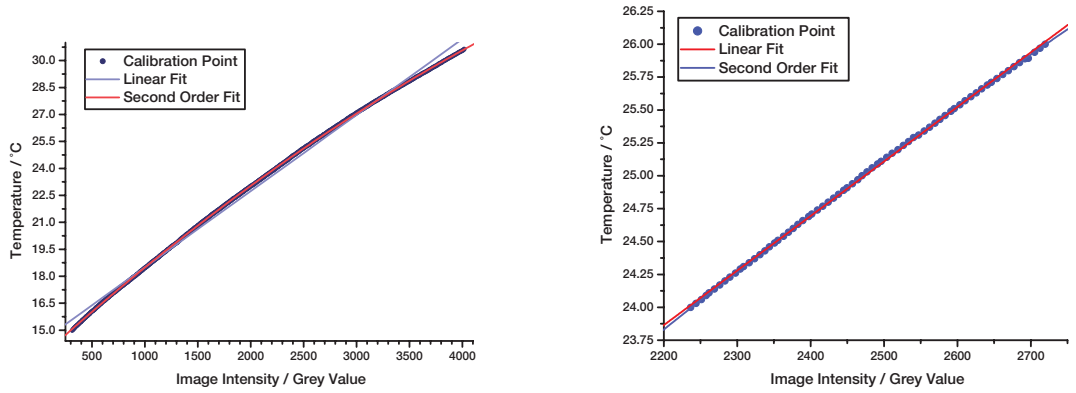

Figure 10.8: *The radiometric calibration covering the whole dynamic range of the IR camera is shown in* ***a*** *, where 584 data points were recorded. At the sea surface only a smaller temperature range is of interest which is shown in* ***b*** *. Here a range of only 2K was recorded with 71 data points.*

constant C_k may in fact also depend slightly on the wavelength λ due to nonlinear effects in the amplification of the signal. Because of the many factors influencing these parameters in the complicated system of a modern IR camera it is generally not possible to theoretically predict the actual signal S of the camera corresponding to a given temperature [Hierl, 2001].

Hence the camera signal S as a function of the temperature of a blackbody has to be measured experimentally. A commercially available blackbody, similar to the one used in the context of this work, is displayed in Figure 10.7. Of interest is the mapping of signal or image intensity of the camera to temperature $T(S)$, that is the inverse function of $S(T)$. This function can not be quantified theoretically but has to be deduced from measurements of a blackbody of known temperature. The temperature mapped to an image intensity is commonly approximated by a polynomial of n-th order, given by

$$T(S) = \sum_n a_n \cdot T^n. \tag{10.3}$$

In the applications presented in the context of this work the temperature range is very limited. For example, the thermal structures imaged at the sea surface have a dynamic range of only a few tenths of a degree. The order of the approximating polynomial is thus usually taken to be first or second order. In the following section it will be analyzed whether this is a valid approximation

10.2.1 Choosing the Optimal Polynomial Order

As given in Equation (10.3) the mapping of image intensity to grey value is approximated by a polynomial of n-th order. This immediately raises the question which order n has to be chosen in order to allow for a mapping sufficiently accurate for subsequent analyses. The F-test presented in Section 6.7 offers a vital statistical tool to answer this question. It allows us to distinguish between two hypotheses and chose the one promising more accurate results under the premiss of statistical significance.

The order of the polynomial will of course depend on the temperature range of interest. Therefore two scenarios were analyzed. As was indicated previously the temperature range at the sea surface is

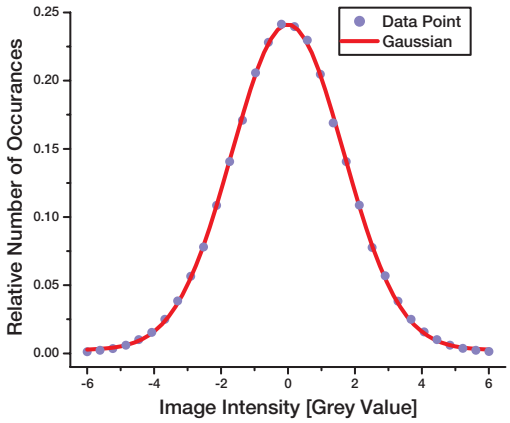

Figure 10.9: *The noise of an infrared camera in grey values. The fit of a Gaussian yields a standard deviation of* $\sigma_{\mathrm{ir}} = 3.3$ *grey values. This value will of course depend on the integration time chosen.*

of the order of one degree. In other applications at room temperature thermal variations will be no more than ± 10 K. To this end an extensive data set was produced with the aid of a *Santa Barbara Infrared*™blackbody shown in Figure 10.7. This set consists of 584 data points spanning a temperature range from $T_1 = 15.00$ °C to $T_2 = 30.63$ °C at a mean step size of $\Delta T = 27$ mK. This covered the dynamic range of the used AMBER Radiance I camera at an integration time of 1.301 ms with the step size ΔT slightly above the nominal noise level of NΔT = 25 mK. A plot of this data set is shown in Figure 10.8. In a first analysis the optimal polynomial order for the whole calibration curve was determined. More applicable to the application at hand was a second analysis in which only a small fraction of the data set was analyzed, spanning a temperature range of 3 K.

The analysis was conducted as follows: First a maximal polynomial order $n_{\max}$ was chosen. It was then hypothesized that a polynomial of order $n_i = n_{\max} - 1$ is an adequate representation of the data and the higher order presents no improvement in a statistical significant sense. This step is performed iteratively until the zeroth order polynomial is tested, represented by a line with intersect. The F-ratio, as defined by Equation (6.60), is then given by

$$F = \frac{\nu_i}{\nu_{i+1}} \frac{r_{i+1}}{r_i}, \quad \text{with} \quad \nu_i = m - (n_i + 1). \tag{10.4}$$

The summed squared residuals by the n_i-th order polynomial model are denoted by r_i and the number of observations or data points by m. The so called degree of freedom is represented by ν_i. The computed value for the F-ratio is then compared to the value $F(\nu_{i+1}, \nu_i)$, given in Appendix C.1 or C.2, depending on the desired confidence value of 5% or 1%.

In order to perform the fit of the polynomial model to the data, a scaling has to be performed as mentioned in to Section 6.1. This is due to the different noise levels present in the data. The deviation of the grey values of the infrared camera σ_{ir} will depend on the integration time chosen. In the present case this noise level was found to be $\sigma_{\mathrm{ir}} = 3.3$ as is portrayed in Figure 10.9. The nominal relative accuracy of the blackbody is given by the manufacturer as $\sigma_{bb} = 0.004$ K. From these values it was found that the order of polynomial is different depending on the range of data selected.

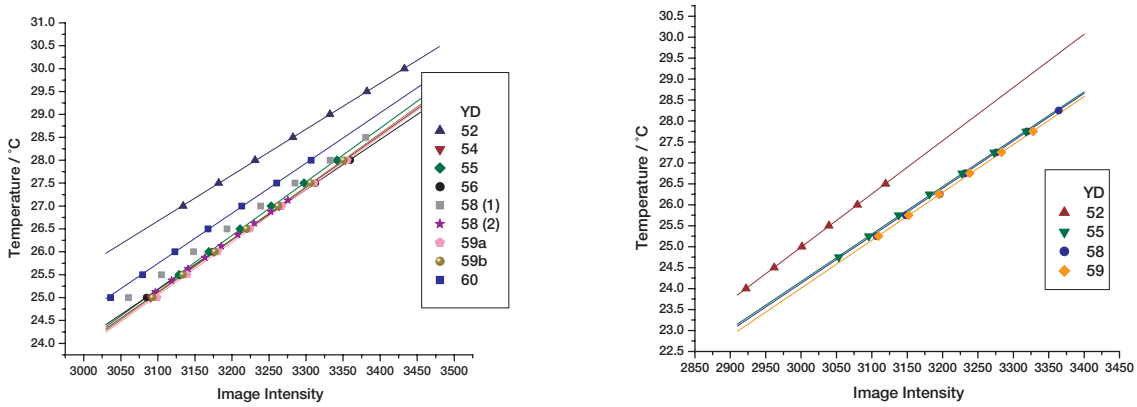

a **b**

Figure 10.10: *In **a** and **b** the calibration curves obtained prior to and after deployment of the instrument. YD (year day) denotes the day when the experiments were carried out. The absolute temperature indicated by the offset was found to change whereas the incline stayed roughly the same. No significant difference was found when changing the direction of temperatures set on the blackbody when changing from low to high values in **a** or the reverse in **b** .*

For the smaller range with less data points a second order polynomial was found to be the best model in the sense of statistical significance. On the full data range polynomials of higher order proved to fit the data better. Due to the shear number of data points the increase in degree of freedom is not as significant as in the case of less datums. Therefore even polynomials of ninth order were found to increase the accuracy of the fit. In practice a polynomial of third order is suggested.

10.2.2 Calibration of GasExII Data

In field experiments the calibration of the infrared camera cannot be conducted with as great an accuracy as under laboratory conditions. Due to time constraints much fewer data points can be recorded. Also the temperature difference between air temperature and that of the sea surface can be quite significant. In the GasExII field experiments temperature differences between the temperature on deck the ship and the water body of more than 15 K were not uncommon. Under these hostile conditions the blackbody takes much longer to equilibrate. In practice it was found that between 8 and 10 data points could be recorded with a temperature range of 3-4 K. Performing the hypothesis testing with the F test as outlined earlier, usually a second order polynomial was sufficient to fit the data. Higher order polynomials produced no significant increase in accuracy.

It is of importance to know how stable the calibration is during the cause of an experiment. In the context of this work temperature differences recorded with the camera are of interest. Therefore the absolute calibration is not as important, as a high relative accuracy. Performing the radiometric calibration procedure before and after the deployment, as well as on different days showed that the relative accuracy is always quite high, whereas the absolute temperature can drift by as much as half a degree. Performing a linear fit this corresponds to a change in the offset but a constant slope of the calibration curve. The data for the calibration of several days is shown in Figure 10.10 with the exact

a

YD	a	b
52	0.0100	-4.409
54	0.0114	-10.312
55	0.0117	-11.159
56	0.0109	-8.695
58(1)	0.0109	-8.213
58(2)	0.0112	-9.586
59a	0.0115	-10.720
59b	0.0116	-10.910
60	0.0111	-8.574

b

YD	a	b
52	0.0127	-13.127
55	0.0113	-9.769
57	0.0116	-10.661
58	0.0113	-9.878
59b	0.0114	-10.272

Table 10.1: *The parameters of the linear calibration $T = a \cdot g + b$, were the image intensity g of the central pixel is mapped to temperature T. In **a** the parameters for the ascending and in **b** of descending calibration curves are shown (see text).*

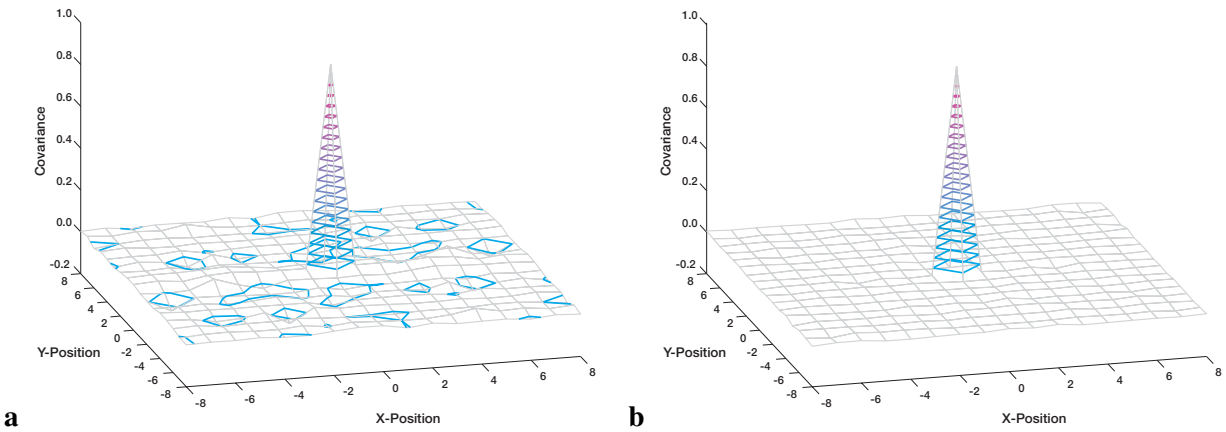

Figure 10.11: *In **a** is the autocorrelation of an image from the Amber Radiance IR Camera and in **b** that of an synthetic image of iid gaussian noise.*

parameters of the linear fit presented in Table 10.1. For comparison only a linear fit was performed because the main features of the fit are evident more easily in this simple model.

From Table 10.1 it can be seen that the incline of the calibration curve is relatively constant for all cases. The mean is (0.01133 ± 0.00026)°C, not counting the results from year day (YD) 52, as this may be viewed as an outlier. From Equation (5.20) the uncertainty in the incline is equivalent to an uncertainty of 0.516 W/m^2 in the heat flux j.

10.3 Noise Structure

As stated in Section 6.3 the total least squares (TLS) estimator will only produce optimal results, in the sense of maximum likelihood, in the presence of iid Gaussian noise. In gradient based optical flow computations, such as the ones presented in the context of this work, it is usually implicitly assumed that this is the case. However, the gradients are computed from convolutions with adequate filters in a

spatio-temporal neighborhood. The majority of pixels will thus be the same in neighboring estimates of the gradient. This makes it somewhat unlikely that neighboring estimates can be thought to be independent.

A discrete convolution is given by [Jähne, 1997]

$$G_{m,n} = \sum_{m'=-r}^{r} \sum_{n'=-r}^{r} H_{m',n'} G_{m-m',n-n'} = \sum_{m'=-r}^{r} \sum_{n'=-r}^{r} H_{-m',-n'} G_{m+m',n+n'}, \tag{10.5}$$

where $G_{m,n}$ is the grey value at the pixel position (m, n) and H the Mask of $k = (2r+1) \times (2r+1)$ coefficients. The two summations of the convolution of Equation (10.5) can be reduced to just one summation by performing lexicographical ordering, resulting in

$$f(G_{m,n}) = \sum_{i=1}^{k} a_i g_i, \tag{10.6}$$

where $\boldsymbol{a} = (a_1, a_2, \ldots, a_k)^\top$ is an adequately ordered vector made up of the elements of the filter kernel. From this equation the gradient at one pixel is computed. In the optical flow computations as proposed in Section 8.5 a number of such pixel enter the estimate to resolve the aperture problem stated in Section 8.4. This can then be simply thought of as a set of linear equations of the form of Equation 10.6, yielding

$$f(G_{m,n}) = \boldsymbol{A}\boldsymbol{g}, \tag{10.7}$$

where the columns of $\boldsymbol{A}$ are made up of the individual vectors $\boldsymbol{a}$. The covariance matrix $\Sigma\!\!\!/$ of such a set of linear equations is then by Equation (6.14):

$$\Sigma\!\!\!/(\boldsymbol{f}) = \boldsymbol{A}\, \Sigma\!\!\!/(\boldsymbol{g})\, \boldsymbol{A}^\top. \tag{10.8}$$

The covariance matrix of the individual pixels can be thought to be given by iid Gaussian noise, that is $\Sigma\!\!\!/(\boldsymbol{g}) = \sigma \mathbb{1}$. This has been verified for the used infrared camera. For perfect iid Gaussian noise the autocorrelation function defined in Equation (2.32) presents a peak at the origin dropping of to zero everywhere else. The autocorrelation of an homogeneous image of the infrared camera from a blackbody is presented in Figure 10.11. This shows that the noise of neighboring pixels can indeed be approximated by iid Gaussian nose quite accurately.

It follows from this that the covariance matrix for the gradient of neighboring pixels is given by

$$\Sigma\!\!\!/(\boldsymbol{f}) = \sigma^2 \boldsymbol{A}\, \boldsymbol{A}^\top. \tag{10.9}$$

This is to show that biases will result from the estimate if iid Gaussian noise is assumed for the gradients of neighboring pixels. For this reason the generalized total least squares estimator (GTLS) proposed in Section 6.6 has to be used together with the covariance matrix $\Sigma\!\!\!/(\boldsymbol{f})$ from Equation (10.9) to achieve unbiased estimates.

To show that the correlation of noise from neighboring gradients is quite strong, the autocorrelation of neighboring gradients have been computed. As a gradient filter the optimized Sobel filter was used, as this is the filter on which subsequent image sequence analysis will be based.

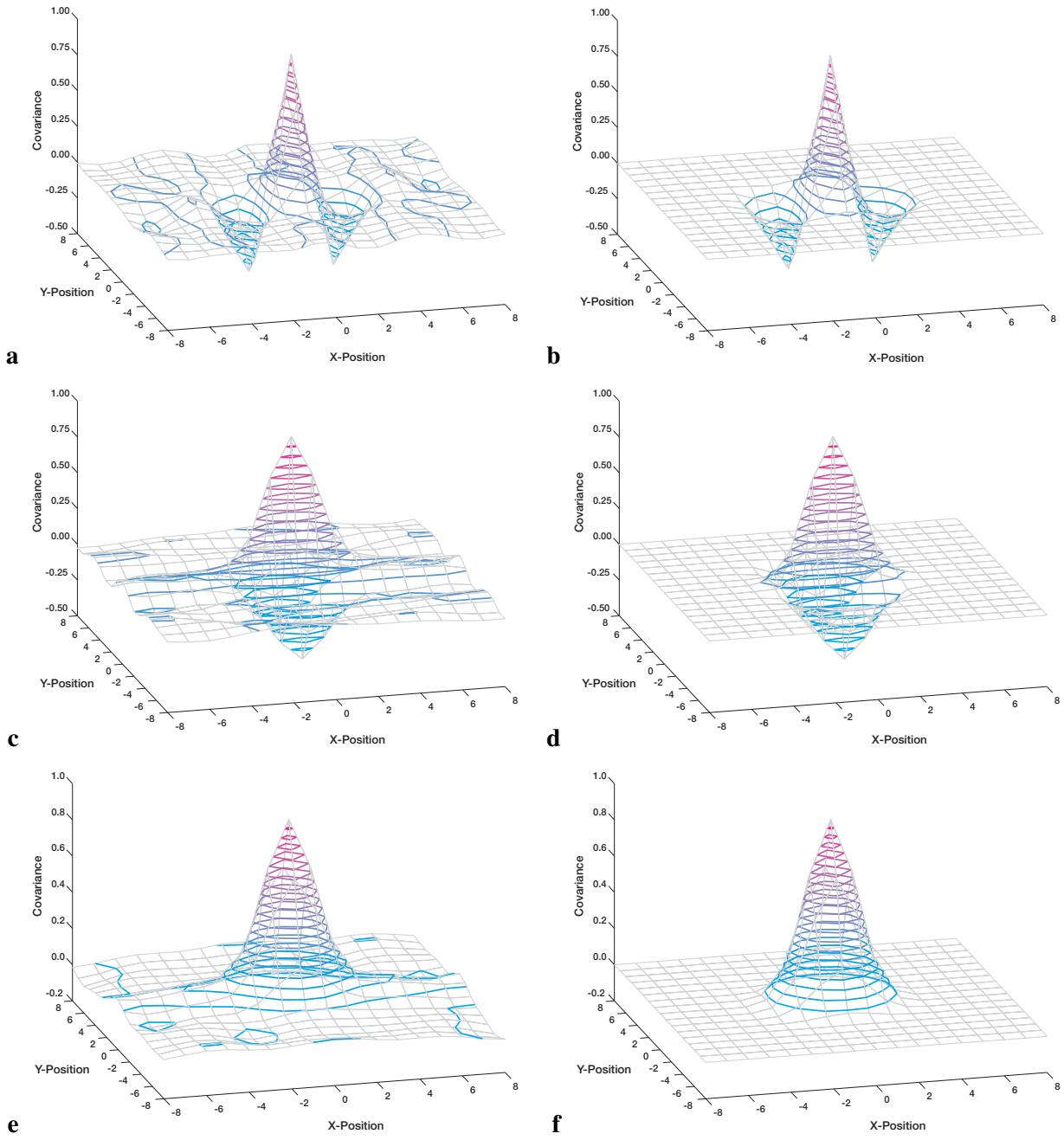

Figure 10.12: *The autocorrelation of an optimized Sobel operator on an IR sequence and on synthetic iid Gaussian noise normalized to one. In* ***a*** *and* ***b*** *for the derivative g_x, in* ***b*** *and* ***c*** *that for g_y and in* ***d*** *and* ***e*** *for g_z for the Amber Radiance and synthetic noise respectively.*

The results of the autocorrelation for the gradients in the three spatio-temporal direction ($x, y, z = t$) are shown in Figure 10.12. The computations have been conducted for real images from the infrared camera and for synthetic images, showing a slight deviation due to imperfections of the camera. In the optimized Sobel operator a convolution is also performed in the directions orthogonal to the gradient to be computed. This effect was analyzed by computing the cross correlation between gradients of

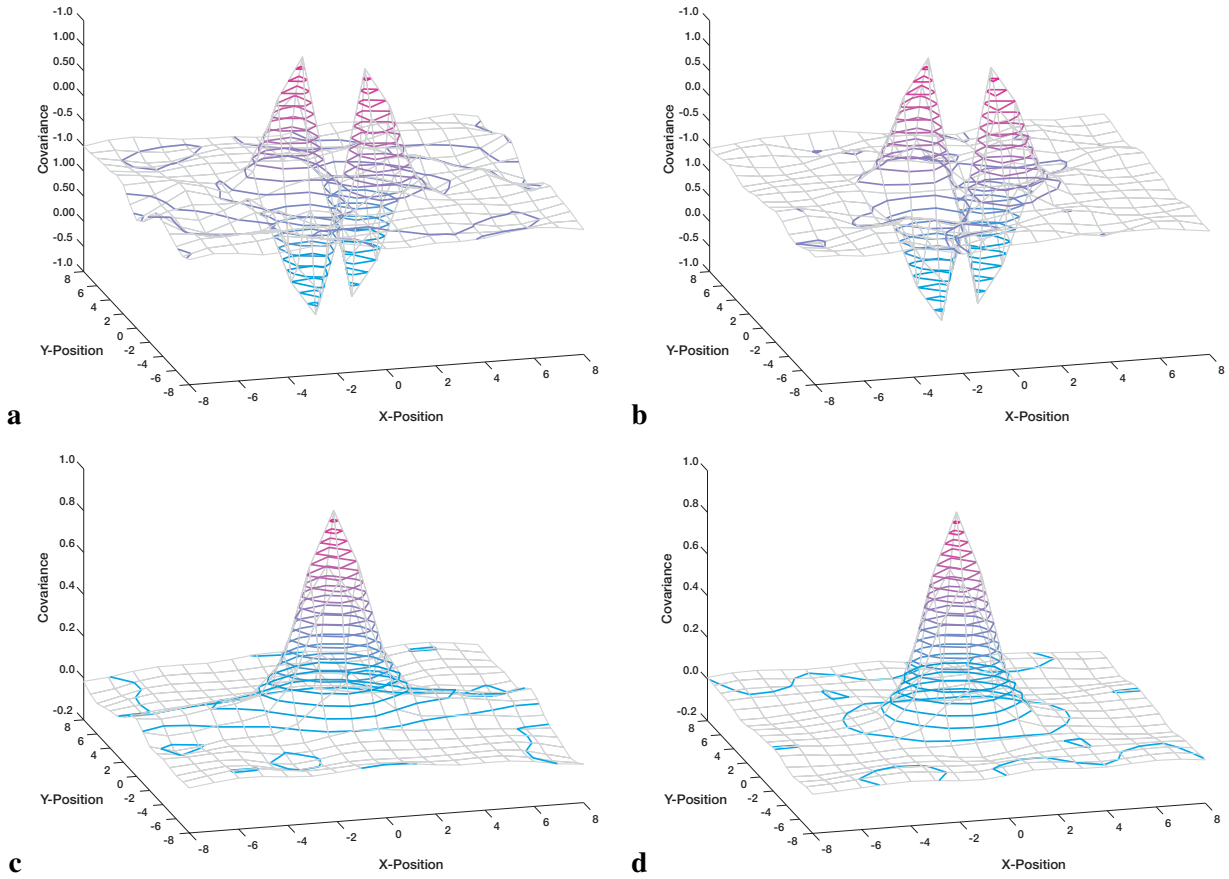

Figure 10.13: *The correlation of g_x and g_y of a IR sequence in* ***a*** *, and the same correlation for synthetic noise in* ***b*** *. In* ***c*** *and* ***d*** *is the correlation of g_x with g_z for Amber Radiance and noise respectively.*

different directions. The correlation can clearly be seen from Figure 10.13. This shows that biases will result from taking the noise of neighboring gradients to follow a iid Gaussian distribution. The covariance matrix has to be estimated from Equation (10.9) and the data scaled according to the technique presented in Section 6.1. Alternatively, the GTLS estimator introduced in Section 6.6 can be used, resulting in a numerically more stable estimate.

10.4 Summary

The concept of geometric and radiometric calibration has been introduced. The importance of both types of calibration has been outlined and the method used in subsequent analyses presented. Due to optimum model selection based on hypothesis testing a second order polynomial is the model of choice for the field data as presented in Chapter 12. It was shown that the noise of neighboring gradients cannot be thought of as iid Gaussian noise and biases result from making this false assumption. On both synthetic and real data from an infrared camera the correlation of the noise in the gradients has been explicitly given.

Chapter 11

Laboratory Flux Measurements

In the newly developed circular wind/wave facility at the University of Heidelberg, the Aeolotron, four measurements at different wind speeds were conducted. The facility is unique because it was specifically designed and build to perform highly accurate air-sea gas and heat exchange measurements. In this respect great care was taken in ensuring optimal thermal properties for employing novel experimental techniques based on infrared cameras, such as the one presented in this work. The Aeolotron thus presented an optimal facility for testing the new method of estimating the net heat flux and comparing results to *ground truth* data. That is the mean net heat flux is computed to a high accuracy from other sensors. The novel technique was tested under various conditions of wind speed, thus testing limitations and accuracy of estimates for later situ measurements presented in Chapter 12.

In the following, first the experimental facility will be introduced and key features stated (Section 11.1). The specific experimental set-up is briefly outlined in Section 11.2 and the realization of the measurements reported. Methods of determining the temperature depression across the thermal boundary layer will be introduced in Section 11.4. Assumptions concerning the probability density function (pdf) of surface renewal are verified in Section 11.5 and measurements of the net sea-surface heat flux conducted in Section 11.6. Ground truth data of this heat flux are used in Section 11.6.1 to ascertain the validity of results obtained with the new technique in Section 11.6.2. This chapter then concludes with a brief overview of the results in Section 11.8.

11.1 The Heidelberg Aeolotron

The Heidelberg *Aeolotron* is a dedicated circular wind wave facility that makes accurate air-water gas and heat exchange measurements feasible. For this reason great effort was undertaken in achieving a gas tight air space [Jähne et al., 1999]. The facility is pictured in Figure 11.1. Wind speeds of up to 15 m/s can be attained by a rotating fibre glass enforced paddle ring, driven by 64 100 W DC motors. To allow precise heat flux measurements the walls of the Aeolotron are insulated by a 9 cm thick layer of Styrodur™ and are coated with a highly reflective aluminium foil in the air space. This ensures that the heat is transported predominantly through the water surface and not the walls of the facility, which is verified experimentally in Section 11.6.1.

In order to vary the heat flux the temperature of the water body can be heated by a 15.2 kW heating

a  **b** 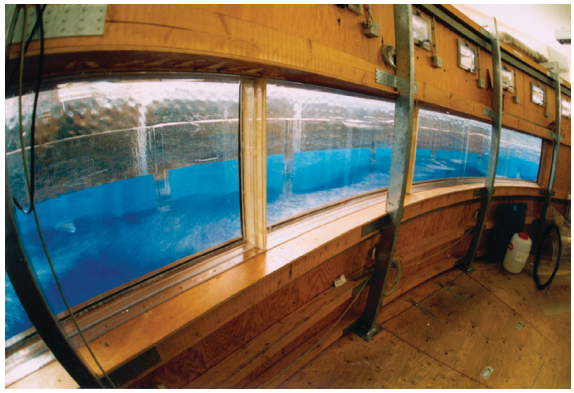

Figure 11.1: *In* ***a*** *a picture of the circular Heidelberg Aeolotron and a view of the wave field in* ***b*** *.*

Channel Height	Channel Width	Inner Radius	Outer Radius	Mean Circumference	Volume of Channel
2.407m	0.616m	4.241m	4.958m	29.217m	44.68m^3

Water Surface Area	Nominal Water Depth	Nominal Water Volume	Maximal Wind Speed
18.00m^2	1.15m	20.70m^3	15m/s

Table 11.1: *Key technical data of the Heidelberg Aeolotron.*

system. The air space can be controlled by a closed loop air conditioning system with independent control of humidity and air temperature. High positive and negative heat fluxes at the water interface of more than 1 kW/m^2 are achievable by 64.1 kW cooling and 15.6 kW heating capacity of the gas space. In this system a controlled amount of gas is first cooled down and after condensation heated back up. For gas exchange measurements separate air renewal systems with rates of up to 1000 m^3/h are available. Gas concentrations can be measured independently in the air and water space with a high relative accuracy [Kalkenings, 2002]. The water body can be cleaned by filters and an UV oxidation system. For experiments water of different salinity ranging from fully deionized water to sea water can be stored in separate 28 m^3 storage tanks, thus allowing a relatively quick water renewal. In the presented work experiments were always conducted in deionized water. To enable accurate measurements at high wind speeds the water body can be directed with speeds of up to 0.6 m/s against the circulation direction of the wind. This allows to create slowly moving or even stationary waves that can be analyzed accurately. A list of important parameters of the Aeolotron can be found in Table 11.1.

11.2 Experimental Set-Up

The techniques presented in this work are passive techniques as no active elements such as lasers are needed for heating up patches of water. The experimental set-up is thus much simpler than of active techniques [Haußecker, 1996]. However, because the temperature structures at the air-water interface

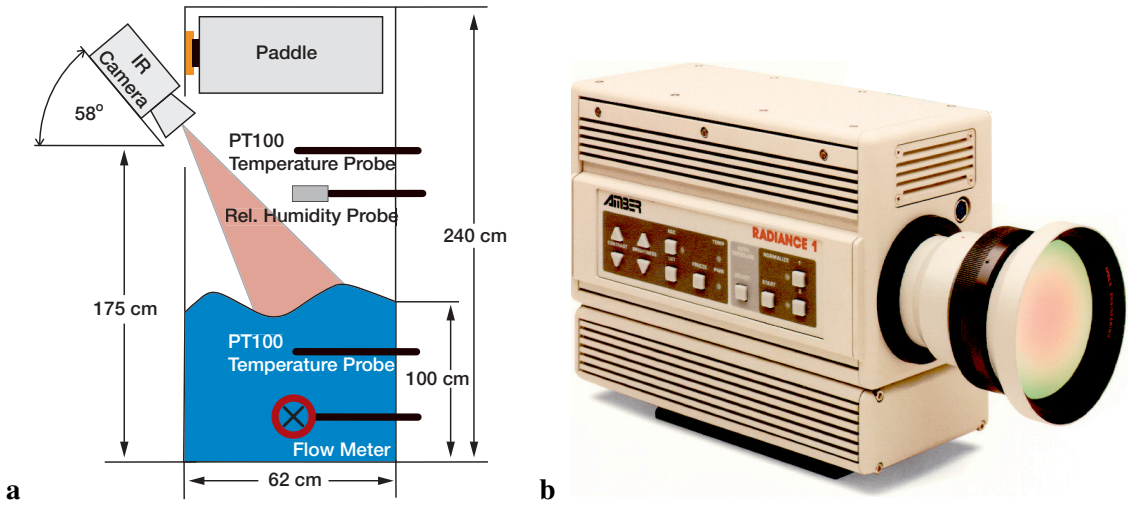

Figure 11.2: *In* ***a*** *a schematic cross section of the Heidelberg Aeolotron can be seen. An infrared camera images a* (50×50) cm^2 *area of the water surface, with an angle of incidence of about 30°. In* ***b*** *is an image of the used Amber Radiance I camera.*

are minute, great experimental care has to be taken not to obscure the investigated processes.

Central to the experimental set-up is of course an infrared camera. In recent years commercial camera systems are readily available providing high frame rates and low noise levels. However, in the present context the temperature differences to be analyzed are very small and thus close to the noise level of modern cameras. The same holds true for the frame rate, as surface drift and wave motion is significant at higher wind speeds, calling for higher sampling rates to circumvent motion blurring or problems due to Shannon's sampling theorem.

As was stated earlier the temperature difference across the air-sea interface is often in the order of $0.01 - 0.3$ K. This is roughly equivalent to the dynamic range of temperature structures at the sea surface. The noise equivalent temperature difference (NEΔT) is of the order of 25 mK in modern IR cameras, giving a signal to noise ratio γ of around $\gamma = 4$. However, the temperature changes with respect to time found at an individual pixel are of the order of around 2 mK/frame. This change is well below the noise level of the camera and can therefore only be resolved by integrating over a spatio-temporal neighborhood. In this respect the techniques presented in this work would improve immensely from imaging devices with even lower noise level.

In this work an Amber Radiance 1 camera was used which is based around a Stirling cooled InSb detector made up of a square 256×256 focal plane array. This sensor is sensitive in a wavelength window of $3 - 5$ µm. A picture of such a camera is presented in Figure 11.2. The individual elements of the focal array are evenly spaced 38 µm with the edge length of active elements measuring 34 µm. The frame rate of the camera is 60 Hz with integration times usually chosen between 1.3 and 1.9 ms, depending on the temperature of the water body. Longer integration times tend to exhibit a better signal to noise ratio while increasing the danger of overflows occurring in the image. The detector has to be kept at a constant temperature of 77K in order to keep the noise in an acceptable range. Otherwise the detector would be flooded with charges due to its own temperature. As stated previously the NEΔT of this camera is 25 mK.

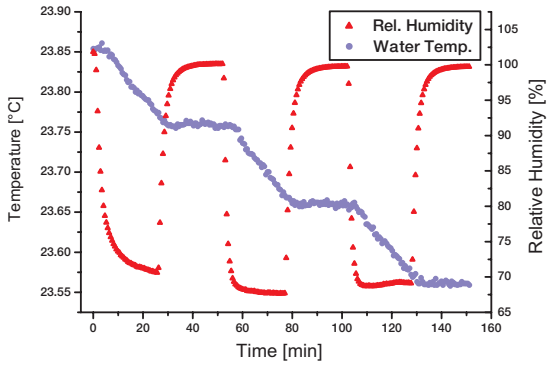

Figure 11.3: *The water temperature and the relative humidity of the experiment conducted at with a wind speed of 4.2 m/s is shown in* ***a*** *.*

11.3 Experimental Procedure

Four experiments in different wind regimes were conducted at the Heidelberg Aeolotron. In this section the experimental procedure as well as the conditions of both air and water space shall be briefly presented.

In order to accurately measure the parameters of air-sea heat exchange and compare results to ground truth data, the heat flux at the water surface has to be periodically switched on and off. In the absence of a heat flux, the temperature difference between the cool surface layer and the warm bulk water equilibrates and the thermal boundary layer disappears, that is $\Delta T = T_{\mathrm{surf}} - T_{\mathrm{bulk}} = 0$. This results in a homogeneous temperature field at the air-water interface with the same absolute temperature as that of the bulk water. The mean temperature $\overline{T_{\mathrm{surf}}}$ measured with the infrared camera during this time is thus equivalent to the temperature of the bulk water T_{bulk}. In the presence of a heat flux the thermal boundary layer develops and the temperature difference ΔT across the sub-layer evolves. Due to the turbulent field impinging on the thermal sub-layer, thermal structures reappear. From these structures the estimation of the parameters of air-water heat transfer can be estimated with the techniques presented in Chapter 5. It was switched periodically between conditions of fluxes and no fluxes to allow for an assessment of the accuracy under reproducible conditions.

As was stated in Section 3.2 the net heat flux j at the air-water interface is made up of three constituent fluxes, namely the sensible heat flux j_{sens}, the latent heat flux j_{lat} and the heat flux due to radiative transfer j_{rad}, thus $j = j_{\mathrm{sens}} + j_{\mathrm{lat}} + j_{\mathrm{rad}}$. In a laboratory facility such as the Heidelberg Aeolotron it is possible to specifically influence these constituent fluxes. Under conditions found on the open ocean during night the net heat flux is mainly dominated by the latent heat flux j_{lat} due to evaporative cooling of water, evidence of which will be presented in Section 12.2.2. In laboratory conditions this is also the constituent flux best suited for purposely imposing strong net heat fluxes. The constituent fluxes of sensible and radiative transport of heat are kept small enough to be negligible in the present context. Effects due to a sensible heat flux j_{sens} are eliminated by ensuring the same temperature of the air and water space, thus $T_{\mathrm{bulk}} \equiv T_{\mathrm{air}}$. Small fluctuations between the two temperatures of less than a K will have an insignificant effect on the net heat flux, as can be seen from

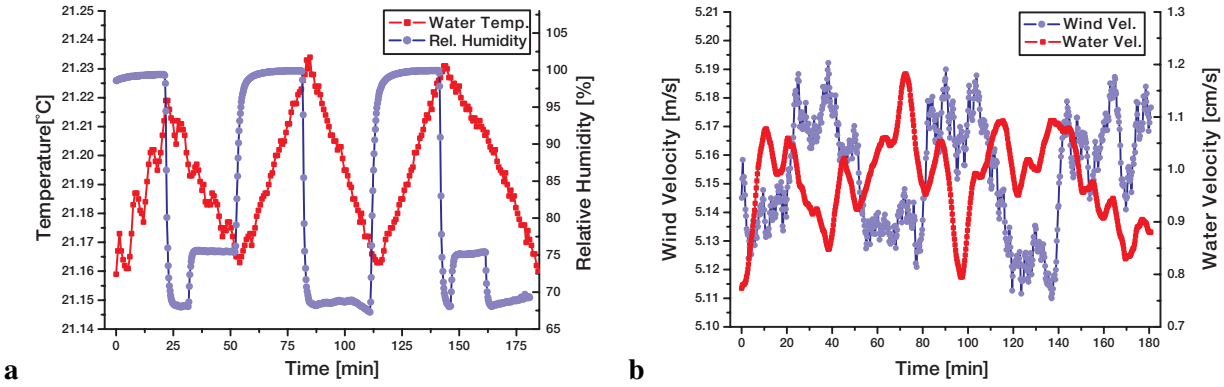

Figure 11.4: *In* ***a*** *a plot of the water temperature and the relative humidity is shown and in* ***b*** *the wind and water velocities. The data was taken at the experiment conducted on the 17.12.2000.*

Equation (3.29). The radiative heat flux j_{rad} is minimized by the coating of the walls of the Aeolotron with highly reflective aluminium foil. The high reflectivity causes almost no absorbtion or emission of heat, leading to an equilibrated state between the irradiance E and the exitance M at the water surface and thus no net heat transport.

By taking these precautions concerning the sensible heat flux j_{sens} and the radiative heat flux j_{rad}, the net heat flux j is exclusively controlled by the latent heat flux j_{lat} and can be thought equal to it within the accuracy limits. As is evident from Equation 3.30 the latent heat flux j_{lat} is controlled by the relative humidity h of the air space. In the experiments conducted in the Aeolotron this constituent flux was thus modulated by regulating the relative humidity h between $h = 100\%$ and $h \approx 60\%$ with an air conditioning system in the closed air space. Due to the resulting heat flux j the water body cools down by an amount specified in Equation (2.20). Both the relative humidity h and the temperature of the water body for a typical experiment can be seen in Figure 11.3. For prolonged experiments it is desirable to counteract the temperature decline due to the heat flux resulting in a constant mean temperature of the air and water space. For an experiment conducted with such an added heat source in the water body, the relative humidity and the temperature of the water body are presented in Figure 11.4. The temperature of the water body is measured at a water depth of about 50 cm.

The experiments were conducted under different wind speeds, estimating the parameters of heat flux with the novel techniques for a variety of different conditions often encountered in the field. The mean wind speeds recorded for the experiments were 2 m/s, 4.2 m/s, 5 m/s and 8 m/s. All the experiments were conducted in the same fashion by varying the relative humidity as described previously. Except for the measurement conducted with a wind speed of 5 m/s no additional heat source was present in the water, counteracting the net heat flux. During this experiment the UV oxidation system was turned on, constantly cleaning the water. The power consumption of the system is in the order of a few kW, heating up the water. Furthermore in this experiment the mass fluxes of CO_2, CH_4 and N_2O was measured at the same time as the net heat flux was measured. Although the accuracy of measuring these gas fluxes have been improved since that measurement [Kalkenings, 2002], the results still provide useful information on the validity of the estimated heat transfer velocity k_{heat}.

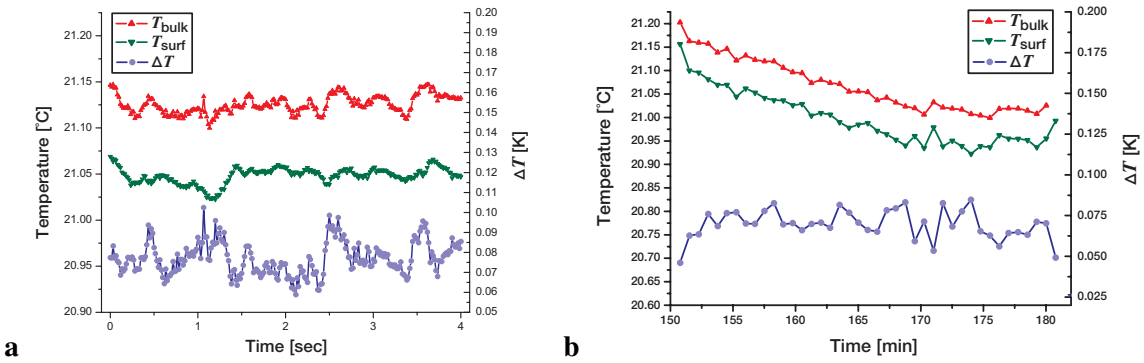

Figure 11.5: *The temperature of the water surface T_{surf} and the water bulk T_{bulk}, as well as the temperature difference across the cool skin ΔT estimated from the infrared imagery. In **a** the high temporal resolution with the frame rate of the camera is shown and in **b** the mean value from the individual sequences, plotted against the time since the start of the measurement. The data was taken at a wind speed of 5 m/s.*

11.4 Estimating the Temperature Depression

The temperature depression ΔT across the cool skin of the ocean can be measured in the Aeolotron in two ways. In the context of this work the most important technique of measuring ΔT is obviously computing the temperature depression from the statistical analysis of the infrared imagery as outlined in Section 5.2. The reason is that only this analysis is equally applicable to the sea surface in field measurements. Also the temperature depression is estimated with the same device as the other parameters of heat exchange, resolving cross calibration issues.

Another way of measuring ΔT can be conducted by intermittently switching the net heat flux j on and off. As has been explained earlier in the absence of a net heat flux the cool skin of the ocean equilibrates and the surface temperature T_{surf} is equivalent to the bulk temperature T_{bulk}. This leads to a homogeneous image in the infrared camera of the bulk temperature T_{bulk}. In the presence of a net heat flux j the thermal boundary layer develops and the surface temperature T_{surf} is different to that of the bulk T_{bulk}. Correcting for a decline of the bulk temperature due to the heat flux, the temperature depression $\Delta T = T_{\mathrm{surf}} - T_{\mathrm{bulk}}$ can be computed from the images gained during flux and no flux conditions. An extensive analysis of this method has been performed by Schimpf [2000] for different wind speeds and surfactants. The results of this method for estimating ΔT were compared to the one from the statistical analysis introduced in Section 5.2, testifying both methods an excellent agreement at all wind speeds examined, ranging from 1.2 m/s up to 6.1 m/s. It was shown that the statistical analysis presents a strong bias towards lower estimates at low wind speeds in the presence of surface slicks. This was attested to a damping of turbulences due to the surface active film [Schimpf, 2000].

Due to the excellent agreement of the techniques here only the method of estimating the temperature depression from the statistical analysis will be used. The measurement for the experiment with a wind speed of 5 m/s is shown in Figure 11.5. Due to the high wind speed, waves and strong sub-surface turbulence are present, resulting in very short time spans t_* a water parcel stays at the surface. Thus surface renewal events are frequent and enough information is attained in every single frame from the infrared camera to warrant the statistical analysis on a per frame basis. Estimates of the temperature depression at the sea surface are thus possible with a high temporal resolution. In

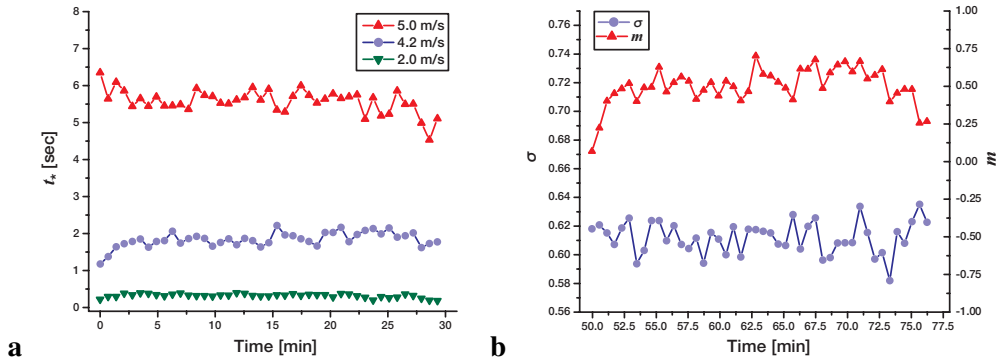

Figure 11.6: *The results of the statistical analysis of times τ between surface renewal events. In* ***a*** *the characteristic time constant t_* for experiments conducted at wind speeds of 2.0,4.2 and 5.0 m/s are shown and in* ***b*** *the parameters σ and m of the logarithmic normal distribution for the experiment at a wind speed of 4.2 m/s.*

weaker winds and less frequent surface renewal events, several frames might be necessary to conduct the analysis in a statistically significant manner.

An error analysis of this method for calculating the temperature depression on synthetic data has been presented in Section 9.4. It was shown that an accuracy of less than 3 mK can be expected, a value well in agreement with the empirical findings by Schimpf [2000]. This implies that the fluctuations seen in Figure 11.5 are not caused by inaccuracies in the estimation due to camera noise, but might be modulations due to waves. However, without a correlation of the infrared data to precise slope information a conclusive analysis is beyond the scope of this thesis.

The results for the experiments conducted at different wind speeds are very similar in appearance. As an example the results of an individual sequence is presented in Figure 11.5. The values estimated for the temperature depression during the different experiments are presented in Table 11.3.

11.5 The PDF of Surface Renewal

Due to the significance of the statistical distribution of times between surface renewal events for the development of models describing the transport, the statistical analysis introduced in Section 5.3 was performed on the measurements conducted at the Aeolotron. The frequency data of the times of residence at the sea surface τ show a remarkable resemblance to the logarithmic normal distribution

$$p(\tau) = \frac{1}{\sqrt{\pi}\sigma\tau/t'} e^{-\frac{(\ln \tau/t' - m)^2}{\sigma^2}}, \quad \tau > 0, \tag{11.1}$$

and are described by it very well. In this equation t' is the unit scaling factor. No significant deviation from this distribution could be detected at any wind speed examined.

From the estimated parameters σ and m the characteristic time of residence at the sea surface can be computed, following Equation (2.52)

$$t_* = \int_0^\infty p(t)\, t/t'\, dt = t' \cdot e^{\frac{\sigma^2}{4}+m}. \tag{11.2}$$

Wind Speed	σ	m	t_* [s]
2.0 m/s	0.62 ± 0.02	1.65 ± 0.003	5.81 ± 0.05
4.2 m/s	0.61 ± 0.02	0.50 ± 0.02	1.82 ± 0.03
5.0 m/s	0.39 ± 0.02	-1.13 ± 0.12	0.32 ± 0.05
8.0 m/s	0.37 ± 0.02	-1.10 ± 0.09	0.34 ± 0.04

Table 11.2: *Results of the statistical analysis.*

A plot of this value for different wind speeds is presented in Figure 11.6. Shown are the results of 43 sequences consisting of 100 images each. The exact values of the parameters σ and m as well as the time constant t_* can be found in Table 11.2.

11.6 Heat Flux Measurements

The main purpose of the measurements conducted in the Heidelberg Aeolotron was to test the validity of proposed algorithms of estimating the net heat flux j at the sea surface. In that respect the different techniques of estimating j had to be compared to each other, as well as to a ground truth measure of the flux. Only through this analysis can the confidence bounds for the techniques be established as well as the limitations revealed.

11.6.1 Ground Truth of Net Heat Flux

The Heidelberg Aeolotron is equipped with a Prema™ 3040 high precision thermometer collecting data from eight calibrated PT100 sensors in the water body. The precision of this thermometer is specified to 0.001 K with an accuracy of measurements with the PT100 elements of 0.004 K [Prema, 2000]. This allows for very precise measurements of the bulk temperature. From this the temperature change of the bulk water can be estimated, which is directly related to the net heat flux. Thus ground truth data for the heat flux j_{true} can be gained and compared to the results estimated by the proposed algorithms. Following Equation (2.19) the heat flux can be calculated according to

$$j_{\mathrm{true}} = \frac{dQ/dt}{A} = \frac{Mc_p}{A}\frac{dT}{dt} = \rho c_p h \frac{dT}{dt}, \tag{11.3}$$

where use was made of the fact that the mass of the water body M is given in the Aeolotron by $M = \rho h A$, with the height of the water h. By measuring the temperature of the bulk water and its change over time, the net heat flux can thus be attained. It is vital for a subsequent evaluation to know the accuracy of the ground truth measurement. From error propagation the error in estimating the ground truth is given by

$$\sigma_j = \rho c_p \sqrt{\left(\frac{dT}{dt}\sigma_h\right)^2 + \left(h\sigma_{dT/dt}\right)^2}, \tag{11.4}$$

and consequently the relative error by

$$\frac{\sigma_j}{j} = \sqrt{\left(\frac{\sigma_h}{h}\right)^2 + \left(\frac{\sigma_{dT/dt}}{dT/dt}\right)^2}. \tag{11.5}$$

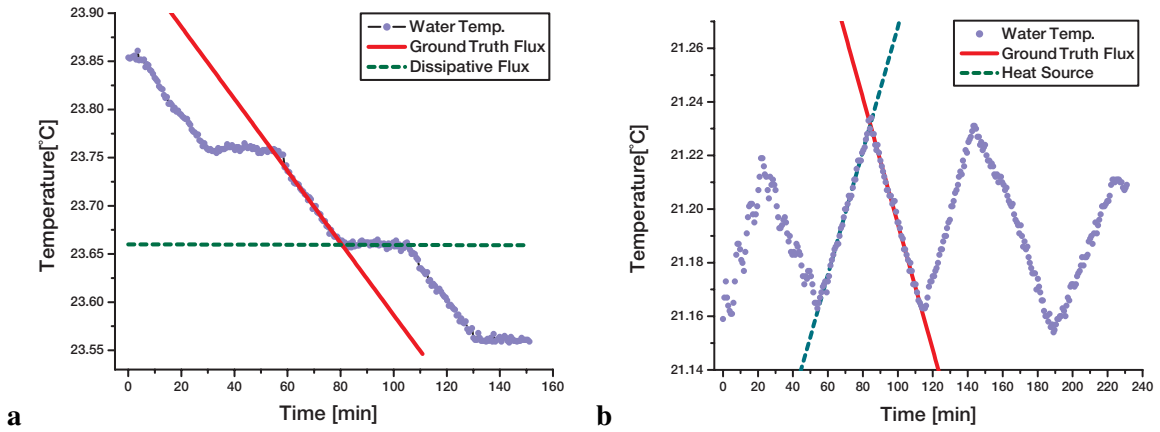

Figure 11.7: *The regression to the temperature decline of the water body. Shown are the temperature gradients from which the relevant fluxes are computed. The ground truth heat flux j_{true} is estimated from fitting a linear temperature decline to the data in the presence of an interfacial heat flux. It has to be corrected for dissipative fluxes through the walls of the facility. Due to the excellent thermal properties of the Aeolotron this term can be neglected as can be seen from the fit in* ***a*** *. When no interfacial heat flux is present, the temperature decline is almost zero. The ground truth heat flux has to be adjusted in the presence of an additional heat source as is visible in* ***b*** *.*

The temperature decline dT/dt is estimated from linear regression by fitting a line with intersect ($y = ax + b$) to the part of the data, where a constant heat flux is present, as is shown in Figure 11.7. The fit can be performed to a relative accuracy of less than 1% and the measurement of the water height in the Aeolotron is performed with an acoustic measuring device, with a relative accuracy much better than that. The total relative accuracy of the net heat flux measured this way is thus equally better than 1%.

For an accuracy evaluation of the proposed algorithms only the net heat flux through the air-water boundary is of interest. Above that, the heat flux j_{true} derived from the temperature change of the water body does also include heat fluxes caused by heat dissipation through the walls of the facility. In that respect it is vital to measure this dissipative heat flux and correct the ground truth flux through the water surface accordingly. This can be done by computing the net heat flux from Equation (11.3) during times devoid of an air-water interfacial heat flux. The flux measured this way was found to be below 0.48 Wm^{-2} during all experiments conducted. Fluxes of this magnitude are of the order of accuracy for the ground truth measurement and thus negligible.

The values of the ground truth heat flux j_{true} estimated from the technique introduced in this section are presented in Table 11.3.

11.6.2 Non-Invasive Heat Flux Estimation

The technique of measuring the net heat flux outlined in the previous section presents a means of deducing highly accurate estimates. However, in this fashion only mean fluxes can be computed as the integration time has to be long enough to detect a significant decline in temperature. It is neither spatially resolved nor applicable in less well controlled conditions as found in the Aeolotron. Hence its use is limited to validating the non-invasive approaches presented in this work.

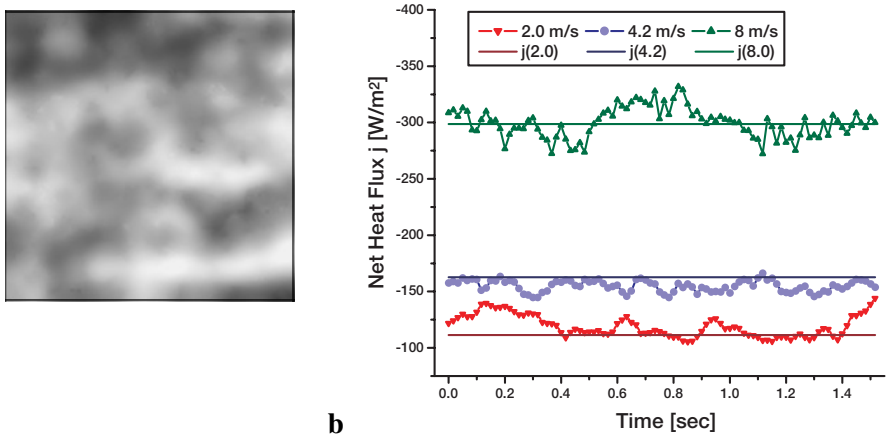

Figure 11.8: *The spatially highly resolved heat flux for an individual frame is shown in* ***a*** *, where bright areas indicate strong heat fluxes. Computing the mean from every frame the fluxes for one sequence is shown in* ***b*** *, underlining the high temporal resolution yet high accuracy as can be seen by comparison to the corresponding values for the ground truth* $j_{\mathrm{true}} = j(x)$*. The estimates seem to be undulated by wave motion.*

Both the square root method for estimating the heat flux j_{sqrt} introduced in Section 5.4.2 as well as the pdf method proposed in Section 5.4.3 were used for computing the heat flux in the experiments. As stated earlier the square root method is the preferred technique for it is not statistical in nature. Apart from making far less assumptions on the nature of the heat transfer process, only this approach makes both spatially and temporal highly resolved estimates possible. Strong experimental evidence that the times between surface renewal events follow a logarithmic normal distribution has been presented in Section 11.5. This makes the approach of the pdf technique seem valid, which is based on just this premiss. The accuracy of the results obtained from the pdf method thus indicate another verification of this assumption, albeit much more indirect than the one presented earlier.

Results of the square root technique are presented in Figure 11.8. Shown is the extraordinary high spatial resolution with estimates resolved to a few millimeters. The accuracy of the technique can also be seen in a sequence in which the mean heat flux estimated from individual images is shown and compared to the ground truth heat flux j_{truth}. It should be noted that the temporal resolution is the frame rate of the infrared camera which was 60 Hz in the measurements conducted in the Aeolotron. The fluctuations in the estimate are not due to errors but seem to be undulated due to waves passing through the imaged area. The question how the heat flux is correlated to the wave slope cannot be answered at the current time. Work is in progress for measuring spatially resolved surface slopes in the footprint of the infrared camera [Fuß, 2003], which might shed some light on this question.

Presented in Figure 11.9 is the resulting heat flux estimate during the time of low relative humidity in the Aeolotron. Shown are the heat fluxes computed from both the square root method and the pdf method, as well as the ground truth value. The values shown are means derived from 90 images. The sudden decrease in the heat flux at the end of the measurements is due to the air conditioning system being turned off, leading to a sharp rise in relative humidity, which in turn causes the heat flux to terminate.

Deviations in the estimate are largely due to fluctuations in the estimation of the temperature

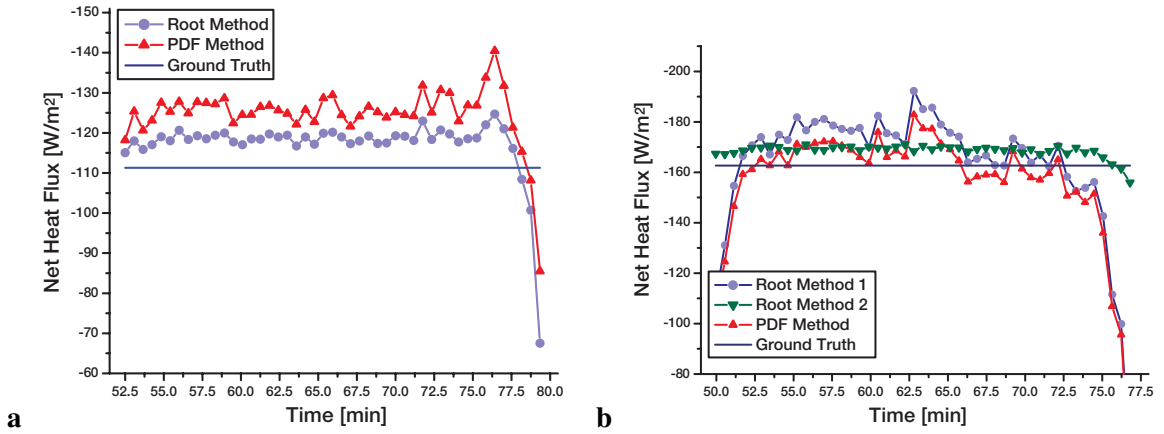

Figure 11.9: *Heat flux estimate for wind of 2 m/s in* ***a*** *and 4.2 m/s in* ***b*** *. Shown are the results from the pdf method j_{pdf} and the square root method j_{root}, as well as the ground truth value j_{true}. In* ***b*** *j_{root} was computed with the value of ΔT estimates from the corresponding sequence (method 1) and also with the same mean value $\overline{\Delta T}$ from all the sequences (method 2). This shows that the fluctuations are due to the fluctuating estimate of ΔT.*

difference ΔT. This is evident from Figure 11.9 **b** where the heat flux was computed using the square root method with the estimated value for ΔT from every single sequence and with the mean value for ΔT from all the sequences. The estimate with the same value for ΔT hardly fluctuates at all.

It can be seen that both the estimates j_{root} and j_{pdf} are very close in accuracy. However, there seems to be a bias for the pdf method at low wind speeds towards higher values, whereas it seems to be closer to the ground truth j_{true} at higher wind speeds as compared to j_{root}. Overall both estimates seem to be closer to the true value in stronger winds than in the low wind case of 2 m/s. An explanation for this wind dependence is that slight surfactant concentrations have a stronger influence in conditions of low wind speed than in higher wind regimes where they tend to break up. The pdf method might perform less well than the square root method in lower wind conditions, because the model of surface renewal with a logarithmic normally distributed probability density function might not describe transport processes as well as in higher wind conditions. This might be due to a change from buoyancy driven transport to a shear driven one in the transition from low wind to high wind conditions.

The mean estimates for all the measurements can be found in Table 11.3.

Wind Speed	ΔT [K]	j_{true} [Wm^{-2}]	j_{pdf} [Wm^{-2}]	j_{sqrt} [Wm^{-2}]
2.0 m/s	0.140 ± 0.003	-111 ± 3	-124 ± 3	-118 ± 3
4.2 m/s	0.100 ± 0.004	-163 ± 2	-162 ± 3	-165 ± 4
5.0 m/s	0.064 ± 0.003	-299 ± 1	-280 ± 8	-298 ± 7
8.0 m/s	0.053 ± 0.003	-304 ± 3	-273 ± 9	-280 ± 8

Table 11.3: *Results of the heat flux measurements.*

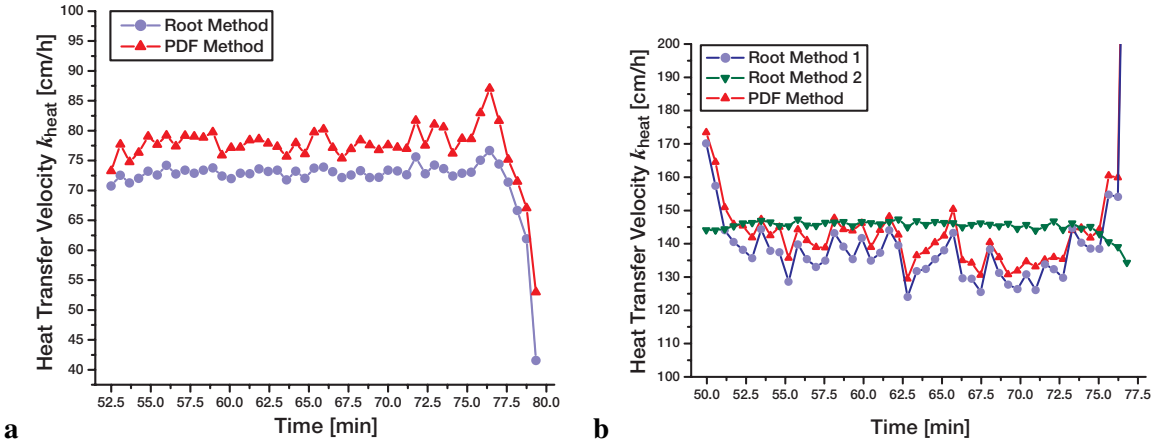

Figure 11.10: *The heat transfer velocity k_{heat} estimated from the square root method and pdf method. In* ***a*** *results for wind speeds of 2 m/s are shown and in* ***b*** *the same for 4.2 m/s. Again deviations are mainly due to deviations in ΔT, which can be seen from* ***b*** *, where method 2 indicates the same value of ΔT for all estimates.*

11.7 Transfer Velocity

The transfer velocity k_{heat} is an important parameter in relating the transfer of heat to that of other substances such as CO_2. The use of heat as a proxy tracer for mass transfer has been thoroughly discussed in Section 3.3. In experiments conducted at the Heidelberg Aeolotron the transfer velocities for heat were computed according to the approaches presented in Section 5.5. The results of these measurements will be given in Section 11.7.1. A highly promising technique of estimating the transfer velocity directly from the divergences has been introduced in Section 5.5. This method is based on the surface strain model presented in Section 2.4.4 from which the heat flux can be estimated following the technique presented in Section 5.4.4. The applicability is demonstrated in Section 11.7.2. To illustrate the relevance of the transfer velocity of heat k_{heat} to that of tracer gasses k_x, in one experiment the transfer velocities for CO_2, N_2O and CH_4 were measured independently and compared to that of heat as presented in Section 11.7.3.

11.7.1 Heat Transfer Velocity

The transfer velocity k_{heat} was computed according to Equation (5.35)

$$k_{\mathrm{heat}} = \frac{j}{\rho c_p \Delta T}, \tag{11.6}$$

where the estimate of the heat flux from the pdf method j_{pdf} was used. As a second alternative Equation (5.38) was used for assessing the transfer velocity k_{heat}, which is essentially the analogon of using j_{root} in Equation (5.35). Since the estimates of k_{heat} are based on the heat fluxes j_{root} or j_{pdf} respectively, the results are similar. Hence the remarks made with respect to spatial and temporal resolution as well as for the accuracy are equally applicable for this parameter. A plot of the resulting heat transfer velocities for the measurements at 2 and 4.3 m/s wind speeds are given in Figure 11.10.

The same observations that were previously made for the heat flux estimates j_{pdf} and j_{root} also hold true for the derived heat transfer velocity k_{heat}. In lower wind speeds the transfer velocity

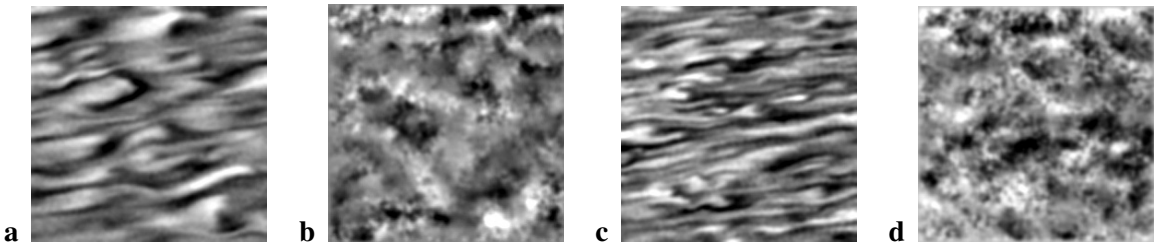

Figure 11.11: *The divergence estimated for the infrared sequences. In* ***a*** *an image recorded in the experiment with a wind speed of* 2 *m/s can be seen with the corresponding divergence in* ***b*** *. The same is shown in* ***c*** *and* ***d*** *for a sequence acquired during an experiment at a wind speed of* 4.2 *m/s. Regions of larger positive divergence are bright and appear to be cumulating in warmer regions of the infrared images, also indicated by a higher grey value.*

computed from the estimate of j_{pdf} is a little higher than that from the formulation in Equation (5.38), similar in principle to computing k_{heat} from j_{root}. In stronger winds the opposite is true. Since j_{pdf} was found to be slightly more accurate in these regimes than j_{root}, the same can be expected for k_{heat} based on these estimates.

The values of the transfer velocities estimated for the different experiments is presented in Table 11.4.

11.7.2 Transfer Velocity from Divergence

The surface strain model introduced in Section 2.4.4 presents a very promising technique for measuring the transfer velocity k_{heat}. In this model the transfer velocity can be estimated from Equation (5.40) given by

$$k_{\mathrm{heat}} = \sqrt{\frac{2}{\pi}\beta\kappa}. \tag{11.7}$$

Here β is the strain rate or divergence of the flow field at the sea surface. The main difference of this formulation and the previous ones derived from the surface renewal model is the lack of dependence on the temperature depression ΔT. The heat transfer velocity in this formulation solemnly depends on the divergence. Thus the need for an accurate estimation of the temperature depression ΔT is circumvented. Also an accurate radiometric calibration of the infrared camera is not as important. This reduces major sources of errors in previous formulations. The downside is of course that a divergence is induced by the projective transformation from real world object onto the image plane. Movement along the optical axis of the camera will result in a divergence and thus falsify results. This method will therefore only be applicable when the distance of the water surface to the camera and changes thereof are known.

This approach of estimating the transfer velocity was employed on the low wind measurements. In these regimes the changes of water height due to wave motion are small as is the error of estimating divergences due to this motion. The divergences at the sea surface are shown in Figure 11.11 for the measurements at wind speeds of 2.0 m/s and 4.3 m/s. The results of the transfer velocity for one image sequence in both wind regimes are presented in Figure 11.12. The results are very promising,

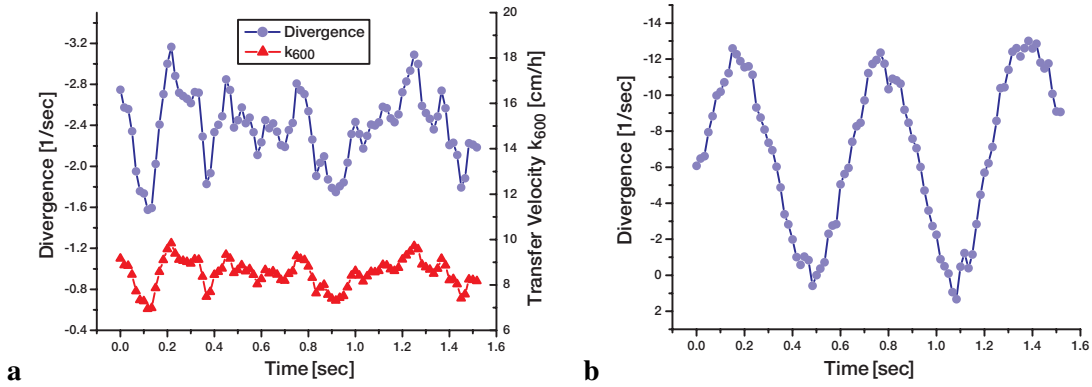

Figure 11.12: *The transfer velocity computed from the divergences at the sea surface. In* ***a*** *the divergence and the corresponding transfer velocity k_{600} are shown for the measurement at wind speeds of 2 m/s. The divergence from the measurement at 4.2 m/s is displayed in* ***b*** *. These high values are almost exclusively due to wave motion.*

although a final validation can only be made once the change of distance form surface to camera is known precisely, allowing a correction of the divergence.

Wind Speed	k_{pdf}	k_{root}	k_{div}
2.0 m/s	76 ± 2	72 ± 2	167 ± 4
4.2 m/s	139 ± 7	142 ± 4	-
5.0 m/s	376 ± 10	400 ± 10	-
8.0 m/s	443 ± 11	454 ± 11	-

Table 11.4: *The heat transfer velocities k_{heat} computed for heat from the pdf method (k_{rmpdf}), the square root method (k_{root}) and the divergence (k_{div}).*

11.7.3 Mass Transfer Velocity

In the experiment conducted on the 17.12.2000 with a wind speed of 5 m/s apart from the heat transfer velocity k_{heat} the transfer velocities for different tracer gases were measured as well. The experiment was conducted as an evasion measurement with the tracers N_2O, CO_2 and CH_4. At the beginning of the measurement the water body is enriched with a certain concentration of the tracer gases. During this time the water body is moving and well mixed whereas the wind is turned off. Due to the absence of wind no waves are present and thus no turbulence mixing the boundary condition. Hence no mass flux from the water body to the gas space can be observed. After enrichment the wind is turned on and the tracer concentrations in the air space measured. For this measurement a commercially available *URAS 14* analyzer from *Hartmann und Braun*™ was used. Periodically the gas space is flushed with a gas devoid of the measured tracers. The exchange of the gas space can be conducted very quickly. From the increase of tracer concentration in the air space the transfer velocity can be computed from a fit to the concentration measurements. The reader is referred to Kalkenings [2002] for an in depth description of the method used. The resulting mean transfer velocities of the tracer gases, as obtained from the three peaks shown in Figure 11.13 are: $k_{N2O} = 26.208$ cm/h, $k_{CO2} = 25.128$ cm/h and

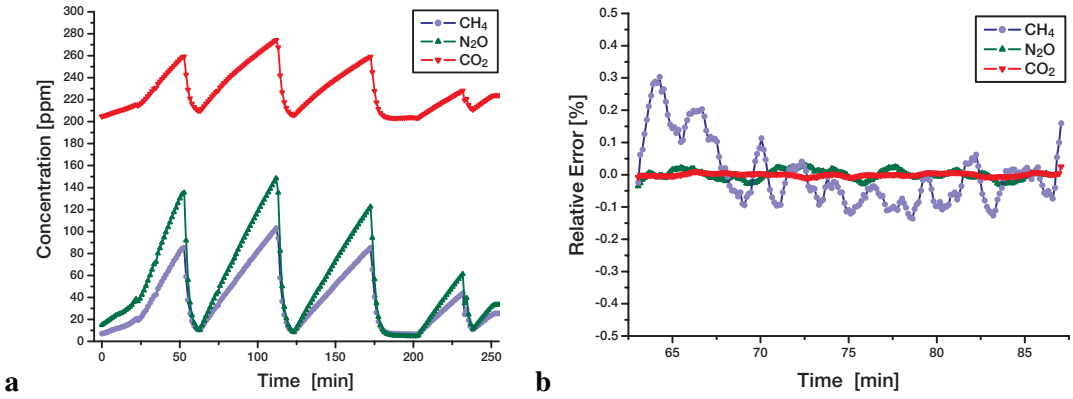

Figure 11.13: *In* ***a*** *the concentration change in the air space of the tracer gases N_2O, CO_2 and CH_4 during the measurement conducted on the 17.12.2000 can be seen. The air space is flushed periodically and a differential equation solved for the concentration increase. In* ***b*** *the relative errors between measured and theoretically predicted tracer concentration in the air space is shown. Data provided by Kalkenings [2001].*

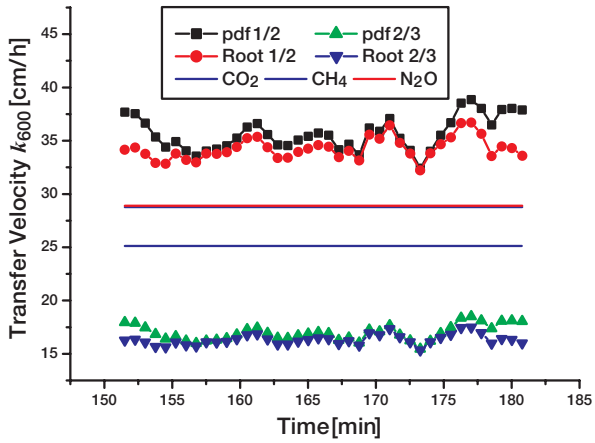

Figure 11.14: *The transfer velocities of the measurement for heat, N_2O, CO_2 and CH_4, all normalized to a Schmidt number of $Sc = 600$. It can be seen that the Schmidt number exponent for of $n = 1/2$ fits the data better.*

$k_{CH4} = 28.404$ cm/h [Kalkenings, 2001]. It should be noted that the wind was turned on in the first peak shown. Therefore this peak was not used in the estimation of transfer velocities.

11.8 Summary

A number of techniques for measuring important parameters of air-water heat and gas exchange have been proposed in Chapter 5. These methods were verified in laboratory studies in the Heidelberg Aeolotron. Very convincing evidence of a logarithmic-normally distributed probability density function could be collected. This distribution had the same principle form under all wind speeds tested. From the parameters of this distribution an estimate of the heat flux could be computed. This estimate of the heat flux was in excellent agreement with the true heat flux measured by other means. A bias in

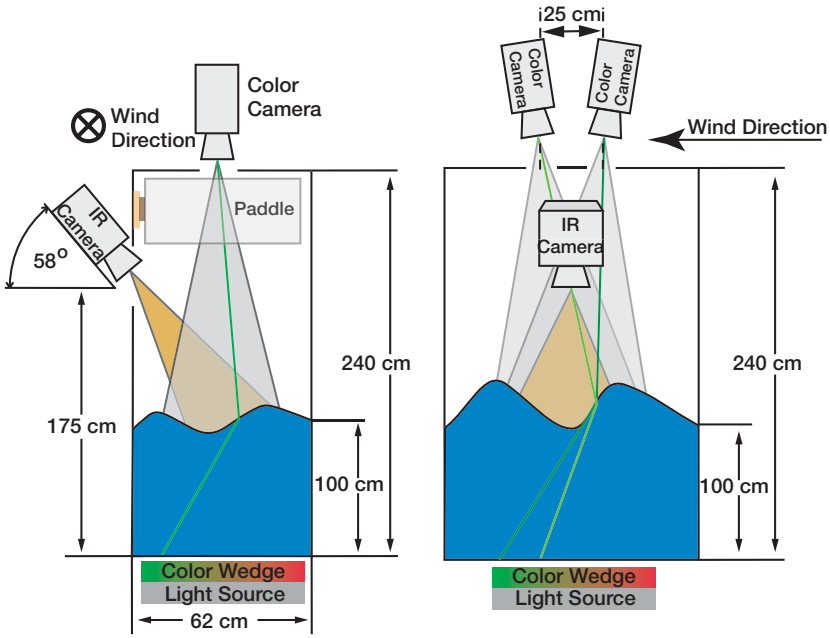

Figure 11.15: *The Stereo ISG.*

this estimate for lower wind speeds could be found. This bias indicates that the surface renewal model with the specific pdf of times between renewal events might not be as accurate in low wind speed regimes as in those of high wind speed. Reason for this might be the stronger effect of surfactant slicks or different driving forces of the sub-surface turbulences. These change from buoyancy driven to shear driven as the wind increases.

Another technique for estimating the net heat flux j was examined. This technique does not make any assumptions concerning the pdf of times between consecutive renewal events. It is very promising as it allows highly spatially and temporal resolved measurements of the heat flux. It was shown that this technique is equally accurate in estimating the heat flux at the sea surface not presenting a bias as strong as that from the pdf method for lower wind speeds. Generally the results were closer to the true value at moderate wind speeds than at high ones. Due to wave motion the estimates were seen to be undulated, an effect measured for the first time. A reliable analysis concerning this effect can only be conducted once accurate spatially resolved measurements of the wave slope in the footprint of the infrared camera are possible. A suitable set-up for such measurements is currently being developed. An illustration of such combined measurements with the *stereo imaging slope gauge (SISG)* is shown in Figure 11.15.

Such a setup would be very valuable in another way. The estimation of the transfer velocity of heat was demonstrated based on the surface strain model. This estimation has the big advantage of relying only on the surface divergence circumventing the need for an accurate temperature calibration or measurements of the temperature depression ΔT. However, with this technique accurate estimates are only possible if the movement of the sea surface along the optical axis of the camera is known. Otherwise this movement will appear as a virtual divergence, falsifying results. With the stereo ISG these virtual divergences could be corrected for and an accurate correlation between wave slope and

motion to heat flux be made.

To show the relevance of heat transfer measurements the transfer velocity was derived from these estimates. In a joint experiment both the transfer velocities of heat and different tracer gases were measured and the correct Schmidt number exponent for the experimental conditions could be verified. Due to the early stage of mass transfer measurements in the facility only first results with high uncertainties could be shown. However, in the close future a thorough analysis will be conducted.

Chapter 12

In Situ Flux Measurements

For studying dynamical transport processes at the air-sea interface in the context of climatic variability it is vital to perform in situ measurements on the ocean. Only through this step is it possible to validate insights gained in laboratory experiments and transfer knowledge to the field.

In the context of this work two field experiments were conducted. The first one was performed just off the coast of *La Jolla Shores*, San Diego, in close proximity to the *Scripps Institution of Oceanography*, San Diego/ USA. This presented a first opportunity to test the technique in the field under a variety of different conditions. For this experiment a freely drifting buoy was constructed and tested, as will be outlined in Section 12.1. The knowledge gained during these measurements was transferred to a second field campaign, where data was acquired in the equatorial Pacific, roughly between 125°W and 142°W longitude as part of the *GasExII* experiment. This part of the ocean is known for its steady light wind conditions and a region of cold upwelling water masses, thus presenting a stable stratified boundary layer as well as a CO_2 source. Results of these measurements will be presented in Section 12.2.

12.1 Heat Fluxes in the Coastal Proximity

For gaining a deeper understanding of the transport phenomena at the air-water interface and finding an accurate parameterization for these processes experiments have been conducted under laboratory conditions. However, insights gained in these kind of experiments can only be transferred to a certain extend to the ocean. Feedback from in situ measurements and comparisons to laboratory data are necessary to improve the models.

To this end a sea going platform was build that incorporates novel experimental techniques previously only applied under laboratory conditions. Common to these techniques are both temporal and spatially highly resolved measurements of parameters governing air-sea gas exchange. As was explained in Chapter 3 important parameters of air-sea gas and heat transfer are the net heat flux j as well as parameters influencing the transfer velocity k_x of tracers x, such as that of heat. Knowledge of these parameters would allow a precise estimation of mass transfer velocities k_m such as that of CO_2 from the transfer velocity of heat k_{heat} following Equation (3.38). Empirical data gained both from field and laboratory measurements indicate that the current parameterization of transfer velocities with

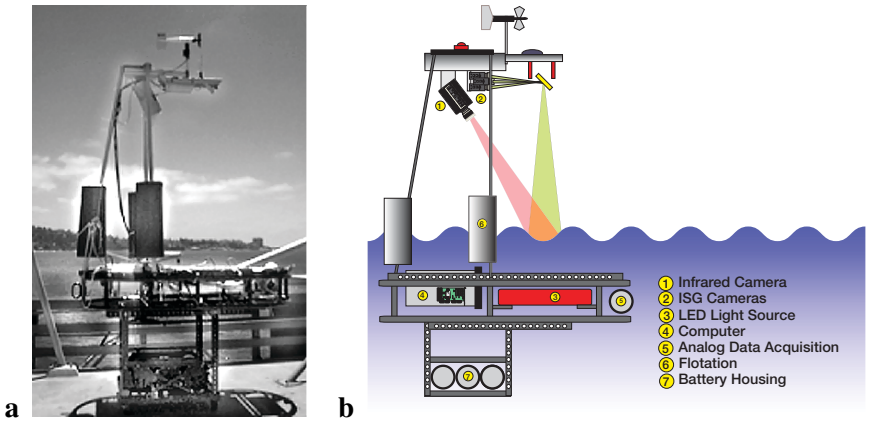

Figure 12.1: *In* ***a*** *a picture of the buoy can be seen and in* ***b*** *a schematic drawing of it (based on Schimpf [2000]).*

the wind speed, such as those proposed by Liss and Merlivat [1986] or Wanninkhof [1992], do not adequately describe the processes at the sea surface. Moreover, the roughness of the sea surface, mainly influenced by surfactants and wind speed, seems to be a much better parameter of transfer processes. It is this parameter that can be expressed as the mean square slope of the wave field.

In cooperation with the *Scripps Institution of Oceanography* a sea going platform for conducting precise measurements of parameters influencing air-water gas was build. For reasons described in Section 12.1.1 a freely drifting buoy was the design of choice. The buoy was deployed of the *Scripps Pier*, a solid construction reaching 320 m into the Pacific Ocean off the coast of La Jolla in Southern California. These deployments had two goals. For one the capabilities of the buoy were to be tested and the design refined to allow for successful deployments of ships in field campaigns. As a second, goal, the techniques for estimating parameters of sea surface heat transfer presented in this thesis were to be tested for their applicability in field conditions.

12.1.1 The Buoy

In cooperation with the *Scripps Institution of Oceanography* of the University of California, San Diego, a freely drifting buoy was constructed, build and tested off the *Scripps Pier*. A picture and a schematic drawing of the buoy can be seen in Figure 12.1. The main benefits of a buoy as compared to a catamaran such as LADAS, which will be introduced in Section 12.2.1, is its close to neutral buoyancy and high mass. Due to this configuration it presents a stable platform that nicely follows gravity waves. For this reason the distance between imaging apparatus and sea surface remains roughly constant, facilitating measurements of small capillary waves on the surface. These small waves with their high slopes represent one main factor influencing air-water gas and heat exchange, making them a good candidate for parameterizing said exchange processes [Jähne, 1987].

The buoy was specifically designed and build to allow measurements of the sea surface slope and parameters of heat transfer in the same footprint. The design of the buoy was thus centered around an *Imaging Slope Gauge* (ISG) for measuring high temporal and spatially resolved wave slopes and an infrared camera for estimating heat fluxes and transfer velocities from the techniques proposed

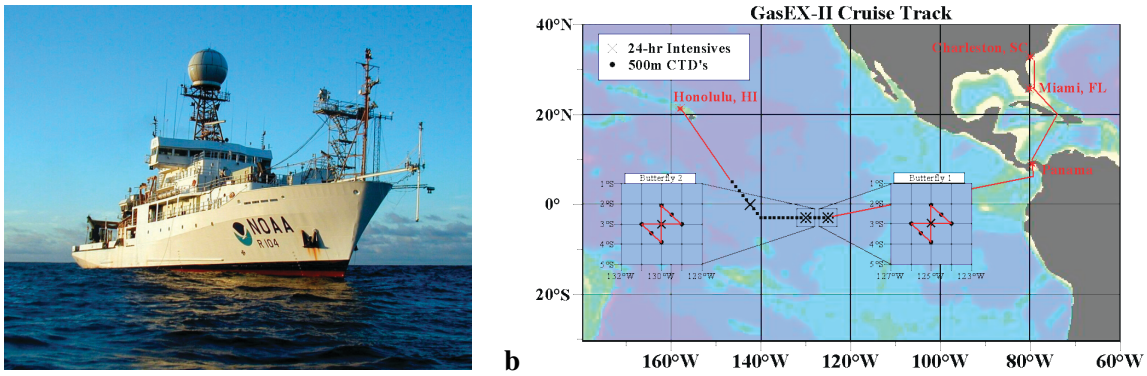

Figure 12.2: *Depicted in* ***a*** *is the NOAA R/V Ronald H. Brown. At the bow of the ship the tower and booms for micro-meteorological measurements can be seen. The track of the GasExII cruise is displayed in* ***b*** *, with the two "butterfly" patterns performed.*

in this work. Not only is the slope data important for finding a valid parameterization of transport processes. Furthermore this data can be used in deriving assertions concerning non-linear wave-wave interactions, a current field of research.

The basic principle of an ISG is a *shape from refraction* technique, reconstructing the wave slope from refractions at the air-water interface. At some distance below this surface a light source produces an intensity gradient which is recorded with a standard CCD camera above the interface. Depending on the slope a different area of the intensity gradient is seen, which can thus be mapped directly to the surface slope via calibration [Klinke, 1996]. In a compromise between power consumption and emitted light intensity an array of highly emitting *light emitting diodes* (LEDs) is used. The LEDs are switched in such a way as to produce an intensity gradient through a diffuser. With high frequencies of 240 Hz the direction of these gradients is switched between the cross- and along-wind direction, resulting in slope data along these orientations.

In the same footprint of the ISG an infrared camera records thermal images of the sea surface. Here, a low noise sterling cooled Amber Galileo™ camera (NEΔT $\approx$ 25 mK) was used, producing images at a frame rate of 120 Hz with a resolution of 256×256 pixels. The area recorded by the ISG is (29×27) cm^2, that of the infrared imager (40×40) cm^2, resulting in a nominal resolution of (1.6×1.6) mm^2 for the infrared imagery.

The construction of the buoy was completed and the device tested in spring/summer of 1999. Subsequent to modifications due to the experience gained from these deployments, a highly capable platform for air-sea interaction measurements has been made available.

12.2 Measurements in the Equatorial Pacific

During experiments conducted with the buoy the novel techniques presented in this thesis have been proven to be well capable of obtaining measures for the heat flux j, the transfer velocity k_{heat} as well as for the temperature depression ΔT across the cool skin of the ocean under less than ideal conditions. Thus the GasExII cruise presented an excellent opportunity to obtain data in the field and

compare the results to current state of the art techniques as introduced in Section 4.

The first GasEx experiment was conducted in the North Atlantic in 1998. In that study, the goal was to analyze the feasibility of direct flux measurements of tracer gases by eddy correlation (cf Section 4.2) and compare results with geochemical mass balance approaches in the water side. As a follow up experiment, the objective of the GasExII experiment was to improve the understanding of the mechanisms involved in air-water gas exchange. As such factors influencing the mass fluxes were to be analyzed by a number of different groups, measuring physical, chemical and biological processes and correlating results. The main focus in measuring mass fluxes was of based on direct Eddy Correlation techniques, as these have been proven feasible during the previous GasEx experiment. The cruise was sponsored by NOAA (National Oceanographic and Atmospheric Administration, part of the Chamber of Commerce) and conducted on their ship, the *NOAA R/V Ronald H. Brown*. The cruise started in January 29, 2001 in the Port of Miami and ended in March 08, 2001 in Pearl Harbor, Hawaii. Images of both the research vessel and the track of the cruise are presented in Figure 12.2. Data was acquired in a a region roughly between 125°W and 132°W longitude and 2°S latitude. This part of the ocean was chosen because it is known to be a region with strong upwelling of cold water masses and relatively low wind speeds during that time of the ENSO (El Niño Southern Oscillations) cycle. The atmospheric boundary layer is thus stably stratified presenting a low turbulence environment, simplifying some meteorological measurements and theoretical models. Also, in this part of the world hardly any data of mass and heat flux has been collected to date.

As a platform for conducting the measurements with techniques introduced in this thesis the *LADAS* catamaran was used, which will be introduced in the next section. The purpose of this catamaran was to measure surfactant enrichments, short capillary and capillary-gravity waves as well as parameters of heat transfer.

12.2.1 The LADAS Catamaran

A buoy such as the one described in Section 12.1.1 proved to be too complicated both in terms of instrumentation but also in terms of deployment in a rough ocean going experiment [Schimpf, 2000]. Therefore the experiment was conducted on the LADAS (Lots A Devices at Sea) catamaran in a collaboration between the *Woods Hole Oceanographic Institution*, the *University of Rhode Island* and the *University of Heidelberg*. Due to its design the catamaran possesses a higher payload than the buoy, allowing a wide range of instrumentation to perform measurements of vital parameters for air-sea gas and heat exchange. Images of LADAS as well as a schematic drawing can be seen in Figure 12.3. Key components of the self propelled catamaran are:

- a meteorological package to quantify the near-surface wind speed and stress as the major forcing of short waves, as well as surface currents and thus LADAS motion relative to the water body,
- a scanning laser slope gauge to measure the wavenumber-frequency spectra of small-scale waves (wavenumber 25-1200 rad/m) and the directional frequency spectra of dominant gravity waves,
- a wave-wire array to measure long-wave spectra,

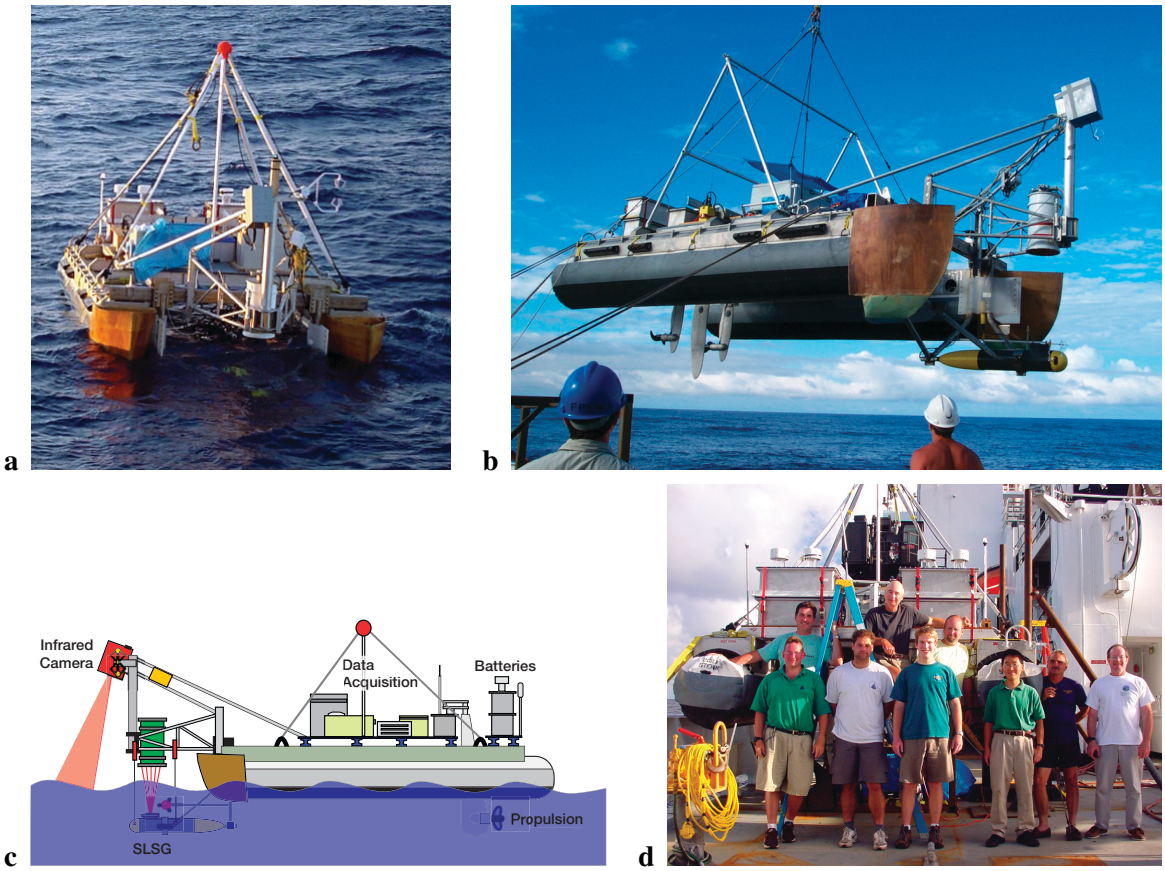

Figure 12.3: *The LADAS catamaran presented the platform for conduction measurements during the GasExII experiment. In* ***a*** *it can be seen during data acquisition.* ***b*** *is a picture of the recovery which grants a view of the Scanning Laser Slope Gauge (SLSG) in front, fully submerged during operation. A schematic drawing of the catamaran is presented in* ***c*** *(by U. Schimpf). The people operating LADAS on the GasExII cruise can be seen* ***d*** *(left to right, E. Bock, U. Schimpf, C. Garbe, T. Hara, M. Rabozo, N. Frew, R. Nelson, N. Witzell and J. Gabrielle).*

- a surface microlayer skimmer and fluorometry system to estimate surface film chemical enrichments and their effect in modulating wave spectra,
- a passive infrared imager in conjunction with a state of the art RAID system for recording digital image sequences (12bit dynamic range) in real time at 100 Hz. The novel techniques presented in this work rely on data of this subsystem.

Also a GPS (Global Positioning System) was installed, allowing a precise synchronization of the instruments on LADAS and the R/V Ronald H. Brown, as well as recording the course taken by LADAS during a deployment, both relative to the research vessel but also in an absolute coordinate frame. Furthermore a motion package was installed, measuring accelerations and tilt and thus allowing for motion corrections.

The LADAS catamaran was deployed off the side of the R/V Ronald H. Brown shortly before sunset and continued to collect data for roughly 4 hours about 100 m upwind of the ship. Both the

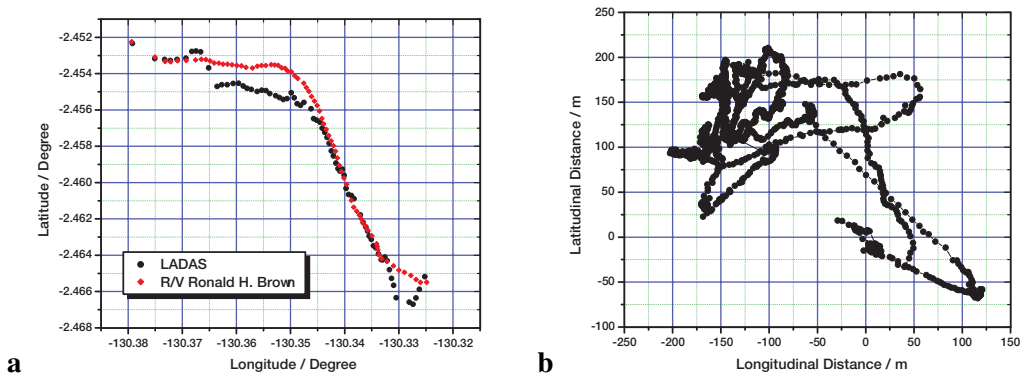

Figure 12.4: *The course of a typical deployment of LADAS computed from GPS data. In* ***a*** *both the course of the R/V Ronald H. Brown and of LADAS can be seen in absolute coordinates and in* ***b*** *the position of LADAS relative to the R/V is shown.*

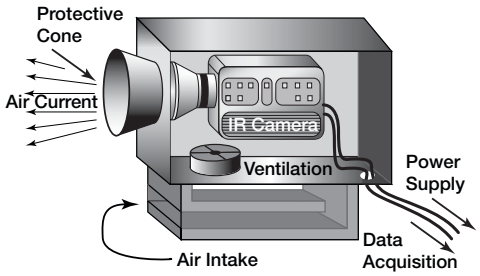

Figure 12.5: *The protective housing guarding the infrared camera from spray and rain.*

absolute and the relative course of LADAS with respect to the R/V is computed from the GPS data and can be seen for a typical deployment in Figure 12.4. The R/V Ronald H. Brown spent 17 days at the measurement site, out of which LADAS was deployed 14 times. One of the deployment was conducted during the early morning hours before sunrise, contrasting common practice. The hours of operation during these deployments together with the status of data acquisition for the different subsystems is listed in Table 12.1.

The Infrared Subsystem on LADAS

The subsystem for acquiring thermal image sequences on LADAS consisted of two almost identical set-ups, allowing to quickly replace components in the event of failure. As a thermal imager two sterling cooled low noise infrared cameras were available, namely the Amber™ Galileo and Amber™ Radiance I cameras. Both cameras are very similar in principle, as they are both centered around an InSb detector, sensitive in a wavelength band of 3-5 μm. The noise level of both cameras is identical within accuracy of measurement and found to be NEΔT $\approx$ 25 mK. Both cameras produce digital images with a dynamical range of 12bit on the Amber HSVB (High Speed Video Bus). The major difference between the two cameras is the achievable frame rate. While the Radiance I camera is limited to 60 Hz, the Galileo can be externally synchronized and was set to 100 Hz by a highly accurate stabilized crystalline oscillator.

LADAS Instruments	YD 40/1 23:40- 03:00	YD 46 03:50- 05:40	YD47 01:25- 05:25	YD49 02:15- 06:10	YD50 01:50- 05:15	YD51 03:10- 04:50	YD52 02:46- 06:20
SLSG	✓	✓	✓	✓	-	-	Partial
IR Imagery	✓	-	Partial	Partial	✓	✓	✓
CDOM Fluorescence	✓	✓	✓	Partial	✓	✓	-
Surfactant Extracts	✓	✓	✓	Partial	✓	✓	-
Anemometer (Air)	✓	✓	✓	✓	✓	-	✓
ADV	-	✓	✓	✓	✓	-	✓
Wave Wire Array	✓	✓	✓	✓	✓	-	-

LADAS Instruments	YD54 02:42- 05:50	YD55 02:24- 06:00	YD56 02:19- 05:30	YD58 02:48- 06:30	YD59A 03:21- 05:45	YD59B 13:30- 15:40	YD60 03:10- 07:30
SLSG	✓	✓	✓	-	-	Partial	✓
IR Imagery	✓	✓	✓	✓	✓	✓	✓
CDOM Fluorescence	✓	✓	✓	✓	✓	✓	✓
Surfactant Extracts	✓	✓	✓	✓	✓	✓	✓
Anemometer (Air)	Partial	✓	✓	✓	✓	✓	✓
ADV	Partial	✓	✓	✓	✓	✓	✓
Wave Wire Array	-	✓	✓	✓	✓	✓	✓

Table 12.1: *The times and dates (in GMT) of LADAS deployments during the GasExII cruise and status of data acquisition during the deployment. Instruments collecting valid data are marked by "✓", only partial collection of data is marked "Partial" and failure to collect data at all is marked by "-". The instruments on LADAS are the "Scanning Laser Slope Gauge" (SLSG) for small-wave wavenumber-frequency slope spectra, the infrared imager, Colored Dissolved Organic Matter (CDOM) fluorescence - microlayer/subsurface @ 450 nm (SCIMS), Microlayer/subsurface surfactant extracts (SCIMS), Anemometer for measuring air currents, Acoustic Doppler Velocimetry (ADV)(mean current), wire-wave staff (long waves).*

The camera was mounted on a mast on the bow of LADAS roughly 2 m above mean sea level. A lens of 50mm focal length was used to image an area of approximately (40×40) cm^2. Due to the close proximity of the camera to the sea surface it has to be protected from sea spray. Also, water droplets on the fragile lens would deteriorate the image quality and might ultimately have damaged the lens. Therefore a camera housing was constructed to protect both camera and lens in the hostile environment, while still allowing the heat produced by the camera to be transported to the outside. A schematic drawing of the case can be seen in Figure 12.5. It was build from a water tight aluminium case with an opening for the camera to image the water surface. Air is sucked into the housing with a very strong ventilator, thus cooling the camera. At the same time the strong current of air being blown out of the case blocks any droplets of water and thus effectively protects the lens and camera from sea spray. Of course care has to be taken in constructing the air intake, as the protective effect of the air current is delimitated if droplets are sucked into the housing at the same time. Therefore an S-shaped duct was employed, which due to the high centrifugal forces along its turning points

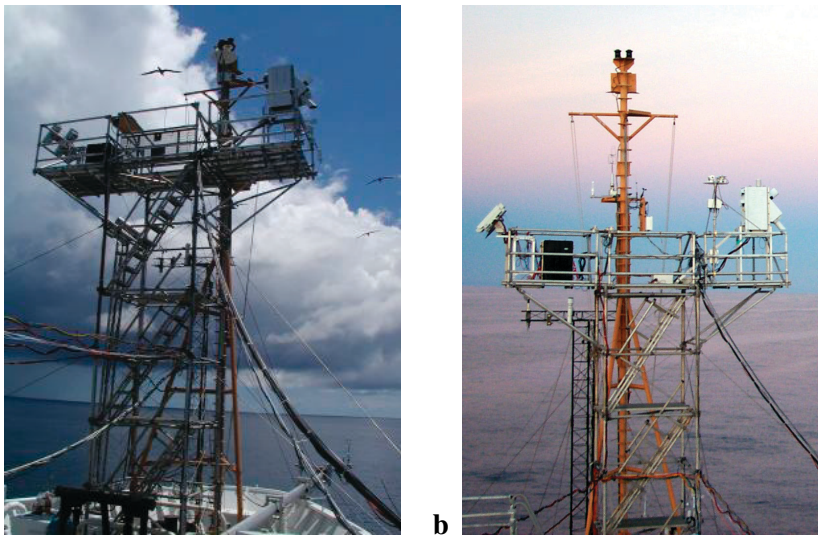

Figure 12.6: *The bow tower on the R/V Ronald H. Brown on which the instruments for the meteorological measurements were mounted.*

would effectively keep any water droplets from entering the housing. Humidity could be controlled by the use of silica gel, the encountered humidity was found to be well within the specifications of the camera and additional protective schemes were thus not necessary.

For acquiring the image sequences the digital data was read directly from the Amber HSVB with a BitFlow™ Roadrunner II digital framegrabber to the acquisition system. This system consists of a customary personal computer based on an Intel™ Pentium III processor clocked at 700 MHz and 512 MByte RAM (Random Access Memory) encased in a water proof box. The data was recorded on a dedicated RAID (Redundant Array of Inexpensive Disks) system consisting of six hard drives in a strip set with parity information (RAID level 3), thus allowing fast data storage and a capacity of well over 375 GByte. The data stream of the Amber Galileo camera is $256 \times 256 \times 100 \times 2 = 12.5$ MByte / sec, where the factor 2 is introduced due to the 2 Bytes the 12 Bit datum has to be stored in. The RAID system is capable of storing such data streams continuously, thus allowing the digital data stream to be recorded in real time. The high amounts of data collected during one deployment were stored on a digital tape drive with a capacity of 25 GByte of uncompressed data per tape. Recording the whole four hours of the deployment continuously would amount to $\approx$ 180 GByte, making this scheme much to data intensive. Even though the data can be easily compressed by a factor of two in the lossless Tiff format, recording data continuously would not be feasible. For this reason a compromise between recording time and amount of data to be recorded was chosen, acquiring 512 or alternatively 1024 images per sequence and recording a sequence every 30 or 60 seconds, respectively. The ratio between latency and image recording was thus always 6/1, leading to the amount of data taken during one deployment to be roughly 30 GByte. Due to a lossless image compression scheme the amount of data was reduced to fit nicely onto one backup tape per deployment.

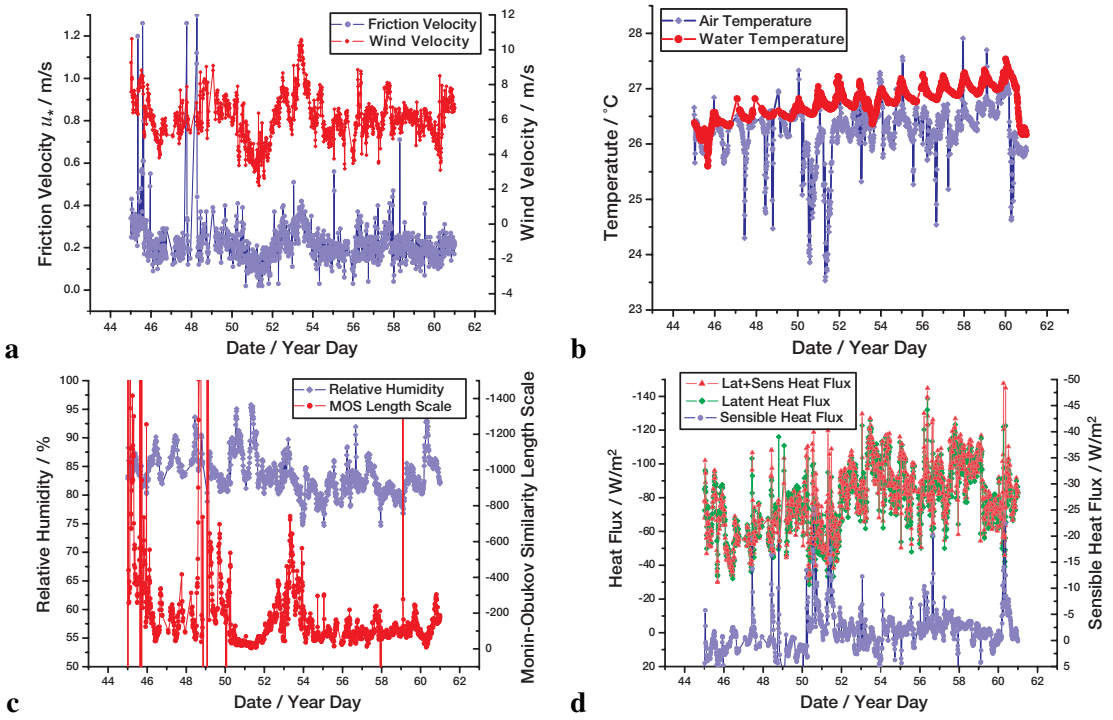

Figure 12.7: *Meteorological measurements of the wind-speed an u_* in* ***a*** *, the temperature of air and water in* ***b*** *, the relative humidity and Monin-Obukhov Scaling Length (MOS) in* ***c*** *and the latent heat and sensible heat flux in* ***d*** *. Shown are the measurements for the whole time at the measurement site [McGillis, 2001].*

12.2.2 Micro Meteorological Measurements

As outlined in Section 4, current state of the art techniques for measuring fluxes rely on measuring micro meteorological parameter such as the humidity, air temperature and wind speed to name but a few. As these techniques have been established for a number of years, it is important to compare the data obtained with the novel technique presented in this work to these standard methods. This comparison can readily be achieved for the field data obtained during the GasExII cruise, as concurrent measurements of the micro meteorological parameter aboard the R/V Ronald H. Brown and infrared sequences on the research catamaran LADAS were obtained. The meteorological data was obtained from Hare [2001], who collected his data on top of the bow tower on board the R/V Ronald H. Brown (see Figure 12.6). The data was averaged over 10 minute intervals. Different sensors were used for obtaining the various meteorological parameters. While the solar short wave irradiance was measured with an Eppley™ PSP (pyranometer), the long wave irradiance was obtained by an Eppley™ PIR (pyrgeometer) which was corrected for effects of temperature on the sensor by two thermistors within the unit.

From the irradiance data sets the short wave and long wave exitances are computed from Equations (4.40) and (4.41) respectively. The exact value for the albedo A in Equation (4.40) is somewhat irrelevant, as measurements were taken after sunset, which made for negligible short wave exitances M_{short} of around 1 W/m^2. Fluxes were obtained from bulk parameterization (see Section 4.1) employing the TogaCoare bulk flux model [Fairall et al., 1996b], from the eddy correlation technique

(see section 4.2) and from inertial dissipation as introduced in Section 4.4.

The meteorological data collected was compared with data recorded by the crew of the R/V Ronald H. Brown and data measured by the group of the Woods Hole Oceanographic Institution (WHOI), headed by Wade McGillis. The flux measurements were found to agreed within error bounds.

It is of course important to obtain a feeling for the climatic variability found during the time spent at the measuring site. Plots of meteorological parameters such as the wind speed, friction velocity, relative humidity and temperature of air and water, as well as the heat fluxes estimated from them are presented in Figure 12.7. The data was provided by McGillis [2001]. As can be seen, the wind speed varied from 4 m/s up to 10 m/s with an average wind speeds of around 6 m/s. The strongest wind of 10 m/s was recorded on year day 53 and the lowest of 4 m/s two days before that, on year day 51. Naturally the air sided friction velocity u_* followed the pattern of the wind with an average of about 0.2 m/s, peaking at 0.4 m/s with a low of 0.1 m/s. The water temperature was found to slowly rise during the time of measurement from a low 26.3°C to a high $27°$ on the last day of measurement. As can be expected this temperature is subject to diurnal cycles due to the high solar irradiation during the day. The relative humidity was found to be of the order of 85% on average. Both latent and sensible heat fluxes j_{lat} and j_{sens} exhibit strong variations, representing the difficulty of measuring these quantities. They were found to be ranging from $40 - 120$ Wm^{-2} with an average of around 85 Wm^{-2}.

In the following the parameters estimated with the novel techniques presented in this thesis will be compared to the data set provided by Hare [2001]. An exemplary plot of this data is presented in Figure 12.8 for the year day 58 (27.2.2001). The data was averaged over intervals of ten minutes to obtain meaningful results. Shown is the air temperature T_{air} and the sea surface temperature T_{surf}, which differ by about one K. Both the cool skin thickness and the temperature depression ΔT were not measured directly but computed from the *TogaCoare* bulk flux model [Fairall et al., 1996b]. The wind speed was generally found to be very constant during the time of measurement, fluctuating around 6 m/s as stated earlier. All the measurements were conducted during night time, so that radiative fluxes j_{rad} due to short wave radiative transport can be neglected. Deployments generally took place shortly before sunset, which explains the high shortwave radiative heat flux at the beginning of the measurement in Figure 12.8.

The heat flux was estimated based on the bulk parameterization, inertial dissipation and eddy correlation techniques, all of which have been introduced in Chapter 4. The net heat fluxes fluctuate strongly with significant deviations in the estimates gained from the different techniques emphasize the experimental difficulty of measuring this parameter. Out of the measurements presented the inertial dissipation and the eddy correlation present comparable results, both in terms of absolute value and in terms of fluctuations. Due to the parameterization there exist a strong correlation between the wind speed measurement and the flux estimate from the bulk technique. For comparisons of the meteorological estimated heat fluxes to the to the ones presented in this thesis, generally the eddy correlation measurements were chosen. The reason is that they present the only direct way of measuring the fluxes from meteorological techniques.

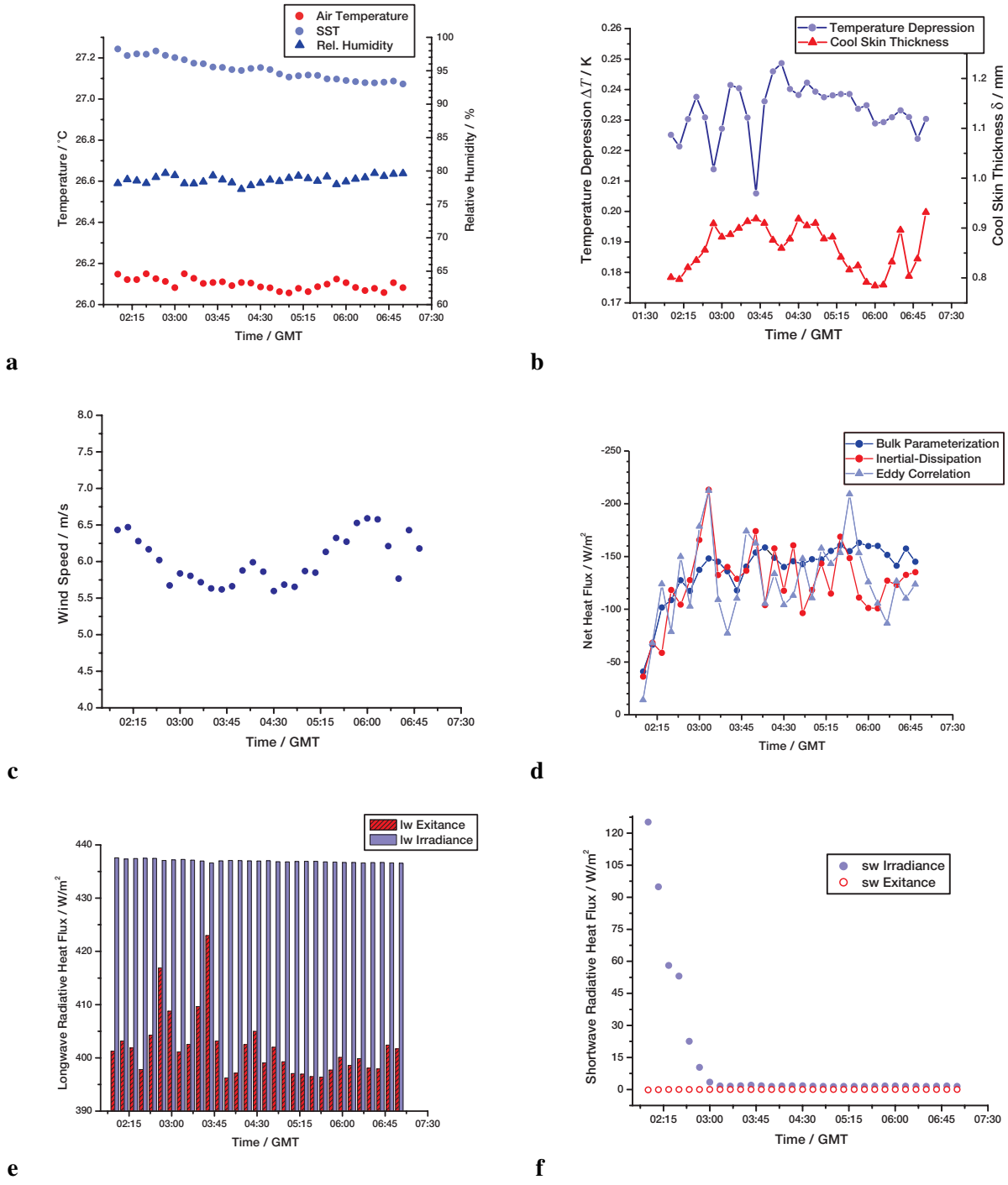

Figure 12.8: *The sea surface temperature T_{surf}, the air temperature T_{air} and the relative humidity is shown in* ***a*** *. The temperature depression ΔT and the cool skin thickness δ are plotted in* ***b*** *. The wind speed* ***c*** *and net heat flux* ***d*** *, the radiative transfer due to long wave exitance and irradiance* ***e*** *and due to short wave exitance and irradiance* ***f*** *. All data were take on board the R/V Ronald H. Brown during times of operation of LADAS on year day 58. Data obtained from Hare [2001].*

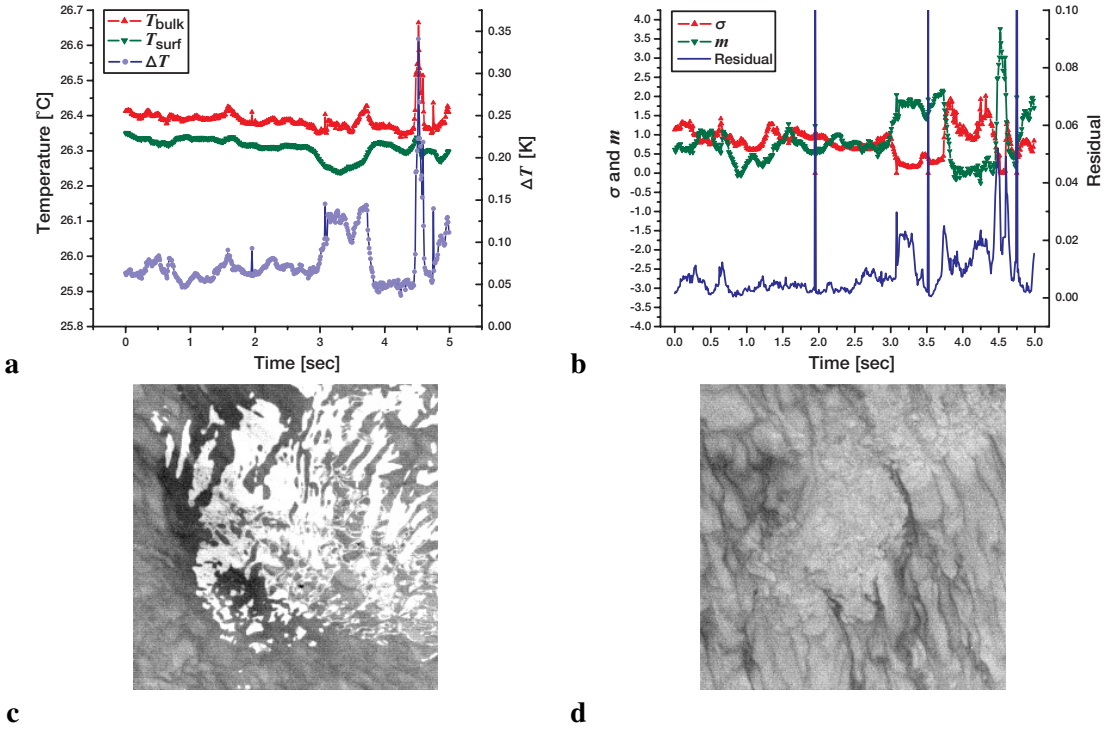

Figure 12.9: *The temperature depression ΔT computed from each individual frame of a sequence, as well as both T_{surf} and T_{bulk} can be seen in* ***a*** *. Not only the residual of the fit from the statistical analysis can be used for discarding wrong estimates, but both σ and m as well, as can be seen in* ***b*** *. The reason for such wrong estimates is shown in* ***c*** *, where due to strong reflexes not enough information is left in the images after segmentation to perform the fit reliably. An image from the beginning of the sequence is shown in* ***d*** *were a correct fit was performed.*

12.2.3 Measurements of ΔT

The importance of measuring the temperature depression at the sea surface has been thoroughly discussed in Chapters 3 and 5. For the evaluation of the data acquired on the GasExII cruise the algorithm proposed in Section 5.2 was used. The influence of reflexes present in the imagery was lessened with the robust motion estimation introduced in Section 8.7. On the corrected image data the statistical analysis derived in Section 5.2 was then performed resulting in values for T_{bulk}, σ and m. It should be remembered that both T_{bulk} and σ can be estimated independently in this way as explained in Section 5.2.1, whereas both the net heat flux j and m are interrelated. In the present context this poses no major drawback, as the statistical analysis of the temperature distribution is only used for deriving ΔT from T_{bulk} and the values of both j and m are irrelevant as they can be deducted by other techniques, as presented in Section 5.3.

The values computed for T_{surf}, T_{bulk} and the corresponding ΔT can be seen in Figure 12.9 for one individual sequence. Also shown are the parameters σ and m estimated by the fit with the corresponding residual. From these parameters irregularities can be directly detected and the corresponding value for T_{bulk} and hence ΔT cast away. This would be the case for some individual data points that are much to high in Figure 12.9, as well as the latter part of the sequence.

However, extended homogeneous reflexes extending over wide areas of the image cause the whole temperature distribution to shift towards warmer temperature. All the fit parameters are thus unchanged with just the bulk temperature T_{bulk} detected as warmer than it actually is. Also the robust motion estimation is only capable of detecting reflexes extending over less than half the spatio-temporal neighborhood used for estimating the extended optical flow. It will therefore fail to detect this kind of large reflexes. Computing the mean of the temperature depression ΔT from such an image sequences would thus lead to biased estimated. Therefore a robust estimate for computing the mean was chosen by an algorithm akin to the one presented in Section 7.3. In this way a reliable estimate of the mean temperature depression can be gained with a still acceptable efficiency, which would not be the case by just computing the median.

The results of the estimation of the temperature depression ΔT for the deployments of year day 52, 54 and the two deployments on year day 59 are presented in Figure 12.10. The temperature depression estimated from meteorological data is also shown for those deployments. It is a striking feature that the method of estimating ΔT from the infrared images is lower than the estimate from the meteorological data by 0.1-0.2 K. This is of course a significant difference in the estimates.

Under laboratory conditions in the absence of surfactants the prediction of the temperature depression ΔT seems to be quite accurate, as has been shown by Schimpf [2000]. Also, no contradictory results were evident in the laboratory experiment performed in this work. However, for added surface slicks Schimpf [2000] found the estimates of ΔT from the statistical analysis to be consistently to small at lower wind speeds. This was attributed to a damping of turbulences in the boundary layer. Hence the surface renewal effect might not be the predominant transport mechanism any more. Surfactants were found to be scarce during the experiment at the measurement site [Frew, 2001]. However, even due to these slight surfactant concentrations a small bias might be introduced in the estimation of ΔT. Yet, this does not explain the large discrepancies to the values estimated from meteorological techniques.

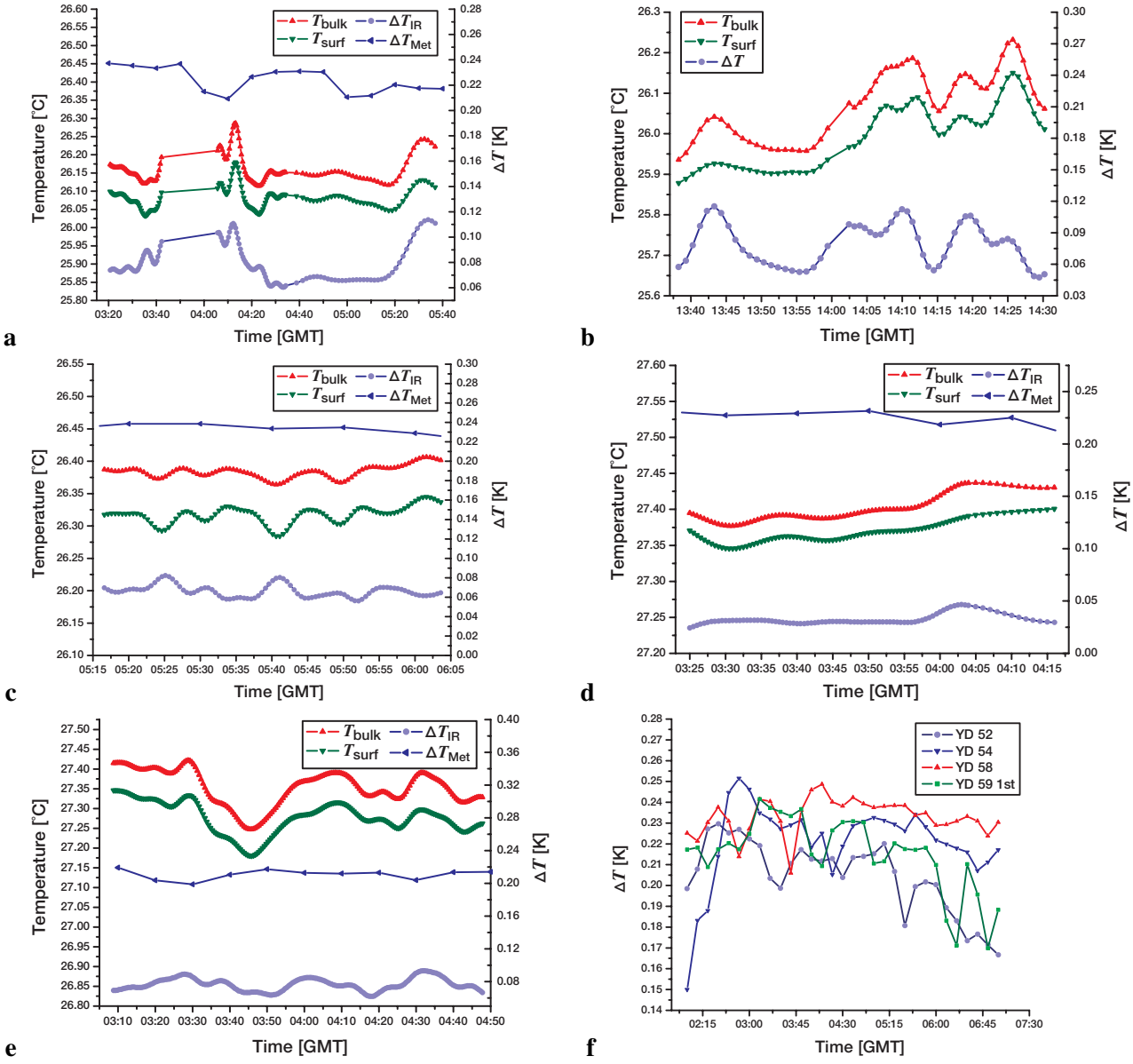

Figure 12.10: *The temperature of both the bulk T_{bulk} and surface T_{surf} as well as the temperature depression ΔT. From the deployments on on year day 59 in* ***a*** *and* ***b*** *respectively and from the deployments on year day 58, 54 and 52 in* ***c*** *,* ***d*** *and* ***e*** *, as well as the equivalent data obtained from Hare [2001] for the corresponding deployments in* ***f*** *.*

It should be noted that the the value for the temperature depression ΔT estimated from meteorological measurements has not been assessed directly from temperature measurements. Moreover it has been computed from bulk parameterization of Fairall et al. [1996a] introduced in Section 3.1.1. In a recent experiment Ward and Redfern [1999] measured ΔT directly and compared their findings to the predictions of the bulk parameterization. They found discrepancies in the order of $0.05 - 0.2$ K between measurement and prediction. Even though they did not analyze the exact same model used by Hare [2001] in estimating the data presented here, they did analyze other related models introduced in Section 3.1.1. In all the models such deviations were found making it safe to assume that the same might be true for the data presented here.

12.2.4 Measurements of Heat Transfer

In measurements conducted at the Heidelberg Aeolotron accuracy bounds and validity of the techniques proposed in this work for measuring parameters of heat transfer have been established. In field experiments these approaches were applied under challenging conditions and the results compared to those obtained from independent measurements of meteorological parameters as outlined in Section 12.2.2.

An important parameter for the model of surface renewal is the probability density function of times between consecutive surface renewal events. Different assumptions have been made ranging from purely periodic to log-normal distributions, see Section 2.4.3. In laboratory experiments conducted at the Heidelberg Aeolotron excellent agreement with the proposed lorgarithmic-normal distribution has been found as was presented in Section 11.5. The analysis is based on the fit of a log-norm distribution given by Equation (2.51) to the frequency data data of the times τ in between consecutive renewal events. This time can be derived from the image sequence analysis as outlined in Section 5.3. The findings of the laboratory experiments were supported by the field data. Minor deviations from this distribution could be attested to image corruption due to reflexes.

The parameters of the fitted logarithmic-normal distribution, σ and m can be used for estimating the characteristic time constant t_* given by the expectancy value of the distribution from Equation (2.52). Values of these estimated parameters for field conditions are presented in Table 12.2.

Year Day	Wind Speed	u_* [m/s]	σ	m	t_* [s]
52	5.23 m/s	0.199	0.51 ± 0.02	0.06 ± 0.06	1.08 ± 0.05
54	4.18 m/s	0.154	0.46 ± 0.02	-0.77 ± 0.02	0.49 ± 0.03
58	5.05 m/s	0.184	0.48 ± 0.02	-0.28 ± 0.02	0.83 ± 0.05
59	4.76 m/s	0.179	0.56 ± 0.02	0.67 ± 0.03	2.13 ± 0.04

Table 12.2: *Results of the statistical analysis of the renewal process.*

The parameters σ and m, describing $p(\tau)$ can be used for estimating the mean net heat flux j_{pdf} according to Equation (5.29) yielding

$$j_{\mathrm{pdf}} = \frac{3}{4}\sqrt{\pi\kappa}c_p\rho\Delta\bar{T}\exp\left[-\left(\frac{\sigma^2}{16}+\frac{m}{2}\right)\right]. \tag{12.1}$$

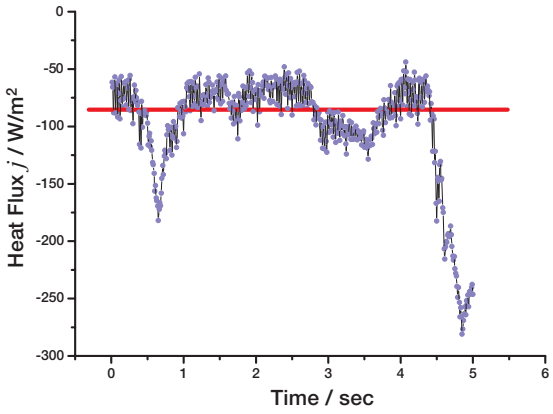

Figure 12.11: *The net heat flux j of an individual image sequence recorded on year day 58.*

Another technique for estimating the net heat flux has been presented in Section 5.4.2. Here the heat flux j_{root} is estimated based on the assumption that water parcels from the well mixed bulk are transported to the surface were they equilibrate. No further requirements on the knowledge of $p(\tau)$ have to be made. The net heat flux j_{root} can thus be computed from Equation (5.20)

$$j_{\mathrm{root}} = \mathrm{sign}(\mathrm{d}T_{\mathrm{surf}}(t)/\mathrm{d}t)\sqrt{\frac{\pi\kappa}{2}}c_p\rho\sqrt{\Delta T(t)\frac{\mathrm{d}}{\mathrm{d}t}T_{\mathrm{surf}}(t)}. \tag{12.2}$$

The temporal derivative $\mathrm{d}T_{\mathrm{surf}}(t)/\mathrm{d}t$ can be estimated at every pixel of an image sequence as explained in Section 8.8.1. It can also be assumed that the temperature of the bulk of the water T_{bulk} is spatially constant over the imaged area. This is due to the relatively small footprint of (40×40) cm^2 and the good mixture in the bulk. Hence the temperature depression $\Delta T = T_{\mathrm{surf}} - T_{\mathrm{bulk}}$ can be computed likewise for every pixel of the sequence. This in turn allows for an estimate of j_{root} with the spatial resolution of the infrared camera. The results for the heat flux at this high temporal resolution is presented in Figure 12.11.

The main difference between the estimate based on j_{root} or j_{pdf} can thus be stated as the higher resolution of j_{root} as it is not statistically based. Also fewer assumptions have to be made in deriving it, this clearly favors this method. Nevertheless it is interesting to compare the performance of both techniques under a variety of conditions. This represents another verification of the assumptions made in estimating j_{pdf}. If both techniques estimate the same value for the net heat flux it can be inferred indirectly that the probability density function $p(\tau)$ accurately models the statistical properties of the surface renewal process.

As stated in Section 12.2.2 meteorological measurements of the heat fluxes were conducted on board the R/V Ronald H. Brown. Apart from verifying consistent results of both estimates j_{root} and j_{pdf} to one another, their results were also compared to the estimates based on meteorological techniques j_{met}. Exemplary the deployments of year day 52 and 58 are shown in Figure 12.12. It can generally be stated that there exists a good agreement between the estimates. The value obtained from j_{pdf} seems to be biased slightly towards higher values of the net heat flux. This has already been noted for the experiments in the Heidelberg Aeolotron in Section 11.6.2. Within the margin of error the agreement to the meteorologically derived heat flux estimates j_{met} seems to be quite good.

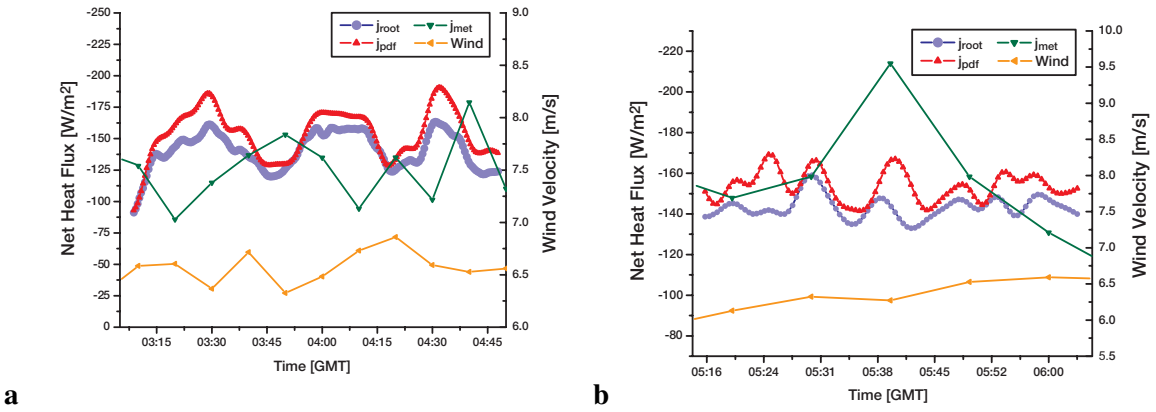

Figure 12.12: *The results of the heat flux estimates from the deployment on year day 52 is shown in* ***a*** *and those for the deployment on year day 58 in* ***b*** *. Plotted are the estimates of j_{root}, j_{pdf} and the one derived from meteorological techniques, j_{met}, as well as the wind velocity.*

Also there seems to be a slight correlation to the wind speed, as can be seen in Figure 12.12 **a** , where peaks in the heat flux are followed by peaks in the wind velocity. However, it should be noted that measurements of the meteorological data was conducted on the bow tower of the research vessel, whereas the techniques based on thermography were conducted on LADAS. Both were separated by about 100 m during the measurements.

A possible explanation for the discrepancy between the measurements of j_{pdf} and j_{root} can be given by analyzing the relevant equations. j_{pdf} is based on a statistical analysis of the times τ between surface renewal events. The values of τ were computed from Equation (5.12). From this equation follows that $\tau \propto \Delta T/\dot{T}_{\mathrm{surf}}$. Higher values of j_{pdf} imply shorter times τ, which can be seen from the experimental values but also from Equation (5.29). This is due to the fact that an increase in j_{pdf} leads primarily to a decrease in m, a measure for the width of the distribution. Assuming that $\dot{T}_{\mathrm{surf}}$ was estimated correctly, too big an estimate for j_{pdf} can thus be due to a slightly to small value for ΔT. The opposite is true for the estimate j_{root}. It is given by Equation (5.20) which states $j_{\mathrm{root}} \propto \sqrt{\Delta T \cdot \dot{T}_{\mathrm{surf}}}$. For too small a value of ΔT the computed value for j_{root} will also be too small. This reflects exactly what can be observed from the measurements presented in Figure 12.12, where j_{root} is always a little lower than j_{pdf}. The estimated values for the heat fluxes can be found in Table 12.3

From the estimates of the net heat flux j the heat transfer velocity k_{heat} is computed. This can be

Year Day	Wind Speed	u_*	j_{met}	j_{root}	j_{pdf}
52	5.23 m/s	0.199	-129.06	-141 ± 4	-144.87 ± 4
54	4.18 m/s	0.154	-116.60	-124 ± 4	-91.37 ± 3
58	5.05 m/s	0.184	-142.47	-143 ± 4	-153.48 ± 4
59	4.76 m/s	0.170	-119.65	-121 ± 3	-112.45 ± 3

Table 12.3: *Results of the statistical analysis of the renewal process. The errors of the meteorological estimates are not known.*

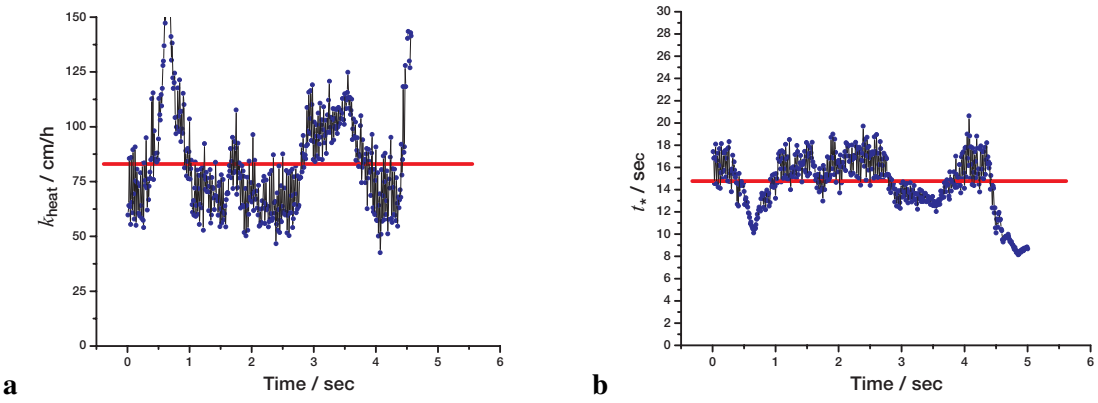

Figure 12.13: *In* ***a*** *is the transfer velocity* k_{heat} *and in* ***b*** *the characteristic time constant* t_* *shown for one sequence.*

done from the technique introduced in Section 5.5. To facilitate the comparison to the values found by other authors, heat transfer velocities are normalized to the Schmidt number $Sc = 600$. This corresponds to the Schmidt number for CO_2 at a water temperature of 20°C. Following Jähne [1980] the Schmidt number exponent n changes from $n = 2/3$ to $n = 1/2$ at an air sided friction velocity u_* of $u_* = 0.3m/s$. As indicated in Table 12.4 the friction velocity measured during the deployments was always below $u_* = 0.2$. Therefore the Schmidt number exponent $n = 2/3$ was used for the scaling from the transfer velocity of heat k_{heat} to k_{600}.

Year Day	Wind Speed	u_* [m/s]	$k_{600,\mathrm{root}}$ [cm/h]	$k_{600,\mathrm{pdf}}$ [cm/h]
52	5.23 m/s	0.199	8.61 ± 0.22	8.84 ± 0.22
54	4.18 m/s	0.154	18.23 ± 0.46	13.49 ± 0.34
58	5.05 m/s	0.184	9.61 ± 0.24	10.30 ± 0.26
59	4.76 m/s	0.170	6.68 ± 0.17	6.23 ± 0.16

Table 12.4: *Results of the heat flux estimates.*

12.3 Summary

In this thesis techniques have been developed for measuring important parameters of air-water heat and gas transfer. These are the heat transfer velocity k_{heat}, the net heat flux j, the temperature depression across the cool skin of the ocean ΔT, as well as the parameters specifying the probability density function of the surface renewal process $p(\tau)$. The techniques for estimating these parameters from thermographic image sequences have been introduced in Chapter 5. In Chapter 11 they have been applied to laboratory measurements, establishing error bounds and their applicability. In this chapter the techniques were applied to field measurements, proving their applicability to challenging conditions in hostile environments.

In a first step the methods have proven their usefullness during first trial deployments on a buoy in conditions close to shore. The knowledge gained during these deployments was transferred to the

GasExII experiment where they were used in an international collaboration on LADAS, a research catamaran. Here spatially resolved estimates for the transfer velocity and the heat flux were acquired a high temporal resolution, never used before in field measurements. The results of the heat flux measurements were compared to mean values derived from current state of the art meteorological measurements. The agreement between these different measuring techniques was found to be well within the accuracy bounds.

Chapter 13

Conclusion and Outlook

The main objective of this thesis has been the development of a novel technique for measuring the net heat flux at the air-water interface with a high spatial and temporal resolution. To achieve this an algorithmic framework was developed and applied to thermographic observations of the sea surface. This development made it feasible to estimate the net heat flux as well as other important parameters of air-water heat and gas transfer accurately. For the first time spatially resolved heat flux measurements at the framerate of an infrared camera have been accomplished. In experiments conducted both under laboratory conditions and in the field, estimates with temporal resolution of well less than a second have been presented. At the same time these novel techniques offer a spatial resolution of only a few millimeters, limited only by the resolution of the infrared camera and the footprint under investigation. These kinds of measurements were unprecedented, both under field and laboratory conditions. This chapter briefly recapitulates the presented accomplishments and discusses perspectives of future work.

13.1 Summary

The transfer of heat or mass across the air-water interface is limited by a boundary layer extending roughly 1mm below the surface in the case of heat. Below this layer fast turbulent transport predominates while in this layer heat can only be transported due to slow conduction. An understanding of the transport phenomena of both mass and heat through this layer is important for a number of air-sea interaction processes.

Phenomenologically it has been known for a long time that the turbulent structure below the surface leads to the development of a less well mixed surface layer roughly 0.1 to 0.2 K cooler than the bulk of the water. Through a statistical analysis this temperature difference can be estimated from infrared imagery (Section 5.2). Although published previously the technique was analyzed in this thesis for the first time both in terms of accuracy and limitations. It has also been extended to be robust with respect to data corrupted by reflexes. This increases the applicability of the technique for in-situ measurements immensely.

In this statistical analysis it is implicitly assumed that water in the thermal boundary layer is periodically replaced with well mixed water from the bulk. The time span between these renewal processes is further assumed to be following a logarithmic normal probability distribution. Solemnly

assuming that water parcels are indeed transported from the well mixed bulk to the surface where they equilibrate in a process similar to molecular diffusion, a technique was developed for estimating the time of residence of such a water parcel at the surface (Section 5.3). From a statistical analysis of these times of residence the probability density function of the surface renewal process was measured from thermography. This probability density function was verified both under controlled laboratory conditions (Section 11.5) and during the NOAA sponsored GasExII cruise on board the LADAS catamaran (Section 12.2.4). Under both conditions a logarithmic-normal distribution of this renewal process could be confirmed and the parameters characterizing the distribution assessed. This justifies the assumption underlying the statistical analysis of the temperature depression estimation mentioned earlier.

Three methods to estimate the net heat flux at the sea surface were presented. In the first technique the parameters characterizing the probability density function of times between surface renewal events were used for estimating the net heat flux (Section 5.4.3). These parameters are derived from the mentioned statistical analysis of times of residence of a water parcel at the sea surface. Consequently this technique can be used for deducing the mean heat flux over the spatio-temporal neighborhood used in the statistical analysis. The second technique requires no assumption concerning the surface renewal process (Section 5.4.2). All that is assumed is that well mixed water parcels from the bulk replace less well mixed water close to the sea surface. Once adjacent to the surface they equilibrate by molecular conduction, changing their temperature as they do so. From this change of temperature the net heat flux can be computed. The third technique make measurements of the net heat flux feasible, based on an estimation of the shear rate on the sea surface (Section 5.4.4). This shear rate is equivalent to the divergence of the flow field at the air-water interface. From extending algorithms of computer vision these divergences can be computed accurately and highly efficient.

From the estimates of the heat flux the transfer velocity for heat can be derived. The transfer velocity is highly relevant in the context of air-sea gas transfer. It is due to a well known relation between transfer velocities that heat can be used as a proxy tracer of mass transfer (Section 3.3). These transfer velocities for heat were computed both in laboratory and field experiments, possessing the same unrivalled properties in terms of accuracy and spatio-temporal resolution (Sections 11.7.3 and 12.2.4). In a joint laboratory experiment mass fluxes of a few volatile tracers as well as the heat flux was measured (Section 11.7.3). This demonstrated the practicability of the novel techniques in the quest for a meticulous parameterization of heat and mass transfer phenomena.

In field and laboratory experiments the novel methods of estimating the net heat flux were compared to state of the art techniques. Excellent agreement to these approaches could be affirmed. Furthermore modulations of the heat flux due to small scale waves were observed for the first time (Section 11.7.1 and 12.2.4). The practicability of a less well known parameterization of heat and gas transfer could be demonstrated (Section 11.7.2). In this formulation the transfer velocity can be computed from the divergence of the sea surface flow field alone.

These advances in estimating the parameters of air-water gas and heat transfer were only realizable due to advances and extension of computer vision algorithms proposed in this work. A commonly used gradient based algorithm for estimating the optical flow was extended to model physically based brightness changes (Section 8.3). Such brightness transformations might for example be due to thermal conduction as present at the sea surface. It could be shown that accuracy of estimating the

parameters of this brightness change as well as the flow field was increased significantly by appropriately treating the errors in the data. Novel estimators to the field of computer vision were introduced to numerically efficiently pertain accurate estimates. These estimators outperform currently used estimators (Sections 6.2 and 6.3) when part of the data is known exactly (Section 6.5) or for an identified covariance matrix of the noisy deviates from independently identically distributed Gaussian noise (Section 6.6). For the type of camera used in the context of this work the importance of these noise models was demonstrated (Section 10.3). The significant improvement in accuracy of these proposed techniques was demonstrated by a thorough performance analysis (Section 9.2).

In the presence of data not adequately described by the employed model assumption the presented estimators will deviate arbitrary far from the sought model parameters. Such cases might be encountered due to reflexes on the sea surface or at motion discontinuities. The presented parameter estimation framework was extended by powerful schemes of robust statistics (Chapter 7). Due to these extension a high 50% of corrupted data can be tolerated and still accurate estimates attained. This was demonstrated on data pertinent to the context of this work (Section 9.3). The relevance of the proposed extensions to current computer vision techniques was demonstrated on applications other than purely estimating parameters at the sea surface (Section 8.8). Hypothesis testing in conjunction with optimum model selection was presented (Section 6.7) and applied to the topic of radiometric calibration of infrared cameras (Section 10.2.1).

13.2 Future Work

With the novel techniques developed a number of interesting research propositions can be named:

- With the novel technique it is now possible to perform systematic measurements in the Heidelberg Aeolotron. The influence of wind speed, surfactant concentrations, varying bulk temperatures and precipitation on air-water heat and gas exchange can be studied.
- To study the onset of instabilities caused by developing wind field and its relation to heat fluxes.
- Combining the techniques presented in this work and current work on accurate measurements of gas transfer velocities, it seems feasible to deduce the parameters influencing heat and gas transfer. The influence of these parameters on the Schmidt number exponent could be analyzed.
- In conjunction with a technique for resolving concentration gradients in the boundary layer by laser induced fluorescence the models of transport at the sea surface can be distinguished and their implications for heat exchange investigated.
- By combining spatially resolved heat flux estimates and wave slope measurements the effect of the wave field on surface fluxes can be examined.
- The surface strain model could be further analyzed in terms of its applicability. This can only be made feasible in combined measurements with a stereo imaging slope gauge from which the exact distance between the camera and the surface can be obtained.

- To bridge the gap between experiment and numerical models the algorithms should be applied to simulated data and the underlying theories tested.
- The developed robust estimators can be applied to the detection and quantification of multiple motions. Examples include motions discontinuities such as occlusions and transparent layers.
- The framework to estimate the parameters governing dynamical processes should be applied to other scientific areas. This ranges from small scale microscopic imagery to satellite data.
- So far the techniques described are limited to linear processes. An interesting task would be the extension to nonlinear processes.

Appendices

Appendix A

Eigensystem Analysis

A.1 The Singular Value Decomposition

If $\boldsymbol{A}$ is a real n by m matrix ($\boldsymbol{A} \in \mathbb{R}^{n \times m}$), then there exist orthogonal matrices

$$\boldsymbol{U} = (\boldsymbol{u}_1, \ldots, \boldsymbol{u}_n) \in \mathbb{R}^{n \times n} \quad \text{and} \quad \boldsymbol{V} = (\boldsymbol{v}_1, \ldots, \boldsymbol{v}_m) \in \mathbb{R}^{m \times m} \tag{A.1}$$

such that

$$\boldsymbol{U}^\top \boldsymbol{A} \boldsymbol{V} = \operatorname{diag}(\lambda_1, \ldots, \lambda_p) \ \in \mathbb{R}^{n \times m} \quad \text{where} \quad p = \min(n, m). \tag{A.2}$$

The *singular values* λ_i, also called *eigenvalues*, are to be ordered $\lambda_1 \geq \cdots \geq \lambda_p \geq 0$. The vectors $\boldsymbol{u}_i$ and $\boldsymbol{v}_i$ are the ith *left singular vector* and the ith *right singular vector* respectively. A proof of the singular value decomposition (SVD) can be found in Golub and van Loan [1996].

The computational cost of the basic SVD can be significantly reduced in the context of this work. Usually not the whole eigensystem is of interest as the solution to the TLS problem consists of the eigenvector to the smallest eigenvalue (see section 6.3). Van Huffel et al. [1987] make use of this fact and device a partial singular value decomposition which computes the singular subspace of a matrix, associated with its smallest singular values. This step allows for a 2-3 times faster computation of the eigenvectors of interest and hence a speed improvement of the TLS of a factor of 2 [Van Huffel and Vandewalle, 1991].

A.2 The Generalized Singular Value Decomposition

Given $\boldsymbol{A} \in \mathbb{R}^{n \times p}$ with $n \geq p$ and $\boldsymbol{B} \in \mathbb{R}^{m \times p}$, then there exist orthogonal $\boldsymbol{U} \in \mathbb{R}^{n \times n}$ and $\boldsymbol{V} \in \mathbb{R}^{m \times m}$ and an invertible $\boldsymbol{X} \in \mathbb{R}^{p \times p}$ such that

$$\boldsymbol{U}^\top \boldsymbol{A} \boldsymbol{X} = \boldsymbol{C} = \operatorname{diag}(c_1, \ldots, c_p) \quad c_i \geq 0 \tag{A.3}$$

$$\boldsymbol{V}^\top \boldsymbol{B} \boldsymbol{X} = \boldsymbol{S} = \operatorname{diag}(s_1, \ldots, s_q) \quad s_i \geq 0, \tag{A.4}$$

where $q = \min(m, p)$. The elements of the set $\lambda_g(\boldsymbol{A}, \boldsymbol{B}) = \{c_1/s_1, \ldots, c_p/s_q\}$ are referred to as the *generalized singular values* of $\boldsymbol{A}$ and $\boldsymbol{B}$. The columns of $\boldsymbol{X} = (\boldsymbol{x}_1, \ldots, \boldsymbol{x}_p)$ satisfy

$$s_i^2 \boldsymbol{A}^\top \boldsymbol{A} \boldsymbol{x}_i = c_i^2 \boldsymbol{B}^\top \boldsymbol{B} \boldsymbol{x}_i, \quad i \in \{1, \ldots, p\}, \tag{A.5}$$

so that for $s_i \neq 0$ the $\boldsymbol{x}_i$ are called the *generalized singular vectors* to the generalized singular values $\lambda_g = c_i/s_i$.

A detailed proof of this decomposition can be found in Golub and van Loan [1996]. For a detailed description of the GSVD algorithm the reader is referred to van Loan [1976], Paige and Saunders [1981], Golub and van Loan [1996] and for a computational implementation of the algorithm to Paige [1986] which was increased in accuracy by Bai and Demmel [1993]. Details of implementation can be found in Anderson et al. [1999], machine specific optimizations which are available for a range different architectures such as the one used in the scope of this work [Intel, 2001].

Appendix B

Temperature Distribution at the Sea Surface

For the derivation of temperature distribution at the sea surface, that is the probability $p(T_{\mathrm{surf}})$ of finding a certain temperature, some model assumptions have to be made. First and foremost, the surface renewal model is assumed where water parcels from the well mixed bulk water replaces water very close to the interface. Close to the interface the heat transport is governed thermal conduction. Next the probability density function $p(t)$ of times in between consecutive surface renewal events has to be presumed. Experiments suggest that this probability density function be logarithmic-normally distributed.

The underlying equation is that of thermal conduction at the interface

$$\Delta T(t) = T(t) = \frac{2j}{\sqrt{\pi\kappa}c_p\rho}\sqrt{\Delta t} = \alpha j\sqrt{\Delta t}, \quad t \geq t_0 \tag{B.1}$$

with $\Delta t = t - t_0$ and $\alpha = 2/(\sqrt{\pi\kappa}\rho c_p)$, which leads to the following expression for Δt:

$$\Delta t(T) = \frac{\pi\kappa c_p^2\rho^2}{4j^2}T^2 = \left(\frac{T}{\alpha j}\right)^2. \tag{B.2}$$

As this method of calculating the heat flux j is of statistical nature, we are interested in the probability of measuring a certain temperature T. This likelihood is higher, of course, when the change of temperature with respect to time is smaller. The gradient $\partial\Delta t(T)/\partial T$ represents a mean to express the time it takes for the temperature to change over an infinitesimal interval ∂T. This is directly proportional to the probability of measuring the temperature T. The probability $p(T|\tau)$ of measuring a temperature T at a given time τ between surface renewals is thus given as

$$p(T|\tau) = \begin{cases} \gamma\frac{\partial t(T)}{\partial T} & = & \gamma\frac{2T}{(\alpha j)^2} & , & \forall & 0 \leq t \leq \tau \\ 0 & & & , & \forall & t > \tau \end{cases}, \tag{B.3}$$

with a constant of proportionality γ. This constant can be solved for by normalizing $p(T|\tau)$ and using

Equation(B.1):

$$\begin{aligned} 1 &\equiv \int_0^{T(\tau)} p(T|\tau)dT \\ &= \frac{2\gamma}{(\alpha j)^2}\int_0^{T(\tau)} TdT = \frac{\gamma T^2}{(\alpha j)^2}\Big|_0^{T(\tau)} \\ &= \frac{\gamma}{(\alpha j)^2}\left(\alpha j\sqrt{\tau}\right)^2 = \gamma\cdot\tau \\ \Rightarrow \gamma &= \frac{1}{\tau}. \end{aligned} \tag{B.4}$$

The chance $p(T)$ of measuring the temperature T can then be calculated if the probability $p(\tau)$ of the time τ between surface renewals is known, that is

$$p(T) = \int_0^{\infty} p(T|\tau)\cdot p(\tau)d\tau = \frac{2T}{(\alpha j)^2}\int_0^{\infty}\frac{p(\tau)}{\tau}d\tau. \tag{B.5}$$

The probability density function of the time between surface renewals $p(\tau)$ is a priori unknown. In Chapter 2.4.3 experimental evidence was presented that a log-normal distribution as given by Equation (2.51) is very likely. Therefore, if we take the probability density function to be

$$p(\tau) = \frac{1}{\sqrt{\pi}\sigma\tau}e^{-\frac{(\ln\tau - m)^2}{\sigma^2}}, \quad \tau > 0. \tag{B.6}$$

we can insert this expression for $p(\tau)$ into Equation (B.5), resulting in:

$$p(T) = \frac{2T}{(\alpha j)^2\sqrt{\pi}\sigma}\int_{t(T)}^{\infty}\frac{e^{-\frac{(\ln\tau - m)^2}{\sigma^2}}}{\tau^2}d\tau. \tag{B.7}$$

The integral in this equation can be solved by introducing the substitute $x = \ln\tau$ which means that $d\tau = \tau dx$. Thus

$$\begin{aligned} \int_{t(T)}^{\infty}\frac{\exp\left[-\frac{(\ln\tau - m)^2}{\sigma^2}\right]}{\tau^2}d\tau &= \int_{\ln t(T)}^{\infty}\frac{\exp\left[-\frac{(x-m)^2}{\sigma^2}\right]}{\exp[x]}dx \\ = \int_{\ln t(T)}^{\infty}\exp\left[-\frac{1}{\sigma^2}x^2 + \left(\frac{2m}{\sigma^2} - 1\right)x - \frac{m^2}{\sigma^2}\right]dx. \end{aligned} \tag{B.8}$$

From integration tables [Beyer, 1984] the following relationship can be derived

$$\int e^{-ax^2-bx-c}dx = \frac{\sqrt{\pi}}{2\sqrt{a}}\exp\left[\frac{b^2}{4a} - c\right]\operatorname{erf}\left[\frac{b+2ax}{2\sqrt{a}}\right], \tag{B.9}$$

which yields

$$\begin{aligned} & \int_{t(T)}^{\infty} \frac{\exp\left[-\frac{(\ln\tau - m)^2}{\sigma^2}\right]}{\tau^2} d\tau \\ = \quad & \frac{\sigma\sqrt{\pi}}{2} \exp\left[\frac{\sigma^2}{4} - m\right] \operatorname{erf}\left[\frac{\sigma}{2} - \frac{m}{\sigma} + \frac{\ln(\tau)}{\sigma}\right] \Bigg|_{t(T)}^{\infty} \\ = \quad & \frac{\sigma\sqrt{\pi}}{2} \exp\left[\frac{\sigma^2}{4} - m\right] \operatorname{erfc}\left[\frac{\sigma}{2} - \frac{m}{\sigma} + \frac{\ln\left(t(T)\right)}{\sigma}\right] \end{aligned} \tag{B.10}$$

with the complementary error function defined in Equation (2.22) as $\operatorname{erfc}(z) = 1 - \operatorname{erf}(z)$ and the error function given by the integral of the Gaussian distribution $\operatorname{erf}(z) = 2/\sqrt{\pi} \int_0^z \exp(-\eta^2) \mathrm{d}\eta$.

The probability density function $p(T)$ is thus given by inserting Equation (B.10) into Equation (B.7) and making use of the expression (B.2) for $t(T)$, which leads to

$$p(T_{\mathrm{surf}}) = \frac{T_{\mathrm{surf}} - T_{\mathrm{bulk}}}{(\alpha j)^2} \exp\left[\frac{\sigma^2}{4} - m\right] \operatorname{erfc}\left[\frac{\sigma}{2} - \frac{m}{\sigma} + \frac{1}{\sigma} \ln\left(\frac{T_{\mathrm{surf}} - T_{\mathrm{bulk}}}{\alpha j}\right)^2\right], \tag{B.11}$$

$$\text{with} \quad \alpha = \frac{2}{\sqrt{\pi\kappa}\rho c_p}.$$

Appendix C

Tables of F-Distribution

C.1 Upper 5% Values

m_2 \ m_1	1	2	3	4	5	6	7	8	9	10	11	12	13	14	15
1	161.5	199.5	215.7	224.6	230.2	234.0	236.8	238.9	240.5	241.9	243.0	243.9	244.7	245.4	246.0
2	18.51	19.00	19.16	19.25	19.30	19.33	19.35	19.37	19.39	19.40	19.40	19.41	19.42	19.42	19.43
3	10.13	9.552	9.277	9.117	9.013	8.941	8.887	8.845	8.812	8.786	8.763	8.745	8.729	8.715	8.703
4	7.709	6.944	6.591	6.388	6.256	6.163	6.094	6.041	5.999	5.964	5.936	5.912	5.891	5.873	5.858
5	6.608	5.786	5.409	5.192	5.050	4.950	4.876	4.818	4.772	4.735	4.704	4.678	4.655	4.636	4.619
6	5.987	5.143	4.757	4.534	4.387	4.284	4.207	4.147	4.099	4.060	4.027	4.000	3.976	3.956	3.938
7	5.591	4.737	4.347	4.120	3.972	3.866	3.787	3.726	3.677	3.637	3.603	3.575	3.550	3.529	3.511
8	5.318	4.459	4.066	3.838	3.687	3.581	3.500	3.438	3.388	3.347	3.313	3.284	3.259	3.237	3.218
9	5.117	4.256	3.863	3.633	3.482	3.374	3.293	3.230	3.179	3.137	3.102	3.073	3.048	3.025	3.006
10	4.965	4.103	3.708	3.478	3.326	3.217	3.135	3.072	3.020	2.978	2.943	2.913	2.887	2.865	2.845
11	4.844	3.982	3.587	3.357	3.204	3.095	3.012	2.948	2.896	2.854	2.818	2.788	2.761	2.739	2.719
12	4.747	3.885	3.490	3.259	3.106	2.996	2.913	2.849	2.796	2.753	2.717	2.687	2.660	2.637	2.617
13	4.667	3.806	3.411	3.179	3.025	2.915	2.832	2.767	2.714	2.671	2.635	2.604	2.577	2.554	2.533
14	4.600	3.739	3.344	3.112	2.958	2.848	2.764	2.699	2.646	2.602	2.565	2.534	2.507	2.484	2.463
15	4.543	3.682	3.287	3.056	2.901	2.790	2.707	2.641	2.588	2.544	2.507	2.475	2.448	2.424	2.403
16	4.494	3.634	3.239	3.007	2.852	2.741	2.657	2.591	2.538	2.494	2.456	2.425	2.397	2.373	2.352
17	4.451	3.592	3.197	2.965	2.810	2.699	2.614	2.548	2.494	2.450	2.413	2.381	2.353	2.329	2.308
18	4.414	3.555	3.160	2.928	2.773	2.661	2.577	2.510	2.456	2.412	2.374	2.342	2.314	2.290	2.269
19	4.381	3.522	3.127	2.895	2.740	2.628	2.544	2.477	2.423	2.378	2.340	2.308	2.280	2.256	2.234
20	4.351	3.493	3.098	2.866	2.711	2.599	2.514	2.447	2.393	2.348	2.310	2.278	2.250	2.225	2.203
21	4.325	3.467	3.072	2.840	2.685	2.573	2.488	2.420	2.366	2.321	2.283	2.250	2.222	2.197	2.176
22	4.301	3.443	3.049	2.817	2.661	2.549	2.464	2.397	2.342	2.297	2.259	2.226	2.198	2.173	2.151
23	4.279	3.422	3.028	2.796	2.640	2.528	2.442	2.375	2.320	2.275	2.236	2.204	2.175	2.150	2.128
24	4.260	3.403	3.009	2.776	2.621	2.508	2.423	2.355	2.300	2.255	2.216	2.183	2.155	2.130	2.108
25	4.242	3.385	2.991	2.759	2.603	2.490	2.405	2.337	2.282	2.236	2.198	2.165	2.136	2.111	2.089
26	4.225	3.369	2.975	2.743	2.587	2.474	2.388	2.321	2.265	2.220	2.181	2.148	2.119	2.094	2.072
27	4.210	3.354	2.960	2.728	2.572	2.459	2.373	2.305	2.250	2.204	2.166	2.132	2.103	2.078	2.056
28	4.196	3.340	2.947	2.714	2.558	2.445	2.359	2.291	2.236	2.190	2.151	2.118	2.089	2.064	2.041
29	4.183	3.328	2.934	2.701	2.545	2.432	2.346	2.278	2.223	2.177	2.138	2.104	2.075	2.050	2.027
30	4.171	3.316	2.922	2.690	2.534	2.421	2.334	2.266	2.211	2.165	2.126	2.092	2.063	2.037	2.015
31	4.160	3.305	2.911	2.679	2.523	2.409	2.323	2.255	2.199	2.153	2.114	2.080	2.051	2.026	2.003
32	4.149	3.295	2.901	2.668	2.512	2.399	2.313	2.244	2.189	2.142	2.103	2.070	2.040	2.015	1.992
33	4.139	3.285	2.892	2.659	2.503	2.389	2.303	2.235	2.179	2.133	2.093	2.060	2.030	2.004	1.982
34	4.130	3.276	2.883	2.650	2.494	2.380	2.294	2.225	2.170	2.123	2.084	2.050	2.021	1.995	1.972
35	4.121	3.267	2.874	2.641	2.485	2.372	2.285	2.217	2.161	2.114	2.075	2.041	2.012	1.986	1.963
36	4.113	3.259	2.866	2.634	2.477	2.364	2.277	2.209	2.153	2.106	2.067	2.033	2.003	1.977	1.954
37	4.105	3.252	2.859	2.626	2.470	2.356	2.270	2.201	2.145	2.098	2.059	2.025	1.995	1.969	1.946
38	4.098	3.245	2.852	2.619	2.463	2.349	2.262	2.194	2.138	2.091	2.051	2.017	1.988	1.962	1.939
39	4.091	3.238	2.845	2.612	2.456	2.342	2.255	2.187	2.131	2.084	2.044	2.010	1.981	1.954	1.931
40	4.085	3.232	2.839	2.606	2.449	2.336	2.249	2.180	2.124	2.077	2.038	2.003	1.974	1.948	1.924
50	4.034	3.183	2.790	2.557	2.400	2.286	2.199	2.130	2.073	2.026	1.986	1.952	1.921	1.895	1.871
100	3.936	3.087	2.696	2.463	2.305	2.191	2.103	2.032	1.975	1.927	1.886	1.850	1.819	1.792	1.768
150	3.904	3.056	2.665	2.432	2.274	2.160	2.071	2.001	1.943	1.894	1.853	1.817	1.786	1.758	1.734
200	3.888	3.041	2.650	2.417	2.259	2.144	2.056	1.985	1.927	1.878	1.837	1.801	1.769	1.742	1.717
250	3.879	3.032	2.641	2.408	2.250	2.135	2.046	1.976	1.917	1.869	1.827	1.791	1.759	1.732	1.707
300	3.873	3.026	2.635	2.402	2.244	2.129	2.040	1.969	1.911	1.862	1.821	1.785	1.753	1.725	1.700
350	3.868	3.022	2.630	2.397	2.240	2.125	2.036	1.965	1.907	1.858	1.816	1.780	1.748	1.720	1.695
400	3.863	3.018	2.627	2.394	2.237	2.121	2.032	1.962	1.903	1.854	1.813	1.776	1.745	1.717	1.691
450	3.861	3.016	2.625	2.392	2.234	2.119	2.030	1.959	1.901	1.852	1.810	1.774	1.742	1.714	1.689

m_2	m_1 1	2	3	4	5	6	7	8	9	10	11	12	13	14	15
500	3.860	3.014	2.623	2.390	2.232	2.117	2.028	1.957	1.899	1.850	1.808	1.772	1.740	1.712	1.686
550	3.858	3.012	2.621	2.388	2.230	2.115	2.026	1.955	1.897	1.848	1.806	1.770	1.738	1.710	1.685
600	3.857	3.011	2.620	2.387	2.229	2.114	2.025	1.954	1.895	1.846	1.805	1.768	1.736	1.708	1.683
650	3.856	3.010	2.619	2.386	2.228	2.113	2.024	1.953	1.894	1.845	1.803	1.767	1.735	1.707	1.682
700	3.855	3.009	2.618	2.385	2.227	2.112	2.023	1.952	1.893	1.844	1.802	1.766	1.734	1.706	1.681
750	3.854	3.008	2.617	2.384	2.226	2.111	2.022	1.951	1.892	1.843	1.801	1.765	1.733	1.705	1.680
800	3.853	3.007	2.616	2.383	2.225	2.110	2.021	1.950	1.892	1.843	1.801	1.764	1.732	1.704	1.679
850	3.852	3.006	2.615	2.382	2.225	2.109	2.020	1.949	1.891	1.842	1.800	1.764	1.732	1.703	1.678
900	3.852	3.006	2.615	2.382	2.224	2.109	2.020	1.949	1.890	1.841	1.799	1.763	1.731	1.703	1.678
950	3.851	3.005	2.614	2.381	2.224	2.108	2.019	1.948	1.890	1.841	1.799	1.762	1.730	1.702	1.677
1000	3.851	3.005	2.614	2.381	2.223	2.108	2.019	1.948	1.889	1.840	1.798	1.762	1.730	1.702	1.676

C.2 Upper 1% Values

m_2	m_1 1	2	3	4	5	6	7	8	9	10	11	12	13	14	15
1	4052	5000	5403	5625	5764	5859	5928	5981	6023	6056	6083	6106	6126	6143	6157
2	98.50	99.00	99.17	99.25	99.30	99.33	99.36	99.37	99.39	99.40	99.41	99.42	99.42	99.43	99.43
3	34.12	30.82	29.46	28.71	28.24	27.91	27.67	27.49	27.35	27.23	27.13	27.05	26.98	26.92	26.87
4	21.20	18.00	16.69	15.98	15.52	15.21	14.98	14.80	14.66	14.55	14.45	14.37	14.31	14.25	14.20
5	16.26	13.27	12.06	11.39	10.97	10.67	10.46	10.29	10.16	10.05	9.963	9.888	9.825	9.770	9.722
6	13.75	10.93	9.780	9.148	8.746	8.466	8.260	8.102	7.976	7.874	7.790	7.718	7.657	7.605	7.559
7	12.25	9.547	8.451	7.847	7.460	7.191	6.993	6.840	6.719	6.620	6.538	6.469	6.410	6.359	6.314
8	11.26	8.649	7.591	7.006	6.632	6.371	6.178	6.029	5.911	5.814	5.734	5.667	5.609	5.559	5.515
9	10.56	8.022	6.992	6.422	6.057	5.802	5.613	5.467	5.351	5.257	5.178	5.111	5.055	5.005	4.962
10	10.04	7.559	6.552	5.994	5.636	5.386	5.200	5.057	4.942	4.849	4.772	4.706	4.650	4.601	4.558
11	9.646	7.206	6.217	5.668	5.316	5.069	4.886	4.744	4.632	4.539	4.462	4.397	4.342	4.293	4.251
12	9.330	6.927	5.953	5.412	5.064	4.821	4.640	4.499	4.388	4.296	4.220	4.155	4.100	4.052	4.010
13	9.074	6.701	5.739	5.205	4.862	4.620	4.441	4.302	4.191	4.100	4.025	3.960	3.905	3.857	3.815
14	8.862	6.515	5.564	5.035	4.695	4.456	4.278	4.140	4.030	3.939	3.864	3.800	3.745	3.698	3.656
15	8.683	6.359	5.417	4.893	4.556	4.318	4.142	4.004	3.895	3.805	3.730	3.666	3.612	3.564	3.522
16	8.531	6.226	5.292	4.773	4.437	4.202	4.026	3.890	3.780	3.691	3.616	3.553	3.498	3.451	3.409
17	8.400	6.112	5.185	4.669	4.336	4.102	3.927	3.791	3.682	3.593	3.519	3.455	3.401	3.353	3.312
18	8.285	6.013	5.092	4.579	4.248	4.015	3.841	3.705	3.597	3.508	3.434	3.371	3.316	3.269	3.227
19	8.185	5.926	5.010	4.500	4.171	3.939	3.765	3.631	3.523	3.434	3.360	3.297	3.242	3.195	3.153
20	8.096	5.849	4.938	4.431	4.103	3.871	3.699	3.564	3.457	3.368	3.294	3.231	3.177	3.130	3.088
21	8.017	5.780	4.874	4.369	4.042	3.812	3.640	3.506	3.398	3.310	3.236	3.173	3.119	3.072	3.030
22	7.945	5.719	4.817	4.313	3.988	3.758	3.587	3.453	3.346	3.258	3.184	3.121	3.067	3.019	2.978
23	7.881	5.664	4.765	4.264	3.939	3.710	3.539	3.406	3.299	3.211	3.137	3.074	3.020	2.973	2.931
24	7.823	5.614	4.718	4.218	3.895	3.667	3.496	3.363	3.256	3.168	3.094	3.032	2.977	2.930	2.889
25	7.770	5.568	4.675	4.177	3.855	3.627	3.457	3.324	3.217	3.129	3.056	2.993	2.939	2.892	2.850
26	7.721	5.526	4.637	4.140	3.818	3.591	3.421	3.288	3.182	3.094	3.021	2.958	2.904	2.857	2.815
27	7.677	5.488	4.601	4.106	3.785	3.558	3.388	3.256	3.149	3.062	2.988	2.926	2.871	2.824	2.783
28	7.636	5.453	4.568	4.074	3.754	3.528	3.358	3.226	3.120	3.032	2.959	2.896	2.842	2.795	2.753
29	7.598	5.420	4.538	4.045	3.725	3.499	3.330	3.198	3.092	3.005	2.931	2.868	2.814	2.767	2.726
30	7.562	5.390	4.510	4.018	3.699	3.473	3.304	3.173	3.067	2.979	2.906	2.843	2.789	2.742	2.700
31	7.530	5.362	4.484	3.993	3.675	3.449	3.281	3.149	3.043	2.955	2.882	2.820	2.765	2.718	2.677
32	7.499	5.336	4.459	3.969	3.652	3.427	3.258	3.127	3.021	2.934	2.860	2.798	2.744	2.696	2.655
33	7.471	5.312	4.437	3.948	3.630	3.406	3.238	3.106	3.000	2.913	2.840	2.777	2.723	2.676	2.634
34	7.444	5.289	4.416	3.927	3.611	3.386	3.218	3.087	2.981	2.894	2.821	2.758	2.704	2.657	2.615
35	7.419	5.268	4.396	3.908	3.592	3.368	3.200	3.069	2.963	2.876	2.803	2.740	2.686	2.639	2.597
36	7.396	5.248	4.377	3.890	3.574	3.351	3.183	3.052	2.946	2.859	2.786	2.723	2.669	2.622	2.580
37	7.373	5.229	4.360	3.873	3.558	3.334	3.167	3.036	2.930	2.843	2.770	2.707	2.653	2.606	2.564
38	7.353	5.211	4.343	3.858	3.542	3.319	3.152	3.021	2.915	2.828	2.755	2.692	2.638	2.591	2.549
39	7.333	5.194	4.327	3.843	3.528	3.305	3.137	3.006	2.901	2.814	2.741	2.678	2.624	2.577	2.535
40	7.314	5.179	4.313	3.828	3.514	3.291	3.124	2.993	2.888	2.801	2.727	2.665	2.611	2.563	2.522
50	7.171	5.057	4.199	3.720	3.408	3.186	3.020	2.890	2.785	2.698	2.625	2.562	2.508	2.461	2.419
100	6.895	4.824	3.984	3.513	3.206	2.988	2.823	2.694	2.590	2.503	2.430	2.368	2.313	2.265	2.223
150	6.807	4.749	3.915	3.447	3.142	2.924	2.761	2.632	2.528	2.441	2.368	2.305	2.251	2.203	2.160
200	6.763	4.713	3.881	3.414	3.110	2.893	2.730	2.601	2.497	2.411	2.338	2.275	2.220	2.172	2.129
250	6.737	4.691	3.861	3.395	3.091	2.875	2.711	2.583	2.479	2.392	2.319	2.257	2.202	2.154	2.111
300	6.720	4.677	3.848	3.382	3.079	2.862	2.699	2.571	2.467	2.380	2.307	2.244	2.190	2.142	2.099
350	6.708	4.666	3.838	3.373	3.070	2.854	2.691	2.562	2.458	2.372	2.299	2.236	2.181	2.133	2.090
400	6.699	4.659	3.831	3.366	3.063	2.847	2.684	2.556	2.452	2.365	2.292	2.229	2.175	2.126	2.084
450	6.692	4.653	3.825	3.361	3.058	2.842	2.679	2.551	2.447	2.360	2.287	2.224	2.170	2.121	2.079
500	6.686	4.648	3.821	3.357	3.054	2.838	2.675	2.547	2.443	2.356	2.283	2.220	2.166	2.117	2.075
550	6.681	4.644	3.817	3.353	3.051	2.835	2.672	2.544	2.440	2.353	2.280	2.217	2.162	2.114	2.071
600	6.677	4.641	3.814	3.351	3.048	2.832	2.669	2.541	2.437	2.351	2.277	2.214	2.160	2.111	2.069
650	6.674	4.638	3.812	3.348	3.045	2.830	2.667	2.539	2.435	2.348	2.275	2.212	2.157	2.109	2.066
700	6.671	4.636	3.810	3.346	3.043	2.828	2.665	2.537	2.433	2.346	2.273	2.210	2.155	2.107	2.064
750	6.669	4.634	3.808	3.344	3.042	2.826	2.663	2.535	2.431	2.345	2.271	2.208	2.154	2.105	2.063
800	6.667	4.632	3.806	3.343	3.040	2.825	2.662	2.533	2.429	2.343	2.270	2.207	2.152	2.104	2.061
850	6.665	4.630	3.805	3.341	3.039	2.823	2.660	2.532	2.428	2.342	2.269	2.206	2.151	2.103	2.060
900	6.663	4.629	3.803	3.340	3.038	2.822	2.659	2.531	2.427	2.341	2.267	2.204	2.150	2.101	2.058
950	6.662	4.628	3.802	3.339	3.037	2.821	2.658	2.530	2.426	2.340	2.266	2.203	2.149	2.100	2.057
1000	6.660	4.626	3.801	3.338	3.036	2.820	2.657	2.529	2.425	2.339	2.265	2.203	2.148	2.099	2.056

Bibliography

R. J. Adcock. A problem in least squares. *The Analyst*, 5:53–54, 1878.

E. H. Adelson and J. R. Bergen. Spatiotemporal energy models for the perception of motion. *Journal of the Optical Society of America A*, 2(2):284–299, 1985.

G. Adiv. Determining three-dimensional motion and structure from optical flow generated by several moving objects. *IEEE Transactions on Pattern Analysis and Machine Intelligence*, 7:384–401, 1985.

A. Agulló. New algorithms for computing the least trimmed squares regression estimator. *Computational Statistics and Data Analysis*, 36:425–439, 2001.

P. Anandan. A computational framework and an algorithm for the measurement of visual motion. *International Journal of Computer Vision*, 2:283–319, 1989.

E. Anderson, Z. Bai, C. Bischof, S. Blackford, J. W. Demmel, J. Dongarra, J. Du Croz, A. Greenbaum, S. Hammarling, A. McKenney, and D. Sorensen. *LAPACK Users' Guide*. Society for Industrial and Applied Mathematics, Philadelphia, PA, third edition, 1999.

E. L. Andreas and E. C. Monahan. The role of whitecap bubbles in air-sea heat and moisture exchange. *Journal of Physical Oceanography*, 30(2):433–442, 2000.

E. G. Andreev and G. G. Khundzhua. Heat exchange and thermal structure of boundary layers of the sea-atmosphere system in the small scale interaction process. *Fizyka Astronomiya*, 16(1):54–59, 1975.

A. C. Atkinson and A. N. Donev. *Optimum Experimental Design*, volume 8 of *Oxford Statistical Science Series*. Clarendon Press, Oxford, 1992.

A. Bab-Hadiashar and D. Suter. Optic flow calculation using robust statistics. In *CVPR*, pages 988–993, Puerto Rico, 1997.

A. Bab-Hadiashar and D. Suter. Motion segmentation: a robust approach. In *IEEE Workshop The Interpretation of Visual Motion*, Santa Barbara, 1998a.

A. Bab-Hadiashar and D. Suter. Robust optic flow computation. *International Journal of Computer Vision*, 29(1):59–77, 1998b.

A. Bab-Hadiashar and D. Suter. Robust total least squares based optic flow computation. In *Asian Conference on Computer Vision*, volume 1, pages 566–573, Hong Kong, January 1998c. Springer Verlag.

Z. Bai and J. W. Demmel. Computing the generalized singular value decomposition. *SIAM Journal on Scientific Computing*, 14(6):1464–1468, 1993.

G. Balschbach. Personal communication, 2001.

J. N. Barnola, D. Raynaud, Y. S. Korotkevich, and C. Lorius. Vostok ice core provides 160,000-year record of atmospheric CO_2. *Nature*, 329:408–414, 1987.

J. L. Barron, D. J. Fleet, and S. Beauchemin. Performance of optical flow techniques. *International Journal of Computer Vision*, 12(1):43–77, 1994.

J. L. Barron and H. Spies. The fusion of image and range flow. In R. Klette, T. Huang, and G. Gimel'farb, editors, *Multi-Image Search and Analysis*, Lecture Notes in Computer Sciences. Springer-Verlag, 2001. in press.

I. Bauer, H. G. Bock, S. Körkel, and J. P. Schlöder. Numerical methods for optimum experimental design in dae systems. *Journal of Computational and Applied Mathematics*, 120:1–25, 2000.

A. E. Beaton and J. W. Tukey. The fitting of power series, meaning polynomials, illustrated on band-spectroscopic data. *Technometrics*, 16:147–185, 1974.

S. S. Beauchemin and J. L. Barron. The computation of optical flow. *ACM Computing Surveys*, 27 (3):433–467, 1995.

J. R. Bergen, P. J. H. R. Burt, and S. Peleg. A three-frame algorithm for estimating two-component image motion. *IEEE Transactions on Pattern Analysis and Machine Intelligence*, 14(9):886–896, 1992.

P. J. Besl and R. C. Jain. Segmentation through variable-order surface fitting. *IEEE Transactions on Pattern Analysis and Machine Intelligence*, 10(2):167–192, 1988.

W. H. Beyer. *CRC Standard Mathematical Tables*. CRC Press, Boca Raton, FL, 27th edition, 1984.

J. Bigün and G. H. Granlund. Optimal orientation detection of linear symmetry. In *ICCV*, pages 433–438, 1987.

J. Bigün, G. H. Granlund, and J. Wiklund. Multidimensional orientation estimation with application to texture analysis and optical flow. *IEEE Transactions on Pattern Analysis and Machine Intelligence*, 13(8):775–790, 1991.

R. B. Bird, W. E. Stewart, and E. N. Lightfoot. *Transport Phenomena*. John Wiley & Sons, New York, 2nd edition, 2001.

A. Björck. Least squares methods. In P. G. Ciarlet and J. L. Lions, editors, *Finite Difference Methods (Part 1)*, volume 1 of *Handbook of Numerical Analysis*, pages 465–652. Elesvier Science Publishers, North-Holland, 1990.

M. J. Black. *Robust Incremental Optical Flow*. PhD thesis, Yale University, 1992.

M. J. Black and P. Anandan. Robust dynamic motion estimation over time. In *CVPR*, pages 296–302, Maui, Hawaii, June 1991.

M. J. Black, D. J. Fleet, and Y. Yacoob. Robustly estimating changes in image appearance. *Computer Vision and Image Understanding*, 78(1):8–31, 2000.

M. J. Black and A. D. Jepson. Estimating optical flow in segmented images using variable-order parametric models with local deformations. *PAMI*, 18(10):972–986, October 1996.

M. J. Black and A. Rangarajan. On the unification of line processes, outlier rejection, and robust statistics with applications in early vision. *International Journal of Computer Vision*, 19(1):57–92, July 1996.

T. V. Blanc. Variation of bulk-derived surface flux, stability, and roughness results due to the use of different transfer coefficient schemes. *Journal of Physical Oceanography*, 15:650–669, 1985.

L. Boltzmann. Ableitung des Stefan'schen Gesetzes, betreffend die Abhängigkeit der Wärmestrahlung von der Temperatur aus der elektromagnetischen Lichttheorie. *Annalen der Physik und Chemie*, 22 (2):291–294, 1884.

J. Boussinesq. *Théorie analytique de la chaleur*, volume 2. Gathier-Villars, Paris, 1903.

P. Bouthemy and E. François. Motion segmentation and quantitative dynamic scene analysis from an image sequence. *International Journal of Computer Vision*, 10(2):157–182, 1993.

E. F. Bradley, P. A. Coppin, and J. S. Godfrey. Measurements of sensible and latent heatflux in the western equatorial pacific ocean. *Journal of Geophysical Research*, 96(Supplement):3375–3389, 1991.

R. L. Branham. A covariance matrix for total least squares with heteroscedastic data. *The Astronomical Journal*, 117:1942–1948, 1999.

W. S. Broecker and T.-H. Peng. *Tracers in the Sea*. Lamont-Doherty Geological Observatory, Columbia University, Palisades, New York, 1982.

W. Brutsaert. The roughness length for water vapor, sensible heat, and other scalars. *Journal of Atmospherical Sciences*, 32(10):2028–2031, 1975a.

W. Brutsaert. A theory for local evaporation (or heat transfer) from rough to smooth surfaces at ground level. *Water Resource Research*, 11:543–550, 1975b.

J. A. Businger. Evaluation of the accuracy with which dry deposition can be measured with current micrometeorological techniques. *Journal of Climate and Applied Meteorology*, 25:1100–1124, 1986.

J. A. Businger and A. C. Delaney. Chemical sensor resolution required for measuring surface fluxes by three common micrometeorological techniques. *Journal of Atmospheric Chemistry*, 10:399–410, 1990.

J. A. Businger and S. P. Oncley. Flux measurements with conditional sampling. *Journal of Atmospheric and Oceanic Technology*, 7:349, 1990.

J. A. Businger, J. C. Wyngaard, Y. Izumi, and E. F. Bradley. Flux-profile relationships in the atmospheric surface layer. *Journal of Atmospherical Sciences*, 28(2):181–189, 1971.

S. J. Caughey and J. C. Kaimal. Vertical heat flux in the convective boundary layer. *Quarterly Journal of the Royal Meteorological Society*, 103(438):811–815, 1977.

F. H. Champagne, C. A. Friehe, J. C. LaRue, and J. C. Wyngaard. Flux measurements, flux estimation techniques, and fine-scale turbulence measurements in the unstable surface layer over land. *Journal of Atmospherical Sciences*, 34(3):515–530, 1977.

T. F. Chan. An improved algorithm for computing the singular vale decomposition. *ACM Transactions on Mathematical Software*, 8(1):72–83, 1982.

M. M. Chang. Simultaneous motion estimation and segmentation. *IEEE Transactions on Image Processing*, 6(9):1326–1333, 1997.

C. H. Chu and E. J. Delp. Estimating displacement vectors from an image sequence. *Journal of the Optical Society of America A*, 6(6):871–878, 1989.

M. Coantic. A model of gas transfer across air-water interfaces with capillary waves. *Journal of Geophysical Research*, 91:3925–3943, 1986.

P. A. Coppin, E. F. Bradley, I. J. Barton, and J. S. Godfrey. Simultaneous observations of sea surface temperature in the western equatorial pacific by bulk, radiative and satelite methods. *Journal of Geophysical Research*, 96:3401–3409, 1991.

T. H. Cormen, C. E. Leiserson, and R. L. Rivest. *Introduction to Algorithms*. MacGraw-Hill, New York, 1990.

C. Cox and W. Munk. Some problems in optical oceanography. *Journal of Marine Research*, 14: 63–78, 1955.

J. Crank. *The Mathematics of Diffusion*. Clarendon Press, Oxford, 2nd edition, 1975.

G. T. Csanady. The role of breaking wavelets in air-sea gas transfer. *Journal of Geophysical Research*, 95(C1):749–759, 1990.

P. V. Danckwerts. Significance of a liquid-film coefficients in gas absorption. *Industrial and Engineering Chemistry*, 43:1460–1467, 1951.

B. De St.Venant. Note á joindre une mémoire sur la dynamique des fluids. *Comptes Rendus*, 17: 1240–1244, 1843.

W. M. Deen. *Analysis of Transport Phenomena (Topics in Chemical Engineering)*. Oxford University Press, New York, 1998.

J. W. Demmel and K. Veseliç. Jacobi's method is more accurate than QR. *SIAM Journal on Matrix Analysis and Applications*, 13(4):1204–1245, 1992.

R. L. Desjardins. *A study of Carbon-Dioxide and Sensible Heat Fluxes Using the Eddy Correlation Technique*. PhD thesis, Cornell University, 1972.

H. D. Downing and D. Williams. Optical constants of water in the infrared. *Journal of Geophysical Research*, 80(12):1656–1661, 1975.

N. Draper and H. Smith. *Applied Regression Analysis*. Wiley series in probability and mathematical statistics. Wiley, 2nd edition, 1981.

B. Duc. Motion estimation using invariance under group transformations. In *Proc. of the 12th IAPR International Conference on Pattern Recognition*, volume 1, pages 159–163, Los Alamitos, CA, 1994. IEEE Comput. Soc. Press.

B. Duc. *Feature Design: Applications to Motion Analysis and Identity Verification*. PhD thesis, École Polytechnique Fédérale de Lausanne, 1997.

A. J. Dyer and B. B. Hicks. Kolmogorov constants at the 1976 ITCE. *Boundary-Layer Meteorology*, 22:137–150, 1982.

C. Eckhart and G. Young. The approximation of one matrix by another of lower rank. *Psychometrica*, 1:211–218, 1936.

J. B. Edson, A. A. Hinton, K. E. Prada, J. E. Hare, and C. W. Fairall. Direct covariance flux estimates from moving platforms at sea. *Journal of Atmospheric and Oceanic Technology*, 15:547–562, 1998.

W. J. Emery and Y. Yu. Satelite sea surface temperature patterns. *International Journal of Remote Sensing*, 18(2):323–334, 1997.

G. Ewing and E. D. McAlister. On the thermal boundary layer of the ocean. *Science*, 131:1374–1376, 1960.

C. W. Fairall, E. F. Bradley, J. S. Godfrey, G. A. Wick, and J. B. Edson. Cool-skin and warm-layer effects on sea surface temperature. *Journal of Geophysical Research*, 101(C1):1295–1308, 1996a.

C. W. Fairall, E. F. Bradley, D. P. Rogers, J. B. Edson, and G. S. Young. Bulk parameterization of air-sea fluxes for tropical ocean-global atmosphere coupled-ocean atmosphere response experiment. *Journal of Geophysical Research*, 101(C2):3747–3764, 1996b.

C. W. Fairall, J. B. Edson, S. E. Larsen, and P. G. Mestayer. Inertial-dissipation air-sea flux measurments: a prototype system using real-time spectral computations. *Journal of Atmospheric and Oceanic Technology*, 7(3):425–453, 1990.

C. W. Fairall and J. E. Hare. Personal comunication, 2001.

C. W. Fairall, J. Kepert, and G. J. Holland. A parameterization of the effect of sea spray on surface energy transports over the ocean. In M. A. Donelan, W. H. Hui, and W. J. Plant, editors, *Proc. of the Symposium on the Air-Sea Interface, Radio and Acoustic Sensing, Turbulence and Wave Dynamics*, pages 523–528, Marseilles, France, 1993. RMAS, University of Miami, FL.

C. W. Fairall and S. E. Larsen. Internal-dissipation methods and turbulent fluxes at the the air-ocean interface. *Boundary-Layer Meteorology*, 34:287–301, 1986.

C. W. Fairall, P. O. G. Persson, E. F. Bradley, R. E. Payne, and S. Anderson. A new look at calibration and use of Eppley Precision Infrared Radiometers: Part I theory and application. *Journal of Atmospheric and Oceanic Technology*, 15:1230–1243, 1998.

G. Farnebäck. Fast and accurate motion estimation using orientation tensors and parametric motion models. In *ICPR*, volume 1, pages 135–139, Barcelona, Spain, September 2000.

O. Faugeras. *Three-Dimensional Computer Vision: A Geometric Viewpoint*. The MIT Press, Cambridge, MA, 1993.

C. Fennema and W. Thompson. Velocity determination in scenes containing several moving objects. *Computer Graphics and Image Processing*, 9:301–315, 1979.

C. Fermueller, R. Pless, and J. Aloimonos. Statistical biases in optic flow. In *CVPR'99*, Fort Collins, Colorado, June 1999.

A. E. Fick. Über diffusion. *Annalen der Physik*, 94(4):59–86, 1855.

D. J. Fleet. *Measurement of Image Velocity*. Kluwer Academic Publishers, Dordrecht, The Netherlands, 1992.

D. J. Fleet and A. D. Jepson. Computation of component image velocity from local phase information. *International Journal of Computer Vision*, 5:77–104, 1990.

G. E. Forsythe and C. Moler. *Computer Solution for Linear Algebraic Systems*. Prentice-Hall, Englewood Cliffs, NJ, 1967.

G. E. Fortescue and J. R. A. Pearson. On gas absorption into a turbulent liquid. *Chemical Engineering Science*, pages 1163–1176, 1967.

J. B. Fourier. Théorie analytique de la chaleur. In *Œuvres de Fourier*. Gauthier-Villars et Fils, Paris, France, 1822.

N. M. Frew. The role of organic films in air-sea gas exchange. In P. S. Liss and R. A. Duce, editors, *The Sea Surface and Global Change*, chapter 5, pages 121–171. Cambridge University Press, Cambridge,UK, 1997.

N. M. Frew. Personal communication, 2001.

C. A. Friehe, W. J. Shaw, D. P. Rogers, K. L. Davidson, W. G. Large, S. A. Stage, G. H. Crescenti, S. J. S. Khalsa, G. K. Greenhut, and F. Li. Air-sea fluxes and surface layer turbulence around a sea surface temperature front. *Journal of Geophysical Research*, 95(C5):8593–8609, 1991.

D. Fuß. *Entwicklung einer Stereo Imaging Wave Slope*. PhD thesis, University of Heidelberg, Heidelberg, Germany, 2003.

P. P. Gallo. Consistency of regression estimates when some variables are subject to error. *Communications in statistics / Theory and methods*, 11:973–983, 1982.

C. S. Garbe. Entwicklung eines Systems zur dreidimensionalen Particle Tracking Velocimetry mit Genauigkeitsuntersuchungen und Anwendung bei Messungen in einem Wind-Wellen Kanal. Master's thesis, University of Heidelberg, Heidelberg, Germany, 1998.

C. S. Garbe, H. Haußecker, and B. Jähne. Measuring the sea surface heat flux and probability distribution of surface renewal events. In E. Saltzman, M. Donelan, W. Drennan, and R. Wanninkhof, editors, *Gas Transfer at Water Surfaces*, Geophysical Monograph. American Geophysical Union, 2001a.

C. S. Garbe and B. Jähne. Reliable estimates of the sea surface heat flux from image sequences. In *Proc. of the 23rd DAGM Symposium*, Lecture Notes in Computer Science, LNCS 2191, pages 194–201, Munich, Germany, 2001. Springer-Verlag.

C. S. Garbe, U. Schurr, and B. Jähne. Thermographic measurements of plant leaves. In X. P. Maldague and A. E. Rozlosnik, editors, *ThermoSense*. The International Society for Optical Engineering, SPIE, 2002. Submitted.

C. S. Garbe, H. Spies, and B. Jähne. Measuring parameters for air-sea gas transfer from infrared image sequences. *Journal of Mathematical Imaging and Vision*, 2001b. Special Edition 'Analysis of Fluid Motion from Images', submitted.

D. Garcia, J.-J. Orteu, and M. Devy. Accurate calibration of a stereovision sensor: Comparison of different approaches. In B. Girod, G. Greiner, H. Niemann, and H.-P. Seidel, editors, *Vision Modeling and Visualization 2000*, pages 25–32, Saarbrücken, Germany, November 2000. Aka GmbH, Berlin.

C. F. Gauss. Theoria combinationis observationum erroribus minimis obnoxiae. *Comment. Soc. Reg. Sci. Gotten. Recent.*, 5:33–90, 1823.

G. L. Geernaert. Bulk parameterization for the wind stress and heat fluxes. In G. L. Geernaert and W. J. Plant, editors, *Surface Waves and Fluxes*, volume 1 - Current Theory, chapter 5, pages 91–172. Kluwer Academic, Norwell,MA, 1990.

G. L. Geernaert, S. E. Larsen, and F. Hansen. Measurements of the wind stress, heat flux, and turbulence intensity during storm conditions over the North Sea. *Journal of Geophysical Research*, 92 (C12):13127–13139, 1987.

A. Gelb. *Applied Optimal Estimation*. M.I.T. Press, Cambridge, MA, 1974.

F. Glazer, G. Reynolds, and P. Anandan. Scene matching through hierarchical correlation. In *Proc. Conference on Computer Vision and Pattern Recognition*, pages 432–441, Washington, 1983.

L. J. Gleser. Estimation in a multivariate "error in variables" regression model: Large sample results. *Annals of Statistics*, 9:24–44, 1981.

H. Goldstein. *Classical Mechanics*. Addison-Wesley Series in Physics. Addison-Wesley, Reading,MA, 2nd edition, 1980.

G. H. Golub and C. F. van Loan. An analysis of the total least squares problem. *SIAM Journal on Numerical Analysis*, 17(6):883–893, December 1980.

G. H. Golub and C. F. van Loan. *Matrix Computations*. The Johns Hopkins University Press, Baltimore and London, 3 edition, 1996.

H. Grassl. The dependence of the measured cool skin of the ocean on wind stress and total heat flux. *Boundary-Layer Meteorology*, 10:465–474, 1976.

H. Gröning. *Monokulares 3D-Tracking und radiometrische Kalibrierung*. PhD thesis, University of Heidelberg, Heidelberg, Germany, 2002. in preparation.

C. W. Groetsch. *Inverse problems in the mathematical sciences*. Vieweg, Braunschweig, 1993.

P. Guillaurne, R. Pintelon, and J. Schoukens. Weighted total least squares estimator for multivariable systems with nearly maximum likelyhood properties. *IEEE Transactions on Instrumentation and Measurment*, 47(4):818–822, 1998.

J. S. Gulliver. Introduction to air-water mass transfer. In S. C. Wilhelms and J. S. Gulliver, editors, *Second International Symposium of Air-Water Gas Transfer*, 1990.

A. M. Gusev, E. G. Andeev, V. V. Gurov, G. G. Khundzhua, and A. A. Budnikov. Heat exchange in a small-scale sea-air interaction. *Soviet Meteorology and Hydrology*, 8:42–45, 1976.

F. R. Hampel, E. M. Ronchetti, P. J. Rousseeuw, and W. A. Stahel. *Robust Statistics: The Approach Based on Influence Functions*. John Wiley and Sons, New York, 1986.

R. A. Handler, G. B. Smith, and R. I. Leighton. The thermal structure of an air-water interface at low wind speeds. *Tellus*, 53(A):233–244, 2001.

J. E. Hare. Personal comunication, 2001.

P. Hariott. A random eddy modification of the penetration theory. *Chemical Engineering Science*, 17: 149–154, 1962.

L. Hasse. The sea surface temperature deviation and the heat flow at the sea-air interface. *Boundary-Layer Meteorology*, 1:368–379, 1971.

H. Haußecker. *Messung und Simulation von kleinskaligen Austauschvorgängen an der Ozeanoberfläche mittels Thermographie*. PhD thesis, University of Heidelberg, 1996.

H. Haußecker. Radiation. In B. Jähne, H. Haußecker, and P. Geißler, editors, *Handbook of Computer Vision and Applications*, volume 1, chapter 2, pages 7–35. Academic Press, San Diego,CA, 1999.

H. Haußecker and D. J. Fleet. Computing optical flow with physical models of brightness variation. *IEEE Transactions on Pattern Analysis and Machine Intelligence*, 23(6):661–673, June 2001.

H. Haußecker, C. S. Garbe, H. Spies, and B. Jähne. A total least squares for low-level analysis of dynamic scenes and processes. In *DAGM*, pages 240–249, Bonn, Germany, 1999. Springer.

H. Haußecker and B. Jähne. In situ measurements of the air-sea gas transfer rate during the MBL/CoOP west coast experiment. In B. Jähne and E. C. Monahan, editors, *Air-Water Gas Transfer - Selected Papers from the Third International Symposium on Air-Water Gas Transfer*, pages 775–784, Heidelberg, 1995. AEON Verlag & Studio Hanau.

H. Haußecker, U. Schimpf, C. S. Garbe, and B. Jähne. Physics from IR image sequences: Quantitative analysis of transport models and parameters of air-sea gas transfer. In E. Saltzman, M. Donelan, W. Drennan, and R. Wanninkhof, editors, *Gas Transfer at Water Surfaces*, Geophysical Monograph. American Geophysical Union, 2001.

H. Haußecker and H. Spies. Motion. In B. Jähne, H. Haußecker, and P. Geißler, editors, *Handbook of Computer Vision and Applications*, volume 2, chapter 13, pages 309–396. Academic Press, San Diego, 1999.

H. Haußecker, H. Spies, and B. Jähne. Tensor-based image sequence processing techniques for the study of dynamical processes. In *Proc. Intern. Symp. On Real-time Imaging and Dynamic Analysis*, pages 704–711, Hakodate, Japan, 1998. International Society of Photogrammetry and Remote Sensing, ISPRS, Commision V.

G. E. Healey and R. Kondepudy. Radiometric ccd camera calibration and noise estimation. *PAMI*, 16 (3):267–276, March 1994.

D. J. Heeger. Optical flow using spatiotemporal filters. *International Journal of Computer Vision*, 1: 279–302, 1988.

B. B. Hicks and R. T. McMillen. A simulation of the eddy accumulation method for measuring pollutant fluxes. *Journal of Climate and Applied Meteorology*, 23(4):637–643, 1984.

T. Hierl. Personal comunication, 2001. Thermosensorik GmbH.

R. Higbie. The rate of absorption of a pure gas into a still liquid during short periods of exposure. *Trans. Am. Inst. Chem. Eng.*, 31:365–389, 1935.

V. Hilsenstein. *Analysis of infrared image sequences with shape from stereo-motion*. PhD thesis, University of Heidelberg, Heidelberg, Germany, 2003.

J. O. Hinze. *Turbulence*. McGraw-Hill series in mechanical engineering. McGraw-Hill, New York, 2nd edition, 1975.

H. Hinzpeter. Atmospheric radiation instruments. In F. Dobson, L. Hasse, and R. Davis, editors, *Air-Sea Interaction - Instruments and Methods*, pages 491–507. Plenum Press, New York, 1980.

B. K. P. Horn. *Robot Vision*. MIT Press, Cambridge, MA, 1986.

B. K. P. Horn and B. Schunk. Determining optical flow. *Artificial Intelligence*, 17:185–204, 1981.

P. J. Huber. Robust estimation of a location parameter. *Annals of Mathematical Statistics*, 35:73–101, 1964.

P. J. Huber. Robust statistics: A review. *Annals of Mathematical Statistics*, 43:1041–1067, 1972.

P. J. Huber. *Robust Statistics*. John Wiley and Sons, New York, 1981.

J. C. R. Hunt, J. C. Kaimal, and J. E. Gaynor. Eddy structure in the convective boundary layer-new measurements and new concepts. *Quarterly Journal of the Royal Meteorological Society*, 114(482): 827–858, 1988.

Intel. Math kernel library, 2001. http://developer.intel.com/software/products/mkl/index.htm.

C. Jacobs, J. F. Kjeld, P. Nightingale, R. Upstill-Goddard, S. Larsen, and W. Oost. The narrowing gap between air-sea transfer velocities determined using deliberate tracers and from eddy correlation measurements: ASGAMAGE observations and a modeling study. Preprint 2001-18, Koninklijk Nederlands Meteorologisch Instituut, De Bilt, NL, 2001a. Submitted to Journal of Geophysical Research.

C. Jacobs, P. Nightingale, R. Upstill-Goddard, J. F. Kjeld, S. Larsen, and W. Oost. Comparison of the deliberate tracer method and eddy covariance measurements to determine the air/sea transfer velocity of CO_2. In E. Saltzman, M. Donelan, W. Drennan, and R. Wanninkhof, editors, *Gas Transfer at Water Surfaces*, Geophysical Monograph. American Geophysical Union, 2001b. in press.

N. G. Jerlov. *Marine Optics*, volume 14 of *Elsevier Oceanography Series*. Elsevier Scientific Publishing Company, Amsterdam, 1976.

A. T. Jessup, C. J. Zappa, and H. H. Yeh. Defining and quantifying microscale wave breaking with infrared imagery. *Journal of Geophysical Research*, 102(C10):23145–23153, 1997.

B. Jähne. *Parametrisierung des Gasaustausches mit Hilfe von Laborexperimenten*. PhD thesis, Institut für Umweltphysik, University of Heidelberg, 1980.

B. Jähne. Transfer processes across the free water surface. Habilitation thesis, University of Heidelberg, Heidelberg, Germany, 1985.

B. Jähne. Image sequence analysis of complex physical objects: nonlinear small scale water surface waves. In *Proc. of 1st International Conference on Computer Vision*, pages 191–200, London, UK, 1987.

B. Jähne. From mean fluxes to a detailed experimental investigation of the gas transfer process. In S. C. Wilhelms and J. S. Gulliver, editors, *Air-Water Mass Transfer, selected papers from the 3nd International Symposium on Gas Transfer at Water Surfaces*, Minneapolis, MI, 1991. ASCE.

B. Jähne. *Spatio-Temporal Image Processing : Theory and Scientific Applications*, volume 751 of *Lecture Notes in Computer Science*. Springer-Verlag, 1993.

B. Jähne. *Practical Handbook on Image Processing for Scientific Applications*. CRC Press, Boca Raton, Florida, 1996.

B. Jähne. *Digital Image Processing*. Springer, Berlin, Germany, 4th edition, 1997.

B. Jähne. Continuous and digital signals. In B. Jähne, H. Haußecker, and P. Geißler, editors, *Handbook of Computer Vision and Applications*, volume 2, chapter 2, pages 9–34. Academic Press, 1999a.

B. Jähne. Multiresolutional signal representation. In B. Jähne, H. Haußecker, and P. Geißler, editors, *Handbook of Computer Vision and Applications*, volume 2, chapter 4, pages 67–90. Academic Press, 1999b.

B. Jähne. Neighborhood operators. In B. Jähne, H. Haußecker, and P. Geißler, editors, *Handbook of Computer Vision and Applications*, volume 2, chapter 5, pages 93–124. Academic Press, 1999c.

B. Jähne and H. Haußecker. Air-water gas exchange. *Annual Reviews Fluid Mechanics*, 30:443–468, 1998.

B. Jähne, H. Haußecker, H. Scharr, H. Spies, D. Schmundt, and U. Schurr. Study of dynamical processes with tensor-based spatiotemporal image processing techniques. In *ECCV*, pages 322–336. Springer, 1998.

B. Jähne, H. Haußecker, U. Schimpf, and G. Balschbach. The Heidelberg Aeolotron - a new facility for laboratory investigations of small scale air-sea interaction. In M. L. Banner, editor, *The Wind-Driven Air-Sea Interface: Electromagnetic and Acoustic Sensing, Wave Dynamics and Turbulent Fluxes*, Sydney, Australia, 1999.

B. Jähne, P. Libner, R. Fischer, T. Billen, and E. J. Plate. Investigating the transfer process across the free aqueous boundary layer by the controlled flux method. *Tellus*, 41B(2):177–195, 1989.

B. Jähne, K. O. Münnich, R. Bösinger, A. Dutzi, W. Huber, and P. Libner. On the parameters influencing air-water gas exchange. *Journal of Geophysical Research*, 92(C2):1937–1949, 1987.

J. Jouzel, C. Lorius, J. R. Petit, C. Genthon, N. I. Barkov, V. M. Kotlyakov, and V. M. Petrov. Vostok ice core: a continuous isotope temperature record over the last climatic cycle (160,000 years). *Nature*, 329:403–408, 1987.

J. C. Kaimal. Sensors and techniques for direct measurements of turbulent fluxes and profiles in the atmospheric surface layer. In D. H. Lenshow, editor, *Atmospheric Technology*, pages 7–23. NCAR, 1975.

J. C. Kaimal, J. C. Wyngaard, Y. Izumi, and O. R. Coté. Spectral characteristics of surface layer turbulence. *Quarterly Journal of the Royal Meteorological Society*, 98(417):563–589, 1972.

R. Kalkenings. Personal communication, 2001.

R. Kalkenings. *?* PhD thesis, Institut für Umweltphysik, University of Heidelberg, Heidelberg, Germany, 2002.

K. Kanatani. *Group-Theoretical Methods in Image Understanding*, volume 20 of *Springer Series in Information Sciences*. Springer-Verlag, Heidelberg, Germany, 1990.

K. Kanatani. Statistical bias of conic fitting and renormalization. *IEEE Transactions on Pattern Analysis and Machine Intelligence*, 16(3):320–326, 1994.

E. T. Kanemasu, M. L. Wesely, B. B. Hicks, and J. L. eilman. Techniques for calculating energy and mass fluxes. In B. L. Barfield and J. F. Gerber, editors, *Modification of the Aerial Environment of Crops*, pages 156–182. Amereican Society of Agricultural Engineering, St. Joseph, MI, 1979.

M. Karczewicz, J. Nieweglowski, and P. Haavisto. Video coding using motion compensation with polynomial motion vector fields. *Signal Processing: Image Communication*, 10(1-3):63–91, 1997.

K. B. Katsaros. The sea surface temperature deviation at very low wind speeds; is there a limit? *Tellus*, 29:229–239, 1977.

K. B. Katsaros. The aqueous thermal boundary layer. *Boundary-Layer Meteorology*, 18:107–127, 1980a.

K. B. Katsaros. Radiative sensing of sea surface temperature. In F. Dobson, L. Hasse, and R. Davis, editors, *Air-Sea Interaction - Instruments and Methods*, pages 293–317. Plenum Press, New York, 1980b.

K. B. Katsaros. Parameterization schemes and models for estimating the surface radiation budget. In G. L. Geernaert and W. J. Plant, editors, *Surface Waves and Fluxes*, volume 2 - Remote Sensing, chapter 18, pages 339–368. Kluwer Academic, Norwell, MA, 1990.

K. B. Katsaros and J. E. DeVault. On irradiance measurment error at sea due to tilt of radiometers. *Journal of Atmospheric and Oceanic Technology*, 3(4):740–745, 1986.

G. G. Khundzhua and Y. G. Andreyev. An experimental study of heat exchange between the ocean and the atmosphere in small-scale interaction. *Izvestiya / Atmospheric and Oceanic Physics*, 10 (10):1110–1113, 1974.

G. R. Kirchhoff. Über das Verhältnis zwischen dem Emissionsvermögen und dem Absorptionsvermögen der Körper für Wärme und Licht. *Annalen der Physik*, 109:275–301, 1860.

C. Kittel and H. Krömer. *Thermal Physics*. W. H. Freeman & Co, San Francisco,CA, 2nd edition, 1995.

J. Klinke. *Optical Measurements of Small-Scale Wind Generated Water Surface Waves in the Laboratory and the Field*. PhD thesis, University of Heidelberg, Heideleberg, Germany, 1996.

K.-R. Koch. *Parameter Estimation and Hypothesis Testing in Linear Models*. Springer-Verlag, Heidelberg, Germany, 1988.

A. N. Kolmogorov. The local structure of turbulence in compressible turbulence for very large Reynolds numbers. *Compt. Rend. Akad. Nauk SSSR*, 30:301, 1941.

A. N. Kolmogorov. A refinement of previous hypotheses concerning the local structure of turbulence in a viscous incompressible fluid at high reynolds number. *Journal of Fluid Mechanics*, 13:82–85, 1962.

J. Kondo. Air-sea bulk transfer coefficients in diabatic conditions. *Boundary-Layer Meteorology*, 9: 91, 1975.

E. B. Kraus and J. A. Businger. *Atmosphere-ocean interaction*. Number 27 in Oxford monographs on geology and geophysics. Oxford University Press, New York, second edition, 1994.

T. v. Kármán. Mechanische Ähnlichkeit und Turbulenz. In *III. Internationale Kongress für Technische Mechanik*, volume 1, pages 85–93, Stockholm, 1930.

V. N. Kudryavtsev and A. V. Soloviev. On the thermal state of the ocean surface. *Izvestiya / Atmospheric and Oceanic Physics*, 17(10):1065–1071, 1981.

P. K. Kundu. *Fluid Mechanics*. Academic Press, San Diego, CA, 1990.

G. J. Kunz, G. de Leeuw, S. E. Larsen, and F. A. Hansen. Over-water eddy correlation measurements of fluxes of momentum, heat, vapor and CO_2. In B. Jähne and E. C. Monahan, editors, *Air-Water Gas Transfer*, pages 685–701. AEON Verlag und Studio, Hanau, Germany, 1995.

S.-H. Lai and B. C. Vemuri. Reliable and efficient computation of optical flow. *International Journal of Computer Vision*, 29(2):87–105, 1998.

L. D. Landau and E. M. Lifschitz. *Mechanik*, volume 1 of *Lehrbuch der theoretischen Physik*. Akademie Verlag, Berlin, 13th edition, 1990.

L. D. Landau and E. M. Lifschitz. *Hydrodynamik*, volume 6 of *Lehrbuch der theoretischen Physik*. Akademie Verlag, Berlin, 5th edition, 1991.

J. M. Lavest, M. Viala, and M. Dhome. Do we really need an accurate calibration pattern to achieve a reliable camera calibration? In H. Burkhardt and B. Neumann, editors, *Proc. of the 5th European Conference on Computer Vision*, volume 1, pages 158–174, Freiburg, D, 1998. Springer-Verlag.

C. L. Lawson and D. J. Hanson. *Solving Least Squares Problems*. Prentice-Hall, Englewood Cliffs, New Jersey, 1974.

D. V. Ledvina, G. S. Young, R. A. Miller, and C. W. Fairall. The effect of averaging on bulk estimates of heat and momentum fluxes for the tropical western pacific ocean. *Journal of Geophysical Research*, 98(C11):20211–20217, 1993.

K.-M. Lee, P. Meer, and R.-H. Park. Robust adaptive segmentation of range images. *PAMI*, 20(2): 200–205, 1998.

R. I. Leighton. Personal communication, 2000.

R. I. Leighton and G. Smith. Parametric modeling of the thermal boundary layer. under Review by JGR, 2000.

R. I. Leighton, G. Smith, and T. Shihi. A comparison of simulated and experimental ir measurements at low to moderate wind speeds. In *IEEE International Geoscience and Remote Sensing Symposium, IGARSS'98*, volume 1, pages 481–483, New York, NY, 1998. IEEE Geosci. & Remote Sensing Soc.

P. Lemmerling, I. Dologlou, and S. Van Huffel. On the formal equivalence between static and dynamic least squares and total least squares models. Technical Report TR 1998-95, Department of Electrical Engineering, ESAT-SISTA, Katholieke Universiteit Leuven, Heverlee, Belgium, 1998.

D. H. Lenshow, J. C. Wyngaard, and W. T. Pennell. Mean-field and second-moment budgets in a barocline, convective boundary layer. *Journal of Atmospherical Sciences*, 37(6):1313–1326, 1980.

P. Libner. *Die Konstantflußmethode: Ein neuartiges, schnelles und lokales Meßverfahren zur Untersuchung von Austauschvorgängen an der Luft-Wasser Phasengrenze*. PhD thesis, Institut für Umweltphysik, University of Heidelberg, Heidelberg, Germany, 1987.

J. K. Lindsey. *Introductory Statistics : The Modelling Approach*. Oxford University Press, Oxford, UK, 1995.

P. S. Liss and L. Merlivat. Air-sea gas exchange rates: Introduction and synthesis. In P. Buat-Menard, editor, *The role of air-sea exchange in geochemical cycling*, pages 113–129. Reidel, Boston,MA, 1986.

J. J. Little, H. H. Bulthoff, and T. A. Poggio. Analysis of differential and matching methods for optical flow. In *IEEE Workshop on Visual Motion*, pages 173–180, Irvine, CA, 1989.

W. T. Liu and J. A. Businger. Temperature profile in the molecular sublayer near the interface of a fluid in turbulent motion. *Geophysical Research Letters*, 2:403, 1975.

W. T. Liu, K. B. Katsaros, and J. A. Businger. Bulk parameterization of air-sea exchanges of heat and water vapor including the molecular constraints at the interface. *Journal of Atmospherical Sciences*, 36(9):1722–1735, 1979.

B. D. Lucas. *Generalized image matching by the method of differences*. PhD thesis, Carnegie-Mellon University, Pittsburgh, PA, 1984.

B. D. Lucas and T. Kanade. An iterative image registration technique with an application to stereo vision. In *DARPA Image Understanding Workshop*, pages 121–130, 1981.

M. R. Luettgen, W. C. Karl, and A. S. Willsky. Efficient multiscale regularization with application to the computation of optical flow. *IEEE Transactions on Image Processing*, 3(1):41–64, 1994.

T. Luhmann. *Nahbereichsphotogrammetrie : Grundlagen, Methoden und Anwendungen*. Wichmann, Heidelberg, 2000.

K. V. Mardia, J. T. Kent, and J. M. Bibby. *Multivariate Analysis*. Probability and Mathematical Statistics. Academic Press, San Diego, 1979.

S. J. Maybank. *Theory of Reconstruction from Image Motion*. Springer-Verlag, Berlin, Germany, 1993.

E. D. McAlister and W. McLeish. Heat transfer in the top milimeter of the ocean. *Journal of Geophysical Research*, 74(13):3408–3414, 1969.

E. D. McAlister and W. McLeish. A radiometric system for airborne measurement of the total heat flow from the sea. *Applied Optics*, 9(12):2697–2705, 1970.

W. R. McGillis. Personal comunication, 2001.

W. R. McGillis, J. B. Edson, J. E. Hare, and C. W. Fairall. Direct covariance air-sea CO_2 fluxes. *Journal of Geophysical Research*, 106(C8):16729–16745, 2001.

W. McKeown and R. I. Leighton. Mapping heat flux. *Journal of Atmospheric and Oceanic Technology*, 16:80–91, 1999.

P. Meer, D. Mintz, and A. Rosenfeld. Robust regression methods for computer vision: A review. *International Journal of Computer Vision*, 6(1):59–70, 1991.

W. Menke. *Geophysical Data Analysis: Discrete Inverse Theory*, volume 45 of *International Geophysics Series*. Academic Press, San Diego, 1989.

A. Merz. Die Oberflächentemperatur der Gewässer, Methoden und Ergebnisse. In *Veröffentlichungen des Instituts für Meereskunde*, volume 5 of *Neue Folge, A*, page 42pp. Universität Berlin, 1920.

P. G. Mestayer. Local isotropy and anisotropy in a high-reynolds-number turbulent boundary layer. *Journal of Fluid Mechanics*, 125:475–503, 1982.

R. Mester and M. Mühlich. Improving motion and orientation estimation using an equilibrated total least squares approach. In *ICIP*, Greece, October 2001.

P. L. Meyer. *Introductory Probability and Statistical Applications*. Addison-Wesley, 2nd edition, 1970.

M. Mühlich and R. Mester. Subspace methods and equilibration in computer vision. Technical Report XP-TR-C-21, Institute for Applied Physics, Goethe-Universitaet, Frankfurt, Germany, November 1999.

J. Miller and C. V. Stewart. Muse: Robust surface fitting using unbiased scale estimates. In *CVPR'96*, pages 300–306, San Francisco, 1996.

L. Mirsky. Symmetric gauge functions and unitarily invariant norms. *The Quarterly Journal of Mathematics*, 11:50–59, 1960.

A. Mitiche and P. Bouthemy. Computation and analysis of image motion: A synopsis of current problems and methods. *International Journal of Computer Vision*, 19(1):29–55, 1996.

Y. Mitsuta and T. Fujitani. Direct measurement of turbulence fluxes on a cruising ship. *Boundary-Layer Meteorology*, 6:203–217, 1974.

E. Mémin and P. Pérez. Dense estimation and object-based segmentation of the optical flow with robust techniques. *IEEE Transactions on Image Processing*, 7(5):703–719, May 1998.

K. O. Münnich, W. B. Clarke, K. H. Fisher, D. Flothmann, B. Kromer, W. Roether, and U. Siegenthaler. Gas exchange and evaporation studies in a circular wind tunnel, continuous radon-222 measurements at sea and tritium/helium-3 measurments in a lake. In A. Favre and K. Hasselmann, editors, *Turbulent fluxes through the sea surface, wave dynamics and prediction*, pages 151–166. Plenum Publishing Corporation, 1978.

T. Münsterer. *LIF Investigation of the Mechanisms Controlling Air-Water Mass Transfer at a Free Interface*. PhD thesis, University of Heidelberg, 1996.

W. J. M. Moll. A thermopile for measuring radiation. In *Proc. Physical Society*, volume 35, pages 257–260, London, 1923.

E. C. Monahan and D. K. Woolf. Comments on "variations of whitecap coverage with wind stress and water temperature". *Journal of Physical Oceanography*, 19(5):706–709, 1989.

H.-H. Nagel. Displacement vectors derived from second-order intensity variations in image sequences. *Computer Graphics and Image Processing*, 21:85–117, 1983.

H.-H. Nagel. On the estimation of optical flow: Relations between different approaches and some new results. *Artificial Intelligence*, 33:299–324, 1987.

H.-H. Nagel. On a constraint equation for the estimation of displacement rates in image sequences. *IEEE Transactions on Pattern Analysis and Machine Intelligence*, 11(1):13–30, 1989.

H.-H. Nagel and A. Gehrke. Spatiotemporal adaptive estimation and seqmentation of OF-fields. In *Proc. of the ECCV*, Lecture Notes in Computer Science, pages 87–102, Freiburg, Germany, 1998. Springer -Verlag.

M. Navier. Mémoire sur les lois du movement des fluides. *Mémoires de l'Academie de Science*, 6: 389–416, 1827.

S. Negahdaripour and C.-H. Yu. A generalized brightness chane model for computing optical flow. In *International Conference in Computer Vision*, pages 2–7, Berlin, 1993.

O. Nestares, D. J. Fleet, and D. Heeger. Likelihood functions and confidence bounds for total-least-squares problems. In *CVPR'00*, volume 1, 2000.

L. Ng and V. Solo. Choosing the optimal neighbourhood size in optical flow problems with error-in-variables modelling. In *Proc. IEEE International Conference on Image Processing*, volume 2, pages 186–190, Los Alamitos, CA, 1998. IEEE Comput. Soc.

P. D. Nightingale, G. Malin, C. S. Law, A. J. Watson, P. S. Liss, M. I. Liddicoat, J. Boutin, and R. C. Upstill-Goddard. In situ evaluation of air-sea gas exchange parameterization using novel conservation and volatile tracers. *Global Biogeochemical Cycles*, 14:373–387, 2000.

J. Nikuradse. Strömungsgesetze in rauhen Rohren. *V. D. I. Forschungsheft*, 361:1, 1933.

A. Nomura. Spatio-temporal optimization method for determining motion vector fields under non-stationary illumination. *Image and Vision Computing*, 18:939–950, 2000.

A. Nomura, H. Miike, and K. Koga. Determining motion fields under non-uniform illumination. *Pattern Recognition Letters*, 16:285–296, 1995a.

A. Nomura, H. Miike, and E. Yokoyama. Detecting motion and diffusion from a dynamic image sequence. *Transactions of IEE Japan*, 115-C:403–409, 1995b. in Japanese.

A. M. Obukhov. Turbulence in an atmosphere with non-uniform temperature. *Boundary-Layer Meteorology*, 2:7–29, 1971. english translation of original article (appeared 1946 in Tr. Akad. Nauk. USSR, Inst. Teoret. Geofiz).

N. Ohta. Optical flow detection using a general noise model. *IEICE Transactions on Information and Systems*, E79-D(7):951–957, 1996.

C. F. Olson. An approximation algorithm for least median of squares regression. *Information Processing Letters*, 63:237–241, 1997.

P. J. Olver. *Applications of Lie Groups to Differential Equations*. Springer-Verlag, 1986.

S. P. Oncley, A. C. Delaney, T. W. Horst, and P. P. Trans. Verification of flux measurements using conditional sampling. *Atmospheric Environment*, 27(A):2417, 1993.

E. P. Ong and M. Spann. Robust optical flow computation based on least-median-of-squares regression. *International Journal of Computer Vision*, 31(1):51–82, February 1999.

C. C. Paige. Computing the generalized singular value decomposition. *SIAM Journal on Scientific Computing*, 7(4):1126–1146, 1986.

C. C. Paige and M. A. Saunders. Towards a generalized singular value decomposition. *SIAM Journal on Numerical Analysis*, 18:398–405, 1981.

G. W. Paltridge and C. M. R. Platt. *Radiative Processes in Meteorology and Climatology*. Elsevier, New York, 1976.

J. E. Paquin and S. Pond. The determination of the kolmogoroff constants for velocity, temperature and humidity fluctuations from second- and third-order structure functions. *Journal of Fluid Mechanics*, 50:257–269, 1971.

C. A. Paulson and T. W. Parker. Cooling of a water surface by evaporation, radiation and heat transfer. *Journal of Geophysical Research*, 77(3):491–495, 1972.

C. A. Paulson and J. J. Simpson. The temperature difference across the cool skin of the ocean. *Journal of Geophysical Research*, 86(C11):11044–11054, 1981.

R. Philipona, C. Fröhlich, and C. Betz. Characterization of pyrgeometers and the accuracy of atmospheric long-wave radiation measurements. *Applied Optics*, 34(9):1598–1605, 1995.

M. Planck. Distribution of energy in the spectrum. *Annalen der Physik*, 4(3):553–563, 1901.

S. D. Poisson. Mémoire sur les equations générales de l'equilibre et du Mouvement des corps solides élastique et des fluides. *Journale de l'Ecole polytechnique*, 13:139–186, 1831.

S. Pond, G. T. Phelps, J. E. Paquin, G. McBean, and R. W. Stewart. Measurements of the turbulent fluxes of momentum, moisture, and sensible heat over the ocean. *Journal of Atmospherical Sciences*, 28:901–917, 1971.

Prema. *User Manual Prema 3040 High Precision Thermometer*. PREMA Semiconductor GmbH, Mainz, Germany, 2000.

W. Press, S. Teukolsky, W. Vetterling, and B. Flannery. *Numerical Recipes in C*. Cambridge University Press, Cambridge, MA, 2 edition, 1992.

J. L. Prince and E. R. McVeigh. Motion estimation from tagged MR image sequences. *IEEE Transactions on Medical Images*, 11(2):238–249, 1992.

M. R. Querry, W. E. Holland, R. C. Waring, L. M. Earls, and M. D. Querry. Relative reflectance and complex refractive index in the infrared for sline environmental waters. *Journal of Geophysical Research*, 82:1425–1433, 1977.

K. N. Rao, R. Narasimah, and M. B. Narayanan. The 'bursting' phenomenon in a turbulent boundary layer. *Journal of Fluid Mechanics*, 48:339–352, 1971.

Raytheon. *User Manual Galileo Infrared Camera System*. Amber Engineering, Goleta, CA, 1995.

S. Reinelt. Bestimmung der transfergeschwindigkeit mittels CFT mit Wärme als Tracer. Master's thesis, Institut für Umweltphysik, University of Heidelberg, Heidelberg, Germany, 1994.

W. J. J. Rey. *Introduction to Robust and Quasi-Robust Statistical Methods*. Universitext. Springer-Verlag, Heidelber, Germany, 1983.

L. F. Richardson. The supply of energy from and to atmospheric eddies. In *Proc. Royal Society London A*, volume 97, page 354, 1920.

W. Roedel. *Physik unserer Umwelt: Die Atmosphäre*. Springer-Verlag, Heidelberg, Germany, 1992.

D. P. Rogers. Air-sea interaction; surface fluxes. Class Notes, 1994.

A. E. Ronner. *P-norm estimators in a linear regression model*. PhD thesis, Groningen University, Groningen, NL, 1977.

P. J. Rousseeuw. Least median of squares regression. *Journal of the American Statistical Association*, 79:871–880, 1984.

P. J. Rousseeuw and A. Leroy. *Robust regression and outlier detection*. Wiley, 1987.

P. J. Rousseeuw and S. Van Aelst. Positive-breakdown robust methods in computer vision. *Computing Science and Statistics*, 31:451–460, 1999.

P. J. Rousseeuw and K. Van Driessen. A fast algorithm for highly robust regression in data mining. In J. G. Bethlehem and P. G. M. van der Heijden, editors, *COMPSTAT. Proceedings in Computational Statistics. 14th Symposium,*, pages 421–426, Utrecht,NL, 2000. Physica-Verlag Heidelberg.

P. M. Saunders. The temperature at the ocean-air interface. *Journal of Atmospherical Sciences*, 24(3): 269–273, 1967.

H. Scharr. *Optimale Operatoren in der Digitalen Bildverarbeitung*. PhD thesis, University of Heidelberg, Heidelberg, Germany, 2000.

H. Scheffé. *The Analysis of Variance*. Wiley Series in Probability and Mathematical Statistics. Wiley, New York, 1959.

U. Schimpf. *Untersuchung des Gasaustausches und der Mikroturbulenz an der Meeresoberfläche mittels Thermographie*. PhD thesis, University of Heidelberg, Heidelberg, Germany, 2000.

U. Schimpf, H. Haußecker, and B. Jähne. Studies of air-sea gas transfer and micro turbulence at the ocean surface using passive thermography. In M. L. Banner, editor, *The Wind-Driven Air-Sea Interface: Electromagnetic and Acoustic Sensing, Wave Dynamics and Turbulent Fluxes*, Sydney, Australia, 1999.

H. Schlichting and K. Gersten. *Grenzschicht-Theorie*. Springer-Verlag, Heidelber, Germany, 9th edition, 1997.

P. Schlüssel, W. J. Emery, H. Grassl, and T. Mammen. On the bulk-skin temperature difference and its impact on satellite remote sensing of sea surface temperature. *Journal of Geophysical Research*, 95(C8):13341–13356, 1990.

B. Schunk. The image flow constraint equation. *Computer Vision, Graphics and Image Processing*, 35:20–46, 1986.

SeaSpace. Seaspace corporation, http://www.seaspace.com, 2001.

W. J. Shaw. Theory and scaling of lower atmospheric turbulence. In G. L. Geernaert and W. J. Plant, editors, *Surface Waves and Fluxes*, volume 1 - Current Theory, chapter 4, pages 63–90. Kluwer Academic, Norwell,MA, 1990.

M. Shizawa and K. Mase. Principle of superposition: A common computational framework for analysis of multiple motion. In *Proc. IEEE Workshop on Visual Motion*, pages 164–172, Princeton,NJ, 1991.

R. Siegel and J. R. Howell. *Thermal Radiation Heat Transfer*. Hemisphere Publishing Corporation, Washington, 3rd edition, 1992.

U. Siegenthaler and J. L. Sarmiento. Atmospheric carbon dioxide and the ocean. *Nature*, 365:119–125, 1993.

S. D. Smith. Coefficients for sea-surface wind stress, heatflux, and wind profiles as a function of windspeed and temperature. *Journal of Geophysical Research*, 93(C12):15467–15472, 1988.

A. V. Soloviev and P. Schlüssel. Parameterization of the cool skin of the ocean and the air-ocean gas transfer on the basis of modeling surface renewal. *Journal of Physical Oceanography*, 24: 1339–1346, 1994.

E. A. Spiegel and G. Veronis. On the boussinesq approximation for a compressible fluid. *Astrophysical Journal*, 131:442–447, 1960.

H. Spies. *Analysing Dynamic Processes in Range Data Sequences*. PhD thesis, University of Heidelberg, Heidelberg, Germany, July 2001.

H. Spies, H. Haußecker, B. Jähne, and J. L. Barron. Differential range flow estimation. In *DAGM*, pages 309–316, Bonn, Germany, September 1999.

J. Stefan. In *Sitzungsbericht der Akademie der Wissenschaften Wien*, volume 79, pages 391–428, 1879.

C. V. Stewart. Bias in robust estimation caused by discontinuities and multiple structures. *PAMI*, 19 (8):818–833, August 1997.

C. V. Stewart. Robust parameter estimation in computer vision. *SIAM Review*, 41(3):513–537, 1999.

C. Stiller and J. Konrad. Estimating motion in image sequences. *IEEE Signal Processing Magazine*, 16(4):70–91, 1999.

G. G. Stokes. On the theories of the internal friction of fluids in motion, and of the equilibrium and motion of elastic solids. *Transactions of the Cambridge Philosophical Society*, 9(II):8–106, 1849.

P. F. Sturm and S. J. Maybank. On plane-based camera calibration: A general algorithm, singularities, applications. In *CVPR'99*, Fort Collins, Colorado, June 1999.

H. U. Sverdrup, M. W. Johnson, and R. H. Fleming. *The Oceans*. Prentice-Hall, Englewood Cliffs, NJ, 1942.

G. Taylor. The spectrum of turbulence. In *Proc. Royal Society*, volume 102, pages 817–822, 1938.

H. Tennekes and J. L. Lumley. *A First Course in Turbulence*. MIT Press, Cambridge,MA, 1972.

G. E. Thomas and K. Stamnes. *Radiative Transfer in the Atmosphere and Ocean*. Atmospheric and Space Science Series. Cambridge University Press, Cambridge, UK, 1999.

T. Torgersen, G. Mathieu, R. H. Hesslein, and W. S. Broecker. Gas exchange dependency on diffusion coefficient. *Journal of Geophysical Research*, 87(C1):546–556, 1982.

P. Torr. *Motion Segmentation and Outlier Detection*. PhD thesis, University of Oxford, 1995.

P. Torr. Model selection for two view geometry: a review. In D. A. Forsyth, J. L. Mundy, V. Di Gesú, and R. Cipolla, editors, *Shape, Contour and Grouping in Computer Vision*, number 1681 in Lecture Notes in Computer Science, pages 277–301. Springer-Verlag, Heidelberg, 1999.

P. Torr and D. W. Murray. The development and comparison of robust methods for estimating the fundamental matrix. *Int. J. Computer Vision*, 24(3):271–300, 1997.

O. Tretiak and L. Pastor. Velocity estimation from image sequences with second order differential operators. In *Proc. 7th International Conference on Pattern Recognition*, pages 20–22, 1984.

R. Tsai and T. Huang. Estimating three-dimensional motion parameters of a rigid planar patch. *IEEE Transactions on Acoustics, Speech and Signal Processing*, 29:1147–1152, 1981.

S. Ullman. *The interpretation of visual motion*. The MIT Press Series in Artificial Intelligence. MIT Press, Cambridge, MA, 1979.

S. Uras, F. Girosi, A. Verri, and V. Torre. A computational approach to motion perception. *Biological Cybernetics*, 60:79–87, 1988.

A. W. van der Vaart. *Asymptotic Statistics*. Cambridge Series on Statistical and Probalistic Mathematics. Cambridge University Press, Camebridge, UK, 1998.

H. A. van der Vorst and G. H. Golub. 150 years old and still alive: eigenproblems. In I. S. Duff and G. A. Watson, editors, *The State of the Art in Numerical Analysis*, pages 93–119. Clarendon Press, Oxford, UK, 1997.

S. Van Huffel. The generalized total least squares problem: Formulation, algorithm and properties. In G. H. Golub and P. Van Dooren, editors, *Numerical Linear Algebra, Digital Signal Processing and Parallel Algorithms*, volume F70 of *NATO Advanced Science Institutes*, pages 651–660. Springer-Verlag, 1991.

S. Van Huffel. On the significance of nongeneric total least squares problems. *SIAM Journal on Matrix Analysis and Applications*, 13(1):20–35, 1992.

S. Van Huffel and J. Vandewalle. Analysis and solutuion of the nongeneric total least squares problem. *SIAM Journal on Matrix Analysis and Applications*, 9:360–372, 1988.

S. Van Huffel and J. Vandewalle. Analysis and properties of the generalized total least squares problem $\boldsymbol{Ax} \approx \boldsymbol{B}$ when some or all columns in a are subject to error. *SIAM Journal on Matrix Analysis and Applications*, 10(3):294–315, 1989.

S. Van Huffel and J. Vandewalle. *The Total Least Squares Problem: Computational Aspects and Analysis*. Society for Industrial and Applied Mathematics, Philadelphia, 1991.

S. Van Huffel, J. Vandewalle, and A. Haegemans. An efficient and reliable algorithm for computing the singular subspace of a matrix, associated with its smallest singular value. *Journal of Computational and Applied Mathematics*, 19:313–330, 1987.

C. F. van Loan. Generalizing the singular value decomposition. *SIAM Journal on Numerical Analysis*, 13:76–83, 1976.

S. Vedula, S. Baker, P. Rander, R. Collins, and T. Kanade. Three-dimensional scene flow. In *ICCV*, pages 722–729, Pittsbrugh, PA, September 2000.

S. B. Verma. Micrometeorological methods for measuring surface fluxes of mass and energy. *Remote Sensing Reviews*, 5:99–115, 1990.

A. Verri and T. Poggio. Against quantitative optical flow. In *Proc. of 1st International Conference on Computer Vision*, pages 171–180, London, 1987.

A. Verri and T. Poggio. Motion field and optical flow: Qualitative properties. *IEEE Transactions on Pattern Analysis and Machine Intelligence*, 11(5):490–498, 1989.

Z. Wan. *MODIS UCSB Emissivity Library*. MODIS Group of the Institute for Computational Earth System Science, UCSB, CA, http://www.icess.ucsb.edu/ zhang/EMIS/html/em.html, 1976.

R. Wanninkhof. Relationship between gas exchange and wind speed over the ocean. *Journal of Geophysical Research*, 97(C5):7373–7382, 1992.

R. Wanninkhof, W. Asher, R. Wepperning, C. Hua, P. Schlosser, C. Langdon, and R. Sambrotto. Gas transfer experiment on georges bank using two volatile deliberate tracers. *Journal of Geophysical Research*, 98(C11):20237–20248, 1993.

R. Wanninkhof, J. R. Ledwell, and W. S. Broecker. Gas exchange - wind speed relationship measured with sulfur hexafluoride on a lake. *Science*, 227(4691):1224–1226, 1985.

R. Wanninkhof, J. R. Ledwell, W. S. Broecker, and M. Hamiltion. Gas exchange on mono lake and crowley lake, california. *Journal of Geophysical Research*, 92(C13):14567–14580, 1987.

B. Ward and S. Redfern. A neural network model for predicting the bulk-skin temperature difference at the sea surface. *International Journal of Remote Sensing*, 20(18):3533–3548, 1999.

A. J. Watson, R. C. Upstill-Goddard, and P. S. Liss. Air-sea exchange in rough and stormy seas measured by a dual tracer technique. *Nature*, 349(6305):145–147, 1991.

A. M. Waxman and K. Wohn. Contour evolution, neighborhood deformation, and global image flow: planar surfaces in motion. *International Journal of Robotics Research*, 4(3):95–108, 1985.

A. M. Waxman, J. Wu, and F. Bergholm. Convected activation profiles and receptive fields for real time measurement of short range visual motion. In *Proc. Conf. Comput. Vis. Patt. Recog.*, pages 771–723, Ann Arbor, 1988.

B. C. Weare. Uncertainties in estimates of surface heat fluxes derived from marine reports over the tropical and subtropical oceans. *Tellus*, A(41):357–370, 1989.

B. C. Weare and P. T. Strub. The significance of sampling biases on calculating monthly mean oceanic surface heat fluxes. *Tellus*, 33:211–224, 1981.

E. K. Webb, G. I. Pearman, and R. Leuning. Correction of flux measurements for density effects due to heat and water vapour transfer. *Quarterly Journal of the Royal Meteorological Society*, 106: 85–100, 1980.

M. Wei. The analysis for the total least squares problem with more than one solution. *SIAM Journal on Matrix Analysis and Applications*, 13(3):746–763, 1992.

G. A. Wick, W. J. Emery, L. H. Kantha, and P. Schlüssel. The behavior of the bulk-skin sea surface temperature difference under varying wind speed and heat flux. *Journal of Physical Oceanography*, 26:1969–1988, 1996.

D. M. Wieliczka, S. Weng, and M. R. Querry. Optical constants of water in the infrared. *Applied Optics*, 28:1714–1719, 1989.

R. M. Williams and C. A. Paulson. Microscale temperature and velocity spectra in the atmospheric boundary layer. *Journal of Fluid Mechanics*, 83:547–567, 1977.

J. W. Wisnowski, D. C. Montgomery, and J. R. Simpson. A comparative analysis of multiple outlier detection procedures in the linear regression model. *Computational Statistics and Data Analysis*, 36:351–382, 2001.

A. H. Woodcock and H. Stommel. Temperatures observed near the surface of a fresh-water pond at night. *Journal of Meteorology*, 4:102–103, 1947.

J. Wu. On the cool skin of the ocean. *Boundary-Layer Meteorology*, 31:203–207, 1985.

J. Wu. Small-scale wave breaking: A widespread sea surface phenomenon and its consequence for air-sea exchanges. *Journal of Physical Oceanography*, 25:407–412, 1995.

J. C. Wyngaard and O. R. Coté. The budgets of turbulent kinetic energy and temperature variances in the atmospheric surface layer. *Journal of Atmospherical Sciences*, 28(2):190–201, 1971.

L. Zhang, T. Sakurai, and H. Miike. Detection of motion fields under spatio-temporal non-uniform illumination. *Image and Vision Computing*, 17:309–320, 1999.

Z. Zhang. A flexible new technique for camera calibration. Technical Report MSR-TR-98-71, Microsoft, Redmond, WA, USA, 1998.

Z. Zhang. A flexible new technique for camera calibration. *PAMI*, 22(11):1330–1334, November 2000.

Z. Zhang and O. Faugeras. *3D Dynamic Scene Analysis*. Springer-Verlag, Berlin, Germany, 1992.

M. D. Zoltowski. Generalized minimum norm and constrained total least squares with application to array processing. In *SPIE Signal Processing III*, volume 975, pages 78–85, San Diego,CA, 1988.

Acknowledgements

I would like to express my gratitude to Prof. Dr. Bernd Jähne for supervising this thesis and the opportunity to spend the first year at the Scripps Institution of Oceanography in San Diego. I also thank Prof. Dr. Ulrich Platt for agreeing to act as the second referee.

Thanks to Jochen Klinke for the good cooperation during my stay at Scripps and Xin Zhang for the interesting discussions. Many thanks to Horst Haußecker for waking my interest in thermography. For his unravelled hospitality and fruitful discussions during my visit at NRL in Washington I thank Richard I. Leighton. I would also like to thank Jeff Hare for providing me with heat flux estimates and other meteorological measurements from the GasExII experiment and answering frequent questions. Also thanks to Wade McGillis for supplying me with his heat flux estimates.

Many thanks to the participants of the GasExII experiment and the crew of the NOAA R/V Ronald H. Brown for making the cruise to such a rewarding experience. Special thanks to the team working on LADAS: Nelson Frew, Bob Nelson, Tetsu Hara, Nick Witzell and Uwe Schimpf.

I am especially grateful to Erik Bock for his constant support.

For answering numerous questions concerning least squares and hypothesis testing my thanks go to Johannes P. Schlöder of the IWR. Also, I would like to thank the members of the research group Digital Image Processing at the Interdisciplinary Center for Scientific Computing and at the Institut für Umweltphysik. Especially Christopher, Günther, Hanno, Hagen, Hermann, Mark, Norbert, Ralf, Reinhard, Stefan, Tobias, Uwe and Volker. Also many thanks to Annette and Elke for enduring my lack of organization.

Last but not least I wish to thank my parents for their continuous support during all these years, my sister and grandparents for their well meant advice and of course my girlfriend Annegret, who put up with me throughout the three long months I spend at sea and the sometimes stressful times when I did not.